



HAL
open science

Exploring potentialities of CIGSn lamellar phases for photoinduced applications

Amal Belhcen

► **To cite this version:**

Amal Belhcen. Exploring potentialities of CIGSn lamellar phases for photoinduced applications. Material chemistry. Nantes Université, 2023. English. NNT : 2023NANU4051 . tel-04624371

HAL Id: tel-04624371

<https://theses.hal.science/tel-04624371v1>

Submitted on 25 Jun 2024

HAL is a multi-disciplinary open access archive for the deposit and dissemination of scientific research documents, whether they are published or not. The documents may come from teaching and research institutions in France or abroad, or from public or private research centers.

L'archive ouverte pluridisciplinaire **HAL**, est destinée au dépôt et à la diffusion de documents scientifiques de niveau recherche, publiés ou non, émanant des établissements d'enseignement et de recherche français ou étrangers, des laboratoires publics ou privés.

THESE DE DOCTORAT

NANTES UNIVERSITE

ECOLE DOCTORALE N° 596
Matière, Molécules, Matériaux et Géosciences
Spécialité : Sciences Des Matériaux

Par

Amal BELHCEN

Exploring potentialities of CIGS_n lamellar phases for photoinduced applications

Thèse présentée et soutenue à Nantes, le 03/10/2023

Unité de recherche : Institut des Matériaux de Nantes Jean Rouxel, 2 rue de la Houssinière, 44322 Nantes

Rapporteurs avant soutenance :

Negar NAGHAVI Directrice de recherche CNRS, IPVF
Thomas COTTINEAU Chargé de recherche CNRS, HDR, ICPEES

Composition du Jury :

Présidente : Sophie CASSAIGNON Professeure des Universités, Sorbonne Université
Examineur : Florent BOUCHER Directeur de recherche CNRS, IMN

Dir. de thèse : Maria Teresa CALDES Chargée de recherche CNRS, HDR, IMN
Co-dir. de thèse : Nicolas BARREAU Maître de conférences, HDR, Université de Nantes

Invité(s)

Catherine GUILLOT-DEUDON Ingénieure de recherche, IMN
Adèle RENAUD Maître de conférences, Université de Rennes 1
Fabrice ODOBEL Directeur de recherche CNRS, CEISAM

« Knowledge is love and light and vision »

Helen Keller

Acknowledgements

As my three-years PhD journey comes to an end, I would like to take a moment to express my sincere gratitude to all the people who have made this thesis project possible.

This thesis was carried out at the IMN (Institut des Matériaux Jean Rouxel de Nantes) laboratory at the University of Nantes. I would like to start by thanking the director of IMN, Dr Florent Boucher, for welcoming me in the institute.

I gratefully acknowledge the members of the jury for accepting to evaluate my work. Dr Negar Naghavi, director of research CNRS at IPVF and Dr Thomas Cottineau, research fellow CNRS at ICPEES as reporters. Florent Boucher, director of research CNRS at IMN as examiner and Sophie Cassaignon, professor at Sorbonne University as examiner and the head of the jury. Thank you for your valuable time to read the manuscript and the constructive discussions.

I would like to extend my special thanks to my supervisors for selecting me among the candidates and giving me the opportunity to achieve one of my dreams.

I would particularly like to thank the director of my thesis, Dr Maria Teresa Caldes, firstly for believing in me all along the journey, without any doubts, and for bringing out the best of me. Thank you for giving me the possibility to work on this challenging and multi-disciplinary topic. I have learnt and progressed scientifically throughout these three-years. I really cannot find the words to express my gratitude to you for your unlimited support and for your time and availability whenever a question comes to my mind and whenever I knock on your office door. Besides the academic guidance, I am glad for your smile, warmth, kindness and understanding. You always tell me that I am the sunshine of the lab, but in fact, it is you who makes the lab shine with your smile and positive energy.

I would like to extend my appreciation to Nicolas Barreau, the co-director of my thesis, for his mentorship, support, patience and commitment. You have not only guided my research in everything to do with the thin films, but you also provided supportive environment. Despite your busy schedule, you always found time to help me and to carry out experiments yourself to help me move forward.

I would like to express my sincere gratitude also to Catherine Guillot deudon, my supervisor, for her kindness, support, presence and help during the experiments, particularly those involving the sealing of the silica tubes. I also thank her for her patience in accompanying me each time I had to prepare the sealed tubes, as fire always frightens me. I am very happy to get the opportunity to work with you and to get to know you as a person.

I am thankful for the countless “girls talk” sessions that I had with Mayte and Catherine whenever I felt stressed or overwhelmed. These moments helped me to face the challenges of my PhD with renewed strength and motivation. Your willingness to go above and beyond your roles as supervisors has made a significant difference in my life in the laboratory.

I am also deeply grateful for Dr Stéphane Jobic for his invaluable insights and encouragements. I appreciate your dedication in following my progress and your valuable time spent explaining things to me over the past three years, your advices have enriched my research and broadened my horizons.

I thank Dr Adèle Renaud first for welcoming me in her laboratory at ISCR in Rennes to perform all the electrochemical measurements during my thesis. I thank you for your friendly welcome, guidance, commitment and presence whenever a question came to my mind. The time spent in Rennes was a real pleasure.

Many people have helped me along the way and without them this thesis would not be what it is. I would like to express my sincere gratitude for Dr Fabrice Odobel and Dr Deborah Romito for welcoming me into their laboratory at CEISAM and for their precious time and help they gave me in carrying out the photocatalytic measurements. I would also like to thank Dr Eric Puzenat for welcoming me to his laboratory at IRCELYON in Lyon and for the time and advice he gave me. Dr H  l  ne Brault, thank you for allowing me to use your microwave for my nanopowders synthesis and for your kindness and discussions around a cup of tea. I would also like to thank the trainee Samuel Hautecoeur for his help in preparing the nanopowders.

Many thanks to Ludovic Arzel for the help provided for the photoluminescence and Raman characterizations, to Benoit Corraze for the conductivity measurements, to H  l  ne Terrisse for the zeta-potential test and to the entire microscopy team at the CMC building: Eric Gautron, Nicolas Gautier and Nicolas Stephant for all their help with the STEM, SEM, EDX elementary analyses and imagery. I also thank Amelle Rebai at IPVF for the spiro-ometad deposition on my prepared thin films, Elodie Grange for the nanopowders and Cl  ment Maheu for your time to read the manuscript. Thanks to the other people who trained me in the various techniques: Jean-Yves Mevellec for Raman, Pierre-Emmanuel Petit for XRD and Florian Massuyeau for diffuse reflectance.

I acknowledge the members of my CSI: Laurent Lombez and Etienne Janod for their time and advices.

I would like to thank all the technical and administrative staff for their help, particularly: Guylaine for her morning smile at the reception, Magalie and Muriel for their help with the paperwork for my mission trips each time and Gaetan for his technical assistance.

Finally, I am grateful to every person with whom I shared a discussion or a smile in IMN and to my MIOPS team in both the main building and the physical department. Especially my office neighbors: Christophe Payen, Philippe Deniard, Rémi Dessapt, Emmanuel Fritsch... for their morning smile and kind discussions. I also thank Ahmed Rhallabi and Shunsuke Sasaki for their friendly discussions whenever I bump into them in the corridors of IMN.

Now coming to my friends in IMN, I would like to take this opportunity to thank all the PhD students, post-doctorals and interns with whom I spent an incredible three years and who have made this lab a better place. The list is long, but I hope I won't forget anyone. Starting with my office mates: Bachchar, Divyesh and Tanguy without forgetting Feodor. I also address my appreciation to my girls: Insaf, Hind and Nassima for the time they spent listening to me during the difficult times and for the beautiful moments we spent together. A big thanks to Lozanne, Matt, Ayoub, Emmanuel, Branimir, Nusik, Maria, Diana, Sabrina, Rebeca, Mohammed, Aswadh, Sandy, Hajar, Zohra, Yassine, Come, Aline, Nouridine, Tatiana, Gudaysew, Michael, Louis, Marcelo, Hannah, Hanyu, Rachid, Eva... To all the PhD students whose paths crossed mine during this journey and with whom I shared beautiful moments, this adventure would not be the same without you guys and especially without Uno time as I was Uno queen for some time. I am leaving today with wonderful memories.

Finally, I want to express my heartfelt gratitude to the unwavering support of my family and friends.

To my beloved parents, Mama and Papa, your love, boundless encouragement and sacrifices have been the driven force to pursuit my dreams. Believing in me allowed me to become the best version of me and made this achievement possible. I simply love you from the depths of my heart.

To my sisters, Sara and Chahd, you have been my best friends, your love, support and presence enlighten my life every day. You have always been there to cheer me up in any situation.

To my dear family and friends, thank you for your encouragements, support and shared moments of joy. I would like to pay tribute to my grandparents in heaven, who I know are watching over me. Your love, wisdom and support continue to inspire me and guide me. This achievement would not have been possible without you.

Finally, to my love Yasser, your faith in my dreams and your unlimited support have been my pillars of strength. Your patience and understanding throughout this journey have been limitless. Your love has made my life infinitely better, and I am thankful for every moment we share. I cannot wait to see what life will bring us, I am sure it will bring beautiful great things.

Table of content

Résumé en français.....	1
General introduction.....	9
References.....	12
Chapter 1: Focus on Cu₂S-In₂S₃-Ga₂S₃ system	13
1. Chalcogenides	13
2. Pseudo ternary system Cu ₂ S-In ₂ S ₃ -Ga ₂ S ₃	14
2.1. Stoichiometric Cu(In,Ga)S ₂ chalcopyrite (CIGS).....	15
2.1.1. Cu(In,Ga)S ₂ characteristics	15
2.1.2. Cu(In,Ga)S ₂ applications	17
Photovoltaics.....	17
Photocatalysis for hydrogen production	18
2.2. CuInS ₂ -In ₂ S ₃ system	19
2.2.1. CuIn ₅ S ₈ characteristics	19
2.2.2. CuIn ₅ S ₈ applications	20
Photovoltaics.....	20
Photocatalysis for hydrogen production	20
2.3. CuGaS ₂ -Ga ₂ S ₃ system.....	21
2.3.1. CuGa ₃ S ₅ and CuGa ₅ S ₈ characteristics	21
2.3.2. Applications.....	22
CuGa ₃ S ₅	22
CuGa ₅ S ₈	22
2.4. GaInS ₃	22
2.5. CIGS _n lamellar compounds	23
2.5.1. Applications.....	28
2.6. Afterwords.....	29

References.....	30
Chapter 2: Optoelectronic properties of CIGS_n lamellar compounds	37
1. Synthesis and characterisation of CIGS _n compounds.....	38
2. Diffuse reflectance.....	42
3. Electrochemistry of semiconductors: basics	44
3.1. Semiconductors.....	44
3.2. Electrochemical cell.....	46
3.3. Interface semiconductor and electrolyte.....	47
4. Electrochemical measurements	51
4.1. Determination of the semiconductor type	51
4.1.1. Determination of the semiconductor type using current potential (I-V) curve measurements under dark.....	51
4.1.2. Determination of the semiconductor type using current potential measurements under chopped illumination	54
4.2. Determination of majority charge carriers lifetime using chronopotentiometry.....	56
4.3. Determination of flat band potential (Fermi level) and charge carriers density by electrochemical impedance spectroscopy	57
5. Characterisation of the electronic properties of CIGS _n compounds: experimental results.....	62
6. Energy diagrams.....	70
7. Photoluminescence.....	74
8. A comparison discussion between CIGS _n and CIGS	76
Appendix chapter 2	78
X-ray diffraction.....	78
Reflectance diffuse	78
Working electrodes preparation	78
Conductivity.....	79
Photoluminescence	80
References.....	81

Chapter 3: CIGS_n Thin films for photovoltaic application	87
1. A look to photovoltaics	87
1.1. Photovoltaic effect	87
1.2. Operating standard conditions of a solar cell	90
1.3. Photovoltaic technologies	91
2. The CIGS-based photovoltaics	93
2.1. The architecture of CIGS solar cells	93
2.2. Requirements for a good CIGS cell	96
2.3. Motivation: CIGS _n lamellar compounds potential use as PV absorbers	97
3. Elaboration of CIGS _n thin films.....	98
3.1. Co-evaporation synthesis	98
3.2. Structural and chemical characterizations of CIGS _n	101
3.3. Energy diagrams and optoelectronic properties.....	108
3.3.1. Optical properties	108
3.3.2. Photoluminescence	110
3.3.3. Electrochemical measurements.....	111
3.3.4. Kelvin probe force microscopy measurements	114
3.3.5. Photo-electrochemical measurements.....	115
3.4. Device assemblies.....	118
3.4.1. Classical CIGS architecture	118
3.4.2. n-i-p architecture	123
4. Conclusions	127
Appendix chapter 3	128
X-ray diffraction	128
Scanning transmission electron microscopy	128
Raman spectroscopy.....	131
Glow discharge optical emission spectrometry GDOES	131
Reflectance diffuse	132
Kelvin probe force microscopy	132
Device characterization	134
Current-voltage JV	134
External quantum efficiency	135

Imagery.....	136
References.....	137
Chapter 4: CIGS_n-type nanopowders for photocatalysis application.....	143
1. A look to photocatalysis.....	143
1.1. Photocatalysis.....	143
1.2. Heterogeneous photocatalysis principle.....	144
1.3. Photocatalytic hydrogen production.....	146
1.3.1. Water splitting - artificial photosynthesis.....	146
1.3.2. Photocatalytic H ₂ production from alcohols.....	148
1.4. Photocatalytic materials.....	148
1.4.1. Requirements of an efficient photocatalyst	148
1.4.2. Chalcogenides	149
1.4.3. CIGS _n lamellar compounds as potential visible light photocatalysts.....	151
2. Elaboration of CIGS _n -type photocatalysts.....	152
2.1. Synthesis and characterization of CIGS ₆ and CIGS photocatalysts.....	152
2.1.1. Microwave assisted solvothermal synthesis.....	152
2.1.2. Synthesis and characterisation of chalcopyrite CuIn _{0.7} Ga _{0.3} S ₂ (CIGS)	155
2.1.3. Synthesis and characterisation of Cu _{1.44} In _{2.77} Ga _{0.76} S ₆ (CIGS ₆).....	160
2.2. Zn ₃ In ₂ S ₆ and GaInS ₃ approach	166
2.2.1. Synthesis and characterization of Zn _{3-x} (Ga _{0.5} Cu _{0.5}) _x In ₂ S ₆ series.....	167
2.2.2. Synthesis and characterization of the Cu _{3x} Ga _{1-x} InS ₃ compounds	170
2.3. Summary.....	174
3. Photocatalytic hydrogen production	176
3.1. Sacrificial electron donor selected	176
3.2. Photocatalytic Set-Up.....	177
3.3. Hydrogen production results.....	178
3.3.1. Hydrogen evolution using acid ascorbic as sacrificial electron donor...179	
3.3.2. Hydrogen evolution using acid ascorbic and a co-catalyst	180
3.3.3. Hydrogen evolution using triethanolamine as sacrificial electron donor	
182	
4. Discussion.....	183

References.....	186
General conclusion	193

Résumé en français

Face aux inquiétudes croissantes concernant le changement climatique et l'augmentation de la demande de sources d'énergie durables, il est devenu impératif de chercher des technologies capables de remplacer les combustibles fossiles.

L'énergie solaire est considérée comme l'une des alternatives les plus prometteuses aux combustibles fossiles; il s'agit d'une source abondante. De plus, l'énergie du rayonnement solaire qui atteint la surface de la terre en seulement une heure est suffisante pour assurer la consommation énergétique de tous les êtres humains pendant un an. En exploitant l'énergie solaire, nous pouvons contribuer de manière significative à l'atténuation des problèmes liés aux changements climatiques et à la promotion du développement durable.

En suivant cette voie, il a fallu développer de nouvelles technologies pour convertir l'énergie solaire. Les systèmes photovoltaïques qui permet de convertir l'énergie solaire en énergie électrique deviennent de plus en plus une technologie bien établie sur le marché de la conversion de l'électricité solaire. Parallèlement, l'énergie solaire peut être transformée aussi en énergie chimique à l'aide de photocatalyseurs. Ainsi, les carburants solaires comme l'hydrogène sont attrayants en tant qu'alternative propre aux carburants fossiles, puisqu'ils peuvent être produits à partir de ressources abondantes telles que l'eau et le dioxyde de carbone. En effet, bien que l'hydrogène soit l'élément le plus abondant dans l'univers, il n'existe sur terre que lié à diverses molécules, notamment l'eau H₂O ou les hydrocarbures. Actuellement, l'hydrogène est majoritairement généré à partir de combustibles fossiles. Cependant, pour que l'hydrogène soit considéré comme une énergie renouvelable propre, il doit être produit à partir d'une source d'énergie renouvelable.

Dans un contexte d'exploitation de la lumière visible, le gap optique du semiconducteur utilisé comme absorbeur dans les dispositifs photovoltaïques ou photocatalytiques, doit être inférieur à 3 eV. Cette exigence ouvre la voie aux matériaux chalcogénures. En effet, contrairement aux oxydes, les chalcogénures métalliques sont des candidats plus appropriés pour le photovoltaïque et la photocatalyse, puisqu'ils bénéficient souvent d'un gap optique optimal. Ils ont donc par une plus grande réponse sur le spectre solaire, ainsi qu'une plus faible masse effective de porteurs, ce qui favorise leur séparation et leur migration. Parmi ces matériaux, les chalcogénures de sulfure à base de cuivre, et en

particulier les composés ternaires et quaternaires, sont intéressants en raison de leur grande flexibilité de composition, qui permet d'ajuster leurs propriétés optiques.

De plus, la présence de plusieurs éléments signifie que ces semi-conducteurs présentent souvent une forte concentration de défauts, qui peuvent être modifiés par ingénierie des défauts pour changer certaines propriétés fonctionnelles, telles que la conductivité électrique et les caractéristiques optoélectroniques. En conséquence, notre groupe travaille sur le système $\text{Cu}_2\text{S-In}_2\text{S}_3\text{-Ga}_2\text{S}_3$. Ce système est bien étudié, en particulier la famille de chalcopyrites $\text{Cu}(\text{In}_{1-x}\text{Ga}_x)\text{S}_2$ connue sous le nom de CIGS. Ces matériaux sont étudiés comme absorbeurs dans les cellules solaires tandem, mais aussi en tant que photocatalyseurs pour l'évolution de l'hydrogène. De plus, notre groupe a identifié dans ce système de nouveaux matériaux lamellaires, pouvant présenter des propriétés optoélectroniques intéressantes, modulables par leur composition.

Ces nouveaux matériaux sont de symétrie hexagonale et présentent un caractère 2D marqué avec un gap de Van der Waals d'environ 3 Å séparant les blocs et une formule générique $(\text{M}(\text{Td}))_{n-2}(\text{In}(\text{Oh}))\text{S}_n$ ($\text{M} = \text{Cu}, \text{In}, \text{Ga}$; $n = 4, 5, 6$ et 7). Ils sont construits à partir de couches d'octaèdres (InS_6) partageant des arêtes sur lesquelles se condensent de part et d'autres des couches de tétraèdres (MS_4) avec $\text{M} = \text{Cu}, \text{In}, \text{Ga}$ partageant des sommets. Le composé CIGS de structure chalcopyrite (symétrie tétragonale), quant à lui, présente un caractère 3D avec uniquement des environnements tétraédriques de soufre pour tous les cations.

La présence de lacunes cationiques intrinsèques et l'occupation mixte des sites tétraédriques (Td) permettent d'ajuster la composition chimique, et par conséquent de modifier les propriétés optiques. De plus, leur gap optique (1.7 - 1.9 eV) est comparable à celui de la chalcopyrite $\text{Cu}(\text{In}_{0.7}\text{Ga}_{0.3})\text{S}_2$, étudiée actuellement comme absorbeur dans des cellules solaires tandem. D'autre part, les phases CIGS_n sont isostructurales des composés ZnIn_2S_4 et $\text{Zn}_3\text{In}_2\text{S}_6$, utilisés également comme photocatalyseurs pour la production d'hydrogène dans le domaine visible. Ceci suggère leur utilisation potentielle dans les domaines du photovoltaïque et de la photocatalyse.

L'objectif de cette thèse est donc d'approfondir l'étude de ces nouveaux matériaux nommés CIGS_n , et d'identifier leur potentiel pour des applications photoinduites (e.g. photovoltaïque et photocatalyse), en comparaison avec la chalcopyrite $\text{Cu}(\text{In}_{0.7}\text{Ga}_{0.3})\text{S}_2$.

Pour ce faire, leurs diagrammes d'énergie ont été établis en combinant des mesures (photo)électrochimiques avec la spectroscopie de photoélectrons X et la réflectance diffuse. Les bandes de conduction et de valence des composés CIGS_n , se positionnent de manière intéressante par rapport aux potentiels redox impliqués dans certaines réactions photocatalytiques. D'autre part, quelques-uns de ces composés présentent un comportement électrique ambipolaire (type p/n), ce qui les rend prometteurs. Des nanopoudres de CIGS_n ont été synthétisées par voie solvothermale assistée par micro-

ondes, afin d'optimiser la microstructure et d'évaluer leur activité photocatalytique pour l'évolution de l'hydrogène en présence d'alcools. Parallèlement, des couches minces de ces matériaux ont été préparées par co-évaporation afin de fabriquer et caractériser des cellules photovoltaïques avec différentes architectures

Ce manuscrit présentera les résultats obtenus concernant les propriétés photoinduites des composés CIGS_n. Il se divise ainsi en plusieurs chapitres:

Chapitre 1 : Focus sur le système Cu₂S-In₂S₃-Ga₂S₃

Ce chapitre présente un aperçu sur des matériaux ternaires et quaternaires dans le système Cu₂S-In₂S₃-Ga₂S₃ en se focalisant sur les composés lamellaires CIGS_n, CIGS stœchiométrique (CuGa_{0.3}In_{0.7}S₂), GaInS₃ et les composés lacunaires ordonnés (OVC), en présentant leurs caractéristiques et leurs applications dans les domaines photovoltaïques et de la photocatalyse.

Chapitre 2 : Propriétés optoélectroniques des composés lamellaires CIGS_n

L'objectif de ce chapitre est de déterminer les propriétés optiques et électroniques des composés lamellaires CIGS_n, en relation avec les critères nécessaires pour des applications photovoltaïques ou photocatalytiques. Une comparaison avec celles du composé CIGS (CuGa_{0.3}In_{0.7}S₂) chalcopyrite sera faite.

Pour ce faire, une série de propriétés intrinsèques doivent être évaluées, telles que l'absorption de la lumière visible, l'énergie de la bande interdite, la nature des porteurs majoritaires (c'est-à-dire le type de semi-conducteur), la durée de vie des porteurs de charges ainsi que le niveau de Fermi. En outre, pour améliorer l'efficacité photovoltaïque ou photocatalytique, un bon alignement des bandes est nécessaire, afin d'optimiser la séparation et la migration des porteurs photogénérés. Ainsi, les diagrammes d'énergie des composés CIGS_n ont été déterminés afin de les comparer à ceux des couches tampons photovoltaïques standards, ainsi qu'aux potentiels redox impliqués dans certaines réactions photocatalytiques. Pour réaliser cette étude, une approche analytique combinant la spectroscopie de réflectance diffuse, les mesures (photo)électrochimiques et la spectrométrie de photoélectrons X a été mise en place.

La première partie du chapitre est dédiée à la synthèse et la caractérisation structurale des composés CIGS_n. Puis, les gaps optiques des composés ont été déterminés par réflectance diffuse.

La deuxième partie du chapitre est consacrée à la caractérisation électrochimique complète des composés CIGS_n, précédée d'une description des mesures électrochimiques effectuées pendant ce travail. Ainsi, des analyses électrochimiques dans l'obscurité et sous illumination ont permis de déterminer la nature des porteurs majoritaires ainsi que le niveau de Fermi de nos matériaux. Des mesures de photoluminescence ont également

été réalisées afin de sonder l'existence de défauts dans le gap de ces matériaux. Ces défauts pourraient influencer la cinétique des charges photogénérées et améliorer l'absorption de la lumière en déplaçant la région d'absorption vers le rouge.

Enfin, pour rationaliser les différentes propriétés électroniques et photoconductrices de la famille CIGS_n par rapport à celles de la chalcopyrite CIGS, les diagrammes d'énergie ont été établis, en combinant des techniques de caractérisation électrochimique et spectroscopiques, dans un but comparatif. En plus, nous avons effectué un calcul supplémentaire pour valider les diagrammes d'énergie obtenus. Cette détermination se fait à l'aide d'une approche basée sur l'électronégativité de Mulliken et le gap optique du matériau.

En raison des potentiels de bande plate similaires, les diagrammes d'énergie de tous les composés lamellaires CIGS_n sont très similaires avec un niveau de Fermi autour de (-4.4, -4.5 eV), qui est différent de la chalcopyrite CIGS avec un niveau de Fermi égal à -5.1 eV et une bande de conduction de plus faible énergie. Ceci est cohérent avec une densité d'électrons plus élevée dans les phases lamellaires qui corrobore le comportement de type n. Il en résulte cependant que les niveaux de Fermi semblent piégés au milieu de la bande interdite pour tous les composés, comme pour un semi-conducteur compensé, dans lequel les défauts des donneurs et des accepteurs sont liés de telle sorte que leurs effets électriques opposés sont partiellement annulés. Toutefois, d'après les mesures électrochimiques, seul le CIGS_6 se comporte comme un composé ambipolaire.

Par ailleurs, une différence dans les durées de vie des porteurs de charge a été observée entre les composés lamellaires et la chalcopyrite CIGS. Il a été constaté que la durée de vie associée au processus de recombinaison des porteurs dans les composés CIGS_n est plus élevée que dans le CIGS. Cela suggère que les composés lamellaires ont besoin d'un temps plus long pour que la recombinaison des porteurs se produise. De plus, il semble également que ce temps de vie augmente avec le nombre de couches tétraédriques dans la structure lamellaire ($\text{CIGS}_6 > \text{CIGS}_5 > \text{CIGS}_4$). En fait, cette différence pourrait s'expliquer par la structure complexe des composés lamellaires, qui se caractérise par la présence de lacunes cationiques intrinsèques et d'une occupation mixte (atomes Cu-Ga-In) sur les sites tétraédriques, ce qui donne lieu à un grand nombre de défauts ponctuels dans le matériau, qui peuvent certainement influencer le processus de recombinaison. Cette hypothèse est confirmée par les mesures de photoluminescence, qui révèlent une densité de défauts dans la bande interdite importante, dans le cas des composés lamellaires. Les mesures de résistivité par la méthode 4 points, n'ont pas pu être réalisées dans le cas des composés lamellaires en raison de leur forte résistivité.

L'alignement des bandes des composés CIGS_n par rapport aux couches tampons les plus courantes (ZnO, CdS et ZnOS) utilisées dans les dispositifs photovoltaïques à base de CIGS est loin d'être optimal. De plus, les composés lamellaires CIGS_n ont montré un

comportement de semi-conducteur de type n pour CIGS₄ et CIGS₅ et un comportement ambipolaire dans le cas du CIGS₆, tandis que la chalcopyrite CIGS est un semi-conducteur de type p. Cela peut amener à changer les couches tampons de type n (ZnO, CdS et ZnOS) ou à s'orienter vers un assemblage totalement nouveau comme l'architecture n-i-p en considérant le matériau ambipolaire comme un composé intrinsèque. Le potentiel des matériaux lamellaires dans les applications photovoltaïques sera discuté dans le chapitre 3.

D'autre part, les bandes d'énergie des composés CIGS_n montrent comme pour CIGS, un positionnement intéressant en ce qui concerne les potentiels redox impliqués dans certaines réactions photocatalysées comme la dissociation de l'eau H₂O et la réduction du CO₂. En fait, les composés CIGS_n semblent pouvoir catalyser la réaction de réduction de l'eau mais pas celle de l'oxydation de l'eau, ce qui les rend inadaptés à la dissociation de l'eau (water splitting). Cependant, les composés CIGS_n pourraient être intéressants pour la réaction de production d'hydrogène en utilisant un alcool comme agent sacrificiel. De plus, nous supposons que le comportement ambipolaire mis en évidence dans ces composés, facilitera de manière similaire les réactions d'oxydation et de réduction, puisqu'aucune de deux réactions sera limitée par la mobilité d'un type de porteurs de charge.

Chapitre 3 : Couches minces de CIGS_n pour les applications photovoltaïques

La première partie de ce chapitre est consacrée à quelques rappels sur les cellules photovoltaïques à base de CIGS. Une description du principe de fonctionnement et de l'architecture standard est présentée. L'objectif de cette étude consiste à évaluer le potentiel des couches minces de CIGS_n en tant qu'absorbants.

La deuxième partie du chapitre est consacrée à l'élaboration des couches minces de CIGS_n. Ainsi, des films minces de CIGS₅ et CIGS₆ ont été déposés sur différents substrats par co-évaporation, suivi des caractérisations structurelles et analyses chimiques. L'étude s'est essentiellement focalisée sur le composé CIGS₅, qui a été la seule phase lamellaire obtenue avec succès sous la forme de couche mince monophasée.

Les propriétés optoélectroniques sont également présentées. Ainsi une étude complète a été réalisée à l'aide de mesures électrochimiques pour caractériser le type du semi-conducteur et estimer le potentiel des bandes plates, afin de déterminer le niveau de Fermi des couches minces préparées. Ensuite, les diagrammes d'énergie ont été établis à l'aide du calcul basé sur l'électronégativité de Mulliken et la bande interdite du matériau. Le diagramme d'énergie déterminé pour la couche mince de CIGS₅, est proche de celui obtenu avec la poudre de référence à haute température, avec des valeurs de niveau de Fermi similaires, également confirmées par les analyses microscopie à sonde de Kelvin (KPFM).

Dans la dernière partie de ce chapitre, la réalisation des assemblages de cellules photovoltaïques est présentée. Pour ce faire, deux architectures différentes (classique et n-i-p) ont été testées. Les paramètres photovoltaïques des dispositifs résultants ont été évalués par des mesures de courant-tension (IV) et de rendement quantique externe (EQE). Les deux configurations différentes de cellules solaires aboutissent à des rendements très faibles.

Les propriétés intrinsèques des films minces de CIGS_n ont démontré qu'ils ne sont pas adaptés aux applications photovoltaïques, en raison de leur résistivité et de la structure complexe des composés lamellaires siège de nombreux défauts ponctuels.

Au cours de cette thèse, l'orientation des couches déposées n'a pas été contrôlée. Par conséquent, pour optimiser l'élaboration des cellules solaires, nous pourrions rechercher un substrat avec des paramètres de maille proches des composés lamellaires CIGS_n , afin d'assurer une croissance contrôlée de l'absorbeur et d'améliorer sa microstructure. Ceci pourrait se traduire par un meilleur transport des porteurs de charge et une augmentation du potentiel de circuit ouvert (V_{oc}) de la cellule.

Par ailleurs, la qualité du dispositif pourrait être améliorée en remplaçant la couche tampon par une couche appropriée permettant un meilleur alignement des bandes de conduction et de valence à l'interface, ce qui se traduirait par de meilleurs paramètres photovoltaïques.

Chapitre 4 : Nanopoudres de type CIGS_n pour des applications photocatalytiques

Ce chapitre traite l'élaboration de matériaux lamellaires CIGS_n dans le but d'examiner leurs potentialités pour la photocatalyse dans le visible.

Dans une partie préliminaire, quelques principes de base sur la photocatalyse sont développés. Les principaux mécanismes photocatalytiques de production d'hydrogène par dissociation de l'eau et déshydrogénation des alcools sont décrits.

La deuxième partie décrit la préparation des nanopoudres par synthèse solvothermale assistée par micro-ondes et leurs caractérisations chimiques, structurales et optoélectroniques.

Ensuite, nous nous concentrerons plus particulièrement sur le composé lamellaire CIGS_6 , qui présente un comportement ambipolaire intéressant, ainsi que sur la chalcopyrite CIGS considérée comme une référence dans le cadre de cette thèse. Les nanoparticules des composés lamellaires et du composé CIGS chalcopyrite ont été synthétisées avec succès. Cependant, les premières tentatives ont montré que le matériau CIGS_6 préparé, comportait une phase secondaire type chalcopyrite. C'est pour cette raison que deux stratégies différentes ont été introduites pour obtenir des nanopoudres monophasées présentant un type structurel CIGS_6 . Ainsi, nous avons décidé d'effectuer une

substitution cationique dans deux composés isostructuraux ($Zn_3In_2S_6$ et $GaInS_3$) du $CIGS_6$. En effet, malgré la présence de plusieurs polymorphes, aucun de ces matériaux ne présente une structure de chalcopyrite.

Enfin, des expériences photocatalytiques sous illumination visible ont été réalisées sur les photocatalyseurs préparés, en utilisant différents agents sacrificiels (acide ascorbique et triéthanolamine). Les rendements de production d'hydrogène sont présentés, permettant une comparaison avec la littérature.

Parmi les composés préparés, $Zn_{2.4}Ga_{0.3}Cu_{0.3}In_2S_6$, $Cu_{0.3}Ga_{0.9}InS_3$ (ZIS-0.6, GIS-0.1 respectivement) et CIGS présentent une surface spécifique élevée, permettant une activité photocatalytique efficace pour la production d'hydrogène. En revanche, la faible surface spécifique des nanopoudres de $CIGS_6$ pourrait expliquer l'absence d'activité photocatalytique.

En comparant les composés lamellaires à la chalcopyrite CIGS, il est évident que les composés lamellaires montrent des performances plus élevées pour la production d'hydrogène, en utilisant l'acide ascorbique comme donneur d'électrons sacrificiel. Cependant, ce n'est pas le cas dans la littérature lorsque Na_2SO_3/Na_2S sont utilisés comme agent sacrificiel. Pour tous les composés, la production de H_2 n'est mesurée qu'après 1.5 heure. Pour les composés lamellaires, elle continue à augmenter fortement dans les 24 heures. En revanche, l'échantillon de CIGS commence à produire de l'hydrogène seulement 4 heures plus tard.

Par ailleurs, le ZIS-0.6 dérivé de $Zn_3In_2S_6$ est le seul échantillon qui a généré de l'hydrogène en utilisant à la fois des solutions acide (acide ascorbique) et basique (triéthanolamine), et qui a affiché les meilleures performances. De manière significative, il a été constaté que le rendement d'évolution d'hydrogène mesuré ($137 \mu\text{mol.g}^{-1}.\text{h}^{-1}$) en milieu acide est comparable à celui des photocatalyseurs $Zn_3In_2S_6$ et $Pt/ZnIn_2S_4$ décrits dans la littérature. De plus, dans le cas de ZIS-0.6, l'ajout d'un co-catalyseur n'est pas nécessaire. D'autre part, le rendement d'hydrogène du composé GIS-0.1 ($52.1 \mu\text{mol.g}^{-1}.\text{h}^{-1}$) est comparable à celui rapporté pour le $CuGa_2In_3S_8$ utilisant Na_2SO_3/Na_2S comme agent sacrificiel ($40 \mu\text{mol.g}^{-1}.\text{h}^{-1}$). En effet, ce dernier composé présente une composition chimique assez proche de celle de GIS-0.1 ($Cu_{0.74}Ga_2In_{3.1}S_8$).

Pour l'ajout d'un co-catalyseur, nous avons choisi de suivre le même protocole que celui utilisé pour le composé lamellaire $CuGa_2In_3S_8$ afin de faciliter la comparaison. L'utilisation du Ni^{2+} comme co-catalyseur réduit l'activité photocatalytique avec le temps. Ceci laisse penser à une altération du photocatalyseur et/ou du co-catalyseur avec le temps. Finalement, les performances s'avèrent meilleures sans utilisation de Ni^{2+} . Par ailleurs, un test avec du Pt comme co-catalyseur a également été réalisé. Cependant, nous n'avons pas réussi à photo-déposer du Pt sur notre échantillon.

Nos matériaux sont des photocatalyseurs prometteurs pour la lumière visible, ce qui ouvre de nouvelles perspectives telles que la réduction du CO₂. Les études de production d'hydrogène seront complétées en utilisant des donneurs d'électrons sacrificiels alternatifs tels que Na₂SO₃/Na₂S. Il nous faut également explorer des co-catalyseurs plus appropriés qui puissent se greffer/photo-déposer avec succès sur les échantillons préparés, afin d'améliorer leur efficacité photocatalytique sans provoquer d'effets délétères. D'autre part, il est absolument nécessaire d'explorer et de comprendre les mécanismes et la cinétique des réactions.

Pour une meilleure exploration, il faut optimiser le protocole de synthèse afin de préparer des nanopoudres de CIGS_n monophasées avec une surface spécifique élevée et des morphologies des nanocristaux optimisées. Toutefois, la caractérisation des nanopoudres de CIGS_n reste un défi pour plusieurs raisons telles que la taille nanométrique des particules, la difficulté de contrôler la stœchiométrie et d'identifier leurs structures. Nous devons donc réussir à briser les agglomérats de nanograins à l'aide d'ultrasons, afin de pouvoir effectuer une caractérisation structurale plus précise par nanodiffraction électronique.

Par ailleurs, dans cette thèse, les composés CIGS_n n'ont été étudiés que comme photocatalyseurs à matériau unique, alors que leur utilisation dans des hétérojonctions pourrait améliorer leurs performances. En effet, d'après la littérature, les hétérojonctions présentent généralement de meilleures performances que les photocatalyseurs à matériau unique, car la séparation des porteurs est améliorée et les pertes par recombinaison sont réduites. Le sulfure MoS₂ est considéré comme un des co-catalyseurs le plus prometteur pour des hétérojonctions. Par exemple, les hétérojonctions MoS₂-ZnIn₂S₄ et MoS₂-Zn₃In₂S₆ ont permis d'obtenir une production d'hydrogène notablement supérieure à celle des photocatalyseurs ZIS_n simples. Par conséquent, il serait également intéressant d'explorer l'hétérojonction MoS₂-CIGS_n.

Le chapitre 5 présente les conclusions et les perspectives du travail.

General introduction

With the increase of the climate change concerns and the need of sustainable energy sources, it became necessary to look for technologies to replace the fossil resources, which remains leading over the years, with providing 63.3% of world global electricity generation compared to 36.7% supplied from renewable energies.¹

Additionally, with the increasing demand of energy, solar energy is considered as among the most promising alternative of fossil fuels; it is an abundant source. Just as well, the sun produces an enormous power, around 120 000 Terawatts in one year.² The remarkable thing is that the solar radiation energy reaching the ground of the earth in only 1 hour is enough to provide all humans energy consumption for a year,² that is about 4.6×10^{20} joules.³ Differently, the total oil reserve on earth is 3 trillion barrels, which is said to contain 1.7×10^{22} of energy. To put this in perspective, this amount is equivalent to the energy that the earth receives from the sun in just 1.5 days,³ this would save the planet as long as we succeed to capture it. The sunlight can be converted into three forms of energy: electricity, chemicals and heat.⁴

By harvesting solar energy, we can make a significant contribution to mitigating climate change and promoting sustainable development. Follow this path, it has been required to develop new technologies to convert the solar energy; either into electrical energy using photovoltaic systems that are becoming increasingly a well-settled technology in the market for the solar-electricity conversion, with 1.5 % of the global electricity generation.⁵ Another way is to convert solar energy into chemical energy using photocatalysis, whereby solar fuels are attractive as another clean alternative of fossil fuels, because they can be produced from abundant resources such as water and carbon dioxide.⁶⁻⁸ Among solar fuels, hydrogen is the future energy. In this context, hydrogen generation through photocatalytic water splitting appears as a key issue.

In this context, in order to absorb in the visible light, the semiconductor optical gap is tuned to be lower than 3 eV, which opens the way towards chalcogenides materials. Therefore, in contrast to oxides, metal chalcogenides are more suitable candidates for photovoltaics and photocatalysis as they often benefit from an optimal optical gap, which translates into a greater response over the solar spectrum, as well as low effective mass of carriers, which favors their separation and migration.

Among these materials, copper-based sulphide chalcogenides and especially ternary and quaternary compounds are interesting, due to their wide range of compositional flexibility, which allows the adjustment of their optical properties.

In addition, the presence of several elements means that these semiconductors often have a high concentration of defects, which can be modified by defect engineering to change certain functional properties, such as electrical conductivity and optoelectronic characteristics. Accordingly, the $\text{Cu}_2\text{S-In}_2\text{S-Ga}_2\text{S}_3$ chalcogenides system is well-studied for different applications as photovoltaics and photocatalysis. This system is currently the seat of exploring new materials, in particular quaternary compounds, as they can be developed by modifying the composition of the elements.

Therefore, this PhD work is included in this framework. To tackle this issue, new lamellar copper-based sulphides named CIGS_n , identified in the $\text{Cu}_2\text{S-In}_2\text{S-Ga}_2\text{S}_3$ system, will be explored for photovoltaics and solar driven photocatalytic hydrogen production.

Indeed, these compounds exhibit an optical gap (1.7 - 1.9 eV) comparable to that of the chalcopyrite $\text{Cu}(\text{In}_{0.7}\text{Ga}_{0.3})\text{S}_2$ (CIGS), studied as absorber in tandem solar cells. On the other hand, the CIGS_n phases are isostructural of the compounds ZnIn_2S_4 and $\text{Zn}_3\text{In}_2\text{S}_6$, used as photocatalysts for hydrogen production under visible light. Furthermore, CIGS was also studied as photocathode in photoelectrochemical water splitting.

The manuscript is divided into the following chapters:

Chapter 1 provides an insight into the $\text{Cu}_2\text{S-In}_2\text{S-Ga}_2\text{S}_3$ system. It defines the $\text{Cu}_2\text{S-In}_2\text{S-Ga}_2\text{S}_3$ pseudo ternary system with focusing on stoichiometric CIGS ($\text{CuGa}_{0.3}\text{In}_{0.7}\text{S}_2$), GaInS_3 and the ordered vacancy compounds (CuIn_5S_8 , CuGa_3S_5 and CuGa_5S_8). It also reports their characteristics and some of their applications in the fields of photovoltaics and photocatalytic hydrogen production. Finally, it introduces an overview on the CIGS_n lamellar compounds, which are the main objective of the thesis.

Chapter 2 presents the fundamental approach followed, in order to determine the CIGS_n compounds optoelectronic properties, compared to CIGS. To do this, a series of intrinsic properties is evaluated such as visible light absorption, band gap energy, the type of the semiconductor (nature of the majority charge carriers), charge carrier lifetimes and the position of the conduction and valence bands as well as Fermi level. It first describes the synthesis and characterisation of powder samples. Then, some notions about (photo)electrochemical methods carried out during this thesis are presented. Moreover, it reports the energy diagrams construction, combining three techniques (diffuse reflectance, electrochemical impedance and X-ray photoelectron spectroscopies). Finally, photoluminescence and conductivity measurements were also performed to complete investigation.

Chapter 3 reports some photovoltaics basics, highlighting the operating principle and the CIGS-based solar cell standard configuration. Then, it describes thin films deposition using co-evaporation and the different structural and optoelectronic characterisations used to provide a better understanding of thin-film properties. In addition, electrochemical measurements were performed to estimate the Fermi level, in order to complete the energy diagrams determined using a calculation based on Mulliken electronegativity. Finally, the photovoltaic parameters obtained using current-voltage and external efficiency measurements from two different device architectures (conventional and n-i-p configurations) are discussed.

Chapter 4 outlines some of the basics of photocatalysis, focusing on hydrogen evolution mechanisms using water splitting and alcohols as sacrificial agents. It also describes the nanopowders synthesis using microwave-assisted solvothermal synthesis, in order to optimize their microstructure properties. In addition, it focuses on the ambipolar CIGS₆ lamellar compound and CIGS chalcopyrite for comparison purposes. Two strategies used to obtain single nanopowders are then presented. Finally, photocatalytic hydrogen evolution tests carried out under visible light, using different alcohols are reported and compared to the literature.

Chapter 5 presents the work conclusions and perspectives.

References

- (1) Ritchie, H.; Roser, M.; Rosado, P. Energy. *Our World Data* **2022**.
- (2) Morton, O. A New Day Dawning?: Silicon Valley Sunrise. *Nature* **2006**, *443* (7107), 19–22. <https://doi.org/10.1038/443019a>.
- (3) Crabtree, G. W.; Lewis, N. S. Solar Energy Conversion. *Phys. Today* **2007**, *60* (3), 37–42. <https://doi.org/10.1063/1.2718755>.
- (4) Gong, J.; Li, C.; R. Wasielewski, M. Advances in Solar Energy Conversion. *Chem. Soc. Rev.* **2019**, *48* (7), 1862–1864. <https://doi.org/10.1039/C9CS90020A>.
- (5) Carrillo, A. J.; González-Aguilar, J.; Romero, M.; Coronado, J. M. Solar Energy on Demand: A Review on High Temperature Thermochemical Heat Storage Systems and Materials. *Chem. Rev.* **2019**, *119* (7), 4777–4816. <https://doi.org/10.1021/acs.chemrev.8b00315>.
- (6) Harriman, A. Prospects for Conversion of Solar Energy into Chemical Fuels: The Concept of a Solar Fuels Industry. *Philos. Trans. R. Soc. Math. Phys. Eng. Sci.* **2013**, *371* (1996), 20110415. <https://doi.org/10.1098/rsta.2011.0415>.
- (7) Montoya, J. H.; Seitz, L. C.; Chakthranont, P.; Vojvodic, A.; Jaramillo, T. F.; Nørskov, J. K. Materials for Solar Fuels and Chemicals. *Nat. Mater.* **2017**, *16* (1), 70–81. <https://doi.org/10.1038/nmat4778>.
- (8) Trainham, J. A.; Newman, J.; Bonino, C. A.; Hoertz, P. G.; Akunuri, N. Whither Solar Fuels? *Curr. Opin. Chem. Eng.* **2012**, *1* (3), 204–210. <https://doi.org/10.1016/j.coche.2012.04.001>.

Chapter 1: Focus on $\text{Cu}_2\text{S-In}_2\text{S}_3\text{-Ga}_2\text{S}_3$ system

The aim of this PhD project is to explore the potential of lamellar CIGSn compounds for photoinduced applications, in particular for photovoltaics and photocatalysis.

Therefore, in this chapter we will summarise some key aspects concerning the $\text{Cu}_2\text{S-In}_2\text{S}_3\text{-Ga}_2\text{S}_3$ pseudo-ternary system, focusing on the stoichiometric chalcopyrite $\text{CuGa}_{0.7}\text{In}_{0.3}\text{S}_2$ that will be our reference during this work. Additionally, GaInS_3 alongside the ordered vacancy compounds (OVC) CuIn_5S_8 , CuGa_3S_5 and CuGa_5S_8 will be also considered. Finally, the report will focus on the new CIGSn lamellar compounds, forming the subject of this thesis. For each of these compounds, we will highlight a few examples of applications in the fields of photovoltaics and solar-driven photocatalytic hydrogen production.

1. Chalcogenides

Chalcogenides are compounds that consists of at least one element from the chalcogen group (sulphur, selenium or tellurium), combined with at least one more electropositive element.¹ These materials have been extensively studied for various applications such as solar energy conversion, energy storage, electronics, optics and many others.

Metal chalcogenides stand out as promising candidates for different visible light applications (such as photovoltaics and photocatalysis) due to their distinctive optical properties.^{1,2} They exhibit excellent transparency exposing to visible light with optical gaps that are less than 3 eV, allowing them to absorb visible energy. They also have a strong solar response and a small effective mass of carriers, which favours charge separation and electronic transfer.

These materials can be classified into two categories, three-dimensional (3D) chalcogenides and two-dimensional (2D) metal chalcogenides, where the layers of atoms are connected by Van der Waals interactions, offering additional advantages. The 2D nature reduces the diffusion length of charge carriers, which improves the kinetics of photoinduced reactions. As well, the band gap energy and band positions of 2D materials usually depend on their thickness, which can be employed to modify their properties.³

In this PhD project, we will focus on copper-based sulphide chalcogenides. As shown in Figure 1, the copper chalcogenide semiconductors include a wide range of materials, ranging from binary compounds (such as Cu_{2-x}S , Cu_{2-x}Se , and Cu_2Te) to ternary (Cu-III-VI , Cu-IV-VI and Cu-V-VI) and quaternary ones (Cu-III-III'-VI and Cu-II-IV-VI (II = Zn, Cd, Hg; III

(III') = Al, Ga, In; IV = Ge, Sn; VI = S, Se, Te)).¹ Copper chalcogenides have the advantage of being abundant. Furthermore, compared with selenium and tellurium, sulphur is much more abundant on earth, ranking fifth among the most common elements on earth, and 17th in the earth crust, according to WebElements.⁴

Among these materials, ternary and quaternary compounds are interesting because of their wide range of compositional flexibility, enabling the band gap and the position of the Fermi energy to be tuned, in order to optimize the optical properties. In addition, these semiconductors have often a high concentration of defects due to their multi-element nature, which may be altered by defect engineering to adjust certain functional features like electrical conductivity and optoelectronic characteristics.

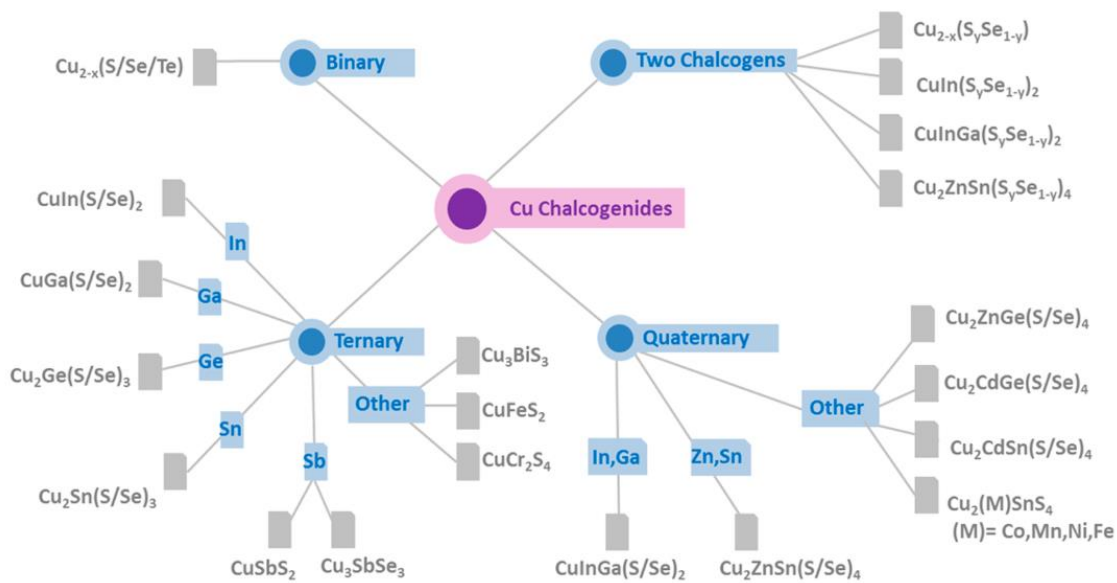


Figure 1: Schematic illustration of the different copper-based chalcogenide semiconductors available in the literature. Figure from Coughlan et al.¹

2. Pseudo ternary system $\text{Cu}_2\text{S}-\text{In}_2\text{S}_3-\text{Ga}_2\text{S}_3$

The non-stoichiometric CIGS quaternary compounds $\text{Cu}_{1-z}(\text{In}_{1-x}\text{Ga}_x)_{1+z/3}\text{S}_2$ (Cu-poor CIGS) has been studied in depth by our group, and an extended pseudo-ternary phase diagram $\text{Cu}_2\text{S}-\text{In}_2\text{S}_3-\text{Ga}_2\text{S}_3$ for the compositions $0.2 \leq x \leq 1$ and $0 \leq z \leq 0.6$ could be established^{5,6} (see Figure 2). Indeed, these materials have received much less attention, even though investigations have been carried out for potential applications in tandem solar cells. It turns out that the sulfide CIGS system is much more complex than the selenide one. The single-phase copper-poor domain with chalcopyrite structure is narrower for sulfides. A chemical crystallographic approach was therefore carried out for the $\text{Cu}_{1-z}(\text{In}_{1-x}\text{Ga}_x)_{1+z/3}\text{S}_2$ compounds, with x the Ga-content and z the copper deficit. In these compounds, the charge balance is quite well fulfilled with normal valence for the cations, that is, Cu(I), In(III), Ga(III), and S(-II). Attempts to synthesize $\text{Cu}_{1-z}(\text{In}_{1-x}\text{Ga}_x)_{1+z/3}\text{S}_2$

compounds, by solid state synthesis, systematically lead to multiphasic samples for $z > 0.1$.

In addition, a particular attention was also paid to $\text{CuInS}_2\text{-In}_2\text{S}_3$, $\text{CuGaS}_2\text{-Ga}_2\text{S}_3$ and $\text{Ga}_2\text{S}_3\text{-In}_2\text{S}_3$ systems, due to the existence of ordered vacancy compounds widely debated in the literature. For example, the CuIn_3Se_5 phase that plays a key role in solar cell performance has no sulphur equivalent (i.e. CuIn_3S_5).

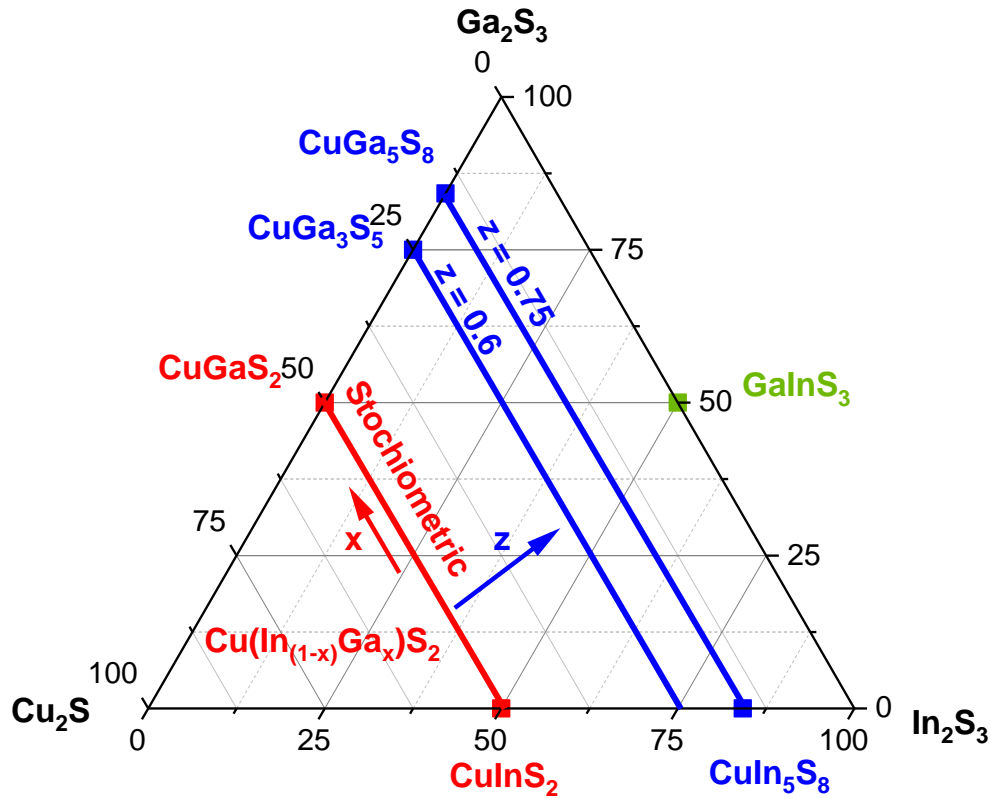


Figure 2: Pseudo-ternary diagram of the $\text{Cu}_2\text{S-In}_2\text{S}_3\text{-Ga}_2\text{S}_3$ system.

2.1. Stoichiometric $\text{Cu}(\text{In,Ga})\text{S}_2$ chalcopyrite (CIGS)

2.1.1. $\text{Cu}(\text{In,Ga})\text{S}_2$ characteristics

The stoichiometric $\text{Cu}(\text{In}_{1-x}\text{Ga}_x)\text{S}_2$ compounds ($z = 0$ and $0 < x < 1$) are represented in the phase diagram by a red line alloying CuGaS_2 and CuInS_2 . They crystallize in a tetragonal chalcopyrite structure with a $I-42d$ space group (see Figure 3).⁶⁻⁸ This structure is derived from the ZnS sphalerite structure that itself derived from diamond structure.⁹

As shown in Figure 3, chalcopyrite is a three-dimensional structure formed of cations (Cu^+ , Ga^{3+} , In^{3+}) in tetrahedral sulphur environments. Lattice parameters of $\text{Cu}(\text{In}_{1-x}\text{Ga}_x)\text{S}_2$ compounds are compositionally variable and they decrease as the size of atom decreases. The compound $\text{CuGa}_{0.7}\text{In}_{0.3}\text{S}_2$ is one of the most studied in the bibliography, with unit cell parameters $a \approx 5.47 \text{ \AA}$ and $c \approx 10.96 \text{ \AA}$.⁷

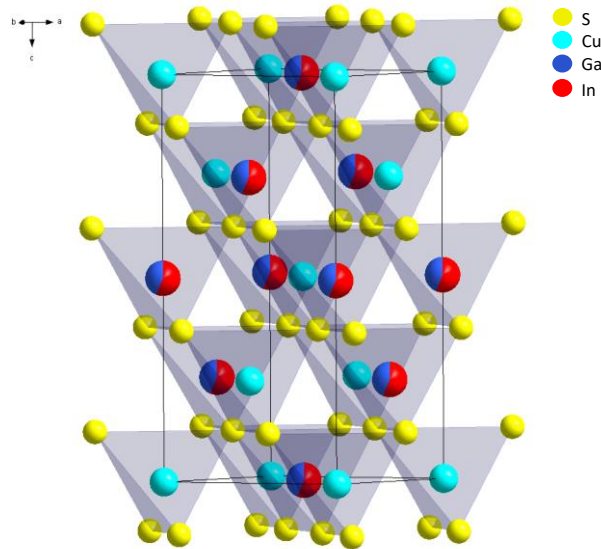


Figure 3: $\text{CuIn}_{0.7}\text{Ga}_{0.3}\text{S}_2$ chalcopyrite structure-type.

CIGS compounds are semiconductors with a direct band gap. The substitution of indium by gallium induces a band gap variation from 1.54 eV (CuInS_2) to 2.43 eV (CuGaS_2), exhibiting a wider band gap than isostructural Se-based compounds CIGSe, as presented in the Figure 4.^{10–12} This wide range offers good prospects for photovoltaics and photocatalysis. The optimum band gap ($E_g = 1.7$ eV) required for the targeted photovoltaic and photocatalysis applications in this thesis is achieved with $\text{CuIn}_{0.7}\text{Ga}_{0.3}\text{S}_2$.

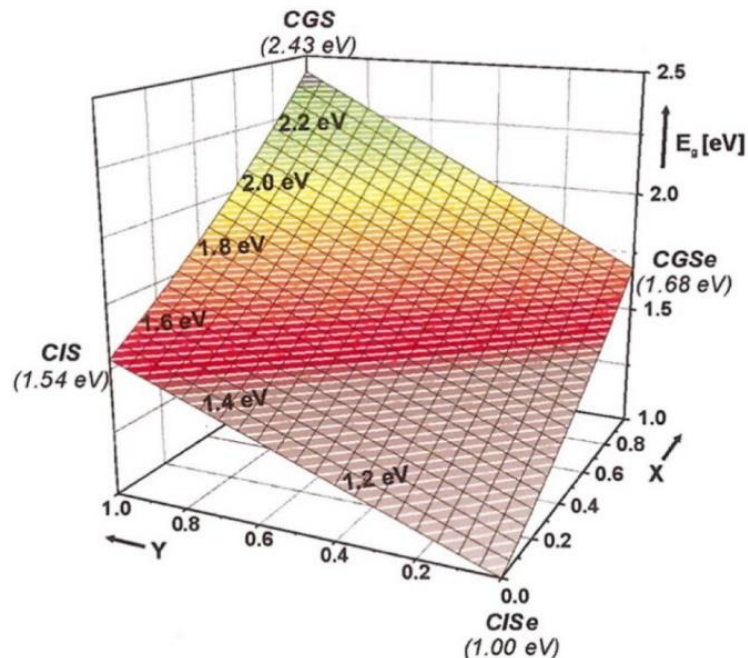


Figure 4: Gap evolution of CIGSSe depending on the composition. Figure from Bär et al.¹⁰

2.1.2. Cu(In,Ga)S₂ applications

Photovoltaics

The first studies conducted on the CuInS₂ (CIS) ternary compound achieved a promising conversion efficiency of 9.7%, dating back to 1986.¹³ However, CIS solar cells presented several drawbacks as its low adhesion to the molybdenum substrate. In 1997, Nakabayashi et al.¹⁴ reported the gallium addition to the CIS with an objective of improving its quality, resulting in the common CIGS.

The CIGS chalcopyrite efficiency is mainly related to different conditions, detailed in chapter 3. However, the specific composition of CIGS can also influence its efficiency. Copper-poor and copper-rich have been extensively studied, leading to different characteristics.¹⁵ It was reported that a copper excess during the deposition results in improving the thin film crystallinity, however it could also lead to the formation of copper sulphide as a secondary phase, that will negatively affect the performance of the solar cell. On the other hand, in the case of copper-poor CIGS ($\text{Cu}/(\text{In}+\text{Ga}) < 1$), the formation of the copper sulphide as a secondary phase is limited, allowing higher efficiencies.¹⁵ Figure 5 shows a comparison of the best-reported efficiencies of the devices made from Cu-poor and Cu-rich absorbers. According to the literature, it is observed that Cu-poor solar cell reported higher performances than that of Cu-rich (with etched copper sulphide).¹⁵ Moreover, 15.5% is the best efficiency of a Cu-poor device, reported by Hiroi et al.¹⁶ versus 12.6% of a Cu-rich, reported by Merdes et al.¹⁷

This efficiency has recently been increased in our group, reaching a record solar efficiency of 16% using CuIn_{0.7}Ga_{0.3}S₂ absorber, demonstrated by Barreau et al.¹⁸

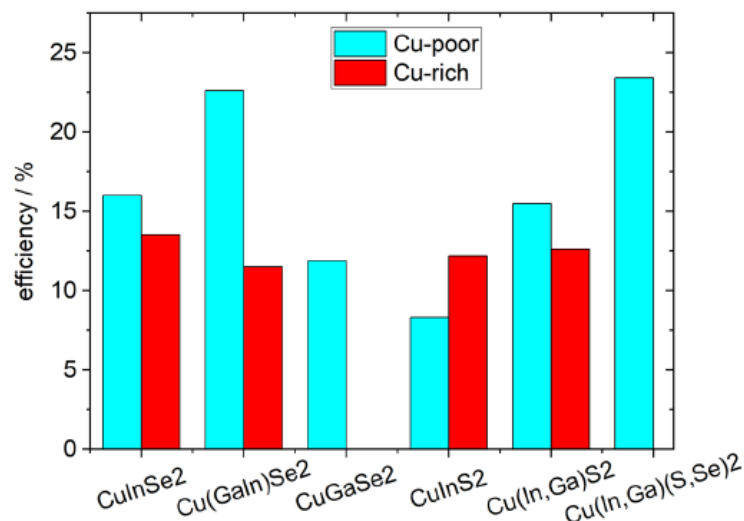


Figure 5: The best reported efficiencies of Cu-poor and Cu-rich chalcopyrites solar cells.
Figure from Siebentritt et al.¹⁵

Photocatalysis for hydrogen production

Compared to photovoltaics, fewer studies have been published on photocatalysis.

The CuInS₂ (CIS) photocatalytic activity for hydrogen production was investigated for the first time by Kobayakawa et al. in 1992.¹⁹ Recently, it reached 59.4 $\mu\text{mol}\cdot\text{h}^{-1}\cdot\text{g}^{-1}$ for visible light hydrogen evolution, using Pt as co-catalyst and Na₂SO₃/Na₂S as sacrificial agent, reported by Zheng et al.²⁰ Further, using MoS₂/CIS heterojunction, the hydrogen production rate was increased up to 316 $\mu\text{mol}\cdot\text{h}^{-1}\cdot\text{g}^{-1}$, according to Yuan et al.²¹

CuGaS₂ (CGS) compounds were also extensively investigated as photocatalysts,^{22–24} reaching up lately 183.6 $\mu\text{mol}\cdot\text{h}^{-1}\cdot\text{g}^{-1}$ using Na₂SO₃/Na₂S as hole scavenger.²⁵

In comparison to the CIS and CGS ternary systems, less investigations have been reported on the quaternary CuIn_{1-x}Ga_xS₂ for photocatalysis application. Yu et al.²⁶ investigated the effect of gallium concentration on the composition of CuIn_{1-x}Ga_xS₂ nanocrystals, proving that CuIn_{0.7}Ga_{0.3}S₂ material exhibited the highest hydrogen evolution rate (750 $\mu\text{mol}\cdot\text{h}^{-1}\cdot\text{g}^{-1}$) using Na₂SO₃/Na₂S as sacrificial agent. The study shows that Ga substitution into CuInS₂ improves the hydrogen production by moving the conduction band upwards, enabling the water splitting reaction. However, a reduced rate of H₂ is measured in the case of high amounts of Ga, due to the band gap broadening related to the Ga insertion, concluding that CuIn_{0.7}Ga_{0.3}S₂ is the suitable composition for H₂ evolution.²⁶

Although there are not many studies on hydrogen production using heterogeneous photocatalysis for CIGS materials, there are available studies on hydrogen production using the photoelectrochemical water splitting method.^{27–29}

Photoelectrochemical (PEC) water splitting is an application that requires the use of a semiconductor as a photoelectrode in order to undergo the water splitting under illumination.³⁰ The main difference between PEC and heterogeneous photocatalysis is the generation of an internal electric field at the semiconductor/electrolyte interface, which in PEC leads to the separation of the photogenerated carriers to their opposite sides.³¹ The semiconductor/electrolyte interface will be detailed in next chapter as well as the heterogeneous photocatalysis in chapter 4.

As shown in Figure 6, the semiconductor can be a photoanode where the oxidation reaction is performed or a photocathode where the reduction reaction occurs. In the case of a photoanode, under illumination, photogenerated holes are directed towards the interface to oxidise water, while photogenerated electrons are migrated to the back contact of the photoanode and are then transported through an external circuit. Whereas for a photocathode, the electrons are drawn to reduce H⁺, while holes are driven through external circuit.

Moreover, when a single semiconductor fails to generate enough voltage for water splitting, a PEC tandem cell of photoanode and photocathode is employed to achieve

overall water splitting.³¹ Therefore, for a higher light absorption, two semiconductors with different optical band gaps are combined. Usually, the photoanode exhibit a higher band gap in order to absorb high-energy photons while the photocathode absorb the photons of a low-energy. The two electrodes will generate water oxidation and reduction, respectively. Additionally, in this configuration, the minimum of the photoanode conduction band needs to be lower than the maximum of the photocathode valence band.

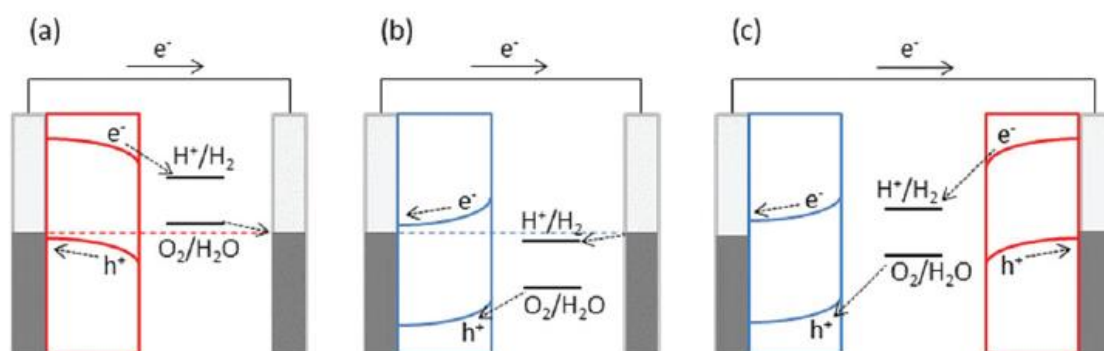


Figure 6: Schematic representation of semiconductors for water splitting application. a) photocathode, b) photoanode and c) photocathode and photoanode tandem configuration.

Figure from Takata et Domen.³¹

CuIn_{0.7}Ga_{0.3}S₂ has been evaluated for PEC water splitting. It was used by Guan et al.²⁹ as a photocathode for water splitting, coated with CdS and using Pt co-catalyst. A high photocurrent density (6.0 mA cm⁻² at 0 V_{RHE}) under AM1.5G simulated sunlight (100 mW.cm⁻²) was measured.

2.2. CuInS₂-In₂S₃ system

2.2.1. CuIn₅S₈ characteristics

Concerning the Cu₂S-In₂S₃ system, the compounds can be described with the formula Cu_{1-z}In_{1+z/3}S₂ in which Cu and In are at +I and +III oxidation state respectively, in order to maintain the charge balance. The stability range of the chalcopyrite is limited. Consequently, as shown in Figure 2, two-phase region exists immediately when z reaches the value ~0.1, between Cu_{1-z}In_{1+z/3}S₂ with a chalcopyrite structure (*I-42d*) and a Cu-poor phase CuIn₅S₈⁷ (Cu_{0.25}In_{1.25}S₂) which exhibits a cubic thiospinel structure-type (*F-43m*). It is worth noting that the CuIn₃S₅ does not exist unlike its selenide homologue.

CuIn₅S₈ is a ternary stable phase, in CuInS₂-In₂S₃ system (Figure 2).^{32,33} The structure, depicted in Figure 7, is a 3D structure with In occupying octahedral environments, while Cu is located on the tetrahedral sites.

CuIn₅S₈ is known as an ordered vacancy compound (OVC). In fact, the off-stoichiometric phases defined as OVC are located on the I₂VI-III₂VI₃ pseudo binary systems.^{34,35} Zhang et

al.³⁶ reported that the creation of OVC is due to the arrangement of the donor-acceptor defect pairs ($2 V_{Cu} + In_{Cu}^{\circ\circ}$) ($2V_{Cu}^{-1} + In_{Cu}^{2+}$) in the Cu-In-VI₂ phase.³⁶⁻³⁸

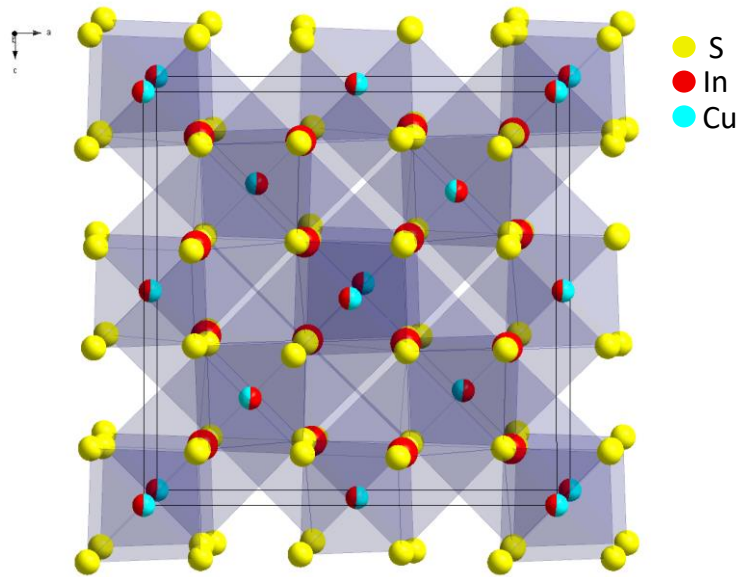


Figure 7: CuIn₅S₈ thiospinel structure-type.

CuIn₅S₈ is an n-type semiconductor with an indirect band gap around 1.5 eV,^{39,40} and has been used for several applications.

2.2.2. CuIn₅S₈ applications

Photovoltaics

There is no mention in the literature of a device composed of a pure CuIn₅S₈ as an absorber, however many studies reported the formation of the CuIn₅S₈ as a secondary phase on the co-evaporated CIGS.⁴¹ This interfacial phase formation was proved harmful to the performance of the device.⁴² Moreover, according Abou-Ras et al.,⁴³ a low cell efficiency was reported for the absorber deposited at high temperature, forming a CuIn₅S₈ phase. This explains the absence of the CuIn₅S₈ phase as an absorber in the literature.

Photocatalysis for hydrogen production

Once again, there is a limited research concerning heterogeneous photocatalysis for hydrogen production using CuIn₅S₈. Conversely, more attention was dedicated to its application for PEC water splitting.

In 1992, Kobayakawa et al.¹⁹ were the first to investigate the CuIn₅S₈ potential for hydrogen evolution. In this study, CuIn₅S₈ photocatalytic activity was compared to that of CIS, the materials were synthesised by chemical precipitation and evaluated using aqueous sodium sulphite as sacrificial agent under UV light. CuIn₅S₈ showed an activity that is twice of CIS and that enhanced in the presence of Ag₂S as a co-catalyst. Nevertheless, the obtained yield was found very low (order of 1/50) compared to CdS.¹⁹

Then in 1985, Scrosati et al.⁴⁴ studied the photoelectrochemical behaviour of CuIn_5S_8 . The n- CuIn_5S_8 photoanode was investigated in several electrolytes, showing a stability in aqueous sulphide-polysulfide solution and a suitable band gap for solar energy use as PEC water splitting.

Later, Gannouni et al.⁴⁵ developed a three electrodes PEC setup for water splitting using n- CuIn_5S_8 film deposited on titanium oxide (ITO) as the photoanode, Pt as the cathode, Ag/AgCl as the reference electrode and Na_2SO_4 aqueous electrolyte. Under UV illumination, they reported the impact of the Cu/In ratio variation, demonstrating the highest photocurrent density with CuIn_5S_8 (Cu/In= 0.28, $E_g = 1.59$ eV).

Furthermore, Feng et al.⁴⁶ also constructed a PEC setup with $\text{CoO}_x/\text{CuIn}_5\text{S}_8$ photoanode and a Pt/ CuInS_2 photocathode, indicating the potential of these materials for water splitting.⁴⁶

In the recent years, more attention has been devoted on the use of pure CuIn_5S_8 as a photocatalyst for CO_2 reduction than for hydrogen production and has shown promising results.^{47,48}

2.3. CuGaS_2 - Ga_2S_3 system

2.3.1. CuGa_3S_5 and CuGa_5S_8 characteristics

In the case of pure gallium compounds $\text{Cu}_{1-z}\text{Ga}_{1+z/3}\text{S}_2$, the charge balance is also achieved with Cu^+ , Ga^{3+} , and S^{2-} . Once a small copper deficit ($z \approx 0.1$) the compounds prefer to adopt a stannite derived structure (SG: $I-42m$) instead of the chalcopyrite one (See Figure 8). Two ordered vacancy compounds(OVC) are identified: CuGa_3S_5 and CuGa_5S_8 ^{6,7}. Contrarily, in the CuInS_2 - In_2S_3 system only CuIn_5S_8 exists but it exhibits a cubic thiospinel structure-type.

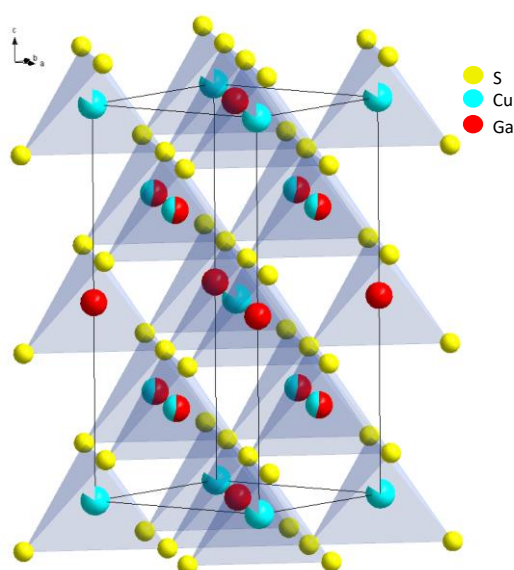


Figure 8: CuGa_3S_5 stannite structure-type.

2.3.2. Applications

CuGa₃S₅

According to the literature, CuGa₃S₅ is not used for PV applications. However, Ueda et al.⁴⁹ investigated its crystallographic and optical properties, expecting that CuGa₃S₅ could be useful to control the band positions at the interface of the absorber and the buffer layer in CIGS-based solar cells.⁴⁹

On the other hand, concerning hydrogen production, Tabata et al.⁵⁰ have studied CuGa₃S₅ for visible light photocatalytic hydrogen production, with different co-catalysts (Pt, Rh, Ir, NiS and FeS) in Na₂S/Na₂SO₃ solution as sacrificial electron donor. This resulted in a higher hydrogen evolution (980 μmol.h⁻¹.g⁻¹) using the NiS sulphide co-catalyst, an amount that was three times higher than that obtained with the noble metals.⁵⁰

CuGa₅S₈

Similarly, CuGa₅S₈ has not been studied for photovoltaic applications, but it has shown promising results for hydrogen production.

Kafa et al.⁵¹ have reported the photocatalytic activity of Rh-loaded CuGa₅S₈ photocatalyst in K₂SO₃/Na₂S solution as electron donor, exhibiting a hydrogen production rate equal to 0.76 L.h⁻¹. In this study, the effect of copper and gallium substitution for Zn_{1-2x}(Cu,Ga)_xGa₂S₄ was also investigated, resulting in a higher hydrogen evolution rate (1.4 L.h⁻¹) in the case of Pd-loaded Zn_{0.4}(Cu,Ga)_{0.3}Ga₂S₄. They demonstrated that the substitution of copper with gallium leads to an enhanced photocatalytic response to visible light.⁵¹

2.4. GaInS₃

GaInS₃ is an identified compound in the pseudo-binary system Ga₂S₃-In₂S₃ (Figure 2), subject to cationic non-stoichiometry phenomena. This fact leads to multiple compounds (Figure 9) exhibiting orthorhombic, monoclinic, cubic and hexagonal structures, listed on the phase diagram of Ga₂S₃-In₂S₃ proposed by Ivashchenko et al.⁵² The chemical composition of these compounds differs slightly from GaInS₃, due to gallium and indium substitution.

Among these compounds, layered structures were identified including GaInS₃⁵³ (a = 3.81 Å, c = 18.19 Å), Ga_{0.75}In_{1.25}S₄⁵⁴ (a = 3.83 Å, c = 12.22 Å) and Ga_{1.74}In_{2.92}S₇⁵⁵ (a = 3.82 Å, c = 21.14 Å) defined in *P-3m1* space group. (GaInS₃)_{3.333}⁵⁶ (a = 3.81 Å, c = 30.65 Å) defined in *P6₃mc* space group and GaInS₃⁵⁷ (a = 3.8 Å, c = 45.89 Å) defined in space group *R3m*.

The layered structures of GaInS₃ are depicted in Figure 8, presenting a marked 2D character. The lamellar stacking of these structures consists of all cations (Cu, In and Ga) with intrinsic vacancies in the tetrahedral sites and In in octahedral sites. The compounds

exhibit a Van der Waals gap and tetrahedral blocks between the octahedral layers sharing faces with different thicknesses.

Kramer et al. reported two additional lamellar compounds ($\text{Ga}_2\text{In}_4\text{S}_9$ ($a=7.64 \text{ \AA}$, $c=74 \text{ \AA}$) and $\text{Ga}_2\text{In}_8\text{S}_{15}$ ($a=3.82 \text{ \AA}$ and $c=100.5 \text{ \AA}$) of ZnIn_2S_4 structure in the Ga-In-S system.⁵⁸

Nowadays, there is still only little research in the applications of GaInS_3 . They have demonstrated a potential use for radiation sensor devices.⁵⁹ However, research in the fields of photovoltaics and photocatalysis is still limited. This could be due to their low conductivity of $7.94 \times 10^{-6} \Omega^{-1} \cdot \text{m}^{-1}$, demonstrated by Ivashchenko et al.⁶⁰

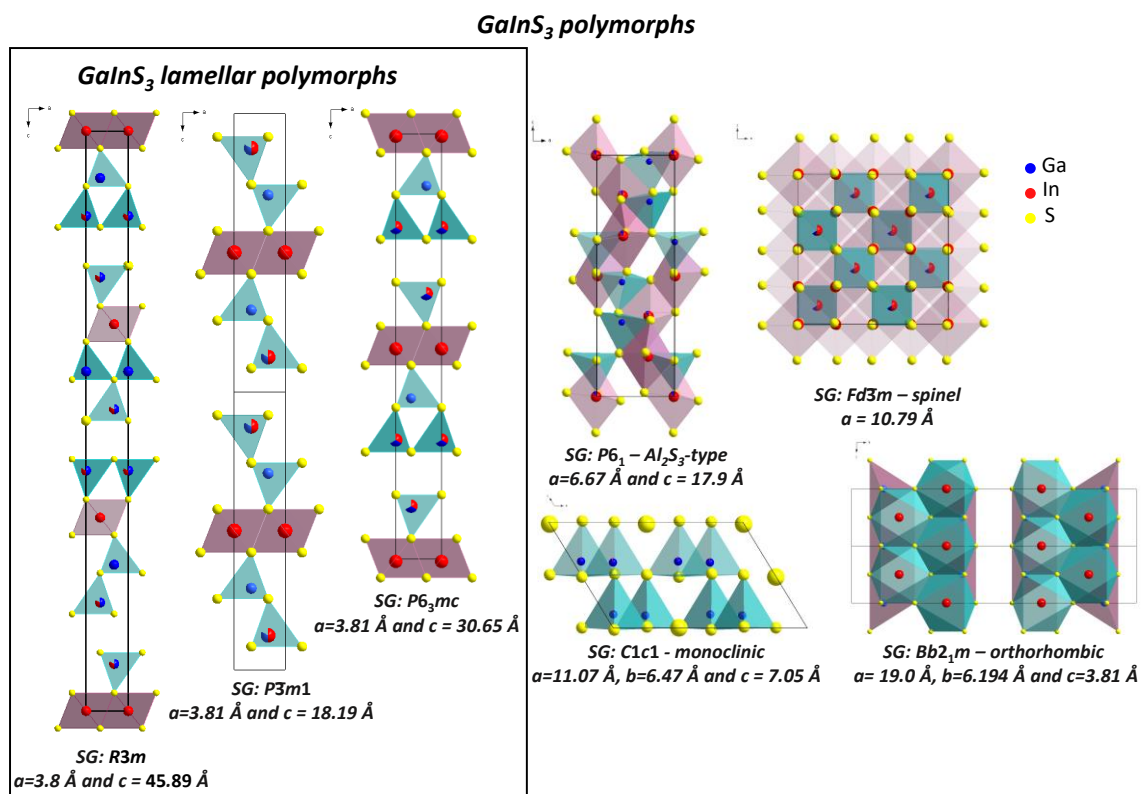


Figure 9: The structures of GaInS_3 different polymorphs, including the lamellar polymorphs.

2.5. CIGS_n lamellar compounds

CIGS_n lamellar compounds⁶¹ have been recently described in the literature by our group. A brief summary is given here to facilitate understanding of the rest of our work.

Our team studied the pseudo ternary system $\text{Cu}_2\text{S-In}_2\text{S-Ga}_2\text{S}_3$, focusing on the compositions: $\text{Cu}_{1-z}(\text{In}_{1-x}\text{Ga}_x)_{1+z/3}\text{S}_2$ series $0.2 \leq x \leq 1$ and $0 \leq z \leq 0.6$. It has been found that the chalcopyrite-type structure is less tolerant to copper non-stoichiometry than selenides. Indeed, for sulphides a small copper deficiency (z) in CIGS (i.e. $\text{Cu}_{1-z}(\text{In}_{1-x}\text{Ga}_x)_{1+z/3}\text{S}_2$) is sufficient to destabilise the chalcopyrite-type structure, which has never been shown for CIGSe ($\text{Cu}(\text{In,Ga})\text{Se}_2$). This deviation to copper stoichiometry leads to the formation of the two-dimensional CIGS_n quaternary compounds.

As copper-deficient phases have a strong influence on the performance of CIGS-based solar cells, new CIGS_n were prepared as single-phase compounds in order to study their optoelectronic properties.

The investigation on the Cu_{1-z}(In_{1-x}Ga_x)_{1+z/3}S₂ (z > 0.1) series, resulted in multiphasic compounds. Figure 10 presents the DRX pattern of a member of this series, Cu_{0.4}(In_{0.5}Ga_{0.5})_{1.2}S₂ (z = 0.6, x = 0.5), revealing the coexistence of several phases. In fact, each of the first three reflections observed in the DRX pattern at very low 2θ angles (15.7, 18.7 and 21.7 Å) corresponds respectively to the inter-reticular distance d (001) of three different new phases. This fact is also confirmed by electron diffraction (ED), since these reflections belong to different reciprocal networks (see ED patterns in Figure 10). Moreover, the inhomogeneous contrast of grains observed in backscattered electron images also evidences the coexistence of several phases. A fourth inter-reticular distance d (001) (i.e. 12 Å) was detected in another targeted composition Cu_{0.4}(In_{0.7}Ga_{0.3})_{1.2}S₂ (z= 0.6, x= 0.3).

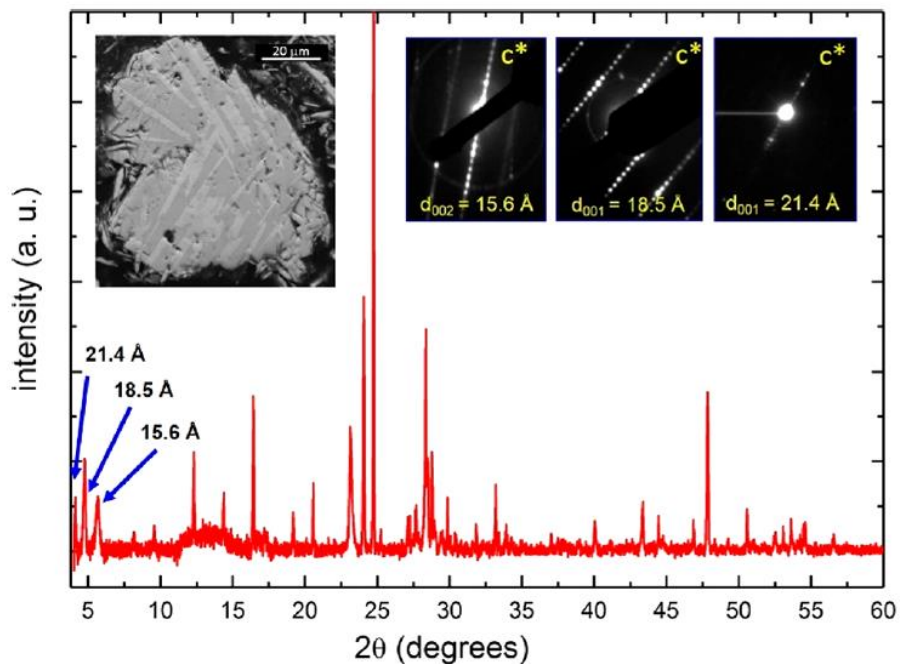


Figure 10: XRD pattern of Cu_{0.4}(In_{0.5}Ga_{0.5})_{1.2}S₂ multiphasic compound. The corresponding electronic diffraction patterns and SEM electron image are inserted in the top of the figure. Figure from Caldes et al.⁶¹

In order to solve the structure of these new phases, four suitable crystals were obtained from powdered samples. Four layered structure-types were thus identified (see Figure 11). They were named CIGS₄, CIGS₅, CIGS₆, and CIGS₇. The notation CIGS_n takes into account the chemical constituents (Cu, In, Ga, S) and the number n of anionic layers necessary to describe the structure.

The chemical composition of each single crystal was obtained by EDX analyses: $\text{Cu}_{0.32}\text{In}_{1.74}\text{Ga}_{0.84}\text{S}_4$ (CIGS₄-type), $\text{Cu}_{0.65}\text{In}_{1.75}\text{Ga}_{1.4}\text{S}_5$ (CIGS₅-type), $\text{Cu}_{1.44}\text{In}_{2.77}\text{Ga}_{0.76}\text{S}_6$ (CIGS₆-type) and $\text{Cu}_{1.1}\text{In}_{2.49}\text{Ga}_{1.8}\text{S}_7$ (CIGS₇-type). The Cu/S ratio of the layered compounds ranges between 0.08 and 0.27, compared to 0.5 for CIGS ($\text{Cu}(\text{In,Ga})\text{InS}_2$). Corresponding unit cell parameters and space groups are listed in Table 1.

Table 1: Main crystal data and structure refinement results for CIGS_n. Table from Caldes et al.⁶¹

	CIGS ₄	CIGS ₅	CIGS ₆	CIGS ₇
<i>a</i> (Å) ⁽²⁾	3.8203(6)	3.7898(2)	3.8506(2)	3.7933(3)
<i>c</i> (Å) ⁽²⁾	12.182(2)	30.664(3)	18.704(2)	21.540(14)
SG	$\overline{P}3m1$	$P63mc$	$\overline{P}3m1$	$P\ 3m1$

CIGS_n compounds present a 2D structure built upon infinite $2/\infty[\text{InS}_2]$ layers (edge-shared InS_6 octahedra) on which condense on both sides, mono-, bi-, or tri- $2/\infty[\text{MS}]$ layers (corner-shared MS_4 tetrahedra) with $\text{M} = \text{Cu}, \text{In}, \text{Ga}$ (see figure besides). $[\text{M}(\text{Td})]_{n-2}(\text{In}(\text{Oh}))\text{S}_n$ slabs are separated from each other by a van der Waals gap, and subscript *n* refers to the number of sulfur layers within the building block. As a result, these compounds could be identified from their inter-reticular distances *d* (001), related to the thickness of the structural blocks: 12.2 Å (CIGS₄), 15.7 Å (CIGS₅), 18.7 Å (CIGS₆) and 21.7 Å (CIGS₇).

In addition, the tetrahedral sites (Td) exhibit intrinsic cationic vacancies and mixed occupancy (Cu^+ , In^{3+} and Ga^{3+}), allowing chemical composition tuning. As consequence, a same CIGS_n structural type (*n* = 4, 5, 6, 7) could exhibit various chemical compositions. In addition, Td sites vacancies never surpasses 20%, except in the case of CIGS₇ that displays a rate of 50% for the mixed site (In – Cu). Finally, it is important to mention that In atoms in Td sites are mainly located at the boundary of the vdW gap, probably due to steric reasons.

Indeed, CIGS₄, CIGS₅ and CIGS₆ structure types are isostructural to ZnIn_2S_4 type I, $\text{Zn}_2\text{In}_2\text{S}_5$ type IIa and $\text{Zn}_3\text{In}_2\text{S}_6$,⁶² respectively (described in chapter 4). The corresponding structural sequences can be written: $\text{Td}_{(\text{Cu},\text{In},\text{Ga},\square)}\text{-Oh}(\text{In})\text{-Td}_{(\text{Cu},\text{In},\text{Ga},\square)}$ (CIGS₄), $\text{Td}_{(\text{In},\text{Ga})}\text{-Td}_{(\text{Cu},\text{Ga},\square)}\text{-Oh}(\text{In})\text{-Td}_{(\text{Cu},\text{In})}$ (CIGS₅) and $\text{Td}_{(\text{Cu},\text{Ga})}\text{-Td}_{(\text{Ga},\text{In},\square)}\text{-Oh}(\text{In})\text{-Td}_{(\text{Cu},\text{Ga})}\text{-Td}_{(\text{Ga},\text{In},\square)}$ (CIGS₆). Furthermore, the CIGS₅ stacking sequence is also similar to that of $\text{Ag}_{1.25}\text{Ga}_{2.5}\text{In}_{3.75}\text{S}_{10}$ ⁵² compound. As well, as previously mentioned, GaInS_3 also exhibits two polymorphs of CIGS₅-type and CIGS₆-type structures. In contrast, the CIGS₇ structure ($\text{Td}_{(\text{In},\text{Ga})}\text{-Td}_{(\text{Cu},\text{In},\square)}\text{-Td}_{(\text{Ga},\square)}\text{-Oh}(\text{In})\text{-Td}_{(\text{In},\text{Ga})}\text{-Td}_{(\text{Cu})}$) presents a completely new layer arrangement.

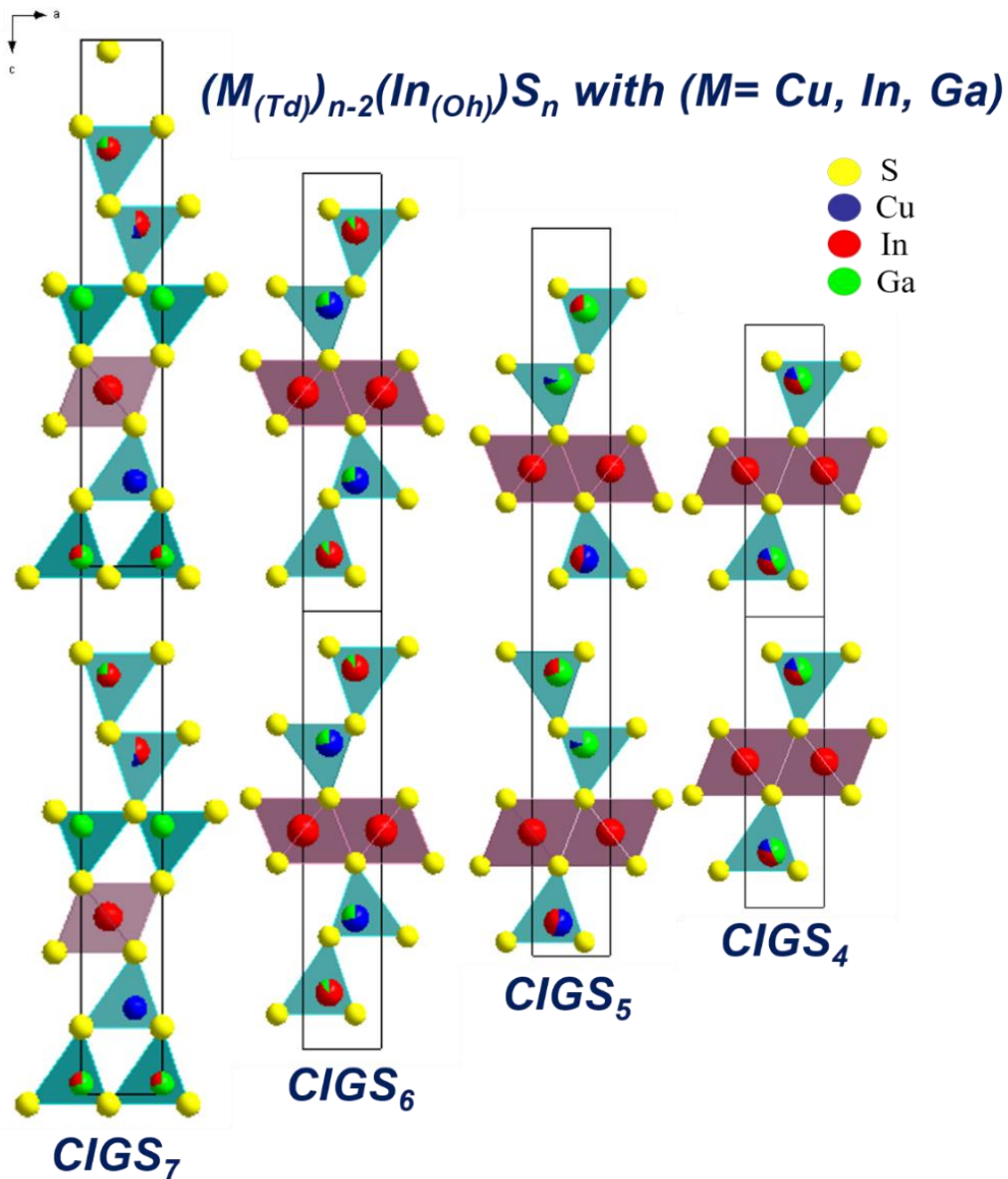


Figure 11: CIGS₇ (Cu_{1.1}In_{2.49}Ga_{1.8}S₇), CIGS₆ (Cu_{1.44}In_{2.77}Ga_{0.76}S₆), CIGS₅ (Cu_{0.65}In_{1.75}Ga_{1.4}S₅) and CIGS₄ (Cu_{0.32}In_{1.74}Ga_{0.84}S₄) lamellar compounds structures.

As for many layered compounds and due to the structural similarity between the $(M_{(Td)})_{n-2}In_{(Oh)}S_n$ blocks, intergrowths and stacking faults could exist in CIGS_n compounds. Figure 12 presents [010] electron diffraction pattern, corresponding TEM image and HAADF-STEM image (on the bottom) of a faulted crystal, highlighting the tendency of these materials to contain intergrowth defects (the value n from $(M_{(Td)})_{n-2}(In_{(Oh)})S_n$ is given for each slab). The van der Waals gaps are imaged as dark contrast lines.

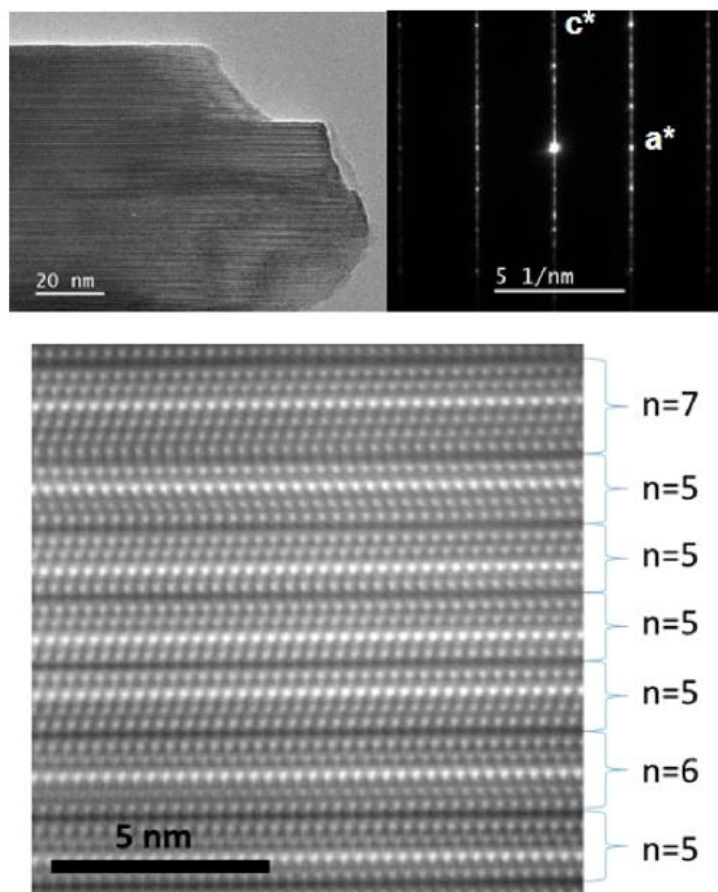


Figure 12: HAADF-STEM image of a faulted crystal. A TEM image of a larger area and corresponding electron diffraction pattern are shown on the top. Figure from Caldes et al.⁶¹

CIGS_n compounds were also prepared as powdered samples using copper, gallium and indium sulphides. The synthesis protocol will be detailed in chapter 2. According to Le Bail refinements, most of the reflections observed for all compounds could be successfully indexed using unit cell parameters and space groups determined by single-crystal X-ray diffraction. However, various polytypes were identified as extra phases. A detailed explanation will be given in chapter 2.

The optical gaps of lamellar compounds are close to that of CuIn_{0.7}Ga_{0.3}S₂ (CIGS) chalcopyrite (1.6 eV), ranging between 1.6 and 1.9 eV.

In addition, X-ray photoelectron spectroscopy (XPS) analyses were carried out to investigate the position of the maximum of the valence band (VBM) level relative to the Fermi level. In Figure 13 are plotted the valence band spectra of CIGS₄, CIGS₅, and CIGS₆ compounds and that of CIGS chalcopyrite, in the 0–10 eV binding energy range. Founded on calculated electronic structures of GaInS₃⁶³, the band peaking at ca. 4 eV observed in CIGS_n spectra, can be associated with copper 3d orbitals hybridized with 3p orbitals of sulfur atoms. The one at ca. 8 eV which is much less intense, can be related to Ga and In orbitals mixed with S.

The valence band maximum (VBM) position relative to the Fermi level was determined for all probed samples by linearly extrapolating the low binding energy (BE) edge of the VB region. For lamellar compounds, the binding energy threshold (i.e distance between the Fermi level and VBM) is around 1.0 eV, while it is 0.8 eV for CIGS chalcopyrite. An in-depth study of the optoelectronic properties of CIGSn compounds will be presented in Chapter 2.

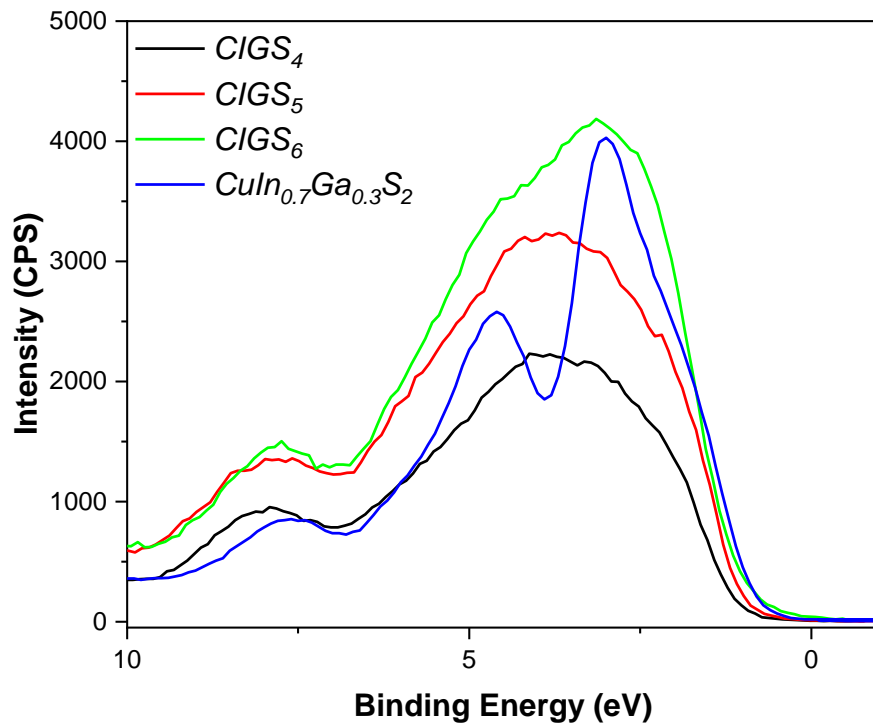


Figure 13: XPS valence band spectra of CIGS_n lamellar compounds and CIGS (CuIn_{0.7}Ga_{0.3}S₂) chalcopyrite.⁶¹

2.5.1. Applications

As CIGS_n compounds have only recently been identified, no applications for the photovoltaic have yet been reported in the literature. However for photocatalysis, CuGa₂In₃S₈⁶⁴ has been reported as photocatalysts for visible light hydrogen production. The authors claim that this compound has a lamellar CIGS₅-type structure. In fact, in the literature, which is not very extensive, there is some controversy about the structural type of this compound. For instance, Haeuseler et al.⁶⁵ mention that in CuIn₅S₈ - CuGa₅S₈ system, a ZnIn₂S₄ - type lamellar structure (isostructural to CIGS₄ structure type) is detected for CuGa_xIn_{5-x}S₈ (1 ≤ x ≤ 2) compounds.

Going back to the photocatalytic properties, Kandiel et al.⁶⁴ investigated CuGa₂In₃S₈ loaded with Ru co-catalyst, achieving a visible light hydrogen evolution rate up to 338 μmol.h⁻¹, in the presence of Na₂S and Na₂SO₃ as sacrificial electron donors. In this study, other co-catalysts such as Rh and Pt were also investigated.⁶⁴

Later, Kandiel et al.⁶⁶ also studied $\text{CuGa}_2\text{In}_3\text{S}_8$ using a different sacrificial agent (acid ascorbic). This time, they investigated $\text{CuGa}_2\text{In}_3\text{S}_8$ modified with hydrophilic ligands using Ni salt as co-catalyst in acidic solution (acid ascorbic), reporting a higher rate of visible light hydrogen evolution ($25 \mu\text{mol}\cdot\text{h}^{-1}$) than when using metal co-catalysts (Pt, Rh and Ru). Furthermore, the $\text{CuGa}_2\text{In}_3\text{S}_8$ nanoparticles produced around $67 \mu\text{mol}\cdot\text{h}^{-1}$ under full solar irradiation.⁶⁶

2.6. Afterwords

Following the initial work on CIGS_n lamellar compounds an in-depth crystal chemistry study could have been carried out, to determine chemical composition ranges compatible with each CIGS_n structure-type already identified (i.e. CIGS_4 , CIGS_5 , CIGS_6 and CIGS_7). In addition, the existence of these compounds in the $\text{Cu}_2\text{Se-In}_2\text{Se-Ga}_2\text{Se}_3$ system or in the mixed sulphide-selenide one could also have been investigated. However, our primary goal was to obtain a rapid overview of potentialities of these new materials for photoinduced applications (photovoltaics and photocatalysis).

Therefore, we decided to postpone the in-depth crystal chemistry study and focus this thesis to explore potentialities of three of four compositions early described, each one exhibiting a CIGS_n structure-type different: $\text{Cu}_{0.32}\text{In}_{1.74}\text{Ga}_{0.84}\text{S}_4$ (CIGS_4), $\text{Cu}_{0.65}\text{In}_{1.75}\text{Ga}_{1.4}\text{S}_5$ (CIGS_5) and $\text{Cu}_{1.44}\text{In}_{2.77}\text{Ga}_{0.76}\text{S}_6$ (CIGS_6). Since in this work each type of CIGS_n structure-type is mainly associated with only one chemical composition, the notation " CIGS_n " has been also used to label each one of three compositions studied.

To address our goal, the optoelectronic properties of CIGS_n compounds have been investigated and their energy diagrams have been determined. Results will be presented in chapter 2. This have paved the way for exploring potential applications. Subsequently, given the limited time available for this work, we have chosen to explore the potentialities for photovoltaics of only two compounds: CIGS_5 and CIGS_6 . Chapter 3 describes the preparation of thin films through to device assembly. Concerning photocatalytic hydrogen production, only CIGS_6 was evaluated. Chapter 4 covers the preparation of nanopowders up to hydrogen evolution. In all cases, the chalcopyrite $\text{CuIn}_{0.7}\text{Ga}_{0.3}\text{S}_2$ (CIGS) has been also studied for comparison purposes.

References

- (1) *Compound Copper Chalcogenide Nanocrystals | Chemical Reviews*.
<https://pubs.acs.org/doi/10.1021/acs.chemrev.6b00376> (accessed 2023-06-05).
- (2) Chandrasekaran, S.; Yao, L.; Deng, L.; Bowen, C.; Zhang, Y.; Chen, S.; Lin, Z.; Peng, F.; Zhang, P. Recent Advances in Metal Sulfides: From Controlled Fabrication to Electrocatalytic, Photocatalytic and Photoelectrochemical Water Splitting and Beyond. *Chem. Soc. Rev.* **2019**, *48* (15), 4178–4280.
<https://doi.org/10.1039/C8CS00664D>.
- (3) Haque, F.; Daeneke, T.; Kalantar-zadeh, K.; Ou, J. Z. Two-Dimensional Transition Metal Oxide and Chalcogenide-Based Photocatalysts. *Nano-Micro Lett.* **2017**, *10* (2), 23. <https://doi.org/10.1007/s40820-017-0176-y>.
- (4) Le Donne, A.; Trifiletti, V.; Binetti, S. New Earth-Abundant Thin Film Solar Cells Based on Chalcogenides. *Front. Chem.* **2019**, *7*.
- (5) Thomere, A. Absorbanceurs Chalcogénures à Grand Gap ~1,7 EV Pour La Réalisation de Cellules Solaires En Couches Minces. These de doctorat, Nantes, 2020.
<https://www.theses.fr/2020NANT4001> (accessed 2023-06-07).
- (6) Thomere, A.; Guillot-Deudon, C.; Caldes, M. T.; Bodeux, R.; Barreau, N.; Jobic, S.; Lafond, A. Chemical Crystallographic Investigation on Cu₂S-In₂S₃-Ga₂S₃ Ternary System. *Thin Solid Films* **2018**, *665*, 46–50.
<https://doi.org/10.1016/j.tsf.2018.09.003>.
- (7) Lafond, A.; Guillot-Deudon, C.; Paris, M.; Caldes, M. T.; Jobic, S. Crystal Chemistry Investigations on Photovoltaic Chalcogenides; 2020.
- (8) Kato, T.; Hayashi, S.; Kiuchi, T.; Ishihara, Y.; Nabetani, Y.; Matsumoto, T. Structural Properties of Cu(Ga_{1-x}In_x)YSz Bulk Alloys. *J. Cryst. Growth* **2002**, *237–239*, 2005–2008. [https://doi.org/10.1016/S0022-0248\(01\)02304-1](https://doi.org/10.1016/S0022-0248(01)02304-1).
- (9) Schock, H.-W. Solar Cell solar Cell, Chalcopyrite-Based solar Cell chalcopyrite-Based Thin Film. In *Solar Energy*; Richter, C., Lincot, D., Gueymard, C. A., Eds.; Springer: New York, NY, 2013; pp 323–340. https://doi.org/10.1007/978-1-4614-5806-7_464.
- (10) Bär, M.; Bohne, W.; Röhrich, J.; Strub, E.; Lindner, S.; Lux-Steiner, M. C.; Fischer, Ch.-H.; Niesen, T. P.; Karg, F. Determination of the Band Gap Depth Profile of the Penternary Cu(In_{1-x}Ga_x)(S_{1-y}Se_{1-y})₂ Chalcopyrite from Its Composition Gradient. *J. Appl. Phys.* **2004**, *96* (7), 3857–3860.
<https://doi.org/10.1063/1.1786340>.
- (11) Chen, Y.; Feng, X.; Liu, M.; Su, J.; Shen, S. Towards Efficient Solar-to-Hydrogen Conversion: Fundamentals and Recent Progress in Copper-Based Chalcogenide Photocathodes. *Nanophotonics* **2016**, *5* (4), 524–547.
<https://doi.org/10.1515/nanoph-2016-0027>.
- (12) Oishi, K.; Yoneda, K.; Yoshida, O.; Yamazaki, M.; Jimbo, K.; Katagiri, H.; Araki, H.; Kobayashi, S.; Tsuboi, N. Characterization of Cu(In,Ga)S₂ Crystals Grown from the Melt. *Thin Solid Films* **2007**, *515* (15), 6265–6268.
<https://doi.org/10.1016/j.tsf.2006.12.145>.
- (13) Lewerenz, H. J.; Goslowky, H.; Husemann, K.-D.; Fiechter, S. Efficient Solar Energy Conversion with CuInS₂. *Nature* **1986**, *321* (6071), 687–688.
<https://doi.org/10.1038/321687a0>.

- (14) Nakabayashi, T.; Miyazawa, T.; Hashimoto, Y.; Ito, K. Over 10% Efficient CuInS₂ Solar Cell by Sulfurization. *Sol. Energy Mater. Sol. Cells* **1997**, *49* (1), 375–381. [https://doi.org/10.1016/S0927-0248\(97\)00090-1](https://doi.org/10.1016/S0927-0248(97)00090-1).
- (15) Siebentritt, S.; Lomuscio, A.; Adeleye, D.; Sood, M.; Dwivedi, A. Sulfide Chalcopyrite Solar Cells—Are They the Same as Selenides with a Wider Bandgap? *Phys. Status Solidi RRL – Rapid Res. Lett.* **2022**, *16* (8), 2200126. <https://doi.org/10.1002/pssr.202200126>.
- (16) Hiroi, H.; Iwata, Y.; Adachi, S.; Sugimoto, H.; Yamada, A. New World-Record Efficiency for Pure-Sulfide Cu(In,Ga)S₂ Thin-Film Solar Cell With Cd-Free Buffer Layer via KCN-Free Process. *IEEE J. Photovolt.* **2016**, *6* (3), 760–763. <https://doi.org/10.1109/JPHOTOV.2016.2537540>.
- (17) Merdes, S.; Mainz, R.; Klaer, J.; Meeder, A.; Rodriguez-Alvarez, H.; Schock, H. W.; Lux-Steiner, M. Ch.; Klenk, R. 12.6% Efficient CdS/Cu(In,Ga)S₂-Based Solar Cell with an Open Circuit Voltage of 879mV Prepared by a Rapid Thermal Process. *Sol. Energy Mater. Sol. Cells* **2011**, *95* (3), 864–869. <https://doi.org/10.1016/j.solmat.2010.11.003>.
- (18) Barreau, N.; Bertin, E.; Crossay, A.; Durand, O.; Arzel, L.; Harel, S.; Lepetit, T.; Assmann, L.; Gautron, E.; Lincot, D. Investigation of Co-Evaporated Polycrystalline Cu(In,Ga)S₂ Thin Film Yielding 16.0 % Efficiency Solar Cell. *EPJ Photovolt.* **2022**, *13*, 17. <https://doi.org/10.1051/epjpv/2022014>.
- (19) Kobayakawa, K.; Teranishi, A.; Tsurumaki, T.; Sato, Y.; Fujishima, A. Photocatalytic Activity of CuInS₂ and CuIn₅S₈. *Electrochimica Acta* **1992**, *37* (3), 465–467. [https://doi.org/10.1016/0013-4686\(92\)87037-Z](https://doi.org/10.1016/0013-4686(92)87037-Z).
- (20) Zheng, L.; Xu, Y.; Song, Y.; Wu, C.; Zhang, M.; Xie, Y. Nearly Monodisperse CuInS₂ Hierarchical Microarchitectures for Photocatalytic H₂ Evolution under Visible Light. *Inorg. Chem.* **2009**, *48* (9), 4003–4009. <https://doi.org/10.1021/ic802399f>.
- (21) Yuan, Y.-J.; Chen, D.-Q.; Huang, Y.-W.; Yu, Z.-T.; Zhong, J.-S.; Chen, T.-T.; Tu, W.-G.; Guan, Z.-J.; Cao, D.-P.; Zou, Z.-G. MoS₂ Nanosheet-Modified CuInS₂ Photocatalyst for Visible-Light-Driven Hydrogen Production from Water. *ChemSusChem* **2016**, *9* (9), 1003–1009. <https://doi.org/10.1002/cssc.201600006>.
- (22) Xu, X.-T.; Pan, L.; Zhang, X.; Wang, L.; Zou, J.-J. Rational Design and Construction of Cocatalysts for Semiconductor-Based Photo-Electrochemical Oxygen Evolution: A Comprehensive Review. *Adv. Sci.* **2019**, *6* (2), 1801505. <https://doi.org/10.1002/adv.201801505>.
- (23) Zhu, D.; Ye, H.; Liu, Z.; Liu, J.; Fu, H.; Huang, Y.; Teng, F.; Wang, Z.; Tang, A. Seed-Mediated Growth of Heterostructured Cu_{1.94}S–MS (M = Zn, Cd, Mn) and Alloyed CuNS₂ (N = In, Ga) Nanocrystals for Use in Structure- and Composition-Dependent Photocatalytic Hydrogen Evolution. *Nanoscale* **2020**, *12* (10), 6111–6120. <https://doi.org/10.1039/C9NR10004K>.
- (24) Zhao, M.; Huang, F.; Lin, H.; Zhou, J.; Xu, J.; Wu, Q.; Wang, Y. CuGaS₂–ZnS p–n Nanoheterostructures: A Promising Visible Light Photo-Catalyst for Water-Splitting Hydrogen Production. *Nanoscale* **2016**, *8* (37), 16670–16676. <https://doi.org/10.1039/C6NR05002F>.
- (25) Liu, Z.; Liu, J.; Huang, Y.; Li, J.; Yuan, Y.; Ye, H.; Zhu, D.; Wang, Z.; Tang, A. From One-Dimensional to Two-Dimensional Wurtzite CuGaS₂ Nanocrystals: Non-Injection Synthesis and Photocatalytic Evolution. *Nanoscale* **2019**, *11* (1), 158–169. <https://doi.org/10.1039/C8NR07353H>.

- (26) Yu, X.; An, X.; Shavel, A.; Ibáñez, M.; Cabot, A. The Effect of the Ga Content on the Photocatalytic Hydrogen Evolution of $\text{CuIn}_{1-x}\text{Ga}_x\text{S}_2$ Nanocrystals. *J. Mater. Chem. A* **2014**, *2* (31), 12317–12322. <https://doi.org/10.1039/C4TA01315H>.
- (27) Jahagirdar, A. H.; Dhere, N. G. Photoelectrochemical Water Splitting Using $\text{CuIn}_{1-x}\text{Ga}_x\text{S}_2/\text{CdS}$ Thin-Film Solar Cells for Hydrogen Generation. *Sol. Energy Mater. Sol. Cells* **2007**, *91* (15), 1488–1491. <https://doi.org/10.1016/j.solmat.2007.03.022>.
- (28) Wang, D.; Wang, C.; Arquer, F. P. G. de; Zhong, J.; Qian, L.; Fang, L.; Liu, P.; Pang, Y.; Liu, M.; Liu, M.; Zheng, G.; Sinton, D.; Sargent, E. H.; Yang, H.; Zhang, B. Band-Aligned $\text{CuIn}_{1-x}\text{Ga}_x\text{S}_2$ Stabilizes $\text{CdS}/\text{CuInGaS}_2$ Photocathodes for Efficient Water Reduction. *J. Mater. Chem. A* **2017**, *5* (7), 3167–3171. <https://doi.org/10.1039/C6TA10222K>.
- (29) Guan, Z.; Luo, W.; Feng, J.; Tao, Q.; Xu, Y.; Wen, X.; Fu, G.; Zou, Z. Selective Etching of Metastable Phase Induced an Efficient $\text{CuIn}_{0.7}\text{Ga}_{0.3}\text{S}_2$ Nano-Photocathode for Solar Water Splitting. *J. Mater. Chem. A* **2015**, *3* (15), 7840–7848. <https://doi.org/10.1039/C5TA01259G>.
- (30) Kurnia, F.; Scott, J. A.; Valanoor, N.; Hart, J. N. A Review of Non-Oxide Semiconductors for Photoelectrochemical Water Splitting. *J. Mater. Chem. C* **2023**, *11* (3), 802–826. <https://doi.org/10.1039/D2TC02533G>.
- (31) Takata, T.; Domen, K. Development of Non-Oxide Semiconductors as Light Harvesting Materials in Photocatalytic and Photoelectrochemical Water Splitting. *Dalton Trans.* **2017**, *46* (32), 10529–10544. <https://doi.org/10.1039/C7DT00867H>.
- (32) Makhova, L. V.; Konovalov, I.; Szargan, R. Growth and Characterization of AgIn_5S_8 and CuIn_5S_8 Thin Films. *Phys. Status Solidi A* **2004**, *201* (2), 308–311. <https://doi.org/10.1002/pssa.200303975>.
- (33) Ivashchenko, I. A.; Olekseyuk, I. D.; Gulay, L. D.; Halyan, V. V.; Kevshyn, A. H.; Tishchenko, P. V.; Strok, O. M. Crystal Structure and Physical Properties of the Quaternary Phase $\text{CuGa}_x\text{In}_{5-x}\text{S}_8$, $1.4 \leq x \leq 2.05$, in the $\text{Cu}_2\text{S} - \text{Ga}_2\text{S}_3 - \text{In}_2\text{S}_3$ System. *J. Solid State Chem.* **2022**, *310*, 123034. <https://doi.org/10.1016/j.jssc.2022.123034>.
- (34) Malar, P.; Pillai, S. S.; Kasiviswanathan, S. Structural, Optical and Compositional Studies of Stepwise Flash Evaporated CuIn_3Te_5 Films. *Mater. Chem. Phys.* **2007**, *101* (1), 118–123. <https://doi.org/10.1016/j.matchemphys.2006.02.024>.
- (35) Boehnke, U.-C.; Kühn, G. Phase Relations in the Ternary System Cu-In-Se . *J. Mater. Sci.* **1987**, *22* (5), 1635–1641. <https://doi.org/10.1007/BF01132385>.
- (36) Zhang, S. B.; Wei, S.-H.; Zunger, A. Stabilization of Ternary Compounds via Ordered Arrays of Defect Pairs. *Phys. Rev. Lett.* **1997**, *78* (21), 4059–4062. <https://doi.org/10.1103/PhysRevLett.78.4059>.
- (37) Kumar, S.; Joshi, S.; Auluck, S. An Ab-Initio Study of CuInSe_2 Based Ordered Defect Compounds. *Mater. Chem. Phys.* **2015**, *162*, 372–379. <https://doi.org/10.1016/j.matchemphys.2015.06.001>.
- (38) Guedez, E.; Mogollón, L.; Marcano, G.; Wasim, S. M.; Sánchez Pérez, G.; Rincón, C. Structural Characterization and Optical Absorption Spectrum of $\text{Cu}_3\text{In}_5\text{Te}_9$ Ordered Defect Semiconducting Compound. *Mater. Lett.* **2017**, *186*, 155–157. <https://doi.org/10.1016/j.matlet.2016.09.122>.

- (39) Usujima, A.; Takeuchi, S.; Endo, S.; Irie, T. Optical and Electrical Properties of CuIn₅S₈ and AgIn₅S₈ Single Crystals. *Jpn. J. Appl. Phys.* **1981**, *20* (7), L505. <https://doi.org/10.1143/JJAP.20.L505>.
- (40) Khemiri, N.; Kanzari, M. Investigation on Dispersive Optical Constants and Electrical Properties of CuIn₅S₈ Thin Films. *Solid State Commun.* **2013**, *160*, 32–36. <https://doi.org/10.1016/j.ssc.2013.02.016>.
- (41) Marsen, B.; Wilhelm, H.; Steinkopf, L.; Klemz, S.; Unold, T.; Scheer, R.; Schock, H.-W. Effect of Copper-Deficiency on Multi-Stage Co-Evaporated Cu(In,Ga)₂S₃ Absorber Layers and Solar Cells. *Thin Solid Films* **2011**, *519* (21), 7224–7227. <https://doi.org/10.1016/j.tsf.2011.01.146>.
- (42) Barreau, N. Indium Sulfide and Relatives in the World of Photovoltaics. *Sol. Energy* **2009**, *83* (3), 363–371. <https://doi.org/10.1016/j.solener.2008.08.008>.
- (43) Abou-Ras, D.; Kostorz, G.; Strohm, A.; Schock, H.-W.; Tiwari, A. N. Interfacial Layer Formations between Cu(In,Ga)Se₂ and In_xS_y Layers. *J. Appl. Phys.* **2005**, *98* (12), 123512. <https://doi.org/10.1063/1.2149166>.
- (44) Scrosati, B.; Fornarini, L.; Razzini, G.; Bicelli, L. P. The Photoelectrochemical Behavior of CuIn₅S₈. *J. Electrochem. Soc.* **1985**, *132* (3), 593. <https://doi.org/10.1149/1.2113912>.
- (45) Gannouni, M.; Ben Assaker, I.; Chtourou, R. Photoelectrochemical Cell Based on N-CuIn₅S₈ Film as Photoanodes for Photocatalytic Water Splitting. *Int. J. Hydrog. Energy* **2015**, *40* (23), 7252–7259. <https://doi.org/10.1016/j.ijhydene.2015.04.057>.
- (46) Feng, X.; Li, R.; Wang, M.; Chen, Y. Switchable Synthesis of p- and n-Type Cu–In–S Grooved Pyramid-like Microcrystals for Unassisted Photoelectrochemical Water Splitting. *J. Mater. Chem. A* **2018**, *6* (24), 11180–11188. <https://doi.org/10.1039/C8TA02386G>.
- (47) Li, X.; Sun, Y.; Xu, J.; Shao, Y.; Wu, J.; Xu, X.; Pan, Y.; Ju, H.; Zhu, J.; Xie, Y. Selective Visible-Light-Driven Photocatalytic CO₂ Reduction to CH₄ Mediated by Atomically Thin CuIn₅S₈ Layers. *Nat. Energy* **2019**, *4* (8), 690–699. <https://doi.org/10.1038/s41560-019-0431-1>.
- (48) Liu, S.; Chen, L.; Liu, T.; Cai, S.; Zou, X.; Jiang, J.; Mei, Z.; Gao, Z.; Guo, H. Rich S Vacant G-C₃N₄@CuIn₅S₈ Hollow Heterojunction for Highly Efficient Selective Photocatalytic CO₂ Reduction. *Chem. Eng. J.* **2021**, *424*, 130325. <https://doi.org/10.1016/j.cej.2021.130325>.
- (49) Ueda, K.; Maeda, T.; Wada, T. Crystallographic and Optical Properties of CuGa₃S₅, CuGa₃Se₅ and CuIn₃(S,Se)₅ and CuGa₃(S,Se)₅ Systems. *Thin Solid Films* **2017**, *633*, 23–30. <https://doi.org/10.1016/j.tsf.2017.01.036>.
- (50) Tabata, M.; Maeda, K.; Ishihara, T.; Minegishi, T.; Takata, T.; Domen, K. Photocatalytic Hydrogen Evolution from Water Using Copper Gallium Sulfide under Visible-Light Irradiation. *J. Phys. Chem. C* **2010**, *114* (25), 11215–11220. <https://doi.org/10.1021/jp103158f>.
- (51) Kaga, H.; Kudo, A. Cosubstituting Effects of Copper(I) and Gallium(III) for ZnGa₂S₄ with Defect Chalcopyrite Structure on Photocatalytic Activity for Hydrogen Evolution. *J. Catal.* **2014**, *310*, 31–36. <https://doi.org/10.1016/j.jcat.2013.08.025>.
- (52) Ivashchenko, I. A.; Danyliuk, I. V.; Olekseyuk, I. D.; Pankevych, V. Z.; Halyan, V. V. Phase Equilibria in the Quasiternary System Ag₂S–Ga₂S₃–In₂S₃ and Optical Properties of (Ga₅₅In₄₅)₂S₃₀₀, (Ga_{54.59}In_{44.66}Er_{0.75})₂S₃₀₀ Single Crystals. *J. Solid State Chem.* **2015**, *227*, 255–264. <https://doi.org/10.1016/j.jssc.2015.04.006>.

- (53) Guseinov, G. G.; Kyazimov, M. G.; Suliev, A. S.; Amiraslanov, I. R.; Mekhtiev, G. S. Crystal Structure of Gallium Indium Sulfide (Ga In S₃). *Doklady - Akademiya Nauk Azerbaidzhanskoi SSR (1988)* **44**, (7) p. 26-30.
- (54) Amiraslanov, I. R.; Veliyev, R. B.; Mysayev, A. A.; Asadov, S. G.; Gyseynov, G. G. On the Phase Formation in Ga₂ Si - In₂ S₃ System and the Crystal Structure of Ga_{0.5} In_{1.5} S₃. *Doklady - Akademiya Nauk Azerbaidzhanskoi SSR (1990)* **46**, p. 33-36.
- (55) Amiraslanov, I. R.; Asadov, F. Yu.; Musaev, A. A.; Gusejnov, G. G. Crystal Structure of a New Layer Semiconductor Ga₁₇₄In₂₉₂S₇. *Kristallografiya* **1989**, **34** (4), 1012–1013.
- (56) AMIRASLANOV, I. R.; ASADOV, Y. G.; VALIEV, R. B.; MUSAEV, A. A.; GUSEINOV, G. G. Structure and Intercalation of the Two-Packet Polytype of GaInS₃ (b, II). *Struct. Intercalation Two-Pack. Polytype GaInS₃ B II* **1990**, **35** (5), 766–767.
- (57) Amiraslanov, I. R.; Gusejnov, G. G.; Kuliev, A. S.; Mamedov, Kh. S.; Amirov, A. S. Crystal Structure of GaInS₃(3) Three-Packed Polytype. *Kristallografiya* **1988**, **33** (3), 767–768.
- (58) Krämer, V.; Nitsche, R.; Ottemann, J. New Single-Crystalline Phases in the System Ga₂S₃-In₂S₃. *J. Cryst. Growth* **1970**, **7** (3), 285–289. [https://doi.org/10.1016/0022-0248\(70\)90052-7](https://doi.org/10.1016/0022-0248(70)90052-7).
- (59) Kityk, I. V.; Yukhymchuk, V. O.; Fedorchuk, A.; Halyan, V. V.; Ivashchenko, I. A.; Oleksieyuk, I. D.; Skoryk, M. A.; Lakshminarayana, G.; El-Naggar, A. M.; Albassam, A. A.; Lebed, O. O.; Piasecki, M. Laser Stimulated Piezo-Optics of γ -Irradiated (Ga₅₅In₄₅)₂S₃₀₀ and (Ga_{54.59}In_{44.66}Er_{0.75})₂S₃₀₀ Single Crystals. *J. Alloys Compd.* **2017**, **722**, 265–271. <https://doi.org/10.1016/j.jallcom.2017.06.072>.
- (60) Ivashchenko, I. A.; Danyliuk, I. V.; Gulay, L. D.; Halyan, V. V.; Olekseyuk, I. D. Isothermal Sections of the Quasi-Ternary Systems Ag₂S(Se)–Ga₂S(Se)₃–In₂S(Se)₃ at 820K and the Physical Properties of the Ternary Phases Ga_{5.5}In_{4.5}S₁₅, Ga₆In₄Se₁₅ and Ga_{5.5}In_{4.5}S₁₅:Er₃₊, Ga₆In₄Se₁₅:Er₃₊. *J. Solid State Chem.* **2016**, **237**, 113–120. <https://doi.org/10.1016/j.jssc.2015.11.022>.
- (61) Caldes, M. T.; Guillot-Deudon, C.; Thomere, A.; Penicaud, M.; Gautron, E.; Boullay, P.; Bujoli-Doeuff, M.; Barreau, N.; Jobic, S.; Lafond, A. Layered Quaternary Compounds in the Cu₂S–In₂S₃–Ga₂S₃ System. *Inorg. Chem.* **2020**, **59** (7), 4546–4553. <https://doi.org/10.1021/acs.inorgchem.9b03686>.
- (62) Haeuseler, H.; Srivastava, S. K. Phase Equilibria and Layered Phases in the Systems A₂X₃-M₂X₃-M'X (A = Ga, In; M = Trivalent Metal; M' = Divalent Metal; X = S, Se). *Z. Für Krist. - Cryst. Mater.* **2000**, **215** (4), 205–221. <https://doi.org/10.1524/zkri.2000.215.4.205>.
- (63) Khyzhun, O. Y.; Halyan, V. V.; Danyliuk, I. V.; Ivashchenko, I. A. Electronic Structure of (Ga₅₅In₄₅)₂S₃₀₀ and (Ga_{54.59}In_{44.66}Er_{0.75})₂S₃₀₀ Single Crystals. *J. Mater. Sci. Mater. Electron.* **2016**, **27** (4), 3258–3264. <https://doi.org/10.1007/s10854-015-4153-2>.
- (64) Kandiel, T. A.; Anjum, D. H.; Takanabe, K. Nano-Sized Quaternary CuGa₂In₃S₈ as an Efficient Photocatalyst for Solar Hydrogen Production. *ChemSusChem* **2014**, **7** (11), 3112–3121. <https://doi.org/10.1002/cssc.201402525>.
- (65) Haeuseler, H.; Elitok, E.; Memo, A.; Arzani, R. Verbindungen mit Schichtstrukturen in den Systemen CuGa₅S₈/CuIn₅S₈ und AgGa₅S₈/AgIn₅S₈. *Z. Für Anorg. Allg. Chem.* **2001**, **627** (6), 1204–1208. [https://doi.org/10.1002/1521-3749\(200106\)627:6<1204::AID-ZAAC1204>3.0.CO;2-V](https://doi.org/10.1002/1521-3749(200106)627:6<1204::AID-ZAAC1204>3.0.CO;2-V).

- (66) Kandiel, T. A.; Hutton, G. A. M.; Reisner, E. Visible Light Driven Hydrogen Evolution with a Noble Metal Free CuGa₂In₃S₈ Nanoparticle System in Water. *Catal. Sci. Technol.* **2016**, *6* (17), 6536–6541. <https://doi.org/10.1039/C6CY01103A>.

Chapter 2: Optoelectronic properties of CIGS_n lamellar compounds

The aim of this chapter is to determine optical and electronic properties of the CIGS_n compounds, in relation to the specifications required for photovoltaic or photocatalysis applications and to compare them to those of the well-reported chalcopyrite CIGS.

For this purpose, a series of intrinsic properties needs to be evaluated such as visible light absorption, band gap energy, nature of majority charge carriers (i.e. semiconductor type), charge carrier lifetimes and Fermi level. Moreover, to improve photovoltaic or photocatalytic efficiency, a good bands alignment is needed, to optimise the separation and migration of the photo-generated carriers. Thus, the energy diagrams of CIGS_n compounds have been also determined to compare to those of standard PV buffer layers as well as to redox potentials involved in some photocatalyzed reactions. To carry out this study, an analytical approach combining diffuse reflectance spectroscopy, (photo)electrochemical measurements and photoluminescence spectroscopy was set up.

Therefore, the first part of the chapter focuses on the synthesis and the structural characterization of CIGS_n compounds. After obtaining the compounds, optical gaps were determined by diffuse reflectance measurements.

The second part of the chapter is devoted to the investigation of the electronic properties of CIGS_n through a full electrochemical study, preceded by a basic description of the electrochemistry measurements performed in this work. Indeed, electrochemical analyses under dark and under illumination were used to determine the nature of the majority carriers as well as the Fermi level position of our materials. Photoluminescence measurements were also performed to investigate the existence of in-gap defect states, which could influence the kinetics of photogenerated charges decay and improve light absorption by red shifting the absorption region.

Finally, in order to rationalize the various electronic and photoconductive properties of the CIGS_n series compared to those of the chalcopyrite CIGS, the energy diagrams were established, combining electrochemical and spectroscopic characterization techniques.

1. Synthesis and characterisation of CIGS_n compounds

The CIGS_n powders presented in this chapter were synthesised by a solid-state reaction route, following the protocol already used by our group.¹ Cu_{0.32}In_{1.74}Ga_{0.84}S₄ (CIGS₄), Cu_{0.65}In_{1.75}Ga_{1.4}S₅ (CIGS₅) and Cu_{1.44}In_{2.77}Ga_{0.76}S₆ (CIGS₆) lamellar compounds besides CuIn_{0.7}Ga_{0.3}S₂ (CIGS) chalcopyrite were prepared from binary precursors (i.e. metal sulphides Cu₂S, Ga₂S₃ and In₂S₃) in stoichiometric ratios, using a reaction at high temperature that proceeds as follows:

- The precursors are weighed, grinded manually and then introduced into silica tubes.
- The silica tubes are sealed under vacuum, approximately 2×10^{-3} mbar, before placing them in a furnace heated up to 800°C for 48h and then cooled down to room temperature by quenching (Figure 1).
- In the case of CIGS₆, annealing is required for a better-homogenized sample. Once we recover the powder from the tube, we grind it again before sealing the mixture in a silica tube and heating under the same conditions as in the previous step.

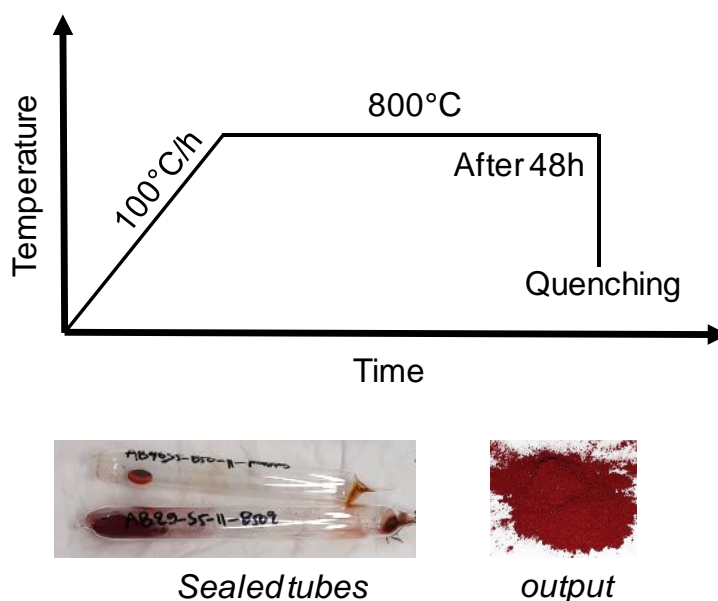


Figure 1: Protocol followed for the synthesis and annealing of high temperature powders by the ceramic route.

The obtained samples were characterised by powder X-ray diffraction (PXRD). Experimental conditions are described in appendix. XRD pattern and Le Bail refinements of CIGS_n compounds are shown in Figures 2-4.

Le Bail refinements attest that we have successfully reproduced the results previously published by our group.¹ Thus, the majority of observed peaks can be indexed considering unit cell parameters and space groups obtained by single crystal X-ray diffraction. However, for CIGS₄ and CIGS₅, two and four polytypes respectively must be considered to

explain all the reflections. They have been identified by combining EDX analysis and electron diffraction.¹

In the case of CIGS_4 , Le Bail refinement based on a fundamental approach, was carried out with the four polytypes identified. It was not possible to refine at the same time the unit cell parameters and the crystallite size for all the polytypes. Moreover, a large preferential orientation was also observed due to the platelet shape of the grains, despite careful sample preparation (pattern recorded on a diffractometer in Bragg-Brentano geometry). Due to the mixed occupancy of the tetrahedral sites (i.e. Cu, Ga, In atoms), over more can be quite different, the contribution of microstrains should also be taken into account for the peak shape profile. This was also not possible because of the complexity of the diagram. Therefore, it results that some residue appear on the curve difference (Figure 2).

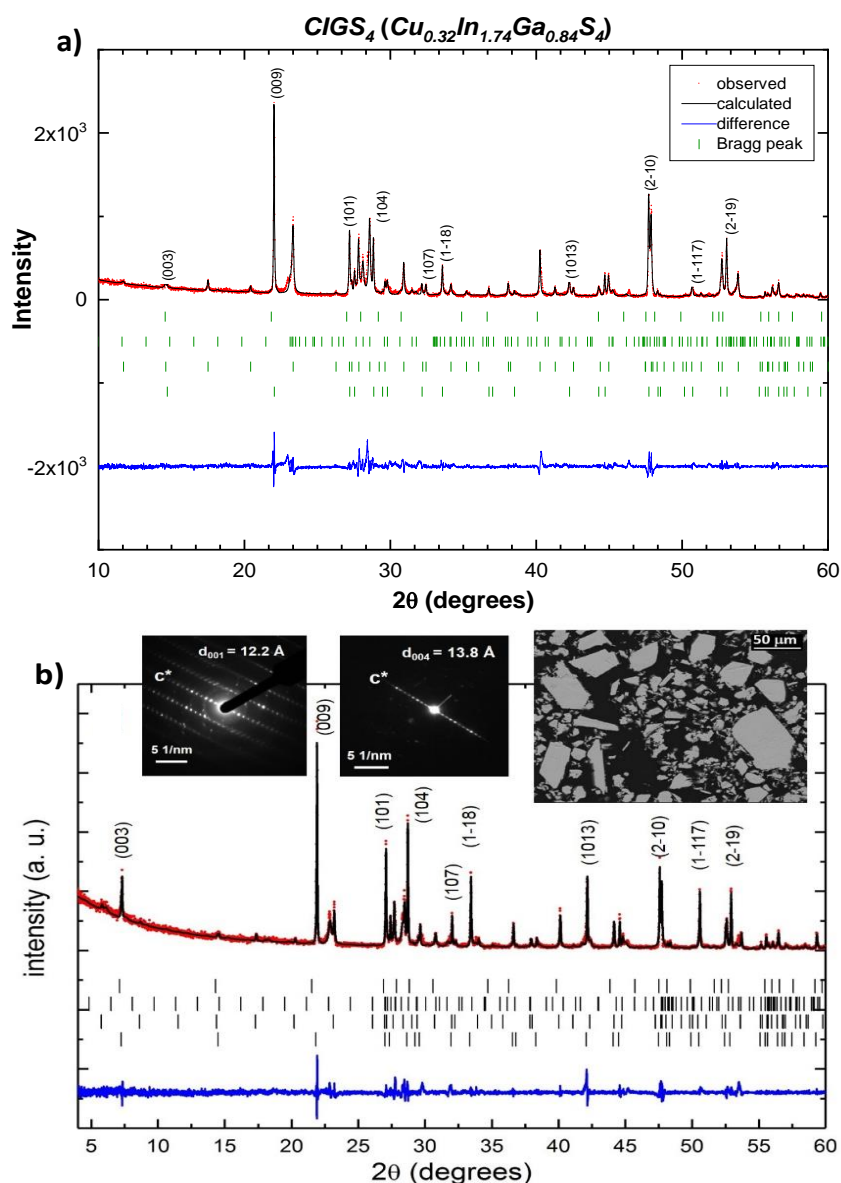


Figure 2: XRD pattern and Le Bail refinement of the $\text{CIGS}_4 (\text{Cu}_{0.32}\text{In}_{1.74}\text{Ga}_{0.84}\text{S}_4)$ compound a) prepared during the thesis b) with electron image and electron diffraction patterns presented in the backscattered. Figure from reference Caldes et al ¹

A Rietveld refinement was not possible due to the absence of a structural model for all polytypes involved. The polytypism of CIGS_n series is not surprising given that this trend has also been described for isostructural $\text{Zn}_m\text{In}_2\text{S}_{3+m}$ series. The polytypes differ in the long-range ordering of the Td-Oh-Td blocks along the stacking axis and the cations distribution.² The polytypism of CIGS_4 is illustrated in Figure 2 b. Indeed, although electron diffraction patterns attest to the existence of at least two kinds of crystals, the homogeneous contrast observed in the backscattered electron image indicates a single chemical composition, confirmed by EDX analyses.¹

Concerning CIGS_5 , the refinement was performed considering two polytypes (Figure 3), and for the same reasons as for the CIGS_4 sample, the difference curve presents also a rough profile.

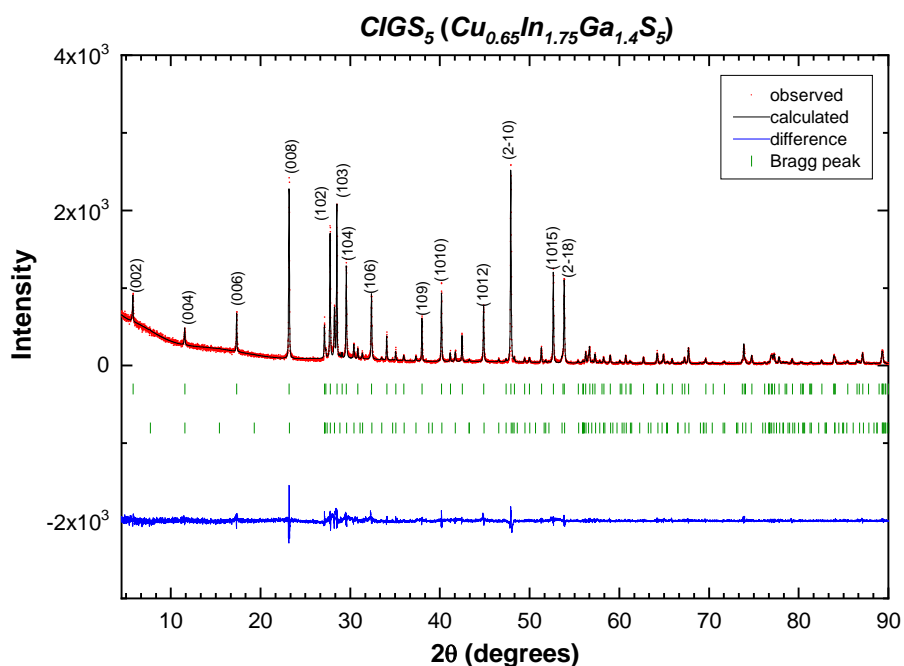


Figure 3: XRD pattern and Le Bail refinement of the CIGS_5 ($\text{Cu}_{0.65}\text{In}_{1.75}\text{Ga}_{1.4}\text{S}_5$) compound.

For CIGS_6 all reflections observed in the PXRD could be indexed by considering a single polymorph (SG: $P\bar{3}m1$, $a = 3.85$, $c = 18.69$ Å). The broad reflection marked by an asterisk on Figure 4, can be considered as a fingerprint of intergrowths defects.

Figure 5 shows the XRD pattern of CIGS chalcopyrite. In contrast with the CIGS_n series, as observed all the peaks are perfectly indexed by considering the single targeted compound. Unlike the lamellar CIGS_n , no extra broad reflections are distinguished.

Table 1 summarizes cell parameters of CIGS_n and CIGS compounds issued from the Le Bail refinements and their corresponding reliability parameters.

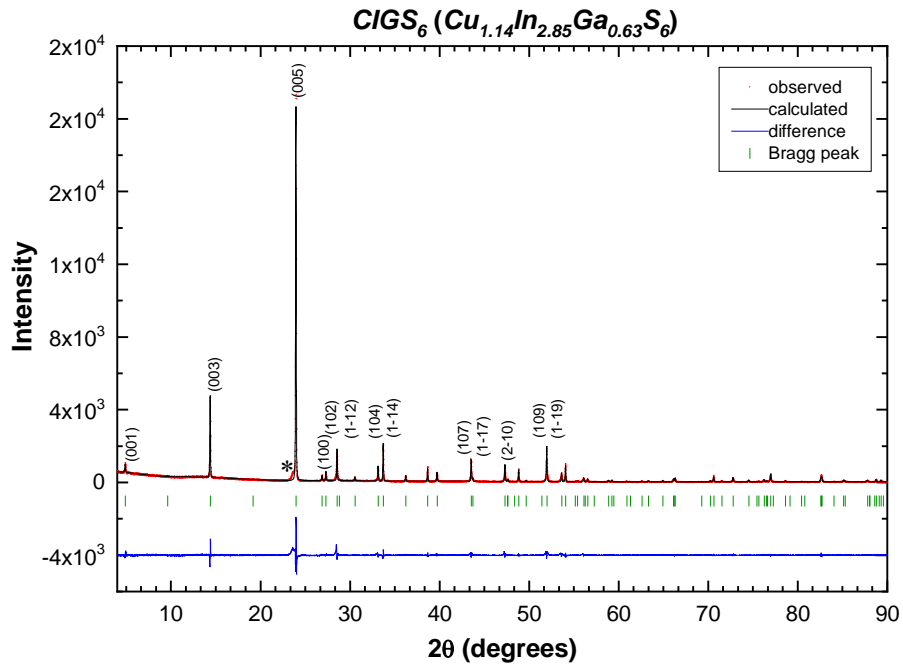


Figure 4: XRD pattern and Le Bail refinement of the CIGS₆ (Cu_{1.44}In_{2.77}Ga_{0.76}S₆) compound. The broad reflections (*) present the intergrowths fingerprints.

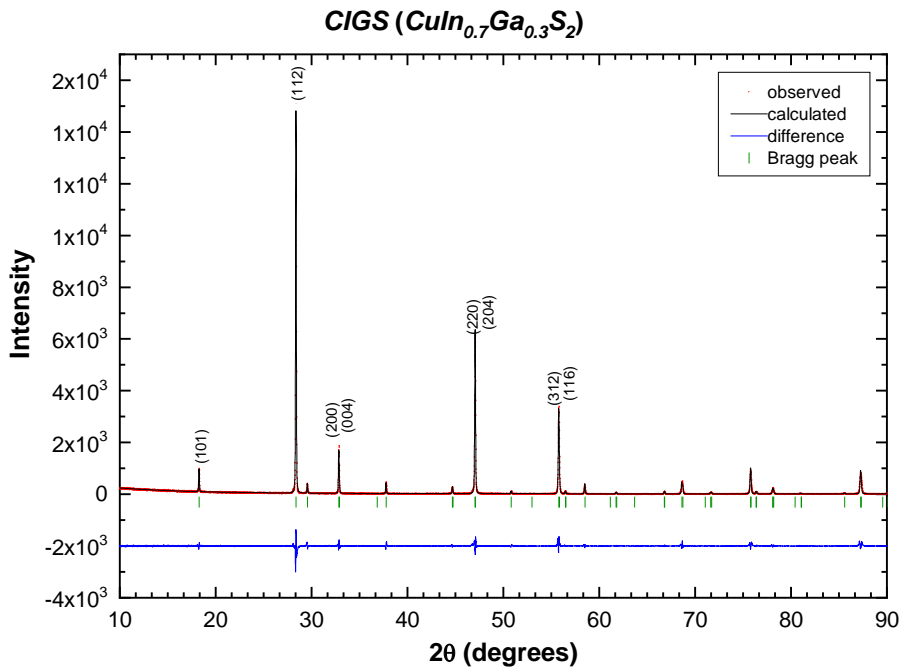


Figure 5: XRD pattern and Le Bail refinement of the CIGS (CuIn_{0.7}Ga_{0.3}S₂) compound.

Table 1: Cell parameters of the prepared CIGS₅, CIGS₆ and CIGS compounds obtained from Le Bail refinement.

Sample	a(Å)	c(Å)	Space group
CIGS₄	3.8399(3)	12.321(1)	<i>P</i> 3̄ <i>m</i> 1
	3.82395(6)	36.6130(8)	<i>R</i> 3̄ <i>m</i>
	3.81115(7)	30.7284(8)	<i>P</i> 3̄ <i>m</i> 1
	3.8552(2)	54.281(3)	<i>P</i> 3̄ <i>m</i> 1
CIGS₅	3.7974(2)	30.7124(2)	<i>P</i> 63 <i>mc</i>
	3.7951(2)	46.0465(1)	<i>P</i> 63 <i>mc</i>
CIGS₆	3.8534(2)	18.6956(2)	<i>P</i> 3̄ <i>m</i> 1
CIGS	5.4768(2)	10.9413(2)	<i>I</i> -42 <i>d</i>

2. Diffuse reflectance

The UV-vis-NIR transmission spectroscopy is the key technique to investigate the optical gap. It can be determined using transmittance according to Beer Lambert^{3,4} law that relates the absorbance to the intensity ratio of the light beam absorption (equation 1)

$$A = -\log(T) = -\log\left(\frac{I}{I_0}\right) \quad (1)$$

where A is the absorbance, T the transmittance, *I* the light beam intensity reflected or transmitted and *I*₀ the incident light beam.

However, to carry out the transmittance, the light must be able to pass through the sample, which is not possible with the powders. For this purpose, the optical gap of the CIGS_n powdered samples were determined by diffuse reflectance spectroscopy (DRS). This method consists in sending an incident beam to the sample that will be reflected once it reaches the surface. The light could be reflected according to several mechanisms depending on the nature of the sample as:

- The diffuse reflection of light emitted in all directions of space (the one used during this study).
- The specular reflection representing a direct reflection with a reflection angle of the material equals to the incidence angle.

For powders, the sample thickness is considered infinite and the sample-holder is assumed not to be involved in the process. The obtained reflection spectrum is then processed by the Kubelka-Munk^{5,6} approximation based on the equation 2:

$$F(R) = \frac{K}{S} = \frac{(1 - R^2)}{2R} \quad (2)$$

where K and S are Kubelka-Munk coefficients of absorption and diffusion respectively and R corresponding to the absolute reflectance measured. For Kubelka-Munk application, a sample of at least 1 mm thick is required.

The maximum absorption corresponds to the minimum value of $K(\lambda)$. Thus, the optical gap is determined either from the intercept of the linear portion of the Kubelka-Munk transformed spectrum with the x-axis (linear extrapolation), or from the derivative of the spectrum.

DRS measurements were performed using a PerkinElmer UV-visible-NIR spectrometer in a reflection mode with a diffuse reflection sphere, following the conditions described in appendix. Figure 6 shows the Kubelka-Munk transformed diffuse reflectance spectra of the $CIGS_n$ lamellar compounds.

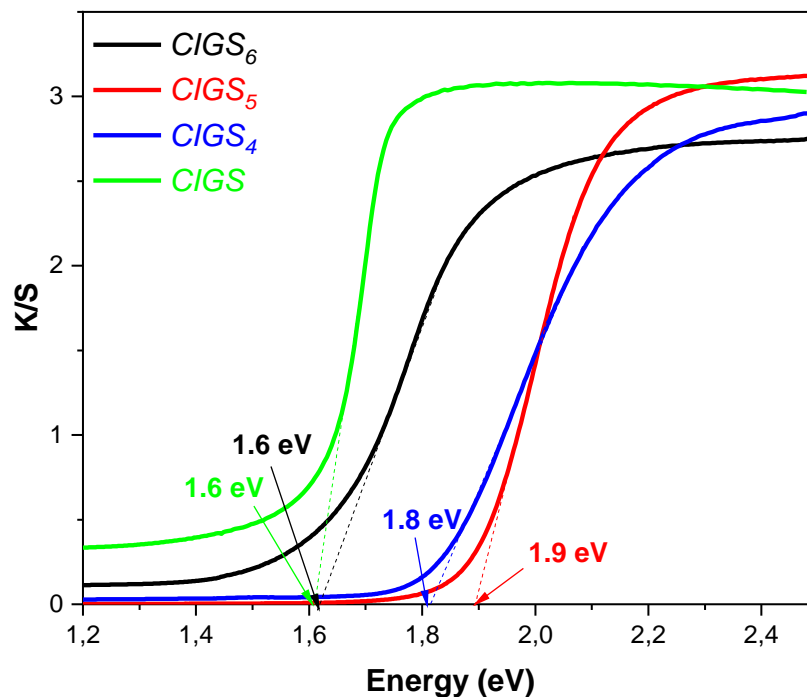


Figure 6: Kubelka-Munk transformed reflectance spectra of the CIGS chalcopyrite and the lamellar compounds: $CIGS_4$, $CIGS_5$ and $CIGS_6$.

Table 2: Optical gap values of $CIGS_4$, $CIGS_5$ and $CIGS_6$ lamellar compounds compared to the one of CIGS.

Sample	Composition	Cu/S	E_g (eV)
$CIGS_4$	$Cu_{0.32}In_{1.74}Ga_{0.84}S_4$	0.08	1.8
$CIGS_5$	$Cu_{0.65}In_{1.75}Ga_{1.4}S_5$	0.13	1.9
$CIGS_6$	$Cu_{1.44}In_{2.77}Ga_{0.76}S_6$	0.2	1.6
CIGS	$CuIn_{0.7}Ga_{0.3}S_2$	0.5	1.6

The optical gaps measured for CIGS_n compounds are close to that of the chalcopyrite CIGS. As mentioned in the previous chapter, the chalcopyrite CuIn_{0.7}Ga_{0.3}S₂ exhibits an efficiency of 16% for photovoltaic application,⁷ and a photocatalytic hydrogen evolution up to 750 μmolh⁻¹g⁻¹.⁸ Thus, regarding the similarity between their optical gaps, we can envisage a potential use of CIGS_n compounds for both applications (i.e. solar cells and photocatalysis).

However, besides optical gap, to evaluate a semiconductor as a potential absorber for photo-induced applications, it is also important to determine other intrinsic properties as: nature of the majority charge carriers, the position of energy levels (Fermi level, conduction and valence bands) and charge carrier's lifetime. Subsequently, these electronic properties were investigated by steady state and transient electrochemistry. These measurements were performed at Institut des Sciences Chimiques de Rennes (ISCR) in collaboration with Dr Adèle RENAUD.

Before presenting the experimental results of these measurements in the following part, some notions concerning the electrochemistry of semiconductors are given, focusing on the semiconductor/electrolyte interface on an electrochemical cell.

3. Electrochemistry of semiconductors: basics

3.1. Semiconductors

The semiconductors (SC) are important materials with many applications, especially for electronic devices due to their energy band structure.

Generally, a semiconductor is characterized by two energy levels limits named the maximum of the valence band (VBM) and the minimum of the conduction band (CBM), as well as the energy band gap (E_g) that refers to the difference between these two levels.

Another key parameter is the Fermi level (E_f), defined as the energy level at which the probability of occupation of an electron is 50%. The probability of the electrons occupancy $f(E)$ in a certain energy state E is expressed by the Fermi-Dirac distribution function⁹ (equation 3)

$$f(E) = \frac{1}{1 + e^{\left(\frac{E - E_f}{k_B T}\right)}} \quad (3)$$

with T is the temperature, k_B is the Boltzmann constant.

As presented in Figure 7, the Fermi level position reflects the distribution of the donors and acceptors of the material.^{10,11}

For an intrinsic semiconductor, where the charge carriers holes (p) and electrons (n) are presented with an equivalent concentration (p = n), the Fermi level is positioned in the middle of the band gap.

A semiconductor that contains impurities is categorised as an extrinsic semiconductor. In this case, levels could be induced in the band gap.

The semiconductor is an n-type, if the majority charge carriers are electrons (n > p). The Fermi level is close to the conduction band following the equation 4, with E_c is the minimum of the conduction band, N_c is the density of states of the conduction band and N_D is the donor density.

$$E_f = E_c - k_B T \times \log\left(\frac{N_c}{N_D}\right) \quad (4)$$

The semiconductor is a p-type, if the majority charge carriers are holes (p > n). The Fermi level is close to the valence band following the equation 5, with E_v is the maximum of the valence band, N_v is the density of states of the valence band and N_A is the acceptor density.

$$E_f = E_v - k_B T \times \log\left(\frac{N_v}{N_A}\right) \quad (5)$$

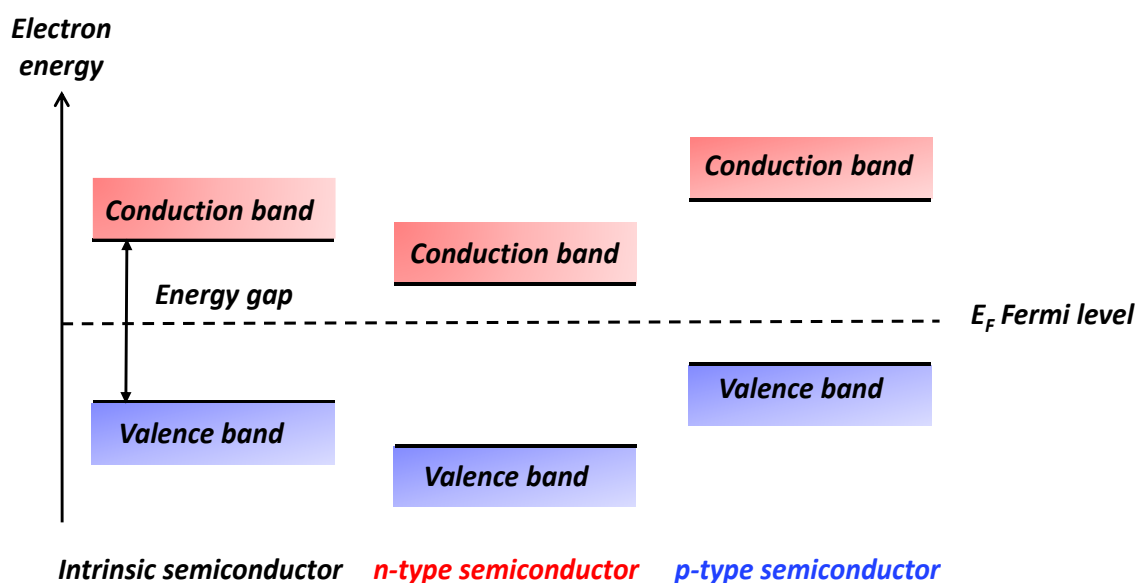


Figure 7: Fermi level positioning for different types of semiconductors (intrinsic, n-type and p-type semiconductors).

Furthermore, as presented in Figure 8, we differentiate between direct and indirect band gap semiconductors.¹²⁻¹⁴ A semiconductor is said to have a direct band gap if its VBM and CBM are associated to the same wave vector ($\Delta k = 0$). Conversely, we speak about indirect band gap when its VBM and its CBM are located at different points of the wave vector ($\Delta k \neq 0$).

The band gap nature is crucial for applications involving electrons and holes. The energy and the wave vector must be preserved throughout the electron-hole pairs formation or recombination. Thus, their conservation is ensured for direct gap semiconductors, since the valence and conduction bands share the same wave vector. The transition of an electron is generated by a photon. Whereas, an indirect band gap requires the presence of a phonon in order to maintain the same vector during the electronic transition. As a result, a direct band gaps transition is guaranteed with only a photon while an indirect gap requires a phonon contribution in order to absorb the photon. This shows that the semiconductors with direct band gap will have stronger light absorption than the ones with indirect gap, as well as a higher charges recombination propensity.

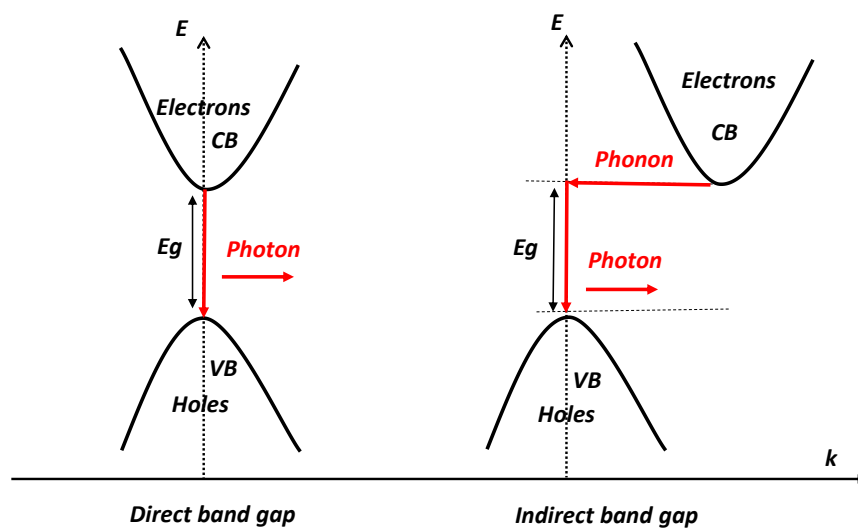


Figure 8: Schematic representation of direct and indirect band gap semiconductors.

Tauc plot ¹⁵ method is used to differentiate between the two types of band gap. To do this, both reflectance and transmission data are needed, making this method more suitable for thin films (as shown in chapter 3).

3.2. Electrochemical cell

Usually, electrochemical measurements are performed using a three electrodes setup: a working electrode (WE) corresponding to the material to be studied, a counter electrode (CE) and a reference electrode (RE) all immersed in an electrolyte (see Figure 9). In our case, the cell is composed of:

- CIGS and CIGS_n compounds as working electrodes. Their preparation conditions are detailed in appendix.
- Platinum wire as counter electrode.
- An Ag/AgCl electrode as reference electrode.

In this thesis, two electrolytes were used: LiClO₄ (0.5 M) or KCl (0.5 M) based-aqueous solutions.

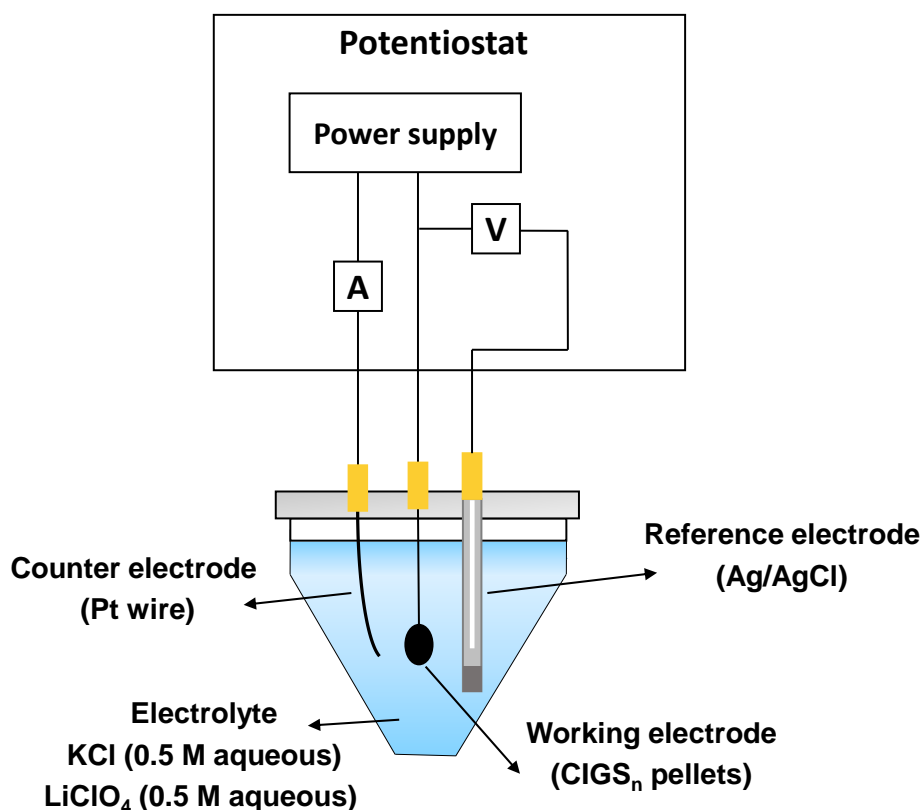


Figure 9: Schematic representation of electrochemical cell with three electrodes, with specific electrodes and electrolyte used during this PhD.

3.3. Interface semiconductor and electrolyte

The interface between the semiconductor and the electrolyte plays an important role in the electrochemical behaviour of the studied compound.¹⁶ Before describing it, a brief background concerning the electrolyte properties is given.

An electrolyte is composed of mobile ions responsible of its conductivity. It can contain redox species, named mediator redox that governs the potential of the solution. According to Nernst's law^{17,18} (equation 6), the redox potential of the mediator depends on the concentration of reduced and oxidized species

$$E_{redox} = E^{\circ} + \frac{R T}{n F} \ln \left(\frac{C_{Oxd}}{C_{Red}} \right) \quad (6)$$

where E_{redox} is the redox potential of the Red/Ox couple, E° is the standard potential, n the number of the electrons, F the faraday constant, R the molar gas constant, T the temperature and C_{Oxd} and C_{Red} are the concentrations of oxidised and reduced species.

If we consider the reduced species (Red) as electron donor levels (occupied orbitals) and the oxidized species (Ox) as electron acceptor levels (empty orbitals), it is possible to draw a parallel with the energy levels described for a solid (valence band and conduction band

respectively). We are able to establish a "pseudo" Fermi level for the oxidizing-reducing pair in a similar manner to that of the Fermi level in solids. The redox potential of the redox mediator corresponds to this intermediate electronic state between the empty and occupied orbitals (Figure 10).

Before contact, the Fermi and pseudo Fermi levels of the semiconductor and the electrolyte are not aligned. When they both come into contact, a charge carrier transfer occurs from the semiconductor to the electrolyte, that leads to equilibrate the electrochemical potentials E_{redox} of the electrolyte and the Fermi level of the semiconductor (see Figure 10).^{10,19}

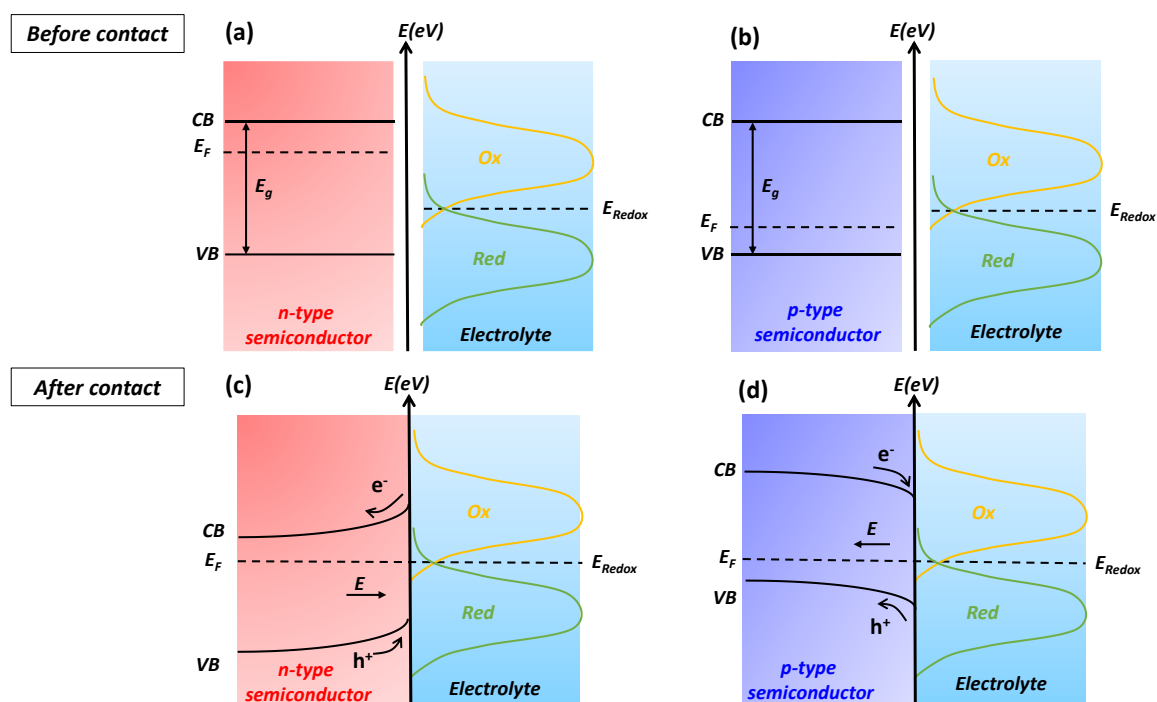


Figure 10: Schematic representation of Fermi levels alignment during the formation of a semiconductor/electrolyte interface.

The charge carriers transfer impacts the surface state of the semiconductor. It results a space charge region SCR that is a seat of a strong electric field.¹⁶ The thickness of this zone ranges between 10 and 1000 nm and the concentration of the electrons and holes notably differs from that of the bulk.²⁰ At the same time, in the electrolyte side, two ionic layers (i.e. the Helmholtz layer and the Gouy-Chapman layer) are formed to ensure the electro-neutrality of the interface.²¹

The Helmholtz layer is the first layer outer surface. It is a dense layer composed of molecular dipoles and solvated ions, oppositely charged compared to the semiconductor surface to compensate the charge gradient in the SCR.^{20,22} The second layer Gouy chapman, corresponding to a more diffuse layer, which can be neglected when the concentration of the electrolyte is higher than 0.1 M.^{20,23}

Figure 11 presents the Helmholtz model in the case of an n-type semiconductor, after the equilibrium in depletion situation, the SCR is positively charged since electrons (the majority charges) are being transferred to the electrolyte and holes (the minority charges) remains at the surface, while the Helmholtz layer is charged negatively.

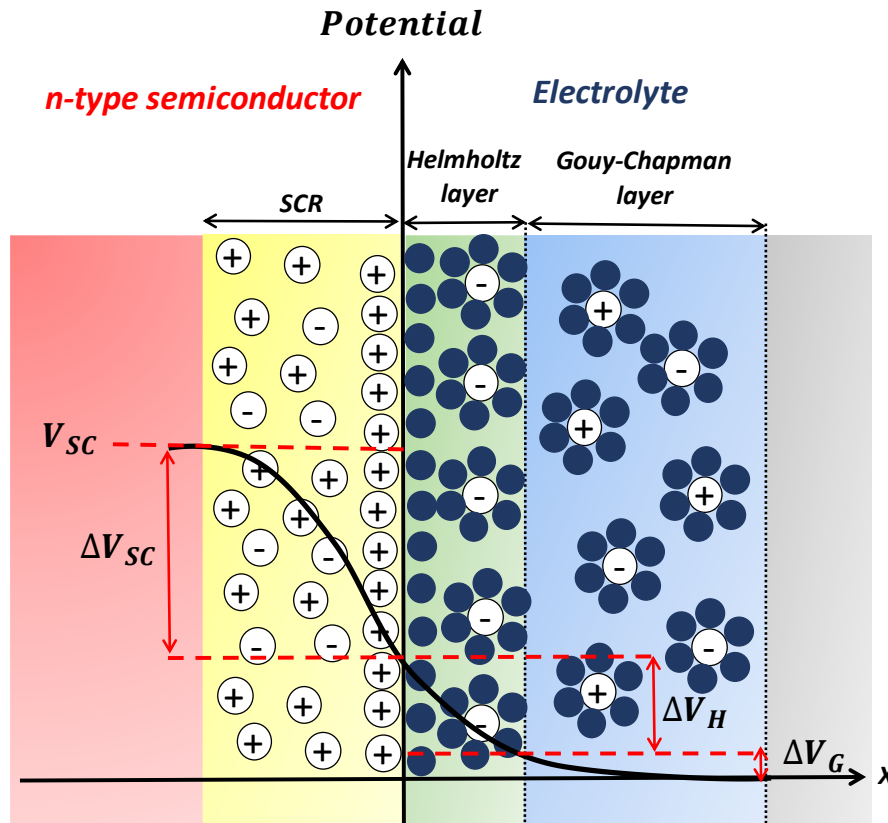


Figure 11: Schematic representation of an n-type semiconductor electrolyte interface with different layers involved: space charge region SCR layer (semiconductor side), Helmholtz layer and Guy Chapman layer (electrolyte side), showing the gradient potential difference between the layers.

The equalization of energy levels gives a rise of a difference of internal potential that generates the electrical field and induces a band bending at the surface of the semiconductor. This band bending depends on the position of the Fermi level.²⁴

Different situations are distinguished for a semiconductor electrolyte contact ²⁴⁻²⁶ illustrated in Figure 12:

- If before contact E_f is equal to E_{redox} , there is no charge accumulation at the interface. The distribution of electrons and holes in the bulk and the surface is similar, resulting no band bending at the semiconductor interface and an absence of a SCR region. We are in flat band situation (Figures 12 a and 12 b).

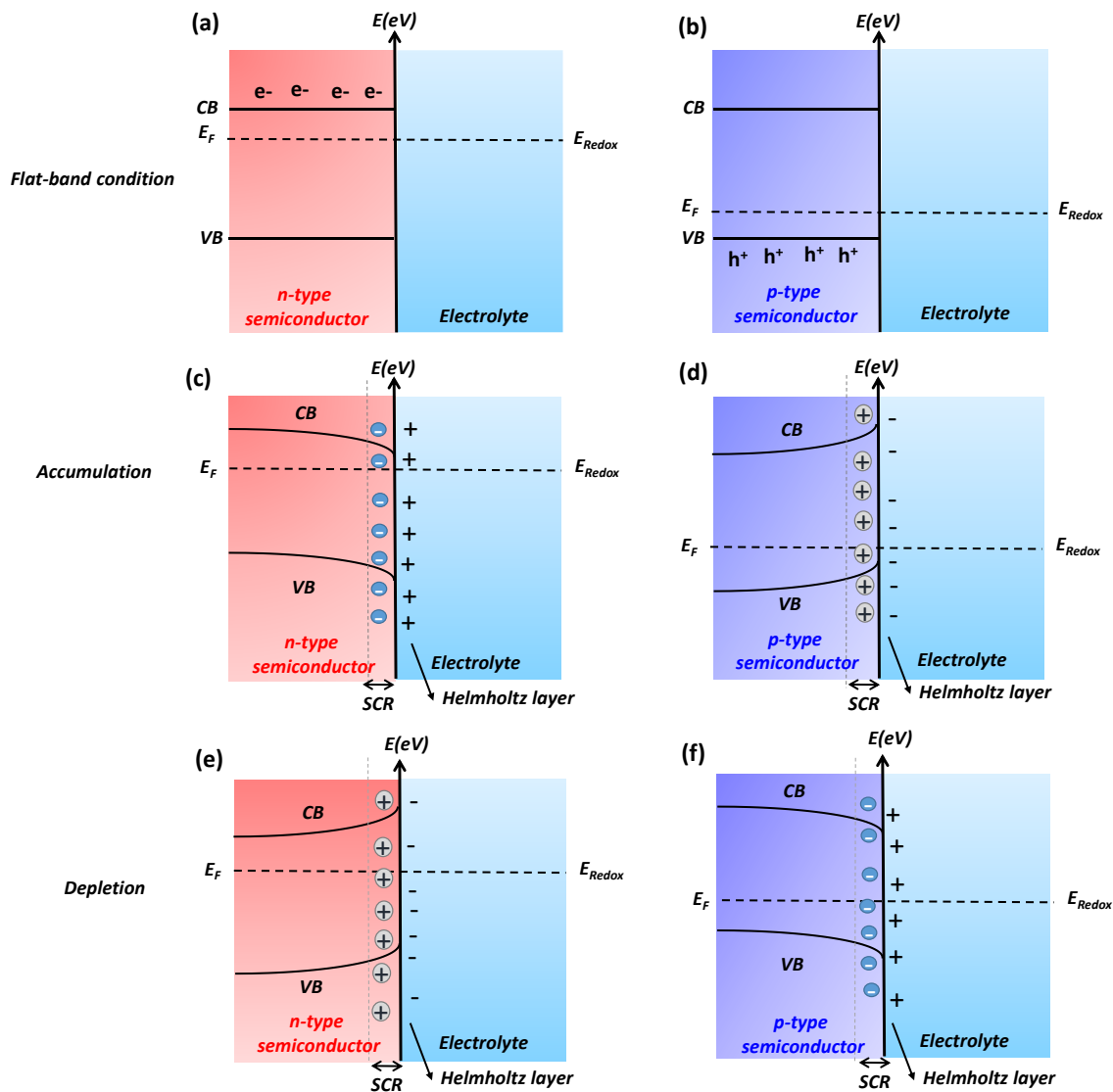


Figure 12: Schematic representation of bands bending for n-type and p-type semiconductors before and during contact with the electrolyte, presenting different situations.

- If before contact $E_f < E_{redox}$ for n-type semiconductor or $E_{redox} < E_f$ for p-type semiconductor: the majority charge carriers will accumulate on the surface. The semiconductor is in accumulation situation (Figures 12 c and 12 d).

For an n-type semiconductor, the electrons will migrate from the bulk to the surface of the semiconductor and accumulate at the interface, resulting an excess of negative charge in the SCR compensated by the positive ions presented in the Helmholtz layer. A bending of the conduction and valence bands of the semiconductor will appear towards low energies. While for a p-type semiconductor, the holes will accumulate on the interface. The excess of the positive charge in SCR will be compensated by the negative ions at the surface in

the electrolyte and the band bending of the semiconductor will appear towards high energies.

- If before contact $E_f > E_{\text{redox}}$ for n-type semiconductor or $E_{\text{redox}} > E_f$ for p-type semiconductor: the majority charge carriers will deplete from the semiconductor to the electrolyte, forming a depletion layer. The semiconductor is in depletion situation (Figures 12 e and 12 f).

For an n-type semiconductor, the electrons will deplete into the electrolyte leaving the positive charges in SCR. This results a downward band bending. While for a p-type semiconductor where the majority charges are holes, the SCR is negatively charged and the bend bending is upward. This is the most common situation.

4. Electrochemical measurements

In this section, we present a basic description of the different electrochemistry methods used to characterize the electronic properties of CIGS and CIGS_n compounds presented in section 5.

4.1. Determination of the semiconductor type

4.1.1. Determination of the semiconductor type using current potential (I-V) curve measurements under dark

Assuming that the electrolyte used is stable in the potential range and the semiconductor material is non-reactive towards the electrolyte, and given the accumulation of charges on both sides of the interface, no electrochemical reaction can take place. When the electrochemical cell system is at its equilibrium without applying any potential or illumination, nothing happens at the macroscopic level, no current is detectable and it is at its zero-bias state.²⁷ The imposition of an external parameter will lead to a deviation of the position of the Fermi level, resulting in a variation of the internal potential and of the carrier charge density inside each medium. This is responsible of the existence of the capacitive current.²⁸ This capacitive current will be exploited later in the impedance spectroscopy measurements.

For photo-electrochemical tests, we analyse the faradic current at the two energy levels: the bottom of the conduction band by the electrons transfer and the top of the valence band by the holes transfer.²⁹ The current is positive for an oxidation current and negative for reduction current. This operation can be controlled by the application of an external potential.^{19,30} The voltage imposed affects the interface of the SC-electrolyte and therefore modifies the band bending. It results electrochemical processes such as redox reactions (Figure 13).

Figure 13 presents the different configurations of n-type and p-type semiconductors under a potential bias.^{10,31}

- If the applied potential is equivalent to the flat band one, the Fermi level remains at the same level and no current is detected because of the absence of the electrical field generated from charge carrier separation (Figures 13 a and 13 b).
- If the applied potentials are more negative than the flat band one, the Fermi level on both cases (n-type and p-type) will shift upwards (Figures 13 c and 13 f). That results to an accumulation situation for an n-type SC and depletion situation for a p-type SC. As explained previously, in an accumulation state, the majority charge carriers will accumulate on the interface and will contribute to the faradic current (reduction current for an n-type semiconductor and oxidation current for a p-type semiconductor).
- Conversely, in a situation of depletion, the majority charge carriers will depopulate the surface by migration into the bulk of the semiconductor leaving an excess of the minority charges on the surface (Figures 13 e and 13 d). The densities of carriers on the surface are very low, which translates by a limitation (saturation) of the current of the minority charge carriers (reduction current for a p-type semiconductor and oxidation current for n-type semiconductor) (Figure 14).
- There is another situation called the inversion situation or deep depletion.^{20,32} When the majority charge carriers go so far and become globally minority on the surface (they fall below the intrinsic level). The minority charges of the solid themselves will promote redox reactions and raises partially the limitation of their current. This condition appears at very negative applied potentials for the p-type semiconductor while at very high potentials for n-type semiconductor (Figures 13 g and 13 h).

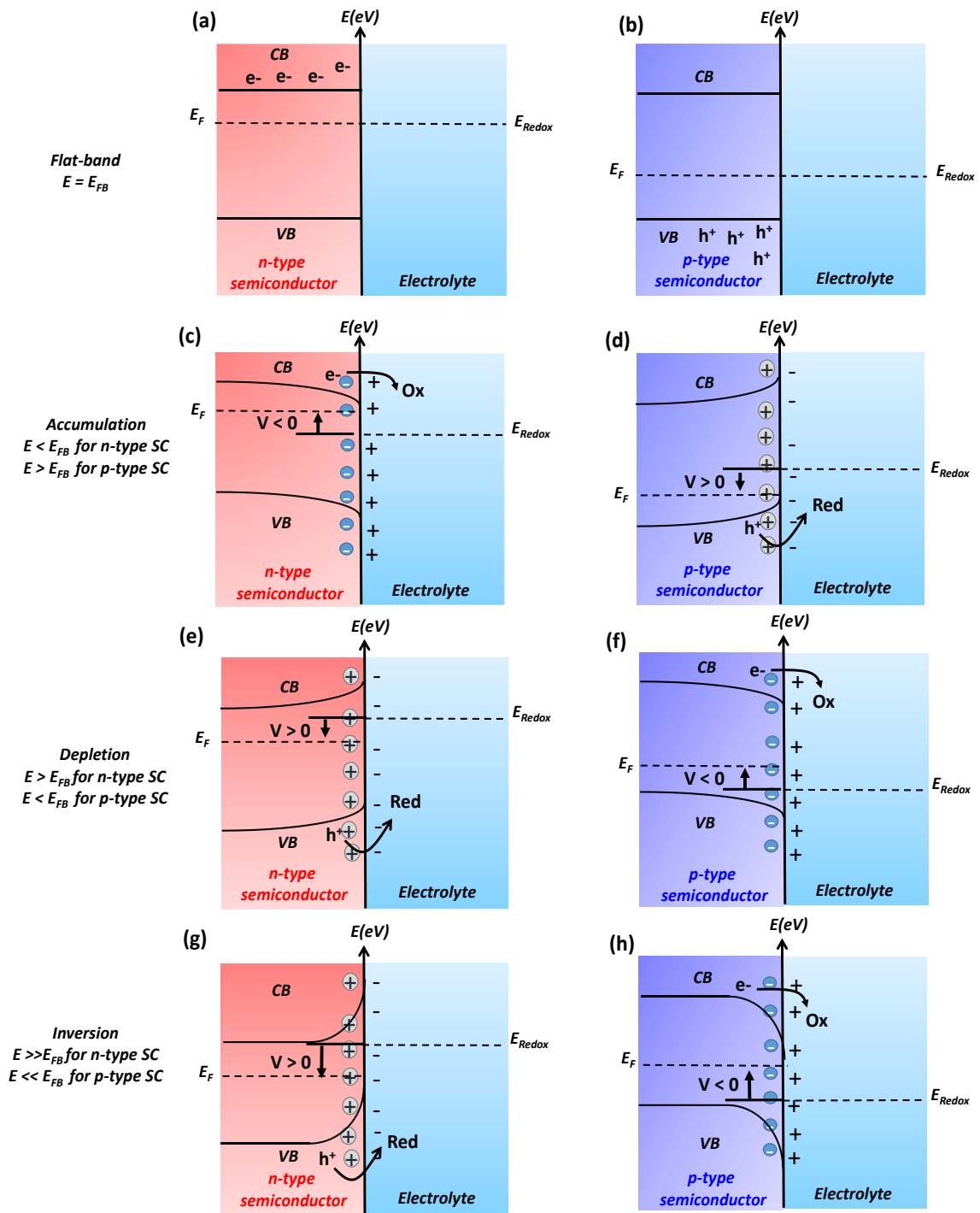


Figure 13: Schematic representation of bands bending for n-type and p-type semiconductors on contact with the electrolyte during applying a potential bias, presenting all possible situations.

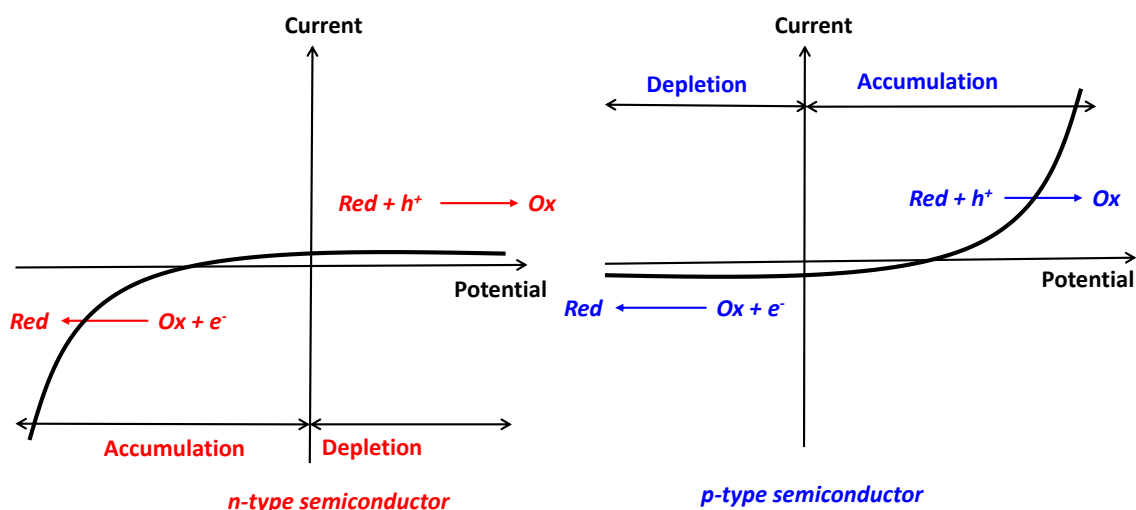


Figure 14: Current potential characteristics depending on the applied potential, presenting a saturated reduction current for p-type semiconductor and a saturated oxidation current for n-type semiconductor.

Figure 14 presents the detectable current induced by the variation of the surface charges for p-type and n-type semiconductors. The current-voltage behaviours seem to be different, which would allow the characterization of the type of the majority carriers in a semiconductor.³¹

However, the Figure 14 shows two ideal cases, where the resistance of the material is negligible and no parasitic reaction occurs such as the reduction of dissolved oxygen at low potential. For this purpose, current potential curves measured under chopped illumination were performed during this thesis, to definitely identify the type of the majority carriers.

4.1.2. Determination of the semiconductor type using current potential measurements under chopped illumination

Current potential IV curves measured under chopped illumination (also called linear sweep photovoltammetry) is a photoelectrochemical technique based on the illumination of the interface of the semiconductor/electrolyte. As shown in the Figure 15, when a semiconductor is excited by an incident photon with higher energy than the band gap energy of the material ($h\nu > E_g$), an electron-hole pair is created by the movement of an electron from the valence band to the conduction band. It results a modification of the charge distribution at the surface of the semiconductor. The majority carriers are dragged towards the bulk of the semiconductor while the minority carriers are led towards the surface under the effect of the band bending. This causes the Fermi level splitting and consequently reduces the band curvature and decrease the width of the SCR. The Fermi level is then split into two pseudo Fermi levels, $E_{f,n}$ for electrons and $E_{f,p}$ for holes, and the difference between the Fermi level position in dark and under illumination is defined as photopotential.^{30,33}

For an n-type semiconductor, electrons are the majority charge carriers. Therefore the $E_{f,n}$ (electrons pseudo Fermi level) is not significantly affected by the illumination. In contrast, $E_{f,p}$ (holes pseudo Fermi level) appears at lower energy value, since the electron hole pair creation modifies the charge distribution at the surface (Figure 15 a). Otherwise, for a p-type semiconductor where holes are the majority charge carriers, $E_{f,n}$ (electrons) is shifted at higher energy (Figure 15 b).

The photogenerated minority carriers at the surface induce photoelectrochemical reactions, resulting in a photo-oxidation current increase for an n-type SC and a photo-reduction current increase for a p-type SC (Figure 16). By alternating the light and dark ranges of the semiconductor, it is thus possible to determine without ambiguity the nature of the charge carriers of the material.

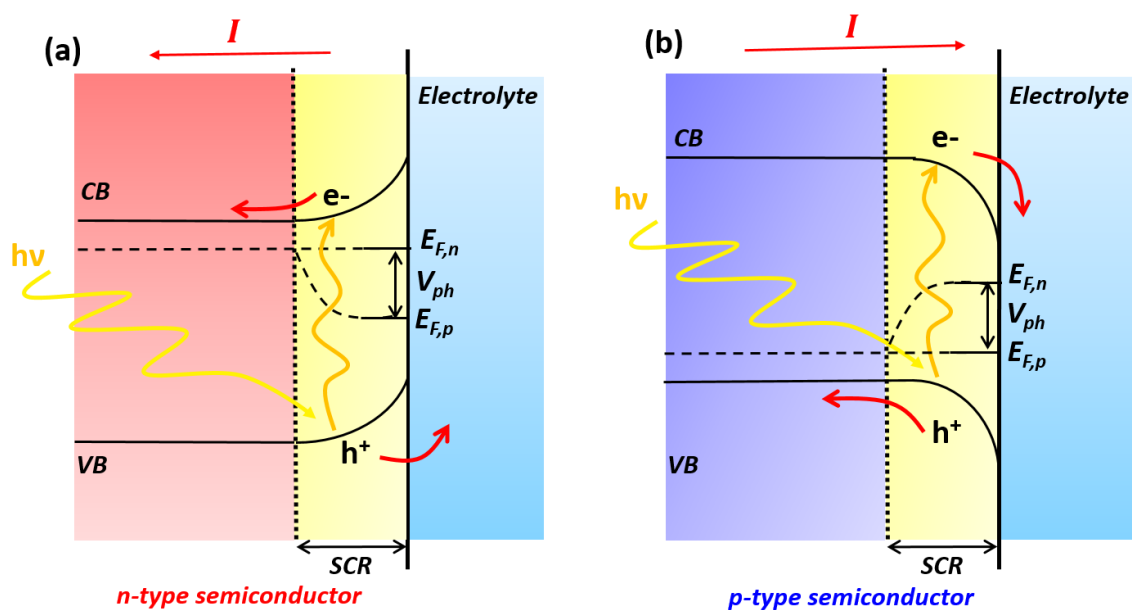


Figure 15: Schematic representation of bands diagrams of n-type and p-type semiconductors under illumination in depletion situation, illustrating the Fermi level split to create a photo voltage.

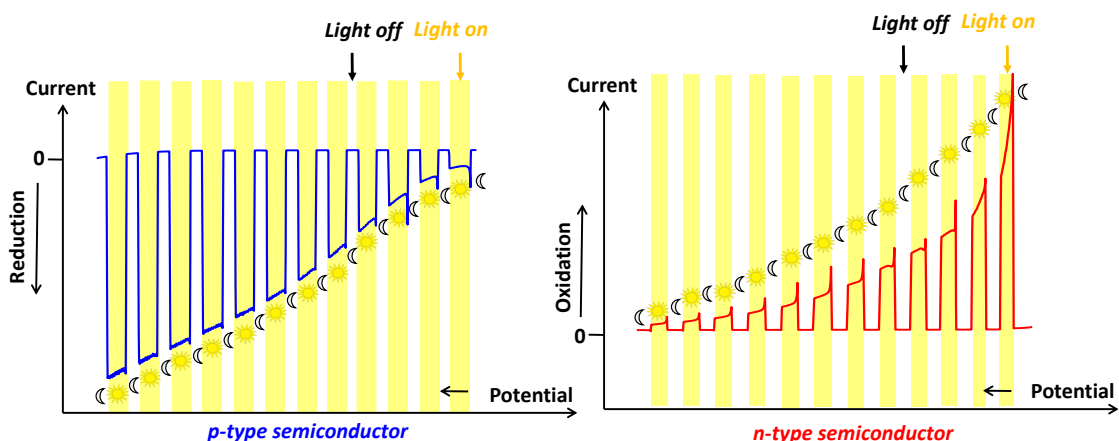


Figure 16: Current potential curves under chopped illumination, for p-type (photo-reduction) and n-type (photo-oxidation) semiconductors.

4.2. Determination of majority charge carriers lifetime using chronopotentiometry

Chronopotentiometry and chronoamperometry are two fast transient electrochemical techniques where either a fixed current or potential is applied and the resulting potential or current evolution versus time is measured, allowing a fast detection of the smallest variations.³⁴ In this work, chronopotentiometry was performed to determine the recombination of the photogenerated charge carriers taking place at the SC/electrolyte interface.

During the chronopotentiometry measurements, the open circuit potential (the potential established between the semiconductor and the electrolyte, with respect to the reference electrode)³⁵ is traced versus time under dark and illumination. As presented in Figure 17, one can easily notice the difference between the photo-response obtained for an n-type or a p-type semiconductor.

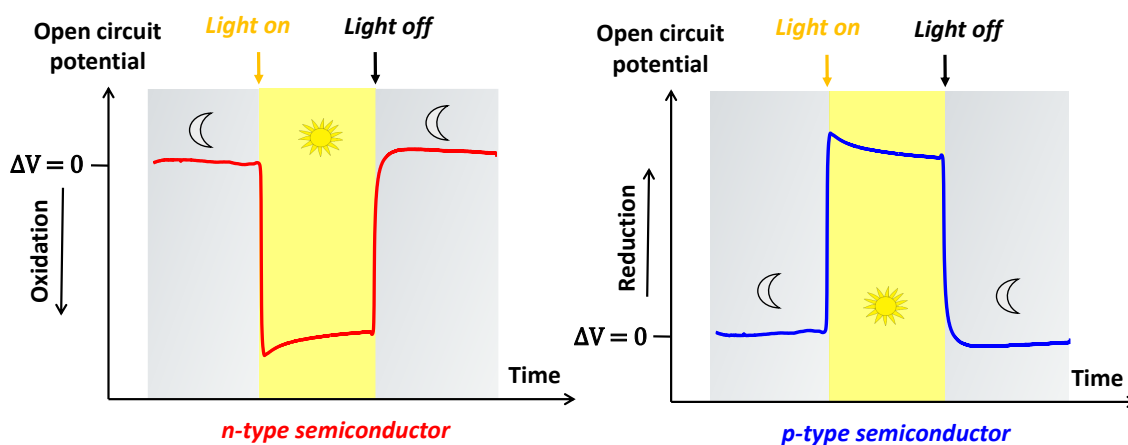


Figure 17: Chronopotentiometry curves under illumination for n-type and p-type semiconductors.

Using this technique, we can explore the charge recombination process. The electron lifetime can be calculated following the equation 7³⁶

$$\tau = \frac{k_B T}{e} \left(\frac{dV_{oc}}{dt} \right)^{-1} \quad (7)$$

where τ is the photoelectron or photohole lifetime according to the type of the semiconductivity, e the elementary charge, K_b the constant of Boltzmann, T is the temperature and V_{oc} the open circuit voltage.

As well, the obtained curve after stopping illumination can be fitted by a binomial exponential function³⁷⁻³⁹ (equation 8)

$$V = V_0 + A_1 \cdot \exp(-t/\tau_1) + A_2 \cdot \exp(-t/\tau_2) \quad (8)$$

where the first exponential is associated to the majority charge carriers (electrons for n-type and holes for p-type) movement across the electrode assembly to reach its steady state and it is defined by the lifetime constant τ_1 . While the second exponential expressed by the second lifetime constant τ_2 is related to the surface recombination process. A_1 describes the maximum value of the collectable voltage, when there is no recombination process, while A_2 is the collectable voltage, when there is the maximum recombination process.^{37,40}

4.3. Determination of flat band potential (Fermi level) and charge carriers density by electrochemical impedance spectroscopy

As previously explained, the interface of the semiconductor electrolyte is composed of three layers: Space charge region SCR, Helmholtz and Gouy chapman layers (Figure 11). The last layer (Gouy chapman) is neglected for electrolyte concentrations higher than 0.1M, which is the case during this thesis.

The SCR and Helmholtz layers corresponds to gradients of opposite charges ΔQ_{SC} and ΔQ_H (that conserve the electronegativity of the interface) assimilated to different capacities C_{SC} and C_H and potentials gradients ΔV_{SC} and ΔV_H (equations 9 and 10). Since a large part of the potential difference is distributed in the SCR of the semiconductor, the capacitance in the SCR is much smaller than the one in the Helmholtz layer (equation 11).^{20,41,42}

$$\Delta Q_{SC} = C_{SC} \cdot \Delta V_{SC} \text{ and } \Delta Q_H = C_H \cdot \Delta V_H \quad (9)$$

$$\text{With } \Delta Q_{SC} = -\Delta Q_H \quad (10)$$

$$\frac{C_{SC}}{C_H} = -\frac{\Delta V_H}{\Delta V_{SC}} \text{ and } \Delta V_{SC} \gg \Delta V_H \rightarrow C_{SC} \ll C_H \quad (11)$$

As a result, the total capacitance of the circuit is approximated as followed (equation 12).^{43,44}

$$\frac{1}{C} = \frac{1}{C_{SC}} + \frac{1}{C_H} \approx \frac{1}{C_{SC}} \quad (12)$$

According to the Mott-Schottky equation, the capacitance of the semiconductor depends on the potential difference in the SCR (equation 13).^{45,46}

$$\frac{1}{C_{SC}^2} = \frac{2}{\varepsilon\varepsilon_0 A^2 eN} \left[(V - V_{fb}) - \frac{k_B T}{e} \right] \quad (13)$$

with $\frac{k_B T}{e} \approx 25 \text{ mV}$ term, generally neglected, thus the capacitance (equations 14 and 15) are expressed as:

- For p-type semiconductor

$$\frac{1}{C^2} = \frac{2}{\varepsilon\varepsilon_0 A^2 eN_A} [V - V_{fb}] \quad (14)$$

- For n-type semiconductor

$$\frac{1}{C^2} = \frac{2}{\varepsilon\varepsilon_0 A^2 eN_D} [V - V_{fb}] \quad (15)$$

where ε_0 corresponds to the vacuum permittivity, ε is the relative permittivity of the semiconductor, A is the interfacial surface region between the semiconductor and the electrolyte, N is the majority charge carrier density (N_A is the acceptor concentration and N_D is the donor concentration), k is the Boltzmann constant, T is the temperature, and e is the electron charge.

Therefore, following the formulas, the capacitance will be modelled to plot C^{-2} as a function of the imposed potential (Mott-Schottky plot).^{45,47} Regarding the form of the plots, we can conclude the semiconductor type. As $V > V_{fb}$, a positive slope is observed for an n-type semiconductor and conversely, a negative slope ($V < V_{fb}$) is obtained for a p-type semiconductor (Figure 18). As well, the flat band potential V_{fb} is determined by extrapolation to the zero ordinate ($C^{-2} = 0$).

In addition, the charge carrier density can be estimated from the Mott-Schottky plot.⁴⁸ The value of the carrier density N can be calculated by the formula (equation 16), which is inversely proportional to the slope⁴⁹

$$N = \left(\frac{2}{\varepsilon\varepsilon_0 A e} \right) \left[\frac{d\left(\frac{1}{C^2}\right)}{dV} \right]^{-1} \quad (16)$$

where ϵ is the dielectric constant of the material, ϵ_0 is the vacuum permittivity which is equivalent to $8.854 \times 10^{-12} \text{ F m}^{-1}$, e is the electronic charge unit ($1.602 \times 10^{-19} \text{ C}$), A the surface of contact electrolyte/SC, V is the potential applied at the electrode and C is the capacitance.

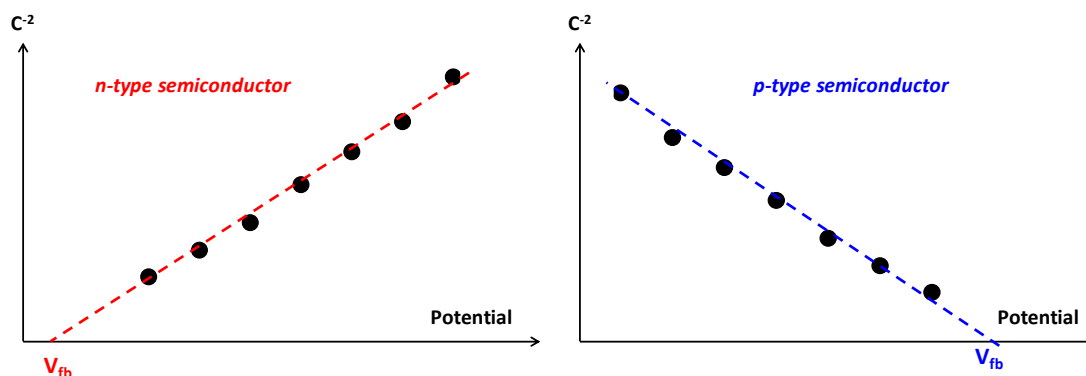


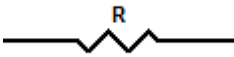
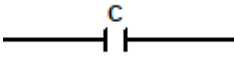
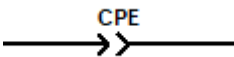
Figure 18: Mott-Schottky plots depending on the applied potential for n-type (negative slope) and p-type (positive slope) semiconductors.

The capacitance is determined by electrochemical impedance. This is a transient technique that allows us to measure the relationship between the current and the potential in a frequency amplitude.^{50,51} It consists in applying a AC voltage by imposition of a fix potential while varying potentials of low amplitude (0.1 mV) around it at variable frequency. The alternating current generated is recorded and the impedance is determined for each potential.

A Nyquist diagram corresponds to the representation of the real part Z_r (resistive part, noted Z') of the impedance, versus its imaginary part Z_i (capacitive part, noted Z''). It is obtained by frequency sweep from the high frequencies leading to low values of Z_r to the low frequencies (high Z_r values).^{39,52}

By fitting Nyquist diagram for each applied potential with an equivalent electric circuit, we can determine the electrical characteristics of each part of the electrochemical circuit and more especially the capacitance of the semiconductor.^{50,53,54} Table 3 presents the fundamental elements of an electrical circuit alongside the equivalent circuit dipole, the resulting impedance and their roles.^{28,46}

Table 3: The electrochemical circuit fundamental elements with their equivalent circuit dipole, their impedance formulas and their roles.

Circuit fundamental elements	Equivalent circuit dipole	Impedance Z	Role
Resistor (R)		$Z_R = R$	Describes the faradic charge transfer reactions through the interface layers
Capacitor (C)		$Z_C = \frac{1}{(j\omega C)}$	Describes the capacitive charge at the interface semiconductor/electrolyte
Constant phase element (CPE)		$Z_{CPE} = \frac{1}{Q(j\omega)^\alpha}$	Describes the non-ideal capacitance at the interface, α coefficient of the ideality factor of CPE by pure capacitance C, $0 < \alpha < 1$
Warburg diffusion (W)		$Z_W = \frac{\sigma \sqrt{2}}{\sqrt{j\omega}}$	Describes the diffusion phenomena of charges on the electrode, σ coefficient of Warburg that depends on the diffusion as a function of charge carriers concentration

Generally, the electrochemical circuit is modelled using the Randles circuit.^{55,56} Figure 19 presents the equivalent Randles circuit, with a serial resistance R_s followed by the capacitance C that is placed in parallel with a charge transfer resistance R_{tc} and a Warburg W. At high frequencies (1 kHz – 100 kHz), the diffusion phenomena are neglected, therefore the semiconductor/electrolyte interface capacitance can be determined using a simplified circuit.³⁹

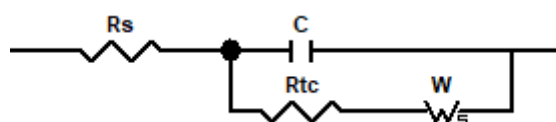


Figure 19: The Randles equivalent circuit of electrochemical cell.

The Randles circuit can be approximated into two simplified circuits, a simple RC circuit or a Randles circuit neglecting the Warburg component (Figure 20). The presented models can be used when the interface studied is ideal.³⁹

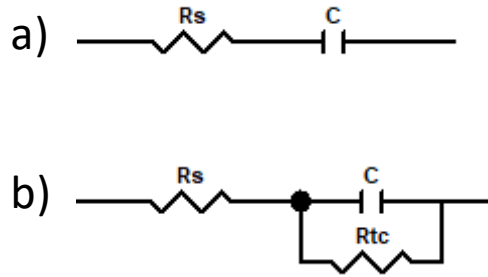


Figure 20: The Randles simplified circuits: a) RC circuit and b) the Randles circuit with a neglected Warburg.

Alternatively, considering the non-ideality of the surface (roughness, porosity, phase inhomogeneity at interface) a more complicated circuit is used (Figure 21) that involves a constant phase element CPE (Figure 22).

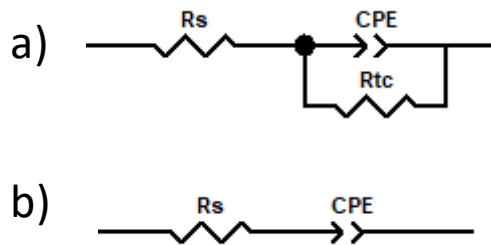


Figure 21: The equivalent circuit of a non-ideal electrochemical cell used at high temperatures (1 kHz – 100 kHz) a) RC circuit and b) the Randles circuit with a neglected Warburg.

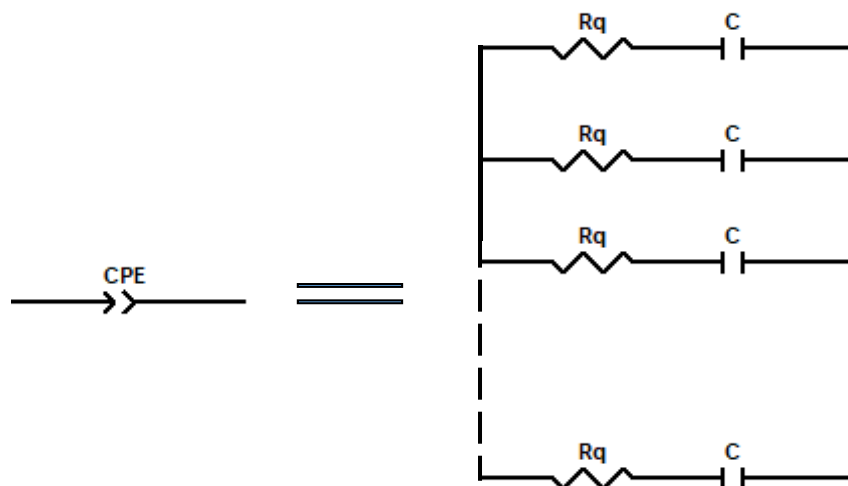


Figure 22: The equivalent circuit used to model CPE with Rq corresponding to the resistance, which reflects the deviation from an ideal capacitive circuit.

To calculate the capacitance at the interface, the Brug⁵⁷ formulas are used: equation (17) in case of RC circuit and equation (18) for a simplified Randles circuit by neglecting the Warburg.

$$C = (R_s^{(1-\alpha)} Q)^{\frac{1}{\alpha}} \quad (17)$$

$$C = \left(\frac{1}{R_s} + \frac{1}{R_{tc}} \right)^{\frac{\alpha-1}{\alpha}} Q^{\frac{1}{\alpha}} \quad (18)$$

where Q is the CPE constant and α is the coefficient of the ideality factor of CPE.

5. Characterisation of the electronic properties of CIGS_n compounds: experimental results

The semiconducting behaviour of chalcogenides was firstly investigated by current potential measurements under chopped illumination. The measurements were performed under both illumination and dark under at the same conditions. The setup realized is an electrochemical setup with three electrodes, reported previously in Figure 9, namely an Ag/AgCl reference electrode, a counter electrode of Pt and a dense pellet of CIGS_n and CIGS as working electrode, all immersed in KCl 0.5 M aqueous as electrolyte. A potential sweep (-0.3 – 0.3 V) was performed and the resulting current was measured (Figure 9). These current-potential measurements were carried out under chopped illumination using an MI-LED illuminator (Edmund Optics). To alternate the ranges of illumination and dark, a chopper was placed between the cell (work electrode) and the lamp. As explained previously, in this experiment when the cell is illuminated, in depletion situation, the photocurrent is due to the minority charge carriers. This leads to an increase of oxidation current for an n-type semiconductor and reduction current for a p-type.

In order to avoid the detrimental redox processes of the material, the evolution of the potential of the CIGS and CIGS_n-based electrodes at equilibrium, namely the open circuit potential (OCP), under chopped-light conditions (Figure 23), was investigated before carrying out a potential sweep (Figure 24 and 25). The OCP increase under the light indicates that the CIGS chalcopyrite electrical current is, as expected, dominated by hole transport whereas the decrease of the OCP for the lamellar CIGS_n phases suggests a current dominated by electron transport. The cathodic photocurrent of CIGS is recorded whatever the potential applied is in line with the literature.^{58,59}

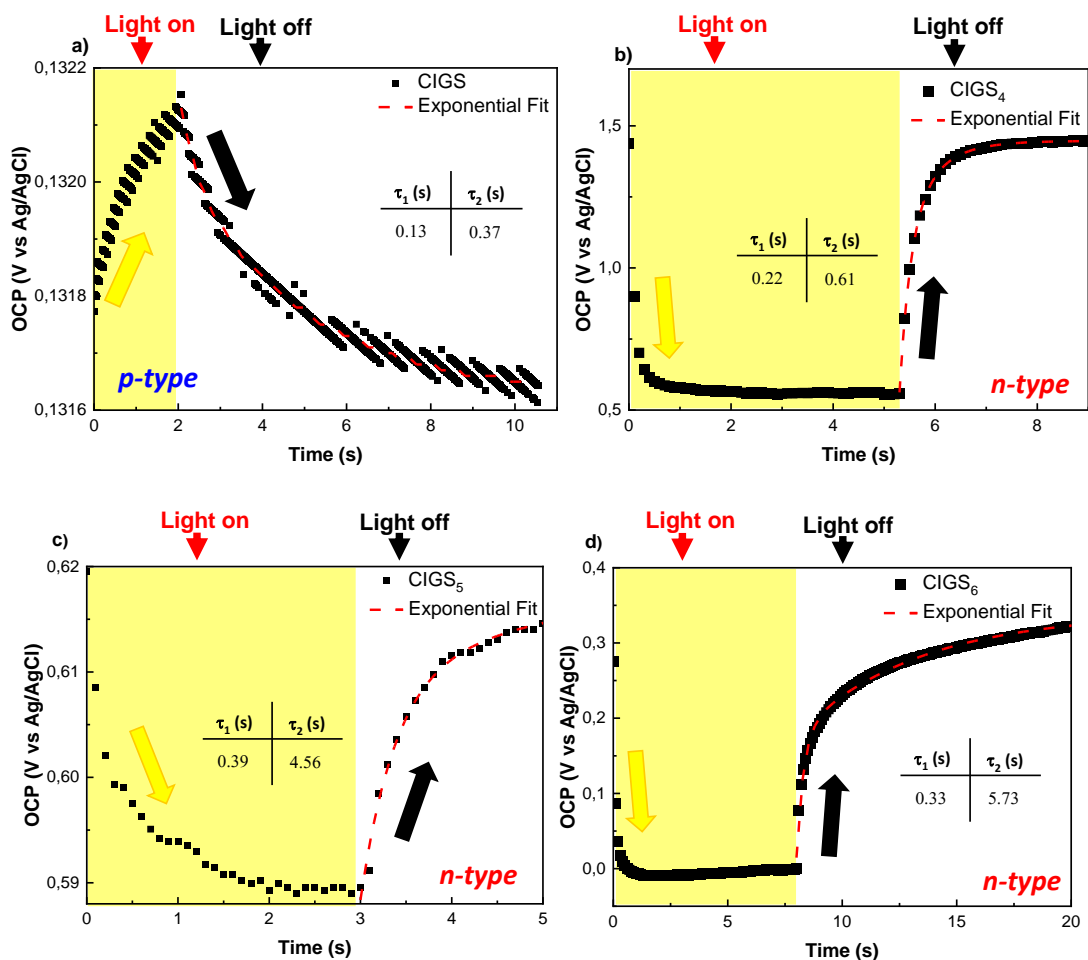


Figure 23: Open circuit potential (OCP) curves under illumination (yellow region) and under dark of a) CIGS, b) CIGS₄, c) CIGS₅ and d) CIGS₆. The photogenerated charge carrier lifetimes in the inserted tables were determined by fitting the OCP decay curves after stopping the illumination by two decreasing exponential functions.

Moreover, by fitting the curves under dark (OCP decays) using exponentials, we can estimate the values of the charge carriers lifetimes τ_1 and τ_2 of all the samples, as it is shown in Figure 23.

τ_1 presents the transport of the majority carriers through the electrode, which are electrons in the case of the CIGS_n lamellar compounds and holes for CIGS chalcopyrite. τ_2 is the time constant to reach the steady state and is linked to the recombination processes. Comparing the values, τ_1 related mainly to the series resistance^{60,61} is comparable for all samples. However, τ_2 related to lifetime of the separate charge state, is longer for the lamellar compounds than for chalcopyrite. Thus, τ_2 of CIGS₅ (4.6 s) and CIGS₆ (5.7 s) reach one order of magnitude higher than that of CIGS (0.37 s). This could result to improve the collection of photogenerated charge and lead to better photoconversion efficiencies.

The current-potential measurements gathered on the Figures 24 and 25, confirm the difference of electronic behaviour between the lamellar CIGS_n compounds and the chalcopyrite CIGS . In depletion conditions, the photocurrent is generated by the minority charge carrier current. Therefore, the increase of the oxidation current under illumination characterizes an n-type semiconductor and vice versa, the increase of the reduction current translates the p-type behaviour. Whatever the applied potential, a reduction current is recorded on the p-type chalcopyrite CIGS phase, whereas an oxidation current is observed for the CIGS_4 and CIGS_5 phases that confirms their n-type behaviour (Figure 23).

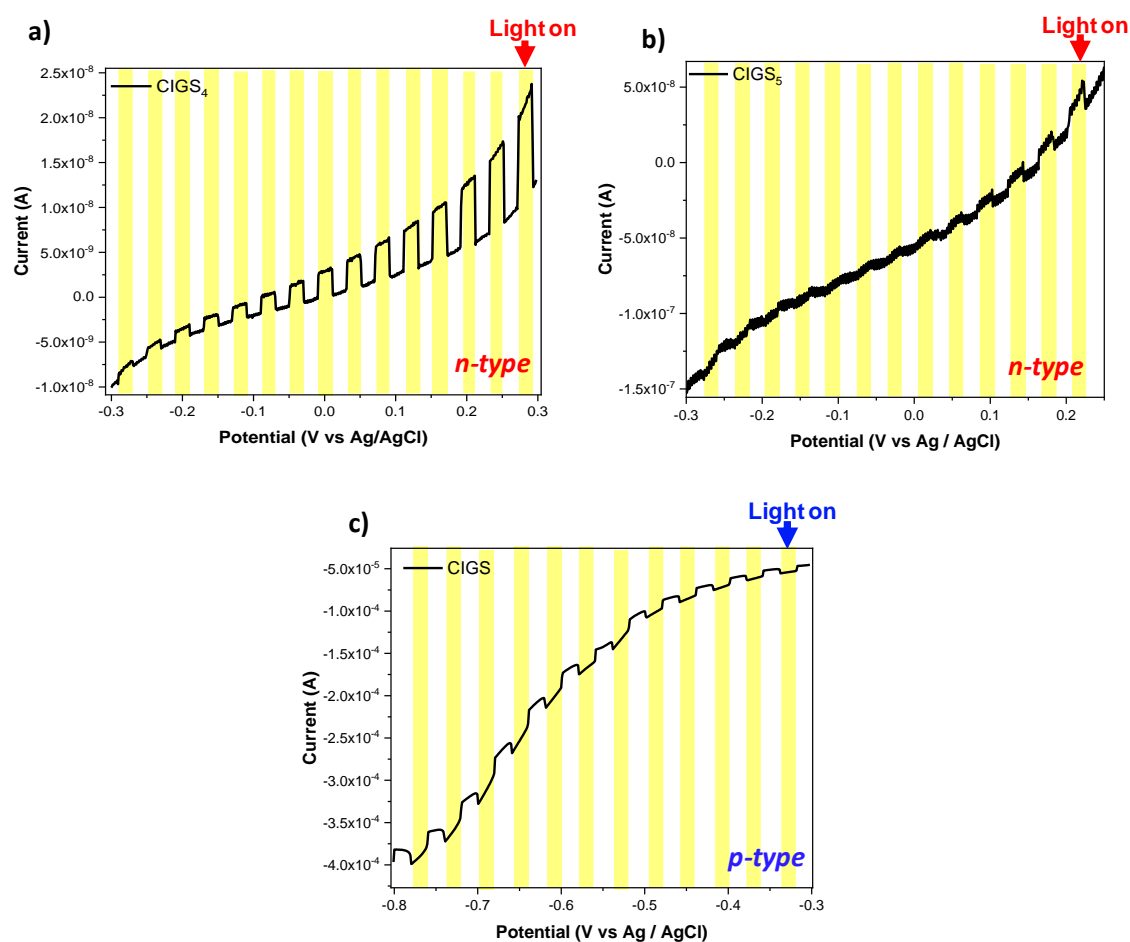


Figure 24: Current-potential curves measured under chopped simulated sunlight with the yellow part corresponding to the illumination time for: a) CIGS_4 , b) CIGS_5 and c) CIGS .

The electrochemical behaviour of the CIGS_6 phase appears slightly different from the other lamellar phases (Figure 25). According to the applied potential, both photocurrents are generated. A photo-oxidation current is detected when the electrochemical cell is illuminated for potentials higher than a reversal potential of -0.06 V vs Ag/AgCl and a photo-reduction current is measured at lower potentials. On either side of this frontier potential, the photocurrent values are in the same order of magnitude that suggests a similar charge transport. This type of behaviour is generally observed on ambipolar

materials, for which the current is not clearly dominated by a type of charge carrier. Indeed, unlike unipolar materials, they can intrinsically transport and transfer simultaneously both charge carriers, holes and electrons in a comparable way,³⁹ without a strong predominance of the current of a type of charge carrier. The ambipolar character of CIGS₆ with a slight predominance of electron transport was thus evidenced by photoelectrochemistry.

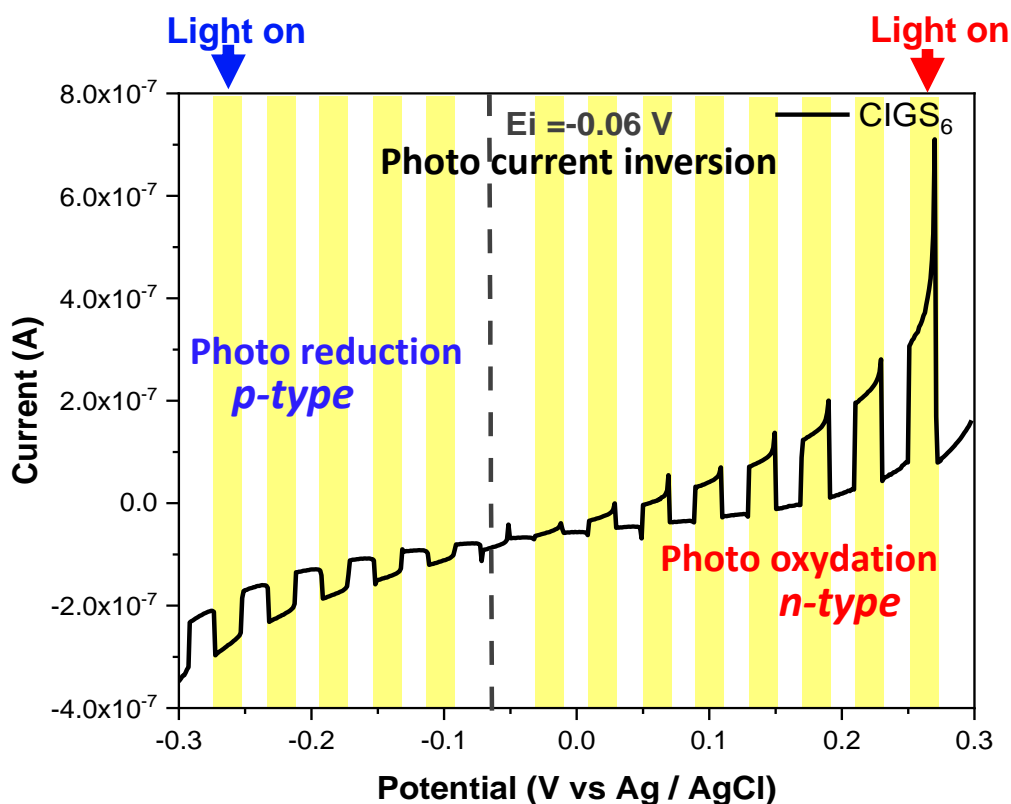


Figure 25: Current-potential curve measured under chopped illumination (yellow part) of CIGS₆.

To go further, electrochemical impedance spectroscopy was carried out, in order to confirm the various electronic behaviours of CIGS_n compounds, as well as to determine flat band potentials to finally built energy diagrams.

Before performing the electrochemical impedance spectroscopy, cyclic voltammetry was conducted at a scan rate of 5mV/s, in order to identify the stable potential range where there are no redox reactions taking place. The principle consists to vary the potential difference between the working electrode and the reference electrode and measure the induced current variations. The cyclic voltammetry of the compounds do not show any redox reaction on the potential ranges chosen between -0.8 to 0.4 V versus Ag/AgCl, as shown in Figure 26.

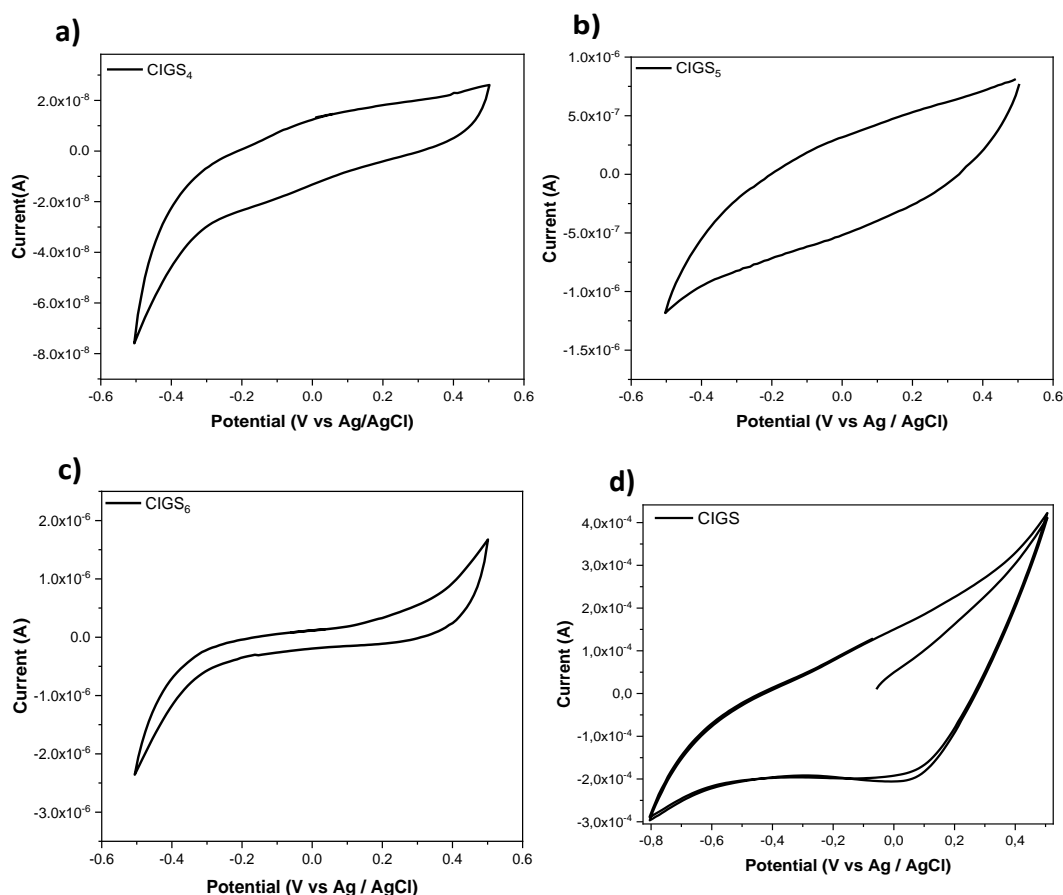


Figure 26: Cyclic voltammetry curves at a scan rate 5 mV/s for a) CIGS₄, b) CIGS₅, c) CIGS₆ and d) CIGS.

The impedance spectra were measured out under dark with the same electrochemical setup used in steady state electrochemical measurements (Figure 9), in a frequency range from 100 Hz to 100 kHz.

Figure 27 presents the Nyquist diagrams obtained at -0.3 V for each compound. They were plotted from the electrochemical impedance spectroscopy (EIS) measurements under dark. The equivalent circuit used to fit them consisted to a simplified (Randles circuit with neglecting Warburg) as shown in the insets of Figure 27.

By comparing these Nyquist diagrams, a difference of resistivity between CIGS and CIGS_n compounds is observed. It is lower for CIGS than for the lamellar compounds. The series resistance (R_s) determined (i.e. when the imaginary part of the impedance tends towards zero) for the chalcopyrite CIGS-based electrode ($R_s = 22 \Omega$) is indeed lower than those obtained from the CIGS_n phases ($R_s = 641, 163$ and 867Ω for $n = 4, 5$ and 6 , respectively). This series resistance corresponds to the addition of the different resistive parts of the electrochemical circuit (i.e. electrolyte, back contact, counter-electrode and working electrode). Due to its high concentration, the resistive contribution of the electrolyte is neglected and the global R_s is highly dominated by the contribution of the CIGS or CIGS_n-based electrode.

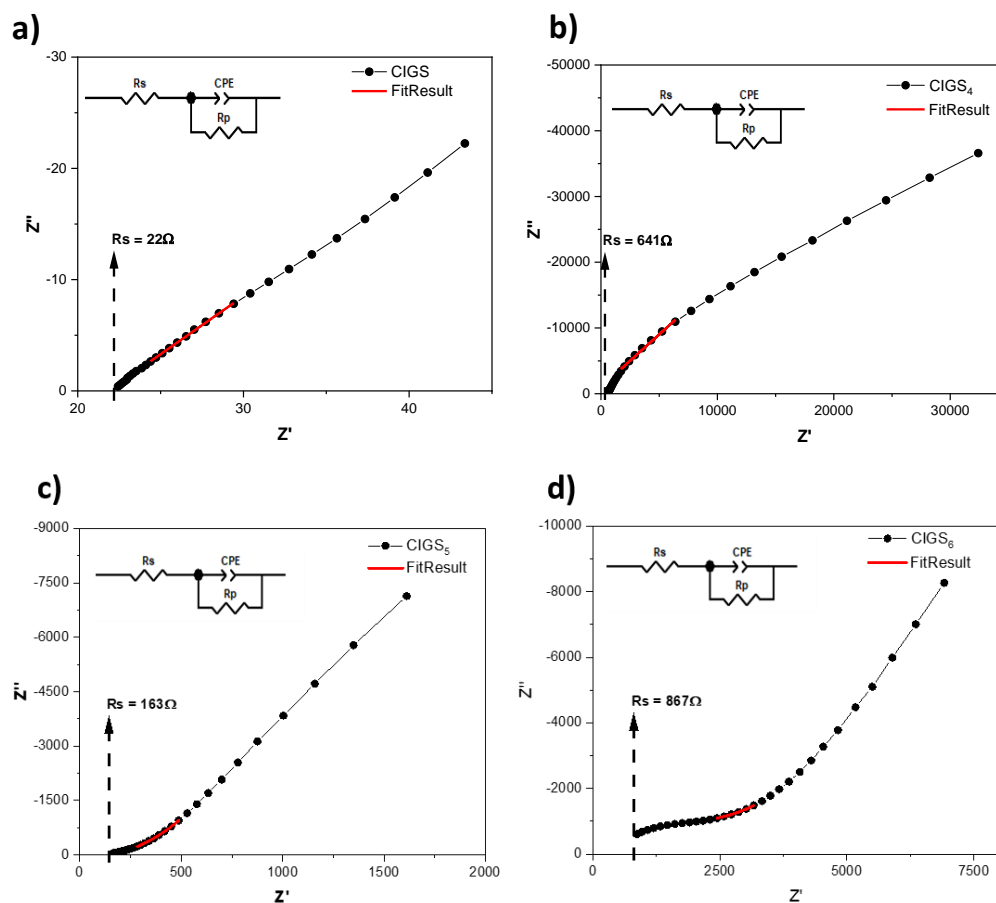


Figure 27: Nyquist plots of the electrochemical impedance circuit in the dark with the applied equivalent circuit for fitting at high frequencies (1– 10 kHz) of: a) CIGS, b) CIGS₄, c) CIGS₅ and d) CIGS₆.

The interface capacitances were then modelled at relatively high frequencies (1– 10 kHz); to neglect the diffusion phenomena and the Mott–Schottky graphs were plotted (Figures 28 and 29) in a potential range of –0.8 to 0.2 V versus Ag/AgCl. Two different trends (C^{-2} evolution) are observed according to the type of semiconductivity of each compound. The negative slope observed on the chalcopyrite CIGS-based electrode (Figure 28 a) characterizes its p-type behaviour whereas the positive slopes of the CIGS₄ and CIGS₅ ones (Figures 28 b and 28 c, respectively) corroborate their n-type behaviour. This inversion of majority charge carriers corresponds to a decrease of the flat band potentials from 0.08 V to –0.54 V and –0.67 V vs Ag/AgCl for CIGS, CIGS₄ and CIGS₅, respectively.

Beyond the characterization of the unipolar compounds, EIS measurements confirm the different electronic behaviour of the CIGS₆ compound compared to that of the other lamellar compounds.

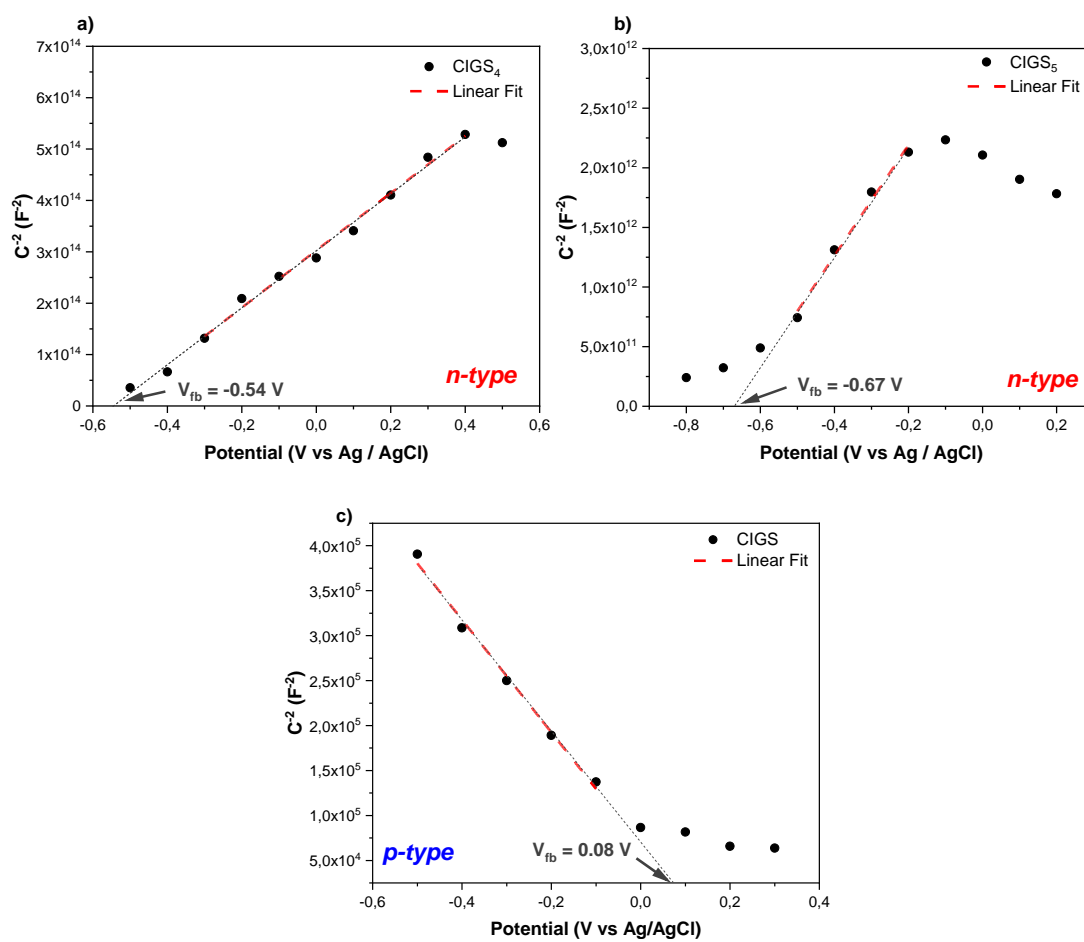


Figure 28: Mott-Schottky $C^2 - E$ (V vs Ag/AgCl) plots modelled at high frequencies (1– 10 kHz), with linear fit of the slopes to determine the flat band potentials for: a) CIGS₄, b) CIGS₅ and c) CIGS.

According to the sweep potential direction, a positive and a negative slope was observed (Figure 29). A negative slope can be plotted when the potential decreases and reversely, a positive slope can be drawn by increasing the applied potential. This suggests a versatility of electronic behaviour that we attribute to the ambipolarity of CIGS₆. Indeed, the application of a potential modifies the concentration of the charge carriers at the interface SC/electrolyte and thus the capacitance of the space charge region in the semiconductor. This variation is all the more visible near to the flat band potential and is even more impactful when the concentrations of holes and electrons are equivalent. However, the flat band potential value is similar whatever the potential sweep direction (-0.65 V vs Ag/AgCl) and is comparable to those obtained for the other lamellar phases that is consistent with a slight predominance of electron transport, as highlighted during the photoelectrochemical measurements.

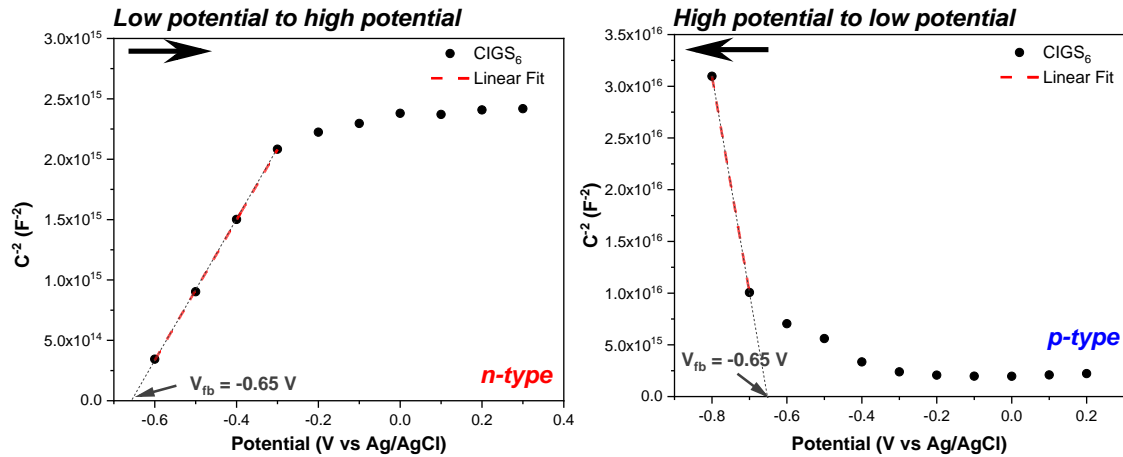


Figure 29: Mott-Schottky plots of CIGS₆ with the flat band potentials, when performing the experiment from low potential to high potential and high potential to low potential.

The charge carrier densities for each compounds were also determined from the values of the slopes of the Mott-Schottky plot. They are gathered in Table 4.

Firstly, the lower values of charge carriers calculated for the lamellar compounds (N_D equals to 10^{15} , 10^{17} and 10^{14} cm^{-3} for CIGS₄, CIGS₅ and CIGS₆, respectively) compared to the chalcopyrite CIGS (N_A equals to 10^{20} cm^{-3}) are consistent with the higher resistivity of these phases suggested above from the comparison of the R_s values. The lower conductivity of the lamellar phases was confirmed by 4-point probe electrical measurements on dense pellets. Figure 30 illustrates the variation of resistivity of CIGS between 12 K and 300 K. The resistivity becomes more important while dropping the temperature and its value at the room temperature is of the order of 515 $\Omega\cdot\text{cm}$ which corresponds to a conductivity of about $1,94\cdot 10^{-3}$ $\Omega^{-1}\cdot\text{cm}^{-1}$. In addition, Figure 31 confirms the semiconductor behavior of this material with an exponential increase of resistivity when the temperature decreases. In the case of the lamellar compounds, the measurements were not possible which validates their higher resistivity, as determined by EIS measurements.

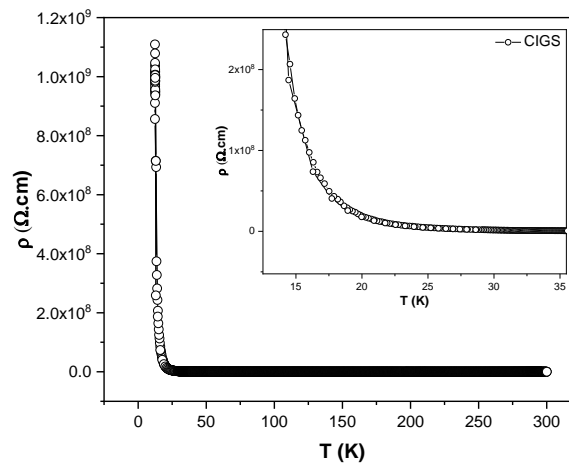


Figure 30: Variation of the resistivity in function of the temperature of the CIGS sample.

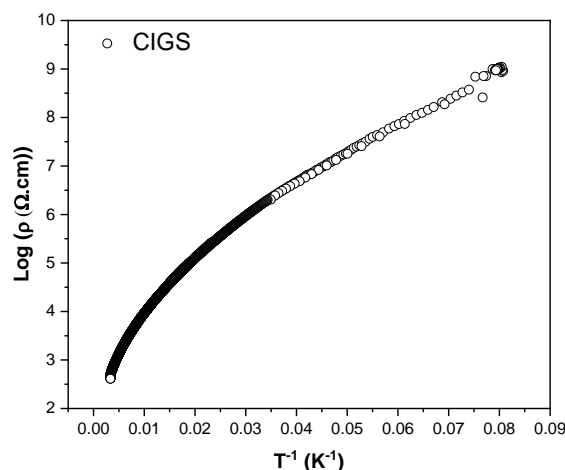


Figure 31: Variation of the exponential of the resistivity of the CIGS sample in function of the temperature.

6. Energy diagrams

- Energy diagrams construction method

The energy diagram were established by combining the electrochemical measurements with X-ray photoelectron spectroscopy (XPS) and diffuse reflectance (Figure 32).⁶² In more details, to construct an energy diagram, firstly the Fermi level calculated from the flat band potential value (equations 19 and 20, see below) from Mott-Schottky plots was positioned on an absolute scale. Then, the top of the valence band was placed from the knowledge of the distance between the valence bands maximum (VBM) and the Fermi level determined by XPS (see Figure 33). Finally, the bottom of the conduction band was located from the VBM value using the optical gap value ($E_g = E_{CBM} - E_{VBM}$).

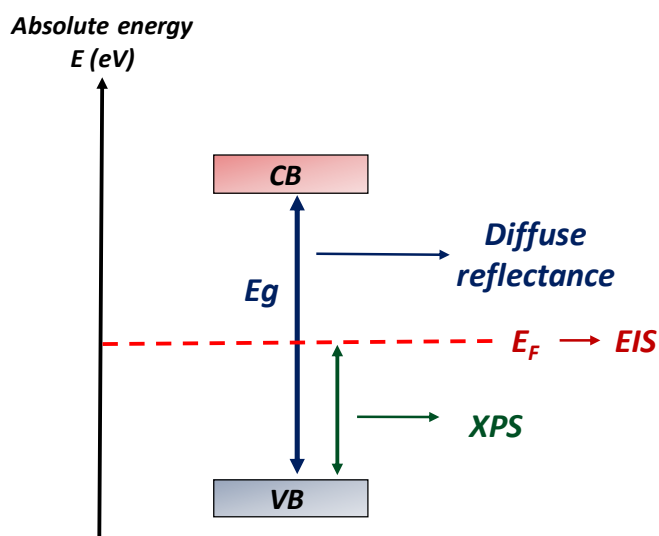


Figure 32: Schematic representation of the energy diagram construction by combining three techniques: diffuse reflectance, electrochemical impedance and x-ray spectroscopy photoelectron spectroscopies.

- Fermi level

Using electrochemical impedance spectroscopy, the flat band potentials of the compounds were determined versus the Ag/AgCl reference electrode, with $V_{Ag/AgCl} = 0.199$ V vs NHE and pH range of 5.68 - 6.56.

Following the formulas (equations 19)^{62,63}, we can calculate the flat band potential versus the reversible hydrogen electrode RHE. The Fermi level is then approximated on an absolute vacuum scale (equation 20)^{39,62}.

$$V_{fb}(RHE) = V_{fb}(Ag/AgCl) + 0.059 pH + V_{Ag/AgCl} \quad (19)$$

$$E_f(eV) = -4.5 - V_{fb}(RHE) \quad (20)$$

- The valence band maximum versus the Fermi level

In XPS, the position of the maximum of the valence band is marked with respect to the Fermi level fixed at 0 eV. The distance between the valence band maximum and the Fermi level set at zero eV, was determined for each compound by linearly extrapolating the low binding energy (BE) edge of the VB region. Figure 33 presents the evolution of the valence bands of the studied compounds previously reported by our group.¹

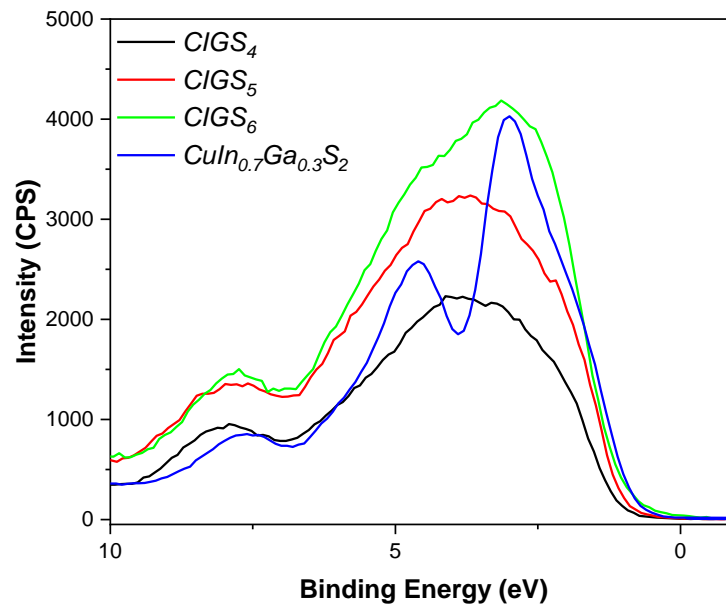


Figure 33: XPS valence band spectra of CIGS₄, CIGS₅, CIGS₆ and CuIn_{0.7}Ga_{0.3}S₂ (CIGS) compounds in the range 10 to 0 eV.¹

- Energy levels of CIGS_n and CIGS compounds

Table 4 sums up the values obtained from the three techniques: the position of Fermi level on an absolute scale, the optical gaps and the position of the maximum of the valence band versus the Fermi level set at zero eV. The energy diagrams of CIGS_n and CIGS are presented in the Figure 34.

Table 4: Optical gaps values, maximum of the valence band (VBM) vs Fermi level position (E_f), estimated Fermi levels using the formulas (21) and (22) and carriers density of $CIGS_n$ and CIGS.

Sample	E_g (eV)	VBM/ E_f ¹	E_f (eV)	Carriers density N (cm^{-3})
$CIGS_4$	1.8	1.1	-4.5	$N_D \sim 10^{15}$
$CIGS_5$	1.9	1.0	-4.4	$N_D \sim 10^{17}$
$CIGS_6$	1.6	1.1	-4.4	$N_D \sim 10^{14}, N_A \sim 10^{12}$
CIGS	1.6	0.8	-5.1	$N_A \sim 10^{20}$

Due to the similar flat band potentials, the Fermi levels of all lamellar $CIGS_n$ compounds are similar and higher in energy than that of the chalcopyrite CIGS (-5.1 eV). This is consistent with a higher electron density in lamellar phases that corroborates the n-type behaviour. Furthermore, according to electrochemical measurements, only $CIGS_6$ behaves as an ambipolar compound.

All compounds exhibit a Fermi level trapped in the middle of the band gap indicating a compensated semiconductor, in which donors and acceptors defects are related in such a way that their opposing electrical effects are partially cancelled. However, it is important to mention that in the case of CIGS, it is surprising to have a mid-gap Fermi level given its high carrier density ($10^{20} cm^{-3}$). This corresponds to the carrier density of a degenerate semiconductor, which should move its Fermi level closer to the valence band.

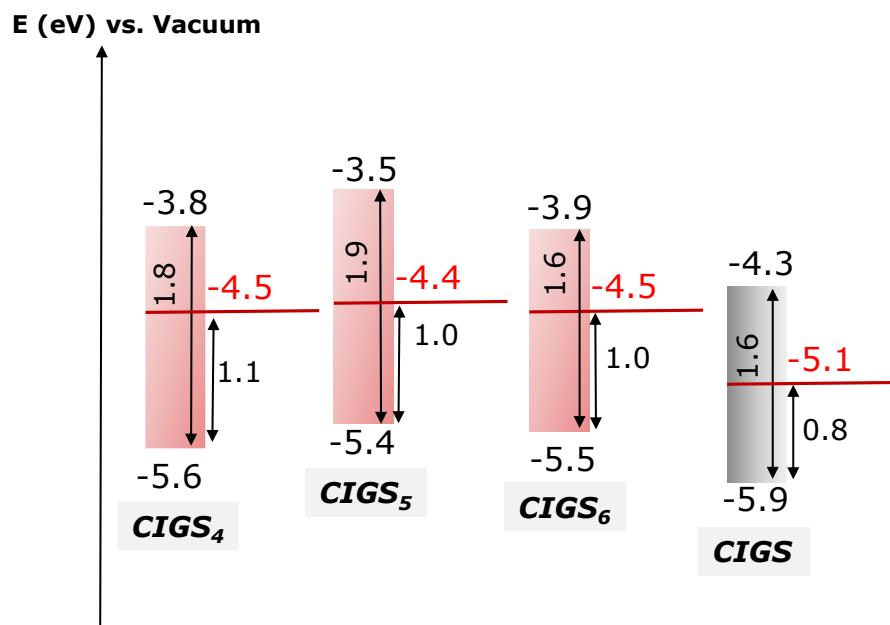


Figure 34: Schematic representation of the energy diagrams of $CIGS_n$ lamellar compounds compared to CIGS chalcopyrite.

The analysis method used in this work to construct energy diagrams was previously used by our group for kesterites compounds ($\text{Cu}_2\text{ZnSnS}_4$), and validated by comparing results with literature data.⁶² However, this strategy cannot be used in our case as there are not many publications indicating band positioning for sulfur-based CIGS (only one publication was found)⁵⁸. Concerning lamellar materials, there is obviously nothing for as they are new materials.

Therefore, to corroborate our results and the analytical method used in this thesis, we carried out an additional calculation^{64,65} to determine the energy levels of the valence and conduction bands. This determination is made using the formula based on the electronegativity and the band gap.⁶⁴ Considering a sulphide of formula $\text{A}_x\text{B}_y\text{S}_z$, it is given as follows (equation 21)

$$E_{BV,BC} = E_0 + (\chi_A^x \chi_B^y \chi_S^z)^{\frac{1}{x+y+z}} \pm \frac{E_g}{2} \quad (21)$$

where $E_0 = -4.5$ eV presenting the difference between the normal hydrogen electrode (NHE) and vacuum and χ_M is the electronegativity of the neutral atom M on the Mulliken scale. Mulliken activity is expressed by the following equation (22)

$$\chi_{Mulliken} = \frac{|EI_1 + AE|}{2} \quad (22)$$

where EI_1 is the energy of first ionization (the energy required to extract an electron from a neutral atom) and AE is the electron affinity (the neutral atom's tendency to capture an electron). Table 5 presents the corresponding values of the elements Cu, In, Ga and S,^{66,67} with the calculated electronegativity using equation (22).

Table 5: First ionization energy and electron affinity values of the elements, with their corresponding electronegativity.

<i>Element</i>	<i>Energy of first ionization EI_1 (eV)</i>	<i>Electron affinity AE (eV)</i>	<i>Electronegativity χ (eV)</i>
Cu	7.72638	1.2358(4)	4.49
In	5.78636	1.56436(15)	3.1
Ga	5.99930	0.43(3)	3.22
S	10.36001	2.0771040(9)	6.25

Then the energies levels of the conduction and valence bands of our compounds are calculated using the equation (21). Figure 35 presents the position of the calculated band energies. Moreover, from the comparison in Table 6, we can observe that we obtain similar values of conduction and valence bands to the experimental data, within the same orders of magnitude. To conclude, this calculation method validates once more the obtained energy diagrams combining the electrochemical measurements with X-ray photoelectron spectroscopy (XPS) and diffuse reflectance.

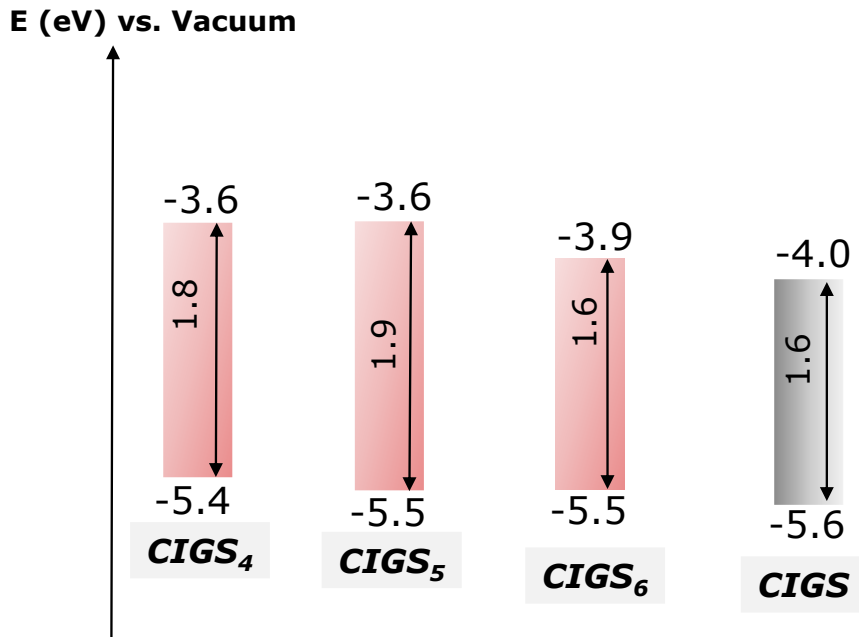


Figure 35: Schematic representation of the calculated energy levels of the conduction and valence band of the $CIGS_n$ lamellar compounds compared to CIGS chalcopyrite.

Table 6: The calculated conduction and valence bands of the compounds, compared to those obtained from the experimental method.

Compound	Experimental		Calculated	
	CB (eV)	VB (eV)	CB (eV)	VB (eV)
$CIGS_4$	-3.8	-5.6	-3.6	-5.4
$CIGS_5$	-3.5	-5.4	-3.6	-5.5
$CIGS_6$	-3.9	-5.5	-3.9	-5.5
$CIGS$	-4.3	-5.9	-4.0	-5.6

7. Photoluminescence

To complete the optoelectronic study of these materials, photoluminescence measurements were carried out at a wavelength excitation of 488 nm.

Figure 37 presents the photoluminescence spectra of $CIGS_5$ and $CIGS_6$ and CIGS chalcopyrite measured at room temperature. It appears that the chalcopyrite CIGS exhibits a PL spectrum composed of two peaks as described in the literature.⁶⁸ A narrow peak at 1.7 eV close to the optical band gap (1.6 eV obtained from linear extrapolation of Kubelka-Munk, which was estimated to 1.7 eV using the derivative⁶⁹), that corresponds to the exciton formation (band-to-band emission) and a broader emission peak at lower energy (1.21 eV) that is probably due to in-gap defects states. The PL emission of this defect band is less intense than that of the exciton peak. Conversely, the emission spectra of the lamellar $CIGS_n$ compounds have only one large peak attributed to a defect-related

band. Indeed, this broad band is centered at lower energy (1.47 eV and 1.36 eV for CIGS₅ and CIGS₆, respectively) than corresponding optical band gaps (E_g equal 1.9 eV and 1.6 eV for CIGS₅ and CIGS₆, respectively). Despite the lower laser power used for the measurements (0.05% vs 1%), this defect-related emission band is broader and more intense for CIGS_n compounds than that of the chalcopyrite CIGS. This fact seems to indicate that the recombination processes through defect states in the gap are much more favoured in the case of the CIGS_n lamellar compounds. This could be directly correlated to the crystal structure. Indeed, as described above, CIGS_n compounds have a quite complex crystal structure with intrinsic cationic vacancies and mixed occupancy (Cu-Ga-In) on tetrahedral sites that can lead to the formation of different types of intrinsic defects (e.g. V_{Cu}' , Cu_{Ga}'' or In_{Cu}°).^{1,70}

The width of the bands and the different values of emission energy translates the multiple types of defects in each compounds and particularly in lamellar phases, that influences the mechanism of charge carrier recombination and thus its kinetics. The presence of much defect states in the gap of CIGS_n lamellar compounds should affect the density of charge carriers and the mechanism of charge transfer that could explain the various electronic behaviours observed above (lower charge carriers density, high resistivity and high charge carriers lifetimes).

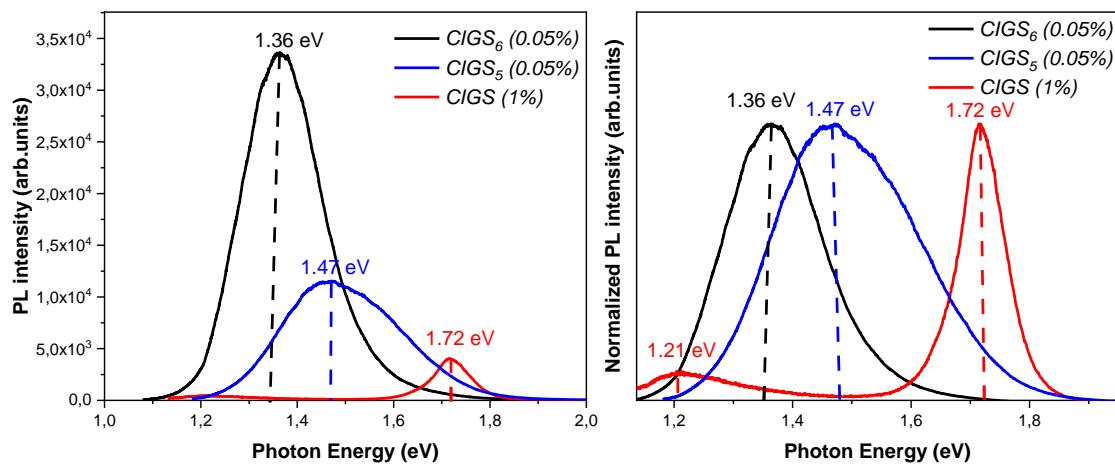


Figure 37: Photoluminescence spectra at 488 nm of CIGS₆ and CIGS₅ lamellar compounds compared to the CIGS chalcopyrite.

Beyond, we can expect that these multiple defect states could impact the carrier recombination. Unfortunately, in the scope of this thesis, we could not carry out time-resolved PL measurements. However, the higher photogenerated charge carrier lifetimes obtained by chronopotentiometry (see Figure 23) for CIGS_n-based electrodes compared to that of CIGS one, seem to assert this hypothesis.

8. A comparison discussion between CIGS_n and CIGS

As explained earlier, the chalcopyrite CuIn_{0.7}Ga_{0.3}S₂ (CIGS) exhibits a p-type semiconductor behaviour, conversely to lamellar compounds that present n-type one. However, only the lamellar compound CIGS₆ reveals an ambipolar character.

The second difference between lamellar phases and the chalcopyrite CIGS concerns the lifetimes of the photogenerated charge carriers. Indeed, as previously mentioned, the lifetime τ_2 , generally related to the carriers recombination processes. Figure 38 presents normalized OCP decays for all compounds highlighting the difference between both types of compounds. It is observed that CIGS chalcopyrite presents a different behaviour than the CIGS_n and that presents a higher time for carriers recombination processes comparing to the lamellar compounds. Besides, it seems that τ_2 increases with the number of tetrahedral layers in the lamellar structure (CIGS₆ > CIGS₅ > CIGS₄). In fact, CIGS_n compounds contain intrinsic cationic vacancies and mixed occupancy (Cu-Ga-In atoms) on the tetrahedral sites, giving rise to a large number of point defects, which can certainly influence recombination process. This fact was corroborated from photoluminescence measurements, revealing much more in-gap defect states in the lamellar compounds. In addition, point defects could also explain the difference in electrical behaviour observed between CIGS and lamellar compounds, which exhibit a lower charge carriers density and quite higher resistivity.

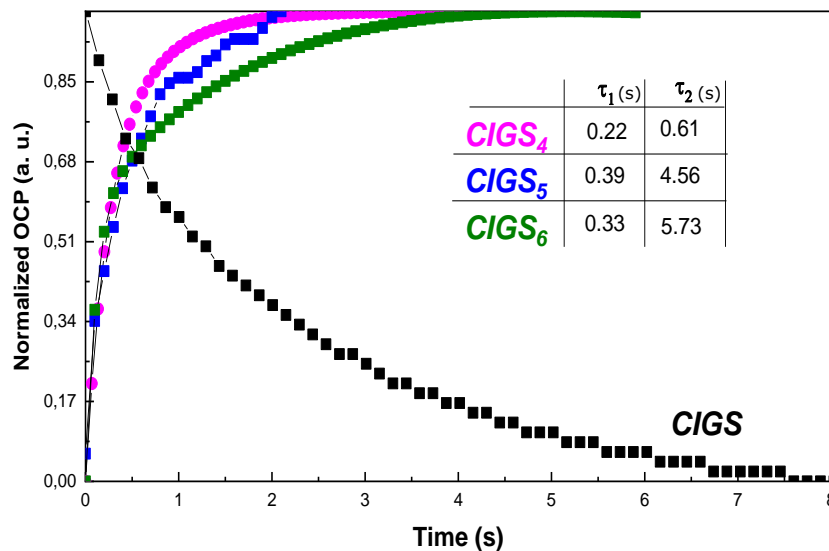


Figure 38: Normalized chronopotentiometry after stopping the illumination of all compounds.

Concerning energy diagrams (see Figure 39), the band alignment of CIGS_n compounds towards the most typical buffer layers (ZnO, CdS and ZnOS)^{71,72} used in CIGS-based PV devices is far from optimal (see Figure 39). In addition, CIGS_n compounds are n-type semiconductors or ambipolar ones, while CIGS chalcopyrite is a p-type semiconductor.

This might open to change the n-type buffer layers (ZnO, CdS and ZnOS) or go towards a total new assembly as n-i-p architecture considering the ambipolar CIGS₆ phase as an intrinsic compound. The photovoltaic potential of the lamellar compounds will be further discussed in the next chapter.

On the other hand, the energy bands of CIGS_n compounds show as CIGS, an interesting positioning with respect to the redox potentials involved in some photo-catalyzed reactions as water splitting and CO₂ reduction⁷³⁻⁷⁵ (Figure 39). In fact, CIGS_n appears to be able to undergo water reduction but not water oxidation, making it unsuitable for water splitting. However, they could be appealing for hydrogen evolution reaction (HER) using an alcohol as sacrificial agent. Moreover, we assume that the ambipolarity behaviour evidenced in these compounds will enhance the efficiency of simultaneous oxidative and reductive reactions, as long as it might not be limited by the mobility of the charge carriers. The photocatalytic properties of CIGS_n compounds will be presented in chapter 4.

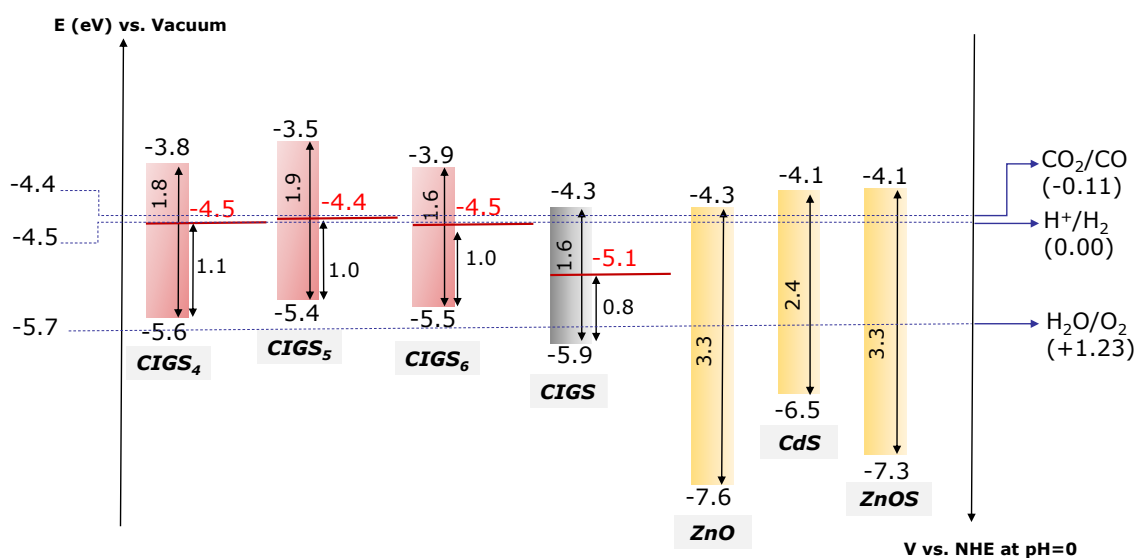


Figure 39: Energy diagrams of CIGS_n lamellar compounds and CIGS chalcopyrite with the corresponding redox potentials involved in photocatalyzed applications.

Appendix chapter 2

X-ray diffraction

The high temperature powders X-ray diffraction XRD measurements were carried out using a Bruker D8 diffractometer in a Bragg-Brentano θ - 2θ configuration equipped with a germanium monochromator to select the Cu-K α radiation ($\lambda=1.540598 \text{ \AA}$). All the samples patterns were recorded in the range 4° to 100° with a stepsize of 0.01° .

To perform a measure on powders, an amount of the sample were placed into the sample holder and a plate of glass was used to flatten the surface of the powder without pressing to prevent any preferential orientation. The experimental data were compared with a database searched on PDF database using EVA software to superimpose them.

Based on these data (cell parameters and space group), Le Bail refinements were performed using Janna2006 software that computes a diagram by adjusting the lattice parameters, till we get as closed as possible to the observed diagram. Indeed, there are three factors to take in consideration, to evaluate the quality of a refinement profile: Rp (unweighted profile factor), wRp (weighted profile factor) and GOF (goodness of the quality of a fit).

Reflectance diffuse

The spectra of the CIGS_n powders were recorded using UV-visible-NIR spectroscopy in a reflection mode, with is a PerkinElmer Lamda 1050 spectrometer equipped with an integration sphere placed at an angle of 8° to the normal to the incident beam. The reflectance measurements were carried out in the 1200 -200 nm range with a resolution of 2 nm. A blank of barium carbonate was used to normalize the measured data. After obtaining the experimental reflection data, the absorption K/S was then calculated based on the Kubelka-Munk⁵ equation $\left(F(R) = \frac{K}{S} = \frac{(1-R^2)}{2R}\right)$.

Working electrodes preparation

For PEC measurements, CIGS sintered pellets were mainly prepared in sealed tubes at 800°C . For lamellar compounds CIGS_n, spark plasma sintering (SPS) was used in order to improve their compactness. The samples were pressed using SPS in a graphite die at high temperature (500°C) for 5 min under a pressure of 38 MPa under argon atmosphere (Figure 40 a).

The working electrodes were prepared by sticking the pellets to a copper wire using a conductive carbon glue, then dipped in the resin and finally polished the electrode to obtain a flatten smooth surface (Figure 40 b).

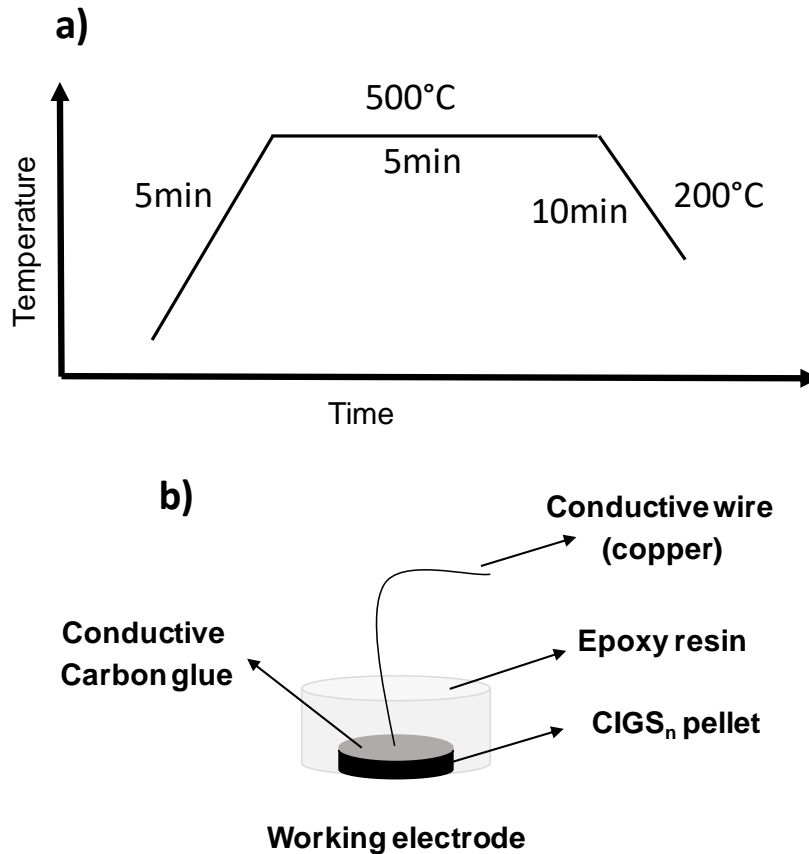


Figure 40: Preparation of the working electrode: a) Temperature protocol of CIGS_n sintering using spark plasma sintering SPS. b) Schematic representation of prepared working electrode.

Conductivity

The conductivity of our compounds was obtained by measuring the variation of resistivity as a function of temperature by the 4-point probe method on cut sample bars. In this technique, the voltage measurement is separated from the current measurement, that allows to neglect surface effect and thus the measurement of the resistance of the bulk material only (Figure 41).

The 4-point probe measurements were realized on a small piece pellet with a rectangular face, the pellets were compressed by SPS under the conditions mentioned earlier. The tests were made by sticking four gold wires on the bars with a conductive carbon glue. These bars are about a size of 2000 μm long, 1500 μm wide and 3000 μm thick. Using this technique, we can detect the resistance R versus the temperature. Then the resistivity ρ and the conductivity σ are calculated following the formulas:

$$\rho = \frac{S}{L} \cdot R = \frac{e \times l}{L} \quad (23)$$

$$\sigma = \frac{1}{\rho} \quad (24)$$

where L : the length and S : is the cross-sectional area that can be divided into e the thickness and l the width.

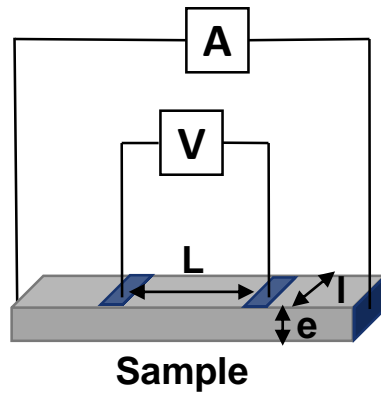


Figure 41: Schematic representation of four-point probe measurements.

Photoluminescence

Photoluminescence (PL) is a method that relies on illuminating the material using a laser beam and then recording the spectrum of emitted photons. The absorption of a photon excites electrons and forms electron-hole pairs that spread into the material and then relax at lower energy levels. The electrons de-excite and the electron-hole pairs recombine emitting light (radiative process) or heat (non-radiative process) when the system relaxes and returns to its original state.

The photoluminescence PL spectra were recorded using a Renishaw InVia Raman microscope setup, which is suitable for both Raman and PL analysis. The measurements were carried out at room temperature with an excitation wavelength of 488 nm, on a wavelength range of 550-1200 nm and an acquisition time of 10s. The conditions used were optimized in order to avoid any possible degradation of the sample surface. For CIGS_n lamellar materials, the measurements were only possible at lower laser power contrary to the CIGS chalcopyrite.

References

- (1) Caldes, M. T.; Guillot-Deudon, C.; Thomere, A.; Penicaud, M.; Gautron, E.; Boullay, P.; Bujoli-Doeuff, M.; Barreau, N.; Jobic, S.; Lafond, A. Layered Quaternary Compounds in the Cu₂S–In₂S₃–Ga₂S₃ System. *Inorg. Chem.* **2020**, *59* (7), 4546–4553. <https://doi.org/10.1021/acs.inorgchem.9b03686>.
- (2) Haeuseler, H.; Srivastava, S. K. Phase Equilibria and Layered Phases in the Systems A₂X₃–M₂X₃–M'X (A = Ga, In; M = Trivalent Metal; M' = Divalent Metal; X = S, Se). *Z. Für Krist. - Cryst. Mater.* **2000**, *215* (4), 205–221. <https://doi.org/10.1524/zkri.2000.215.4.205>.
- (3) Mayerhöfer, T. G.; Pahlow, S.; Popp, J. The Bouguer-Beer-Lambert Law: Shining Light on the Obscure. *ChemPhysChem* **2020**, *21* (18), 2029–2046. <https://doi.org/10.1002/cphc.202000464>.
- (4) Swinehart, D. F. The Beer-Lambert Law.
- (5) Kubelka, P. and F. Munk "Ein Beitrag zur Optik der Farbanstriche" *Zeitschrift für Technische Physik, No. 11a, 1931* | Hagley Museum and Library Archives. https://findingaids.hagley.org/repositories/3/archival_objects/204786 (accessed 2023-03-26).
- (6) Makuła, P.; Pacia, M.; Macyk, W. How To Correctly Determine the Band Gap Energy of Modified Semiconductor Photocatalysts Based on UV–Vis Spectra. *J. Phys. Chem. Lett.* **2018**, *9* (23), 6814–6817. <https://doi.org/10.1021/acs.jpcclett.8b02892>.
- (7) Barreau, N.; Bertin, E.; Crossay, A.; Durand, O.; Arzel, L.; Harel, S.; Lepetit, T.; Assmann, L.; Gautron, E.; Lincot, D. Investigation of Co-Evaporated Polycrystalline Cu(In,Ga)S₂ Thin Film Yielding 16.0 % Efficiency Solar Cell. *EPJ Photovolt.* **2022**, *13*, 17. <https://doi.org/10.1051/epjpv/2022014>.
- (8) Yu, X.; An, X.; Shavel, A.; Ibáñez, M.; Cabot, A. The Effect of the Ga Content on the Photocatalytic Hydrogen Evolution of CuIn_{1-x}Ga_xS₂ Nanocrystals. *J. Mater. Chem. A* **2014**, *2* (31), 12317–12322. <https://doi.org/10.1039/C4TA01315H>.
- (9) Physics and Properties of Semiconductors—A Review. In *Physics of Semiconductor Devices*; John Wiley & Sons, Ltd, 2006; pp 5–75. <https://doi.org/10.1002/9780470068328.ch1>.
- (10) Rajeshwar, K. Fundamentals of Semiconductor Electrochemistry and Photoelectrochemistry. In *Encyclopedia of Electrochemistry*; John Wiley & Sons, Ltd, 2007. <https://doi.org/10.1002/9783527610426.bard060001>.
- (11) Martin, J.; Olier, R.; Clechet, P. COMPORTEMENT PHOTOÉLECTROCHIMIQUE DES OXYDES SEMI-CONDUCTEURS. *J. Phys. Colloq.* **1977**, *38* (C5), C5. <https://doi.org/10.1051/jphyscol:1977534>.
- (12) Brander, R. W. A Review of the Merits of Direct and Indirect Gap Semiconductors for Electroluminescence Devices. *Rev. Phys. Technol.* **1972**, *3* (3), 145. <https://doi.org/10.1088/0034-6683/3/3/I01>.
- (13) Favet, T. Conversion de l'énergie solaire en carburant H₂ par photoélectrolyse de l'eau sur des matériaux nanohybrides à base de TiO₂/nanoparticules. phdthesis, Université de Strasbourg ; Institut national de la recherche scientifique (Québec, province), 2019. <https://theses.hal.science/tel-03186944> (accessed 2023-05-23).
- (14) Gelb, F. Développement d'une Méthode de Caractérisation Photoélectrochimique Localisée Pour Déterminer l'impact de Modifications Morphologiques et Électroniques Sur l'efficacité de Photoconversion Des Nanotubes de TiO₂. These de

- doctorat, Strasbourg, 2020. <https://www.theses.fr/2020STRAF028> (accessed 2023-05-23).
- (15) Tauc, J.; Grigorovici, R.; Vancu, A. Optical Properties and Electronic Structure of Amorphous Germanium. *Phys. Status Solidi B* **1966**, *15* (2), 627–637. <https://doi.org/10.1002/pssb.19660150224>.
- (16) Arutyunyan, V. M. Physical Properties of the Semiconductor-Electrolyte Interface. *Sov. Phys. Uspekhi* **1989**, *32* (6), 521. <https://doi.org/10.1070/PU1989v032n06ABEH002726>.
- (17) Bard, A. J.; Faulkner, L. R.; White, H. S. *Electrochemical Methods: Fundamentals and Applications*; John Wiley & Sons, 2022.
- (18) Pletcher, D. *A First Course in Electrode Processes*; Royal Society of Chemistry, 2019.
- (19) Bott, A. W.; Avenue, K. Electrochemistry of Semiconductors. *Curr. Sep.* **1998**.
- (20) van de Krol, R. Principles of Photoelectrochemical Cells. In *Photoelectrochemical Hydrogen Production*; van de Krol, R., Grätzel, M., Eds.; Electronic Materials: Science & Technology; Springer US: Boston, MA, 2012; pp 13–67. https://doi.org/10.1007/978-1-4614-1380-6_2.
- (21) Xu, X.-T.; Pan, L.; Zhang, X.; Wang, L.; Zou, J.-J. Rational Design and Construction of Cocatalysts for Semiconductor-Based Photo-Electrochemical Oxygen Evolution: A Comprehensive Review. *Adv. Sci.* **2019**, *6* (2), 1801505. <https://doi.org/10.1002/advs.201801505>.
- (22) Helmholtz, H. Ueber Einige Gesetze Der Vertheilung Elektrischer Ströme in Körperlichen Leitern Mit Anwendung Auf Die Thierisch-Elektrischen Versuche. *Ann. Phys.* **1853**, *165* (6), 211–233. <https://doi.org/10.1002/andp.18531650603>.
- (23) Gouy, M. Sur la constitution de la charge électrique à la surface d'un électrolyte. *J. Phys. Théorique Appliquée* **1910**, *9* (1), 457–468. <https://doi.org/10.1051/jphysap:019100090045700>.
- (24) Zhang, Z.; Yates, J. T. Jr. Band Bending in Semiconductors: Chemical and Physical Consequences at Surfaces and Interfaces. *Chem. Rev.* **2012**, *112* (10), 5520–5551. <https://doi.org/10.1021/cr3000626>.
- (25) Grätzel, M. Photoelectrochemical Cells. *Nature* **2001**, *414* (6861), 338–344. <https://doi.org/10.1038/35104607>.
- (26) Guijarro, N.; Prévot, M. S.; Sivula, K. Surface Modification of Semiconductor Photoelectrodes. *Phys. Chem. Chem. Phys.* **2015**, *17* (24), 15655–15674. <https://doi.org/10.1039/C5CP01992C>.
- (27) Nozik, A. J.; Memming, R. Physical Chemistry of Semiconductor–Liquid Interfaces. *J. Phys. Chem.* **1996**, *100* (31), 13061–13078. <https://doi.org/10.1021/jp953720e>.
- (28) Renaud, A. Semi-Conducteurs de Type p Pour Une Application En Cellules Solaires à Colorant. These de doctorat, Nantes, 2013. <https://www.theses.fr/2013NANT2084> (accessed 2023-03-22).
- (29) Olier, R. Etude du comportement photoélectrochimique d'oxydes semiconducteurs de quelques métaux de transition.
- (30) Jiang, C.; Moniz, S. J. A.; Wang, A.; Zhang, T.; Tang, J. Photoelectrochemical Devices for Solar Water Splitting – Materials and Challenges. *Chem. Soc. Rev.* **2017**, *46* (15), 4645–4660. <https://doi.org/10.1039/C6CS00306K>.
- (31) Guyomard, D. Mise au Principes de base de l'électrochimie des semi-conducteurs. *J. Chim. Phys.* **1986**, *83*, 355–391. <https://doi.org/10.1051/jcp/1986830355>.

- (32) Hagfeldt, A.; Graetzel, M. Light-Induced Redox Reactions in Nanocrystalline Systems. *Chem. Rev.* **1995**, *95* (1), 49–68. <https://doi.org/10.1021/cr00033a003>.
- (33) Li, J.; Wu, N. Semiconductor-Based Photocatalysts and Photoelectrochemical Cells for Solar Fuel Generation: A Review. *Catal. Sci. Technol.* **2015**, *5* (3), 1360–1384. <https://doi.org/10.1039/C4CY00974F>.
- (34) Leslie, N.; Mauzeroll, J. Spatially Resolved Electrochemical Measurements. In *Reference Module in Chemistry, Molecular Sciences and Chemical Engineering*; Elsevier, 2023. <https://doi.org/10.1016/B978-0-323-85669-0.00004-0>.
- (35) Mischler, S.; Munoz, A. I. Tribocorrosion. In *Encyclopedia of Interfacial Chemistry*; Wandelt, K., Ed.; Elsevier: Oxford, 2018; pp 504–514. <https://doi.org/10.1016/B978-0-12-409547-2.13424-9>.
- (36) Li, L.; Zhai, L.; Liu, H.; Li, B.; Li, M.; Wang, B. A Novel H₂O₂ photoelectrochemical Sensor Based on Ternary RGO/Ag-TiO₂ Nanotube Arrays Nanocomposite. *Electrochimica Acta* **2021**, *374*, 137851. <https://doi.org/10.1016/j.electacta.2021.137851>.
- (37) Noack, V.; Weller, H.; Eychmüller, A. Electron Transport in Particulate ZnO Electrodes: A Simple Approach. *J. Phys. Chem. B* **2002**, *106* (34), 8514–8523. <https://doi.org/10.1021/jp0200270>.
- (38) Le Formal, F.; Pendlebury, S. R.; Cornuz, M.; Tilley, S. D.; Grätzel, M.; Durrant, J. R. Back Electron–Hole Recombination in Hematite Photoanodes for Water Splitting. *J. Am. Chem. Soc.* **2014**, *136* (6), 2564–2574. <https://doi.org/10.1021/ja412058x>.
- (39) Renaud, A.; Jouan, P.-Y.; Dumait, N.; Ababou-Girard, S.; Barreau, N.; Uchikoshi, T.; Grasset, F.; Jobic, S.; Cordier, S. Evidence of the Ambipolar Behavior of Mo₆ Cluster Iodides in All-Inorganic Solar Cells: A New Example of Nanoarchitectonic Concept. *ACS Appl. Mater. Interfaces* **2022**, *14* (1), 1347–1354. <https://doi.org/10.1021/acsmi.1c17845>.
- (40) Kormányos, A. Photoelectrochemistry of Conducting Polymer-Based Nanohybrid Electrodes. PhD, Szegedi Tudományegyetem, Szeged, Hungary, 2018, p 9701. <https://doi.org/10.14232/phd.9701>.
- (41) Bisquert, J.; Fabregat-Santiago, F. IMPEDANCE SPECTROSCOPY: A GENERAL INTRODUCTION AND APPLICATION TO DYE-SENSITIZED SOLAR CELLS. In *Dye-sensitized Solar Cells*; EPFL Press, 2010.
- (42) van de Krol, R. Photoelectrochemical Measurements. In *Photoelectrochemical Hydrogen Production*; van de Krol, R., Grätzel, M., Eds.; Electronic Materials: Science & Technology; Springer US: Boston, MA, 2012; pp 69–117. https://doi.org/10.1007/978-1-4614-1380-6_3.
- (43) Fabregat-Santiago, F.; Garcia-Belmonte, G.; Bisquert, J.; Bogdanoff, P.; Zaban, A. Mott-Schottky Analysis of Nanoporous Semiconductor Electrodes in Dielectric State Deposited on SnO₂ (F) Conducting Substrates. *J. Electrochem. Soc.* **2003**, *150* (6), E293. <https://doi.org/10.1149/1.1568741>.
- (44) Fundamentals of Electrochemical Impedance Spectroscopy. In *Impedance Spectroscopy*; John Wiley & Sons, Ltd, 2012; pp 1–21. <https://doi.org/10.1002/9781118164075.ch1>.
- (45) Tung, R. T. (董梓則). The Physics and Chemistry of the Schottky Barrier Height. *Appl. Phys. Rev.* **2014**, *1* (1), 011304. <https://doi.org/10.1063/1.4858400>.

- (46) Bredar, A. R. C.; Chown, A. L.; Burton, A. R.; Farnum, B. H. Electrochemical Impedance Spectroscopy of Metal Oxide Electrodes for Energy Applications. *ACS Appl. Energy Mater.* **2020**, *3* (1), 66–98. <https://doi.org/10.1021/acsaem.9b01965>.
- (47) Albery, W. J.; O'Shea, G. J.; Smith, A. L. Interpretation and Use of Mott–Schottky Plots at the Semiconductor/Electrolyte Interface. *J. Chem. Soc. Faraday Trans.* **1996**, *92* (20), 4083–4085. <https://doi.org/10.1039/FT9969204083>.
- (48) Lang, D.; Cheng, F.; Xiang, Q. Enhancement of Photocatalytic H₂ Production Activity of CdS Nanorods by Cobalt-Based Cocatalyst Modification. *Catal. Sci. Technol.* **2016**, *6* (16), 6207–6216. <https://doi.org/10.1039/C6CY00753H>.
- (49) Swain, G.; Sultana, S.; Moma, J.; Parida, K. Fabrication of Hierarchical Two-Dimensional MoS₂ Nanoflowers Decorated upon Cubic CaIn₂S₄ Microflowers: Facile Approach To Construct Novel Metal-Free p–n Heterojunction Semiconductors with Superior Charge Separation Efficiency. *Inorg. Chem.* **2018**, *57* (16), 10059–10071. <https://doi.org/10.1021/acs.inorgchem.8b01221>.
- (50) Ciucci, F. Modeling Electrochemical Impedance Spectroscopy. *Curr. Opin. Electrochem.* **2019**, *13*, 132–139. <https://doi.org/10.1016/j.coelec.2018.12.003>.
- (51) Lasia, A. Electrochemical Impedance Spectroscopy and Its Applications. In *Modern Aspects of Electrochemistry*; Conway, B. E., Bockris, J. O., White, R. E., Eds.; Modern Aspects of Electrochemistry; Springer US: Boston, MA, 2002; pp 143–248. https://doi.org/10.1007/0-306-46916-2_2.
- (52) Bais, P. Investigation Cristallographique Avancée Des Composés Photovoltaïques Dérivés de Cu₂ZnSnS₄. These de doctorat, Nantes, 2017. <https://www.theses.fr/2017NANT4046> (accessed 2023-03-23).
- (53) Irvine, J. T. S.; Sinclair, D. C.; West, A. R. Electroceramics: Characterization by Impedance Spectroscopy. *Adv. Mater.* **1990**, *2* (3), 132–138. <https://doi.org/10.1002/adma.19900020304>.
- (54) Sculfort, J. L.; Baticle, A. M. Impédance Des Jonctions Entre Une Électrode Polycristalline d'alliage GaIn_{1-x}P et Un Électrolyte Aqueux. *Surf. Sci.* **1979**, *85* (1), 137–148. [https://doi.org/10.1016/0039-6028\(79\)90239-5](https://doi.org/10.1016/0039-6028(79)90239-5).
- (55) Randles, J. E. B. Kinetics of Rapid Electrode Reactions. *Discuss. Faraday Soc.* **1947**, *1*, 11–19. <https://doi.org/10.1039/DF9470100011>.
- (56) Suni, I. I. Impedance Methods for Electrochemical Sensors Using Nanomaterials. *TrAC Trends Anal. Chem.* **2008**, *27* (7), 604–611. <https://doi.org/10.1016/j.trac.2008.03.012>.
- (57) Brug, G. J.; van den Eeden, A. L. G.; Sluyters-Rehbach, M.; Sluyters, J. H. The Analysis of Electrode Impedances Complicated by the Presence of a Constant Phase Element. *J. Electroanal. Chem. Interfacial Electrochem.* **1984**, *176* (1), 275–295. [https://doi.org/10.1016/S0022-0728\(84\)80324-1](https://doi.org/10.1016/S0022-0728(84)80324-1).
- (58) Septina, W.; Gunawan; Ikeda, S.; Harada, T.; Higashi, M.; Abe, R.; Matsumura, M. Photosplitting of Water from Wide-Gap Cu(In,Ga)S₂ Thin Films Modified with a CdS Layer and Pt Nanoparticles for a High-Onset-Potential Photocathode. *J. Phys. Chem. C* **2015**, *119* (16), 8576–8583. <https://doi.org/10.1021/acs.jpcc.5b02068>.
- (59) Septina, W.; Sugimoto, M.; Chao, D.; Shen, Q.; Nakatsuka, S.; Nose, Y.; Harada, T.; Ikeda, S. Photoelectrochemical Water Reduction over Wide Gap (Ag,Cu)(In,Ga)S₂ Thin Film Photocathodes. *Phys. Chem. Chem. Phys.* **2017**, *19* (19), 12502–12508. <https://doi.org/10.1039/C7CP01348E>.

- (60) Lemaire, A.; Perona, A.; Caussanel, M.; Duval, H.; Dollet, A. Open-Circuit Voltage Decay: Moving to a Flexible Method of Characterisation. *IET Circuits Devices Syst.* **2020**, *14* (7), 947–955. <https://doi.org/10.1049/iet-cds.2020.0123>.
- (61) Green, M. A. MINORITY CARRIER LIFETIMES USING COMPENSATED DIFFERENTIAL OPEN CIRCUIT VOLTAGE DECAY.
- (62) Bais, P.; Caldes, M. T.; Guillot-Deudon, C.; Renaud, A.; Boujtita, M.; Jobic, S.; Lafond, A. Influence of the Copper Deficiency and Anionic Composition on Band-Energy Diagram of Bulk Kesterite CZTSSe. *Mater. Res. Bull.* **2021**, *139*, 111285. <https://doi.org/10.1016/j.materresbull.2021.111285>.
- (63) Gunawan; Haris, A.; Widiyandari, H.; Septina, W.; Ikeda, S. Surface Modifications of Chalcopyrite CuInS₂ Thin Films for Photoanodes in Photoelectrochemical Water Splitting under Sunlight Irradiation. *IOP Conf. Ser. Mater. Sci. Eng.* **2017**, *172* (1), 012021. <https://doi.org/10.1088/1757-899X/172/1/012021>.
- (64) Castelli, I. E.; Landis, D. D.; Thygesen, K. S.; Dahl, S.; Chorkendorff, I.; Jaramillo, T. F.; Jacobsen, K. W. New Cubic Perovskites for One- and Two-Photon Water Splitting Using the Computational Materials Repository. *Energy Environ. Sci.* **2012**, *5* (10), 9034–9043. <https://doi.org/10.1039/C2EE22341D>.
- (65) Butler, M. A.; Ginley, D. S. Prediction of Flatband Potentials at Semiconductor-Electrolyte Interfaces from Atomic Electronegativities. *J. Electrochem. Soc.* **1978**, *125* (2), 228. <https://doi.org/10.1149/1.2131419>.
- (66) Electron Affinity (Data Page). *Wikipedia*; 2023.
- (67) Ionization Energies of the Elements (Data Page). *Wikipedia*; 2023.
- (68) Shukla, S.; Adeleye, D.; Sood, M.; Ehre, F.; Lomuscio, A.; Weiss, T. P.; Siopa, D.; Melchiorre, M.; Siebentritt, S. Carrier Recombination Mechanism and Photovoltage Deficit in 1.7-EV Band Gap near-Stoichiometric Cu(In,Ga)S₂. *Phys. Rev. Mater.* **2021**, *5* (5), 055403. <https://doi.org/10.1103/PhysRevMaterials.5.055403>.
- (69) Landi, S.; Segundo, I. R.; Freitas, E.; Vasilevskiy, M.; Carneiro, J.; Tavares, C. J. Use and Misuse of the Kubelka-Munk Function to Obtain the Band Gap Energy from Diffuse Reflectance Measurements. *Solid State Commun.* **2022**, *341*, 114573. <https://doi.org/10.1016/j.ssc.2021.114573>.
- (70) Shukla, S.; Sood, M.; Adeleye, D.; Peedle, S.; Kusch, G.; Dahliah, D.; Melchiorre, M.; Rignanese, G.-M.; Hautier, G.; Oliver, R.; Siebentritt, S. Over 15% Efficient Wide-Band-Gap Cu(In,Ga)S₂ Solar Cell: Suppressing Bulk and Interface Recombination through Composition Engineering. *Joule* **2021**, *5* (7), 1816–1831. <https://doi.org/10.1016/j.joule.2021.05.004>.
- (71) Kaur, K.; Kumar, N.; Kumar, M. Strategic Review of Interface Carrier Recombination in Earth Abundant Cu–Zn–Sn–S–Se Solar Cells: Current Challenges and Future Prospects. *J. Mater. Chem. A* **2017**, *5* (7), 3069–3090. <https://doi.org/10.1039/C6TA10543B>.
- (72) Haque, F.; Daeneke, T.; Kalantar-zadeh, K.; Ou, J. Z. Two-Dimensional Transition Metal Oxide and Chalcogenide-Based Photocatalysts. *Nano-Micro Lett.* **2017**, *10* (2), 23. <https://doi.org/10.1007/s40820-017-0176-y>.
- (73) Nahar, S.; Zain, M. F. M.; Kadhum, A. A. H.; Hasan, H. A.; Hasan, M. R. Advances in Photocatalytic CO₂ Reduction with Water: A Review. *Materials* **2017**, *10* (6), 629. <https://doi.org/10.3390/ma10060629>.

- (74) Du, C.; Wang, X.; Chen, W.; Feng, S.; Wen, J.; Wu, Y. A. CO₂ Transformation to Multicarbon Products by Photocatalysis and Electrocatalysis. *Mater. Today Adv.* **2020**, *6*, 100071. <https://doi.org/10.1016/j.mtadv.2020.100071>.
- (75) Liao, G.; Li, C.; Li, X.; Fang, B. Emerging Polymeric Carbon Nitride Z-Scheme Systems for Photocatalysis. *Cell Rep. Phys. Sci.* **2021**, *2* (3), 100355. <https://doi.org/10.1016/j.xcrp.2021.100355>.

Chapter 3: CIGS_n Thin films for photovoltaic application

The first part of this chapter is devoted to the state of art of the CIGS photovoltaic cells. A description of the operating principle and the standard architecture is described. The motivation of the thesis is then introduced. It consists in investigating the CIGS_n thin films potential as absorbers.

The second part of the chapter is therefore dedicated to the elaboration of the CIGS_n thin films, starting with the thin films synthesis using co-evaporation, followed by chemical and structural characterizations. We will be interested more particularly in CIGS₅, that was obtained as monophasic thin film. The optoelectronic properties will be presented alongside with the two electrochemical techniques (photo-electrochemical and electrochemical impedance spectroscopy analyses) used during the thesis to characterize the nature of the semiconductor and estimate its flat band potential, in order to finally determine the energy diagrams of the thin films prepared.

In the last part of this chapter, the realization of the photovoltaic stacks assemblies will be presented. For this purpose, two different architectures (classical and n-i-p architectures) were tested. The photovoltaic parameters of the resulting devices were evaluated by current-voltage IV and external quantum efficiency measurements.

1. A look to photovoltaics

1.1. Photovoltaic effect

Semiconductors are materials used to construct solar cells; they are able to generate electron-hole pairs by absorbing a photon of energy $h\nu$. A small amount of energy is required to excite an electron, moving from the maximum of the valence band to the minimum of the conduction band. Under irradiation, the semiconductor will absorb the photons $h\nu$ whose energy is higher or equal to its band gap energy E_g . As a result, electron-hole pairs will be photogenerated, and the energy excess is lost through thermalization of the electron in the conduction band, heating up the material.

The photovoltaic effect allows the conversion of light energy to electrical energy. This is achieved through the formation of a p-n junction, which can be either a homojunction or a heterojunction. In a homojunction, the p and n zones are formed from the same

semiconductor, such as silicon cell as presented in Figure 1 a. While in a heterojunction, the p and the n zones are made from different semiconductors, as in the case of CIGS cell as shown in Figure 1 b.

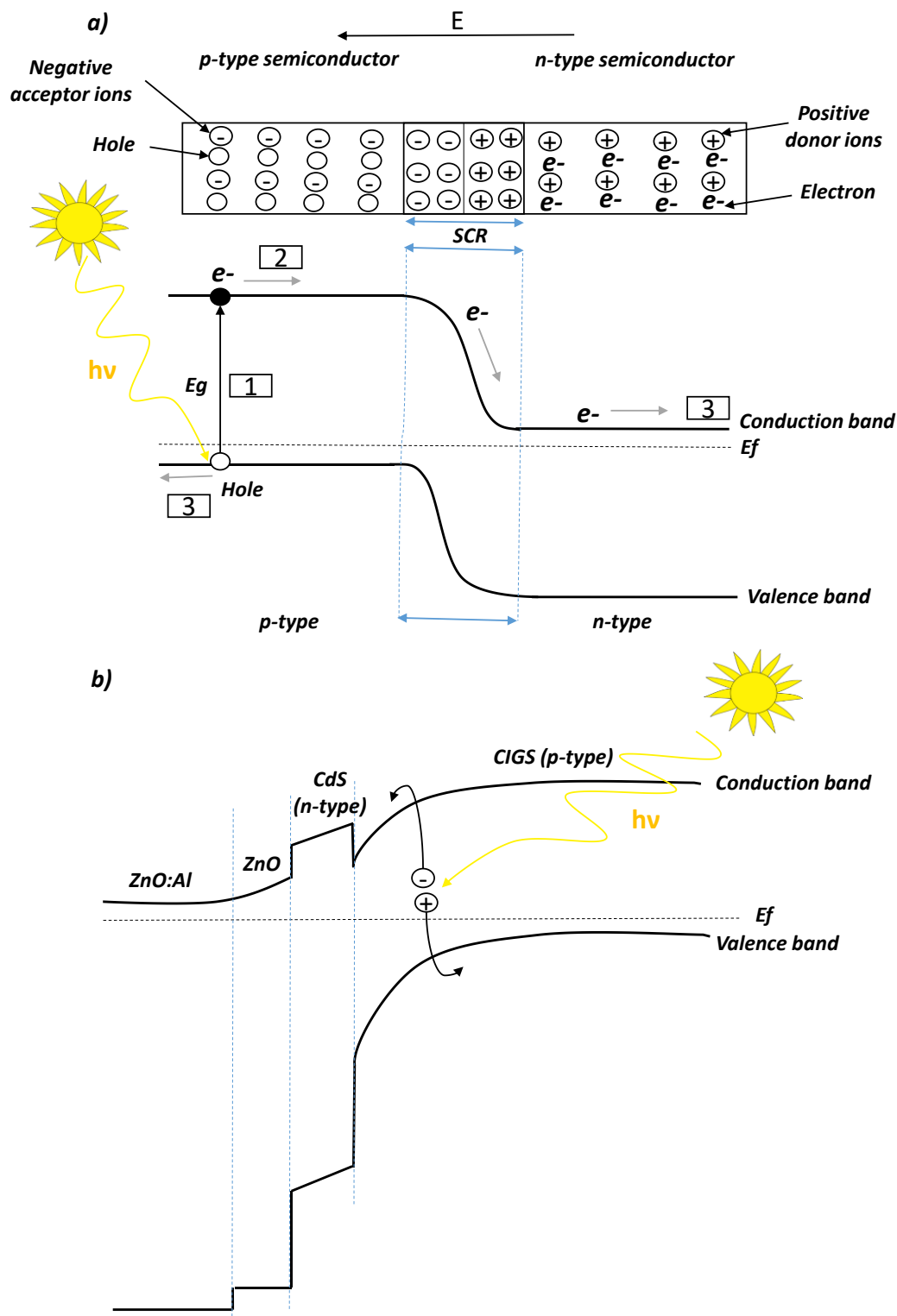


Figure 1: Schematic representation of a) the p-n junction and the mechanism of a silicon based solar cell presenting p-n homojunction. b) The band diagram of p-n heterojunction (CIGS solar cell).

The separation of electron-hole pairs is then accomplished by bringing a p-type and n-type semiconductors into contact. More precisely, this contact will induce an exchange of electrons and holes in order to equalize the concentration of carriers from one region to another (the electrons from the n-region will diffuse into the p-region while the holes will diffuse from the p-region to n-region). When equilibrium is established, a space charge region (SCR) (or called majority carrier depletion region) and quasi-neutral regions (QNR) are formed at the interface. At the SCR, given that n-region is positively charged and p-region is negatively charged, the electrical field is created through a circuit from n-layer to p-layer due to the potential difference across the junction. The resulted electrical field drives the electrons generated in the SCR directly through, whereas the electrons generated in QNR must first diffuse towards the SCR before crossing the junction.

The Fermi levels of the two regions align at equilibrium, and the cell operates as a diode, where forward biasing reduces the potential barrier and facilitates electron diffusion, while reverse biasing increases the potential barrier and blocks the electrons transfer.

To achieve photovoltaic conversion; the device must perform the following three tasks:

Firstly, the semiconductor absorption of photons under sunlight radiation and the generation of electron-hole pairs.

Secondly, the charge carriers separation. The difference in electrochemical potential between the materials promotes the separation of electrons and holes carriers in the SCR, as well as the movement of each type of carrier due to the electrostatic field. The probability of collection is maximum in the depletion region while in quasi-neutral zones, carriers move by diffusion and only those carriers whose diffusion length is sufficient will be collected through their transition.

Finally, the collection of the separated charge carriers in an external circuit. The electrodes placed on the front and back contacts of the p-n junction are used to collect the separated carriers (holes are collected towards the positive pole of the cell and electrons towards the negative pole), resulting a flow of current created through the device.

This photovoltaic effect was reported for the first time in 1839, by Alexandre Edmond Becquerel.¹ In 1883, Fritts succeed to develop the first thin film solar cell based on Se.² But it wasn't until the mid-20th century and exactly in 1954, that the first silicon solar cell was fabricated at the Bell laboratories by Chapin et al with an efficiency record of 6% for space missions use.³ This led to investigate and understand the based semiconductors p-n junctions in the decades followed.² By the 1970s, photovoltaics had become a viable technology for use in terrestrial applications, and the first large scale solar plants were built.⁴

1.2. Operating standard conditions of a solar cell

Commonly, solar cells are evaluated under standard conditions, including an AM1.5G spectrum at an incident power of $1000 \text{ W}\cdot\text{m}^{-2}$ and a temperature of 25°C . The AM 1.5G presents the typical solar spectrum at sea level after crossing 1.5 layers of standard atmosphere and with a light incidence angle equivalent to 41.8° , taking into account global direct and diffusion radiations. Figure 2 shows the standard AM 1.5G solar spectrum obtained from American society for testing materials ASTM.⁵ It is worth mentioning that the efficiency of a cell varies with the illumination power received, and decreases as the temperature increases.

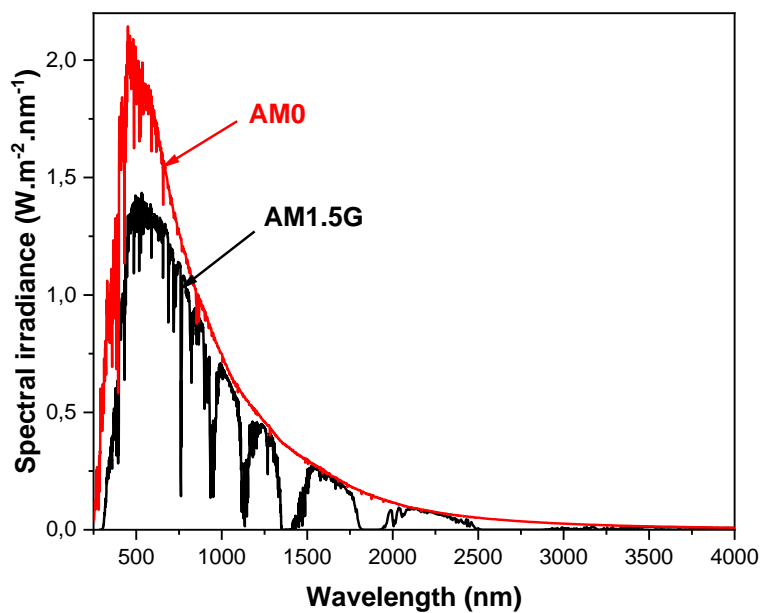


Figure 2: AM 1.5G solar spectrum compared to the AM0 spectrum outside the atmosphere.⁵

The cell efficiency is limited by losses at various levels. Photons with energies below the gap are not absorbed; a part of the energy is lost through thermalization and the generation of carriers recombination. According to Shockley and Queisser,⁶ the maximum efficiency of a photovoltaic cell using a p-n junction is around of 30 % (Shockley-Queisser limit). This limit was calculated as a function of the material gap for the ideal case, where all recombinations are radiative, charge carrier transfer is unlimited, and all photons of energy equal to the material gap are absorbed.

Figure 3 illustrates a simplified photovoltaic cell modelled by a circuit with a diode, in order to take these losses in consideration, with a parallel resistor (R_{sh}) representing the different shunt currents and a series resistor (R_s) representing the contact and connection resistors.^{7,8} A high performance cell features a higher parallel resistance to decrease current losses and a lower series resistance to reduce voltage losses.

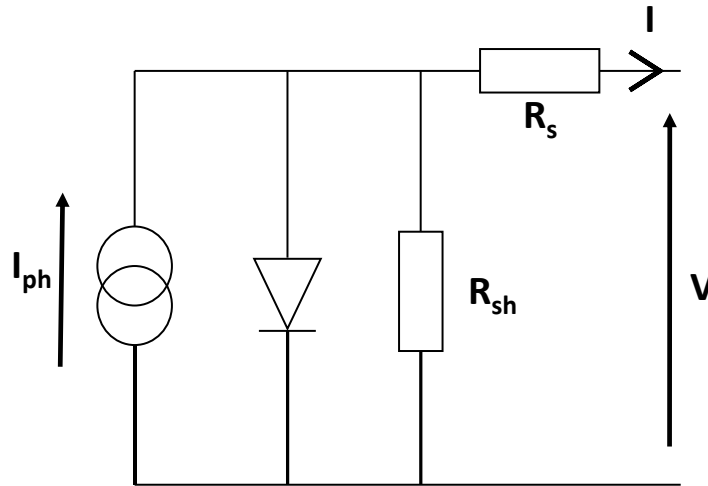


Figure 3: Equivalent electrical circuit of a photovoltaic cell with I_{ph} : the photogenerated current, R_s : series resistor and R_{sh} : parallel resistor.

1.3. Photovoltaic technologies

Generally, there are three generations of solar cells: First generation based on traditional crystalline silicon PV cells, which have been the most expanded in solar panels market for decades (92%).⁹ They are efficient and reliable, the higher record reported for crystalline Si is 26.81% by LONGI in 2022.¹⁰ Second-generation presents the inorganic thin films PV cells. Finally, the third generation refers to the organic thin films, hybrid solar cells and the perovskites. Figure 4 cites all the different existing technologies summarized by National Renewable Energy Laboratory (NREL) with their increasing performances records with time (from 1975 to today).¹⁰

Second generation presents the inorganic thin films PV cells, which is divided to 3 categories amorphous silicon cells, CdTe based cells and CIGS (copper indium gallium selenium or/and sulphur).

In the current PhD, we are interested in this particular type of solar cells, and exactly on CIGS (copper indium gallium sulphur).

2. The CIGS-based photovoltaics

CIGS-based thin films PV has attracted attention as a promising technology to overpass the silicon PV,¹¹ since they demonstrated high efficiencies: 23.35% for CIG(S,Se)₂,¹² 22.6% for pure CIGSe selenide,¹³ while 15.5% for pure sulphides¹⁴ and recently in our group, this efficiency was increased up to 16%.¹⁵

A lot of research is conducted on Cu(In,Ga)S₂ (noted CIGS) chalcopyrite compounds as absorbers due to their band gap that varies between 1.54 eV and 2.43 eV,¹⁶ which fits perfectly with the sunlight spectrum and makes CIGS relevant for PV applications. CIGS sulphur compounds are getting more attention since they demonstrate a wider band gap than CIGSe selenium.

At the present, the highest efficiencies were always achieved using semiconductors with a band gap near to 1.7 eV as in the case of CuIn_{0.7}Ga_{0.3}S₂,¹⁷ that adopts a chalcopyrite type structure similar to CIGSe used to attain the highest performances.^{12,13}

2.1. The architecture of CIGS solar cells

The basic architecture of a CIGS solar cell consists of a stack of 6 layers deposited on a substrate using different techniques (Figure 5).

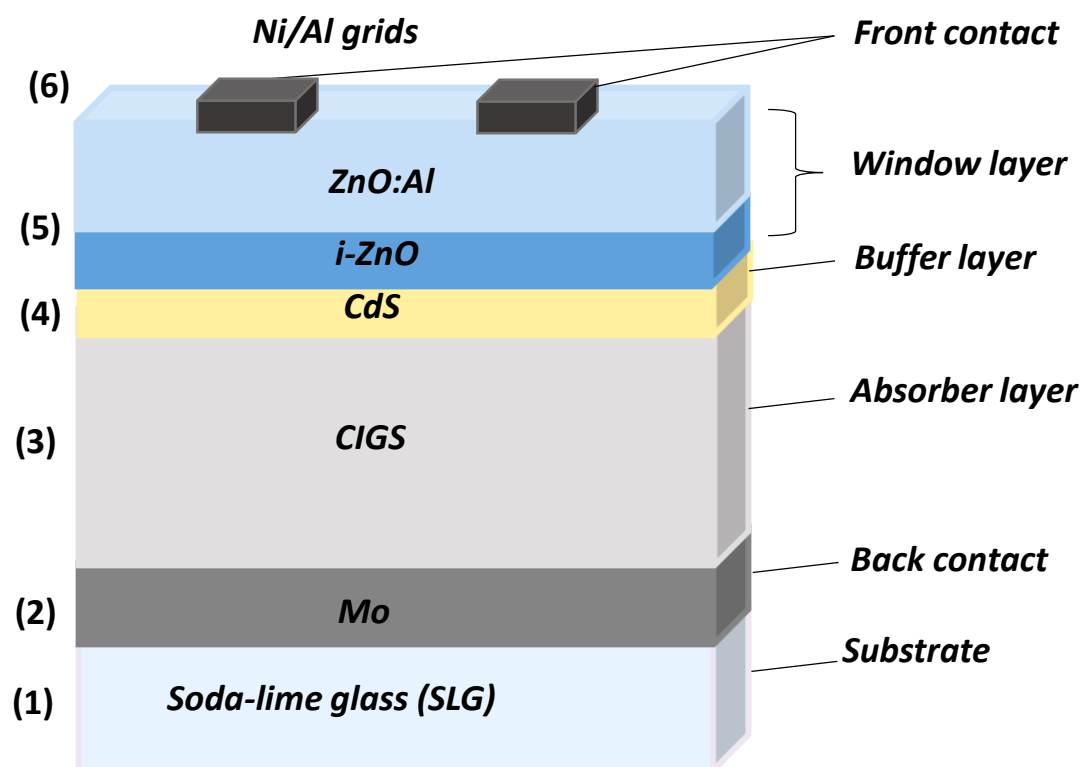


Figure 5: Schematic representation of a standard CIGS cell.

The main layers of CIGS solar cell are:

1- Substrate

Role

The most used substrate is soda lime glass (SLG) since it is largely available and cheap, other substrates as metals or polymers can be also used for flexible and light weight cells applications.^{18,19}

The thermal expansion coefficient of SLG is well adapted to CIGS and is stable at high temperatures. The diffusion of sodium from the glass into the absorber is known to positively affects the properties of the cell.^{20,21}

The films investigated in this PhD thesis were synthesised at high substrate temperature, around of 580 °C, this requires a substrate that is able to handle high temperatures as in the case of SLG (the softening point of the glass substrate is 600°C).

2- Back contact

Role

A metallic layer that serves as the electrical contact on the backside of the cell, in order to collect the photo-generated carriers (collects holes and acts as a positive electrode).

Material growth

Commonly, it is a layer of molybdenum (Mo) layer grown on the SLG that is deposited using DC-sputtering. Mo can withstand high temperatures but more importantly, it is reported that an ohmic contact is formed at the interface between Mo/CIGS or Mo/CIGSe layers due to the formation of MoS₂ or MoSe₂, respectively.²²⁻²⁴

3- Absorber

Role

The absorber is the Cu(In,Ga)S₂ material, the layer where the electron-hole pairs are released. It is a p-type semiconductor with a direct band gap, which provides a high absorption coefficient. Thus, only an absorber thickness of few microns is enough to allow the absorption of the majority of the incident photons with energy higher than E_g.

Material growth

Several techniques of the CIGS thin films deposition were developed. Growth techniques can be divided into two categories. Vacuum based CIGS deposition, as in the case of co-evaporation^{15,25} and sputtering (or called SAS sulfurization after selenization process).^{12,14}

The second category consists in the deposition at the atmospheric pressure such as electrodeposition,^{26–28} spin coating,^{29–31} inks^{32,33} ...

The highest CIGS photovoltaic efficiencies were achieved using the vacuum based growth techniques and the obtained CIGS modules are already commercialized on the PV market nowadays. Nevertheless, the production cost remains relatively high, compared to the non-vacuum methods that still present lower conversion yields.

Co-evaporation approaches can either include one, two or three stages. The most used co-evaporation synthesis of CIGS is performed in three steps (3 stage process). This process was developed for the first time by the National Renewable Energy Laboratory NREL³⁴ and have since allowed the achievement³⁴ of high efficiency.

The CIGS_n thin films prepared during this work were synthesized using the co-evaporation technique, which is well established in our laboratory.

4- Buffer layer

Role

Commonly, it is an n-type semiconductor, which will create a p-n junction with the CIGS absorber. Compared to the absorber, the buffer layer material should exhibit a wider optical band gap to permit the incident photons to reach the CIGS absorber.

Material growth

The most used film is cadmium sulphide (CdS) deposited by chemical bath deposition (CBD).¹⁵ Still, because of the Cd toxicity and its relatively low band gap (2.4 eV)³⁵, alternative materials were studied, as Zn(O,S) that demonstrated cell efficiencies comparable to the ones with CdS.^{36,37} This promising buffer layer can be deposited by CBD and it presents a large optical gap (3.3 eV) providing better band alignment with CIGS than CdS.³⁸

Besides, the devices with Zn(O,S,OH)_x/Zn_{0.8}Mg_{0.2}O double buffer layers revealed a record efficiency of 23.35% surpassing the CdS devices.¹²

5- Window layer

Role

It needs to be a transparent layer in order to allow the light to pass through. Generally, it is an n-type transparent conducting oxide (TCO) layer with high-energy band gap. The role of this film is to provide the collection of the charges by the front grids.

Material growth

During this PhD, we used the standard bilayer i-ZnO/ZnO:Al deposited by RF sputtering deposition as a window film. The first layer called “second buffer layer” is an intrinsic zinc oxide with a band gap of 3.3 eV and a high resistivity to limit the defects effects of the CdS and allow a better band alignment with ZnO:Al. The second layer is Al-doped zinc oxide film with a band gap of 3.6 eV that serves as TCO.

6- Front contact

Role

This part of the cell used to collect the photo-generated electrons.

Material growth

Front contacts are metallic contacts that are deposited on the window layer by thermal evaporation using e-beam across a shadow mask. The standard front contacts used in CIGS solar cells are Ni/Al grids, which were used in this work. Other contacts were also used as Au and Ag.

2.2. Requirements for a good CIGS cell

Several conditions are required to be fulfilled, for a solar cell to operate efficiently:

1. High absorption coefficient: to enhance sunlight absorption, the CIGS absorber must be able to efficiently absorb sunlight over a wide range of wavelengths of the solar spectrum. The CIGS thin film must be sufficiently thick to absorb a significant amount of sun radiation, yet thin enough to reduce internal absorption losses. In addition, adjusting the indium and gallium content in the absorber affects the optical characteristics of the material.
2. Suitable band gap: a CIGS band gap of the order of 1 to 2 eV enables the cell to absorb in the visible region of the solar spectrum.
3. Direct band gap: A material with a direct band gap provides a direct electronic transition between the valence and the conduction bands due to their similar wave-vector location points, which improves light absorption and the generation of electron-hole pairs.
4. p-type semiconductor: the CIGS absorber is preferred to be a p-type semiconductor. In the classical CIGS architecture, the buffer layer deposited on the CIGS is an n-type semiconductor, enabling the formation of a p-n junction, facilitating the charge carriers separation and minimizing recombination losses.
5. High carriers density: a high carriers density is needed, to increase the quantity of available electrons and holes carriers. The carriers density value should be about 10^{17} cm^{-3} , in order to provide a sufficient amount of accessible electronic states,

allowing efficient charge carrier generation. Moreover, the photogenerated carriers by the absorber must be able to move easily through the material to be collected and create an electric current in the cell. Therefore, a high degree of charge mobility is required.

6. Long charge carrier lifetime: the charge carriers lifetime in the absorber is important for the solar cell stability. A longer lifetime essentially allows the carriers to remain available for a specific time before they eventually recombine or lose their energy. It could be impacted by defects and interactions at the interfaces. Thus, in order to improve the lifetime, the deposition must be well controlled avoiding any impurities, as well as optimizing the interfaces.
7. Chemical and thermal stability: for a long device lifetime, the CIGS must be chemically stable to withstand long-term degradation and thermally stable to resist any high temperatures.

It is important to note that even a device that meets all these requirements remains difficult to explore.

2.3. Motivation: CIGS_n lamellar compounds potential use as PV absorbers

As reported in the previous chapter, a full study is implemented as a first step in this work to determine the optoelectronic properties of our compounds. According to the results obtained from diffuse reflectance, the optical gaps of our lamellar compounds were found to be 1.8 eV, 1.9 eV and 1.6 eV for CIGS₄, CIGS₅ and CIGS₆, respectively; which is close to the one of CIGS chalcopyrite $\text{CuIn}_{0.7}\text{Ga}_{0.3}\text{S}_2$ (1.7 eV), therefore our compounds might be potentially used as absorbers as well. Further, the 2D structure with a van der Waals gap of our compounds might lead to different layers orientation deposition, either parallel or perpendicular layers deposition to the substrates.

Moreover, the CIGS_n thin films present copper poor compositions (Cu/S= 0.1, 0.2, 0.3) comparing to the CIGS chalcopyrite (Cu/S =0.5). Thus, it is possible to use a one-stage process and avoid the CuS segregation at the surface as for CIGS chalcopyrite, while providing a homogeneous composition, since this approach does not produce compositional profile grading like in the three-stage process.

In the rest of the chapter, we will report the experimental details and the results obtained on the CIGS_n lamellar compounds to answer the question whether our compounds can operate as absorbers on a solar device and it will be organized as follows:

- CIGS_n thin films synthesis using co-evaporation.
- Thin films characterizations: Chemical, structural, optical and electrochemical characterizations.
- Electrical measurements using two different architectures.

3. Elaboration of CIGS_n thin films

3.1. Co-evaporation synthesis

The synthesis of CIGS_n thin films was carried out in the co-evaporation machine BAK-640 under high vacuum (a residual pressure of between 10^{-7} and 10^{-6} mbar). The elementary sources of copper, indium, gallium and sulphur evaporate simultaneously onto a substrate heated thanks to halogen lamps.

Inside the chamber (Figure 6), the sources are placed in effusion cells and the substrate is placed above next to them on the sample holder. The substrate holder can contain up to three microscope slides of 7.5 cm by 2.5 cm (A, B, C). Generally, the composition remains homogeneous on the entire surface of the substrates.

A calibration of the evaporation fluxes as a function of the temperature of the metal sources (copper, indium and gallium) is implemented using a quartz microbalance. As a result, the atomic fluxes of each element for the targeted composition corresponds to a specific heating temperature (Figure 7). Meanwhile sulphur is evaporated in excess, in order to avoid the formation of an absorber with a lack of sulphur. The ratio between the atoms adsorbed on the substrate and all the atoms evaporated towards it, is mainly similar in the case of Cu, In and Ga. In the case of S this ratio is lower. The unreacted excess of S re-evaporates, because the pressure in the chamber is lower than its vapour pressure at this substrate temperature.

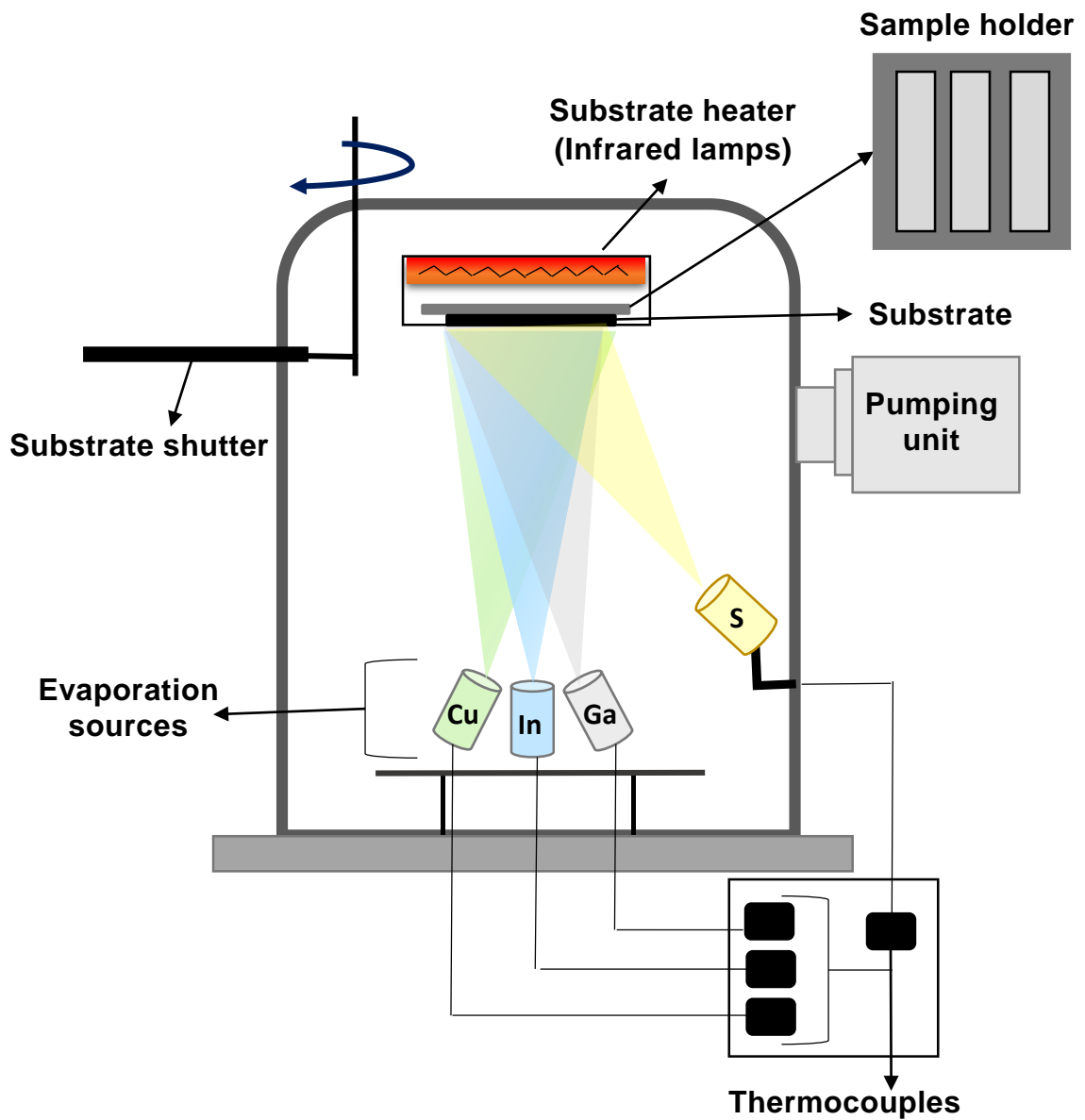


Figure 6: Schematic representation of a co-evaporation deposition chamber.

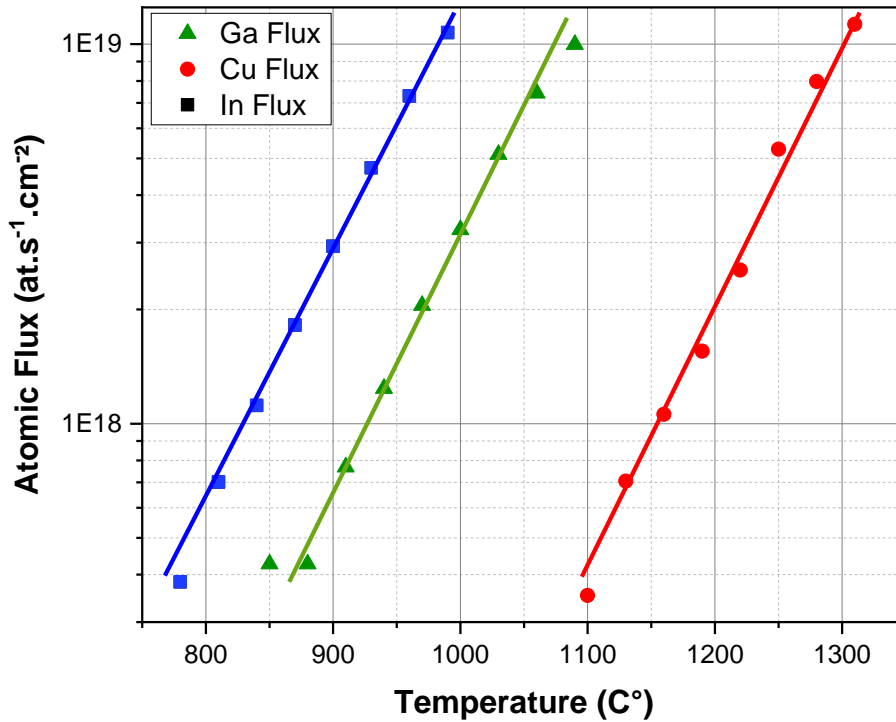


Figure 7: Calibration of the atomic flux of the elemental sources (Cu, In and Ga) as a function of the temperature.

A single stage process was used to prepare CIGS_n lamellar layers with the stoichiometric compositions Cu_{1.44}In_{2.77}Ga_{0.76}S₆ and Cu_{0.65}In_{1.75}Ga_{1.4}S₅ for CIGS₆ and CIGS₅ respectively. The Figure 8 presents the one stage co-evaporation process followed for CIGS₅ and CIGS₆. During this process, the substrate temperature remains constant and all the raw materials Cu, In, Ga and S are evaporated simultaneously at fixed temperatures that refers to the atomic flux corresponding to the targeted composition as mentioned before. The deposition parameters are presented on the Table 1.

In this work, different substrates were used for the CIGS deposition such as SLG and SLG/Mo. Besides, TCO coated on SLG such as SLG/FTO (Fluorine doped tin oxide SnO₂: F) and SLG/ITO (Indium tin oxide) are also employed. It's worth to mention that TCO are beneficial for the CIGS tandem cells due to transparency.³⁹ Particularly for CIGS tandem,³⁹⁻⁴¹ bifacial⁴²⁻⁴⁴ or superstrate^{44,45} solar cells applications. In these configurations, the sunlight will enter either from the substrate/back contact or from both sides.

A temperature of 580°C is applied to the substrates for both CIGS₅ and CIGS₆, this temperature is considered as the maximum value without causing any substrate deformation. In the first attempts, this temperature was decreased to lower values, but the targeted composition was not obtained.

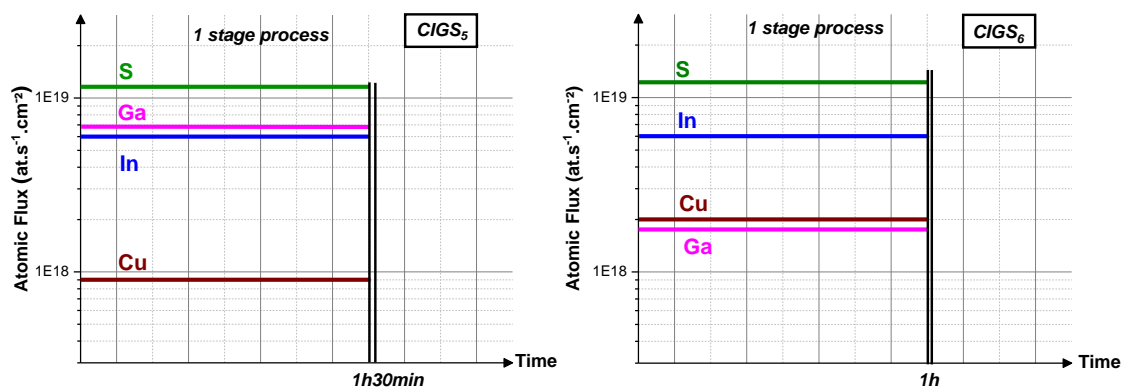


Figure 8: The 1-stage process followed for CIGS₅ and CIGS₆ deposition.

Table 1: CIGS₆ and CIGS₅ deposition parameters.

<i>CIGS₆ deposition protocol</i>	<i>CIGS₅ deposition protocol</i>
<i>Cu source temperature: 1200 °C</i> <i>In source temperature: 950 °C</i> <i>Ga source temperature: 960 °C</i> <i>S source temperature: 140 °C</i> <i>Substrate temperature: 580 °C</i> <i>Time of the deposition: 1h</i> <i>Co-evaporation chamber pressure: 10⁻⁵ mbar</i>	<i>Cu source temperature: 1150 °C</i> <i>In source temperature: 950 °C</i> <i>Ga source temperature: 1050 °C</i> <i>S source temperature: 140 °C</i> <i>Substrate temperature: 580 °C</i> <i>Time of the deposition: 1h30min</i> <i>Co-evaporation chamber pressure: 10⁻⁵ mbar</i>

Figure 9 shows CIGS₅ and CIGS₆ deposited on soda lime glass with an average thickness of about ~1µm. It is observed that both samples exhibit a colour similar to the one obtained with high temperature powders (a black sample in the case of CIGS₆ and red for CIGS₅ thin film).



Figure 9: The deposited CIGS₆ and CIG₅ samples on soda lime glass.

3.2. Structural and chemical characterizations of CIGS_n

The CIGS_n samples were investigated by XRD, to identify the crystalline phase of the material. The measurements were performed using 3 different diffractometers (Bruker D8 in a Bragg - Brentano θ -2 θ configuration, INEL with Debye Scherrer geometry and XtaLAB Synergy-S Rigaku, see appendix). The XRD patterns recorded of CIGS₆ and CIGS₅ thin films deposited on SLG and Mo/SLG substrates are presented in this section and compared to the CIGS_n powders prepared by high temperature solid state reaction, serving as our reference, in order to figure out if the targeted structure has been obtained.

In Figure 10, the diagram of the layer deposited on SLG (in green) shows more peaks compared to the layer deposited on SLG/Mo (in pink) for which the substrate is well crystallized and the peaks relative to Mo overshadow all. In addition, the crystallites in the co-evaporated thin films are much smaller than in the case of the high temperature powders, as a result the peaks correspond to the deposited material are less wide and intense. For this reason, plotting the diagram in a logarithmic scale allows us to see more peaks as shown in Figure 11. Unfortunately, the intensities of the peaks remain low. For this purpose, the scratched thin film is analysed with INEL diffractometer using a capillary, in order to avoid any sort of preferential orientation that might appear due to the substrate.

Several observed diffraction peaks of the CIGS₆ scratched thin film (in blue, Figure 10) match perfectly with the (003), (102) (1-12), (1-14) and (2-10) reflections of the reference powder CIGS₆ (in red). Unfortunately, CuIn₅S₈ was identified as a secondary phase, allowing an explanation of all the reflections. Moreover, in Table 2, the results obtained from EDX demonstrate the co-existence of two phases, one composition (Cu_{1,9}In₃Ga_{0,48}S₆) close to the CIGS₆ lamellar phase and the other one (Cu_{1,2}In_{2,1}Ga_{2,8}S₈) corresponding to a composition that can be formulated as spinel CuIn₅S₈.

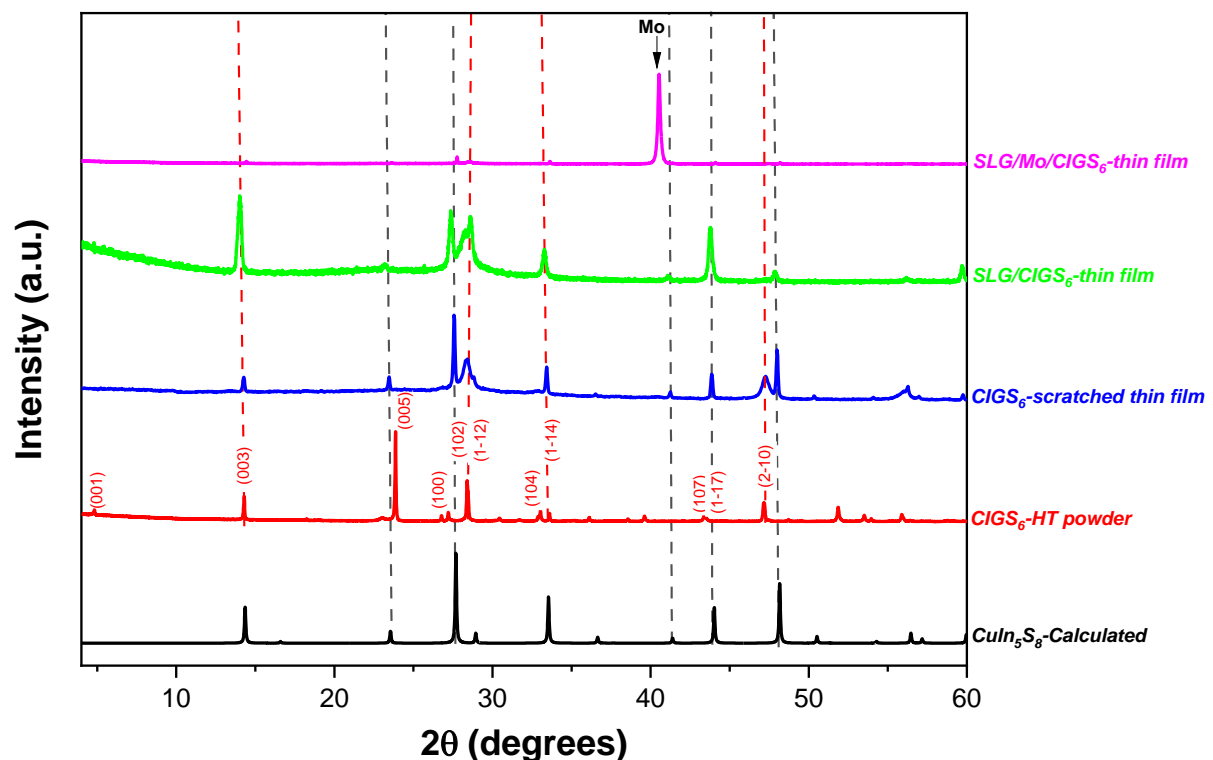


Figure 10: X-ray diffraction patterns of the deposited CIGS₆ thin films on glass and on Mo covered soda lime glass compared to the reference powder of the same target composition Cu_{1,44}In_{2,77}Ga_{0,76}S₆ and the secondary phase observed CuIn₅S₈.

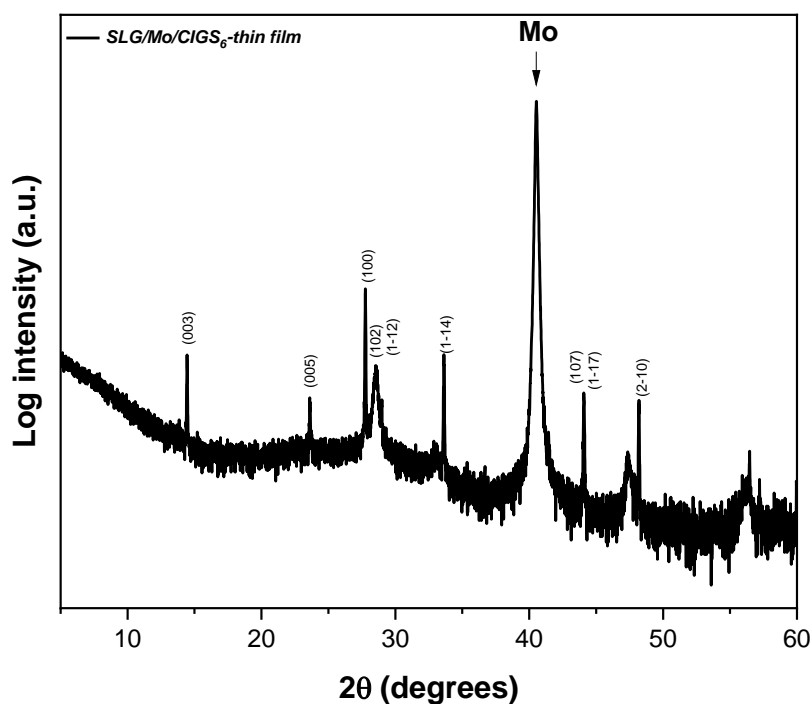


Figure 11: X-ray diffraction pattern of CIGS₆ deposited on Mo-covered soda lime glass on a logarithmic scale.

In the case of CIGS₅, the scratched thin film is analysed with INEL diffractometer using a capillary (Figure 12). All the peaks observed on the X-ray patterns of the scratched thin films can be indexed to the reference CIGS₅ powder as observed in Figure 12. The large dominant peak around $2\theta \approx 28^\circ$ suggests the presence of numerous peaks which correspond to the set of peaks in the $27^\circ \leq 2\theta \leq 29^\circ$ range of the reference. Besides, as displayed in the zoom inset, the first reflection (002) observed around low 2θ ($2\theta = 5.7^\circ$) meets the CIGS₅ lamellar material signature reported by our group⁴⁶. All the lamellar materials CIGS_n exhibit a specific d-spacing observed at low 2θ and that is equivalent to 15.6 Å for CIGS₅.

On the other hand, the scratched thin film is also analysed using XtaLAB Synergy-S Rigaku diffractometer with a better resolution and intensity in a capillary form (see appendix). Figure 13 presents the obtained pattern plotted versus $d(\text{Å})$. The most intense reflections of the CIGS₅ reference are overlapping with the principal peaks of the powder from scratched thin film. Consequently, by this comparison, a CIGS₅ type structure for this last compound is validated. This fact is corroborated by EDX. A homogeneous monophasic composition ($\text{Cu}_{0.63}\text{In}_{1.9}\text{Ga}_{1.26}\text{S}_5$) close to the CIGS₅ targeted one was detected with comparable atomic ratios values (See Tables 2 and 3).

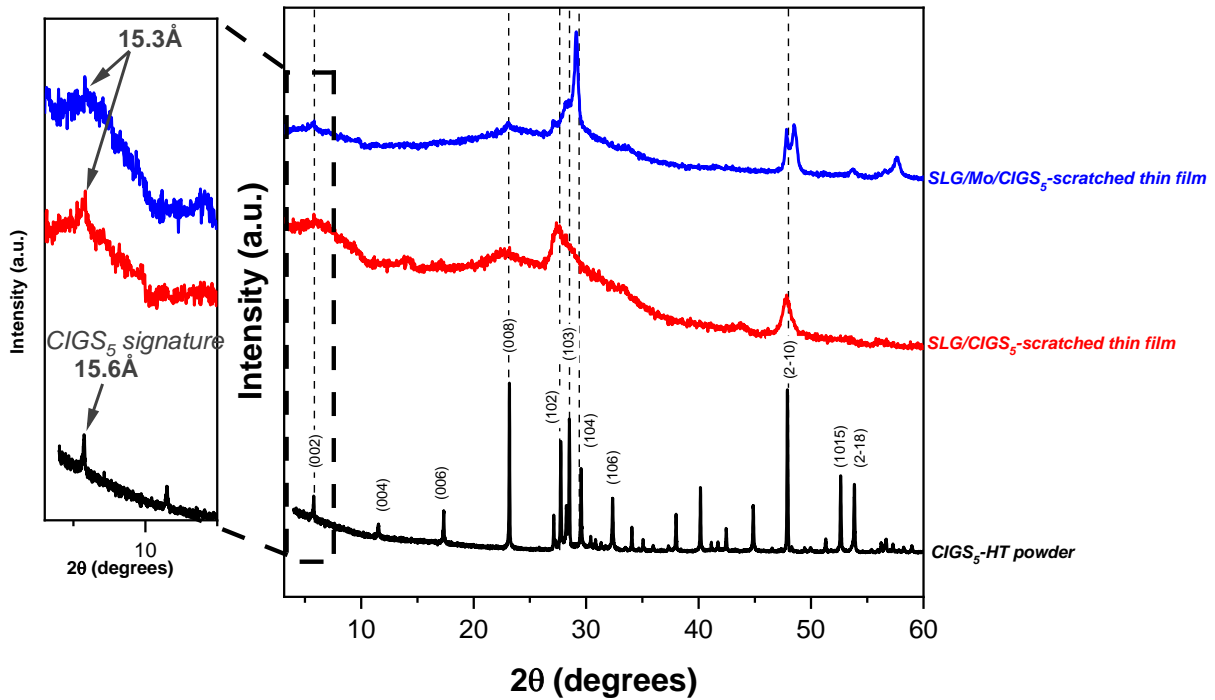


Figure 12: X-ray diffraction patterns of the powders from scratched CIGS₅ thin films on glass and on Mo covered soda lime glass compared to the reference powder of the same target composition $Cu_{0.63}In_{1.9}Ga_{1.26}S_5$.

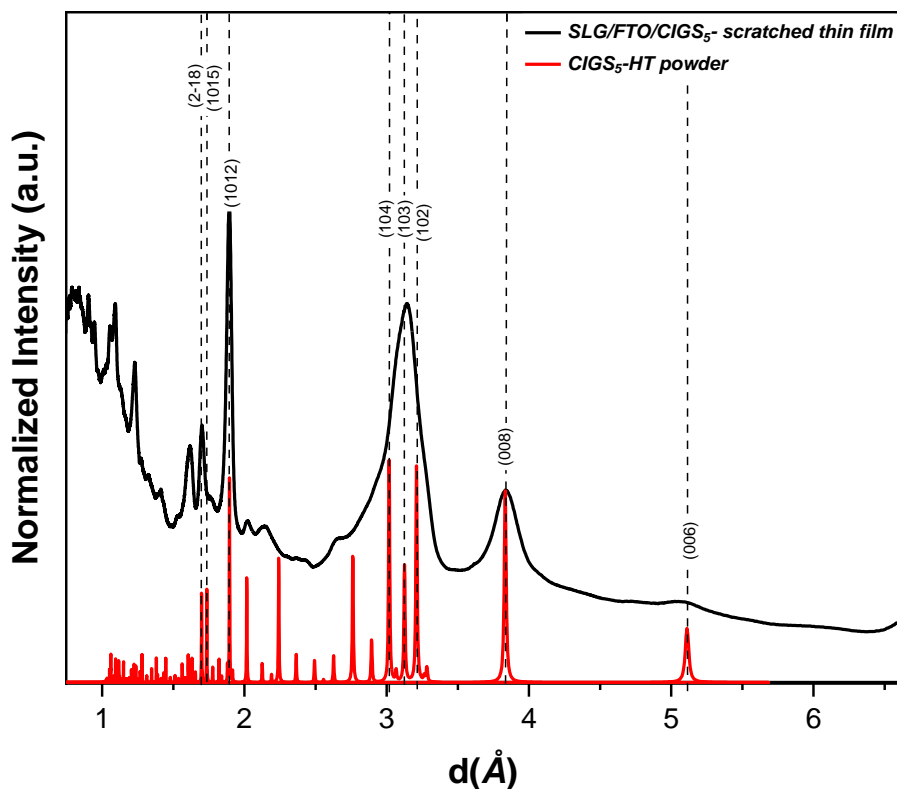


Figure 13: X-ray diffraction patterns of the powder from scratched CIGS₅ thin films on FTO covered soda lime glass compared to the reference powder of the same target composition $Cu_{0.63}In_{1.9}Ga_{1.26}S_5$.

Table 2: CIGS₅ and CIGS₆ targeted composition compared to the compositions of the phases determined with EDX.

Samples	Targeted composition	EDX composition
CIGS₆ thin film	Cu _{1,44} In _{2,77} Ga _{0,76} S ₆	1- Cu _{1,9} In ₃ Ga _{0,48} S ₆ 2- Cu _{1,2} In _{2,1} Ga _{2,8} S ₈
CIGS₅ thin film	Cu _{0,65} In _{1,75} Ga _{1,4} S ₅	Cu _{0,63} In _{1,9} Ga _{1,26} S ₅

Table 3: EDX atomic ratios of the phases determined in CIGS₅ and CIGS₆ thin films.

Atomic % ratios	Cu/S	In/S	Ga/S
CIGS₆ target	0.2	0.5	0.1
CIGS₆ deposited	0.3	0.5	0.1
	0.2	0.2	0.4
CIGS₅ target	0.1	0.4	0.3
CIGS₅ deposited	0.1	0.4	0.3

Figure 14 presents EDX mapping of the scratched thin film performed by STEM, showing clearly the homogeneous distribution of the elements Cu, In, Ga and S. Further, the stacking layers of the sample are depicted through HAADF-STEM image in Figure 15. Apparently, the lamellar structure is well viewed with the representative layers in the images.

The HAADF imaging depends on the atomic number Z (the contrast is proportional to Z²); the higher is the atomic number of the elements, the brighter they appear. Hence, the In-S layers are illustrated as the brighter lines and the Van der Waals gap is spotted as the dark lines. The measured distance between the octahedral In-S layers was found to be around 15 Å, which is comparable to the CIGS₅ specific d-spacing. This confirms once again the CIGS₅ lamellar phase synthesis as a thin film. Nevertheless, we need to highlight the risk of intergrowths and the possibility of the presence of other CIGS_n lamellar compounds, due to the gap of Van der Waals between the blocks that might impact the diffusion according to the c-axis.

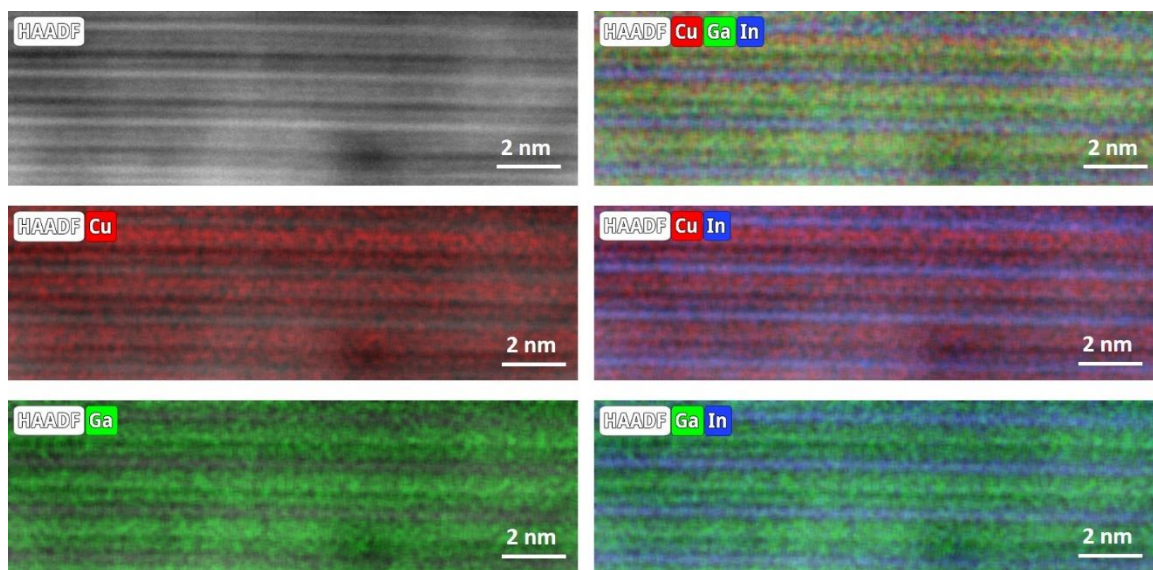


Figure 14: HAADF image and qualitative STEM-EDX mappings of Cu, In, Ga and S of the powder from scratched CIGS₅ thin film.

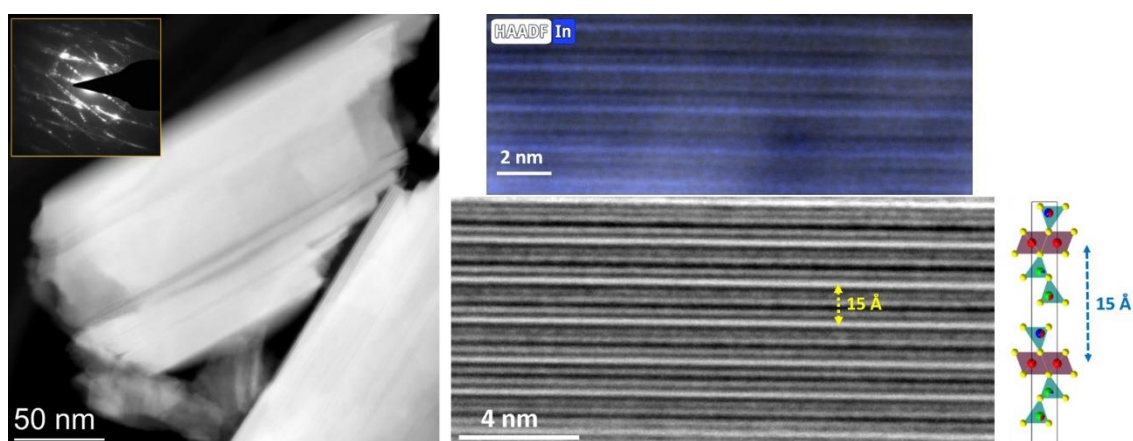


Figure 15: HAADF-STEM images of the powder from scratched CIGS₅ thin film, highlighting the stacking layers on the compound (on the left). The In-S layers are imaged as the bright lines and the van der Waals gaps as the dark lines.

The Raman spectra of CIGS₅ thin films on SLG, on SLG/Mo and on SLG/FTO, as well as the reference powder of CIGS₅ and the CuIn_{0.7}Ga_{0.3}S₂ chalcopyrite also prepared at high temperature named CIGS, are presented in Figure 16 for a comparative analysis. The CIGS spectrum is characterised by the strong signal centred at 294 cm⁻¹ that is attributed to the main A1 mode of chalcopyrite structure.^{47,48} With increasing amount of Ga within Cu(In,Ga)S₂ structure, the A1 mode value could shift from 291 cm⁻¹ to 311 cm⁻¹ for pure CuInS₂ and CuGaS₂, respectively.⁴⁷

For the lamellar compounds spectra, the dominant peak is larger than in the case of CIGS and shifted towards 340 cm⁻¹ with additional peaks at 132, 219 and 698 cm⁻¹. The digital print of the spectra of CIGS₅ thin films and the powder are in very good agreement as expected, corroborating the result obtained from XRD and STEM.

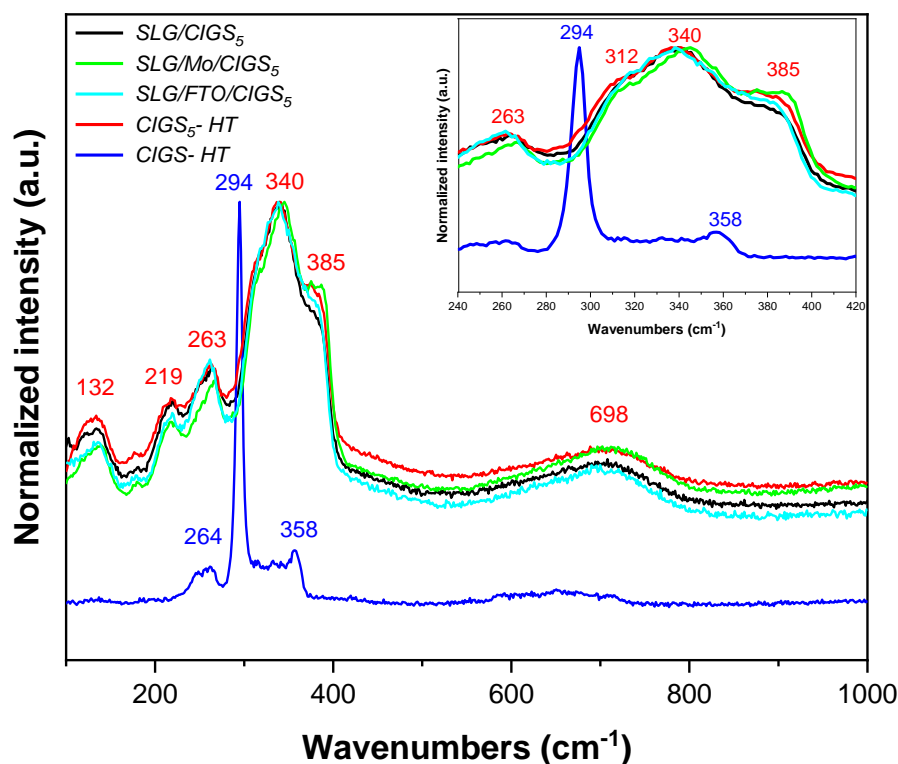


Figure 16: Raman spectra at excitation wavelength 514 nm of CIGS₅ thin films deposited on SLG, on SLG/Mo and SLG/FTO compared to the CIGS₅ reference powder and the CIGS chalcopyrite, with a zoom on the range (240 – 420 cm⁻¹) on the top.

Glow discharge optical emission spectrometry (GDOES) is another technique used to determine the homogeneity of the samples compositions within the thickness of the thin film. GDOES measurement was performed at IPVF.

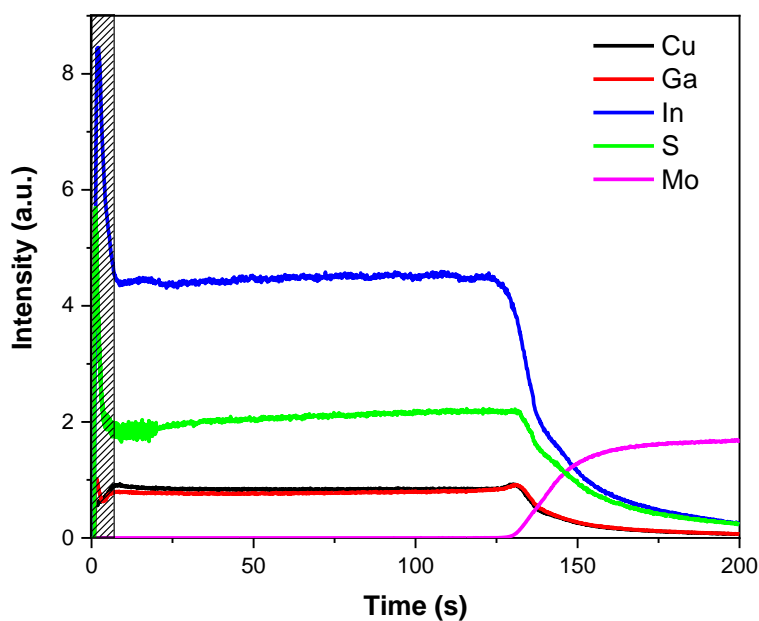


Figure 17: GDOES depth profile elementary analysis of CIGS₅ thin film deposited on Mo covered soda lime glass.

Figure 17 presents the different elements profiles performed on the CIGS₅ thin film deposited on Mo/SLG. We can observe that the concentration of the four elements Cu, In, Ga and S remains constant throughout the entire thickness of the film, right up to the interface between the CIGS₅ layer and the substrate Mo, which is determined by the sudden increase of Mo.

As a first conclusion, it was not possible to obtain a monophasic CIGS₆ thin film, although CIGS₅ has been successfully deposited. Thereby, it was decided to have a full implemented study only on the monophasic compound.

3.3. Energy diagrams and optoelectronic properties

3.3.1. Optical properties

To calculate the optical gap of the thin film, UV-visible spectroscopy was used in two different configurations: Transmittance (T) and reflection (R). The tests were carried out on the CIGS₅ sample deposited on glass for its transparency in the visible range. The experimental and fitting conditions are presented in the appendix.

The experimental results obtained from T and R, alongside the computed data using a fitting algorithm are depicted in Figure 18 a. The fitted data are then written as Fresnel coefficients⁴⁹ (n: refractive index and k: the extinction coefficient) and the resulting values after a certain number of iterations are displayed in Figure 18 b.

Figure 19a presents the absorption coefficient (α) determined by Fresnel method.⁴⁹ Using Tauc plot method,^{50,51} we can estimate the optical gap value from the extrapolation of the linear part of the plotted $(\alpha h\nu)^n$ versus $(h\nu)$ photon energy curve at $(\alpha h\nu)^n = 0$ (n=2 for direct band gap and n=1/2 for indirect band gap) (See Figures 19 b and 19 c).

The CIGS₅ thin film exhibits a direct band gap energy indicated by the linear part of the curve, which is approximated to $E_g = 2.19$ eV as presented on the Figure 19b. This value is close to that estimated from the absorption (2.04 eV) (Figure 19 a).

In addition, it yielded two optical gaps of 1.84 eV and 1.3 eV for the indirect transitions, according to the observed linear portions in the Figure 19c. Usually, Tauc plots offer a method of differentiating between the two different types of band gaps transitions. However, in the case of the compound investigated, it seems that they fall short to provide a clear conclusion on the type of permitted transition.

Nevertheless, looking to the resulted Tauc plots, we can consider that the CIGS₅ thin film displays a direct band gap with a huge density of intrinsic defects presented by the Urbach tail,^{52,53} as expected looking to their structures and to the photoluminescence measurements presented in the next section.

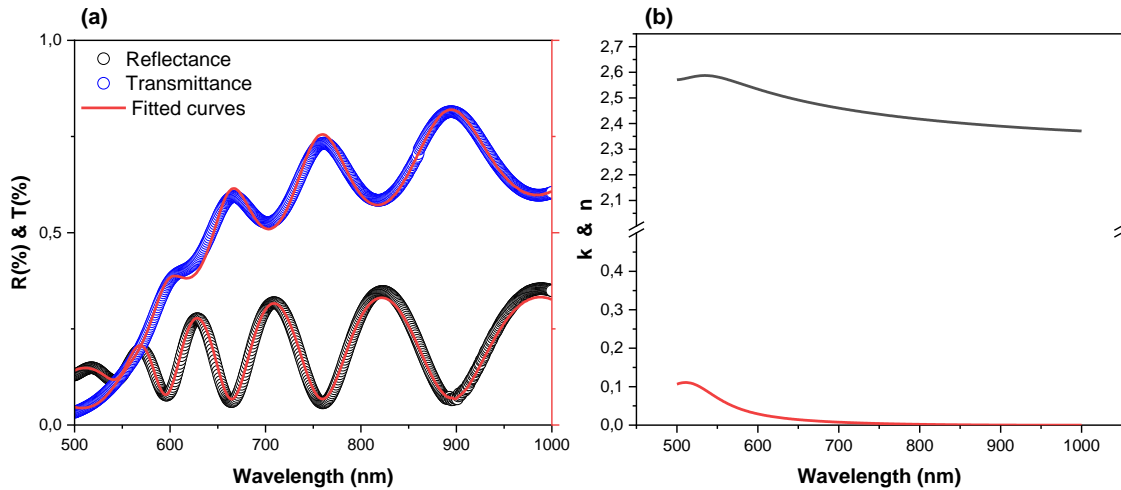


Figure 18: a) The experimental optical transmission T and the reflection R spectra of $CIGS_5/SLG$ and their fitted curves. b) The refractive index n and the extinction coefficient k computed after a certain number of iterations.

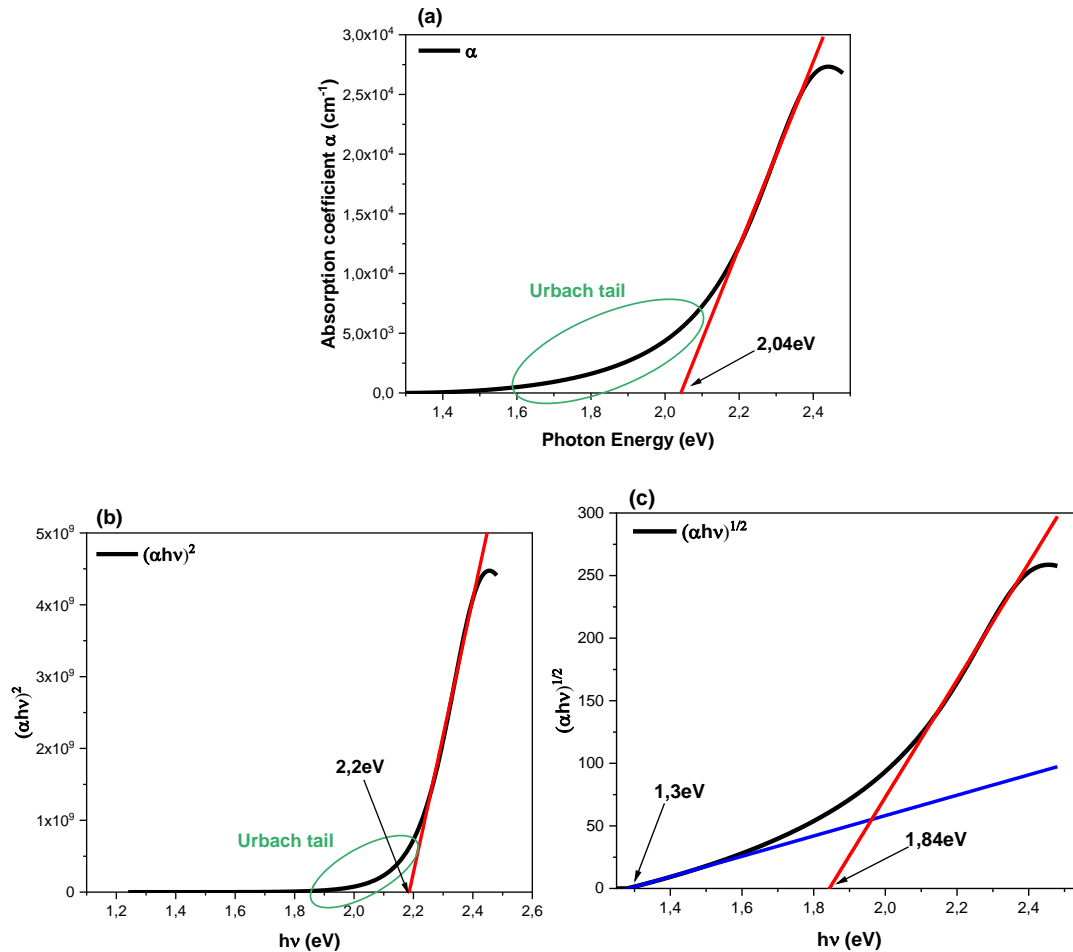


Figure 19: The $CIGS_5/SLG$ a) absorption coefficient plotted spectrum. b) Tauc plot $(\alpha hv)^2$ versus (hv) that corresponds to direct optical band gap. c) Tauc plot $(\alpha hv)^{1/2}$ versus (hv) that corresponds to indirect optical band gap. With extrapolation of the linear part to 0 indicating the obtained values.

Another method to obtain the optical gap of thin films is the external quantum efficiency EQE that will be viewed in the IV paragraph. By comparing the two techniques, it is more difficult to determine the optical gap of the thin films using the reflectance measurements than EQE due to its dependency on the layer thickness, the surface roughness of the material and the reflectance of the substrate.

According to EQE, it was found that the optical gap equal to $E_g = 2.0$ eV for CIGS_5 deposited on both substrates (SLG/Mo and SLG/FTO) which is close to the value obtained using the absorption and direct Tauc plot. The value is close to the one of the reference powder ($E_g = 1.9$ eV).

3.3.2. Photoluminescence

The photoluminescence spectra of CIGS_5 thin film and CIGS chalcopyrite conducted at room temperature are presented in Figures 20 a and 20 b, respectively.

The CIGS_5 thin film PL spectrum shows a broad emission centred at much lower energy (1.57 eV) than the corresponding optical band gaps ($E_g = 2.0$ eV obtained either from EQE and reflectance diffuse). Unlike CIGS chalcopyrite, which displays a main narrow emission indicated at 1.7 eV close to the measured optical gap, with another low broad peak observed at lower energy due to in-gap defects states.⁴⁷

The lamellar compound spectrum exhibits an intense wide shifted band as shown in the Figure 20 a. This could be attributed to the presence of deep defects in the gap that are much more present in the lamellar compounds than for chalcopyrite. Since, as explained earlier, the lamellar compounds demonstrate a structure full of defects as intrinsic cationic vacancies and mixed occupancy (Cu, Ga and In) on tetrahedral sites,⁴⁶ leading to the formation of several defects as V_{Cu}' , Cu_{Ga}'' or $\text{In}_{\text{Cu}}^{\circ\circ}$ (V_{Cu}^{1-} , $\text{Cu}_{\text{Ga}}^{2-}$ or $\text{In}_{\text{Cu}}^{2+}$).^{17,46}

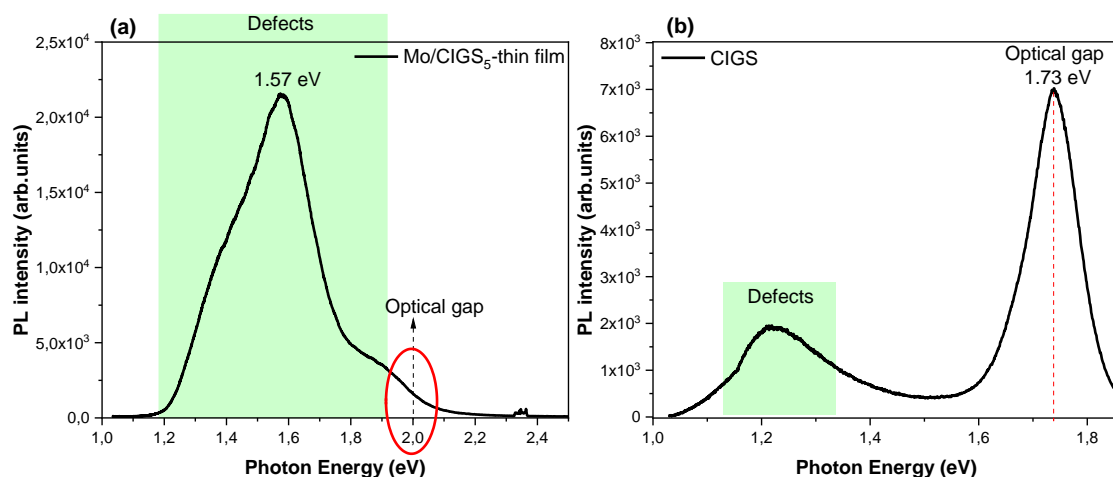


Figure 20: Photoluminescence spectra at 488 nm of (a) thin film of CIGS_5 lamellar compound (b) CIGS chalcopyrite.

3.3.3. Electrochemical measurements

Similarly as in the previous chapter for powders, (photo)electrochemical measurements were conducted on CIGS_5 thin films deposited on two different substrates SLG/Mo and SLG/FTO, in order to further investigate the thin films semiconductors type and the bands configurations compared to the results obtained on the powder.

To do this, we performed electrochemical impedance spectroscopy (EIS) measurements at pH of 5.84 and 5.88 for SLG/Mo/ CIGS_5 and SLG/FTO/ CIGS_5 , respectively, under the same conditions as the powders measurements.

As presented in Figure 21, the tests were carried out with a three electrodes setup, using Ag/AgCl as reference electrode, platinum as counter electrode, CIGS_5 thin film as working electrode and LiClO_4 (0.5 M aqueous) as electrolyte.

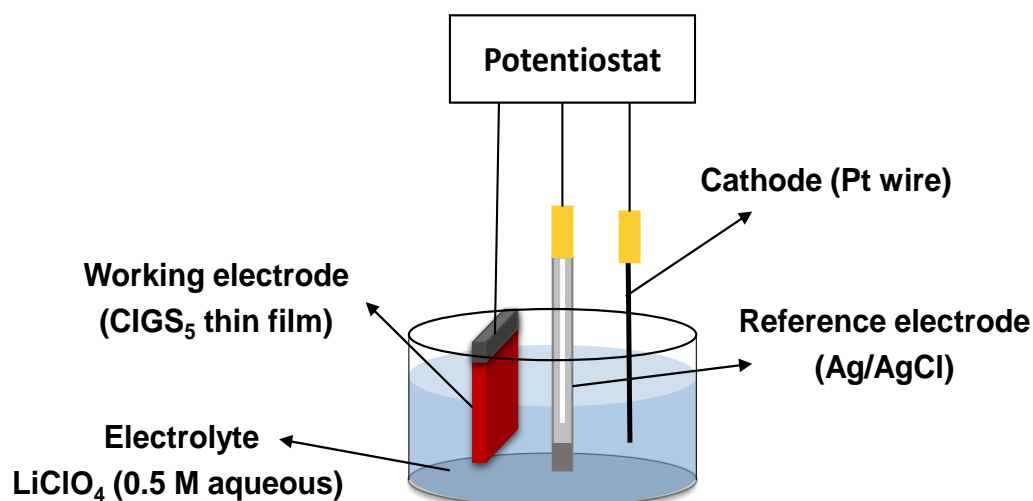


Figure 21: Schematic representation of the three electrodes cells used during the electrochemical and photo-electrochemical measurements on CIGS_5 thin films.

The EIS data were measured under dark on a potential range of 0.2 V to -0.8 V versus Ag/AgCl reference electrode, at each applied voltage a range of frequencies is recorded between 100 Hz and 100 kHz. The curves have been analysed at high frequencies (1-10 kHz), to avoid surface and diffusion phenomena (Figure 22).

Figure 22 presents the Nyquist diagrams obtained at -0.3 V of CIGS_5 thin films, which will be fitted by a simplified Randles circuit with neglecting Warburg, in order to determine the capacitance C to plot the Mott-Schottky plots (Figure 24). From the representation of C^{-2} as a function of the applied potentials, we can conclude the nature of the semiconductor from the slope sign and the flat band potential, as explained in chapter 2.

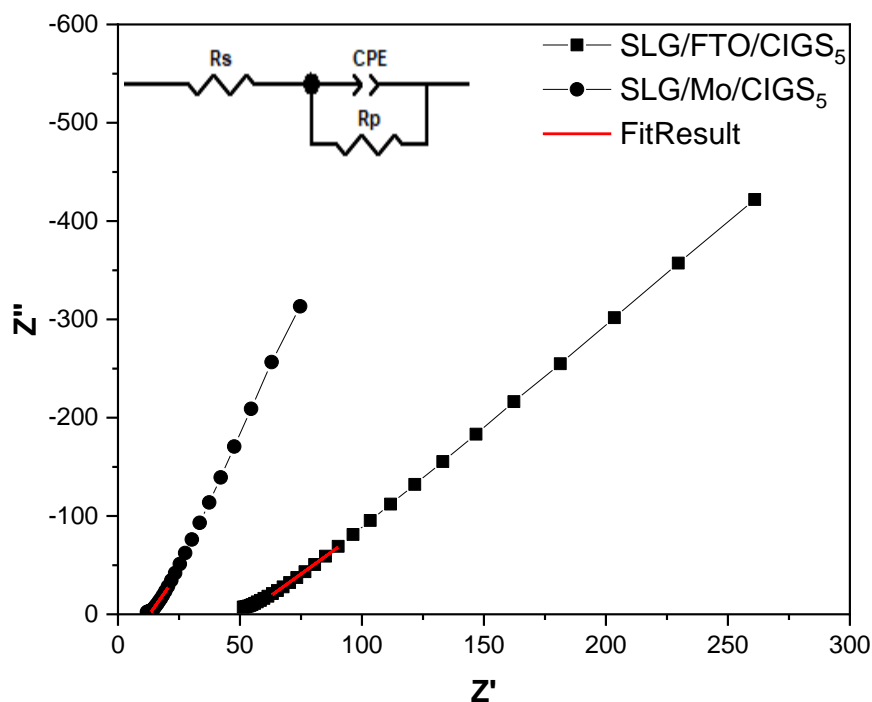


Figure 22: Nyquist curves at -0.3 V obtained from electrochemical impedance spectroscopy with the applied equivalent circuit for fitting at high frequencies (1-10 kHz) (red line) of CIGS₅ thin films deposited on SLG/Mo and on SLG/FTO.

Beforehand, cyclic voltammetry (CV) tests were carried out to define the stable potential range for electrochemical impedance spectroscopy tests, and to detect any redox reactions that might occur during the experiments.

Figure 23 presents the obtained CV curves between (-0.4 V – 0.4V) and (-0.5 V – 0.5V) of CIGS₅ thin films deposited on Mo and FTO, respectively, showing no specific sign of a reduction-oxidation reaction over the chosen range.

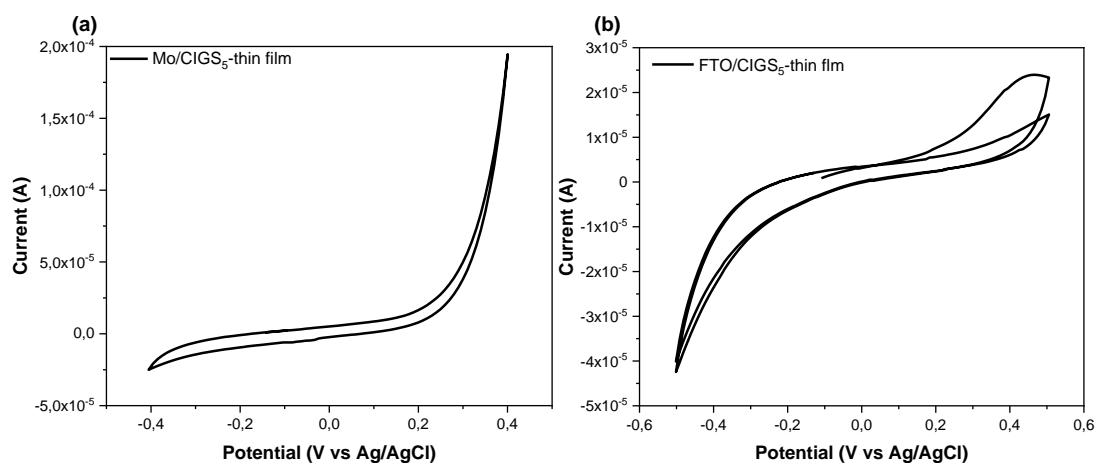


Figure 23: Cyclic voltammetry curve at a scan rate of 5 mV/s of CIGS₅ thin films deposited on a) SLG/Mo and b) on SLG/FTO.

The Mott-Schottky plots of the SLG/Mo/CIGS₅ and SLG/FTO/CIGS₅ thin films demonstrate an n-type semiconductor behaviour according to the positive slopes observed in Figure 24. Moreover, the flat band (V_{fb}) is extrapolated at zero from the ordered slope and the carrier density (N) is inversely proportional to the slope. The calculated flat band potentials were equal to ($V_{fb} = -0.61$ V/Ag/AgCl and $V_{fb} = -0.39$ V/Ag/AgCl for SLG/Mo/CIGS₅ and SLG/FTO/CIGS₅, respectively) and donor densities estimated to be around ($N_D = \sim 10^{11}$ cm⁻³ and $N_D = \sim 10^{11}$ cm⁻³ for SLG/Mo/CIGS₅ and SLG/FTO/CIGS₅, respectively).

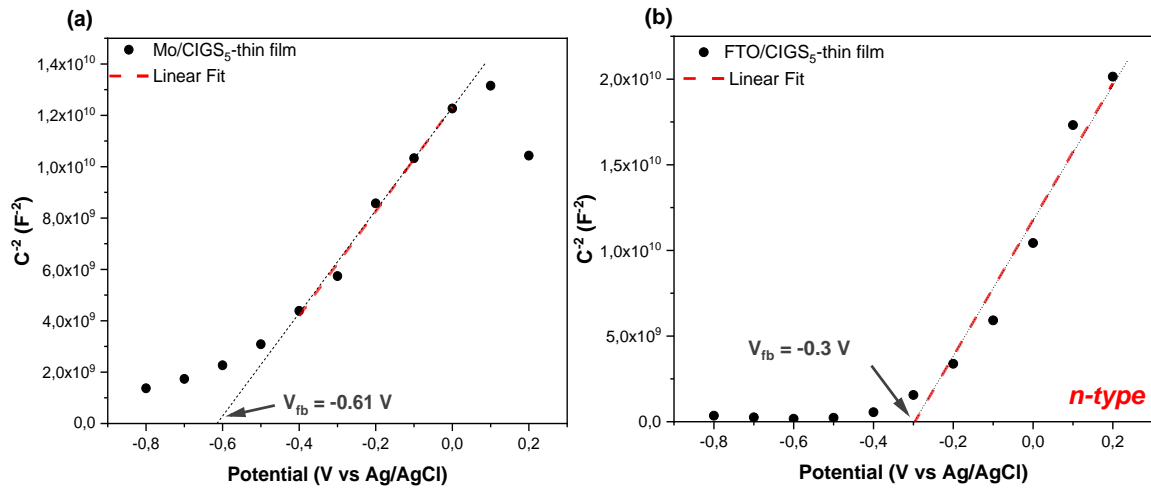


Figure 24: Mott Schottky plots of a) SLG/Mo/CIGS₅ and b) SLG/FTO/CIGS₅ thin films with the estimated flat band potentials from the linear fit of the slopes.

These measurements have allowed us to place the Fermi level of each material following the two equations (1) and (2), which will serve to propose the energy diagrams of the samples.

$$V_{fb} \text{ vs RHE} = V_{fb} \text{ vs Ag/AgCl} + 0.059 \text{ pH} + V(\text{Ag/AgCl}) \quad (1)$$

$$E_f \text{ (eV)} = -4.5 - V_{fb} \text{ vs RHE} \quad (2)$$

In the previous chapter, the energy diagrams were determined by combining three techniques: the electrochemical measurements with spectroscopic measurements, namely X-ray photoelectron spectroscopy (XPS) and diffuse reflectance. However, since we carried the XPS tests only on powders and not on thin films, we established the energy diagrams using the calculation based on Mulliken electronegativity and the band gap (explained in chapter 2). This method showed results equivalent to the experimental ones.

Indeed, Table 4 summarises the characteristics of energy diagrams of the thin film compared to the powder. The calculated Fermi levels on an absolute scale were approximated to ($E_f = -4.4$ eV and $E_f = -4.6$ eV for SLG/Mo/CIGS₅ and SLG/FTO/CIGS₅, respectively), these values are in good agreement with that estimated with the CIGS₅ powder ($E_f = -4.4$ eV).

It is checked that band structure energy values of the thin films are close to the previously obtained with CIGS₅ powder. This is an important point as it already confirms that it is reproduced (Figure 25). Furthermore, the obtained charge carrier densities ($N_D \sim 10^{11} \text{ cm}^{-3}$) are extremely low, which indicates the intrinsic property of the prepared thin films.

Table 4: Characteristics of optical gaps, the maximum of the valence band vs the Fermi level position and the estimated Fermi levels using the formulas (4) and (5) of the CIGS₅ thin films and powder.

Samples	Donor density N_D (cm^{-3})	VBM (eV)	CBM (eV)	Fermi level E_f (eV)	Work function (eV)
CIGS ₅ powder	$\sim 10^{17}$	-5.4	-3.5	-4.4	---
SLG/Mo/CIGS ₅ thin film	$\sim 10^{11}$	-5.7	-3.7	-4.4	4.3
SLG/FTO/CIGS ₅ thin film	$\sim 10^{11}$	-5.7	-3.7	-4.6	4.7

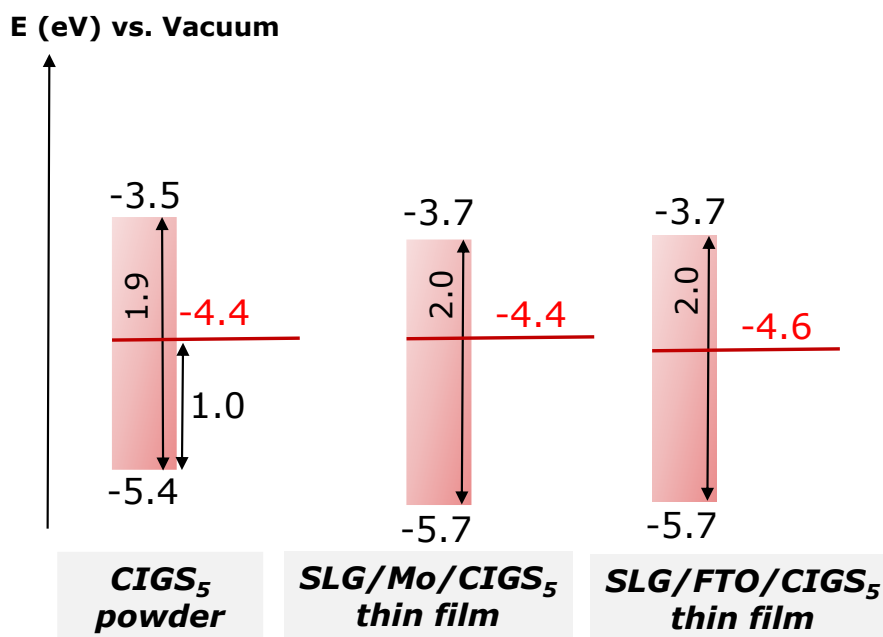


Figure 25: Schematic representation of the energy bands on absolute scale with respect of the vacuum of the CIGS₅ thin films compared to the reference CIGS₅ powder.

3.3.4. Kelvin probe force microscopy measurements

Additionally, kelvin probe force microscopy (KPFM) measurements were carried out on the thin films in order to establish the results; KPFM provides information of the work function that is assimilated to the Fermi level. The experimental conditions are described in the appendix.

The measured results are 4.3 eV and 4.7 eV for SLG/Mo/CIGS₅ and SLG/FTO/CIGS₅ respectively. These outcomes are consistent with the Fermi energies calculated on an absolute scale with respect to the vacuum level ($E_f = -4.4$ eV and $E_f = -4.6$ eV for SLG/Mo/CIGS₅ and SLG/FTO/CIGS₅ respectively) which corroborate the results obtained previously from EIS and confirm the energy diagrams positioning.

3.3.5. Photo-electrochemical measurements

In order to verify the nature of the majority charge carriers of the thin films, photoelectrochemical measurements were performed under the same conditions as those used for EIS presented in Figure 21, under chopped illumination using MI-LED illuminator (Edmund Optics).

Figure 26 presents the chronopotentiometry curves of the CIGS₅ thin films deposited on SLG/Mo and on SLG/FTO substrates. The samples reveal as expected from the EIS analyses an identical behaviour (n-type semiconductor) as the reference powder. The n nature is indicated with the open circuit potential increase under illumination.

Besides, the values of the lifetime charge carriers were determined through exponential decay fitting of the OCP curve after stopping the illumination, as shown in the Figure 27. As previously explained in chapter 2, τ_1 presents the time to reach equilibrium state of the majority carriers and τ_2 is the lifetime linked to recombination process. The corresponding lifetime charges were estimated to ($\tau_1 = 0.07$ s, $\tau_2 = 0.56$ s) and ($\tau_1 = 0.06$ s, $\tau_2 = 0.24$ s) for SLG/Mo/CIGS₅ and SLG/FTO/CIGS₅, respectively.

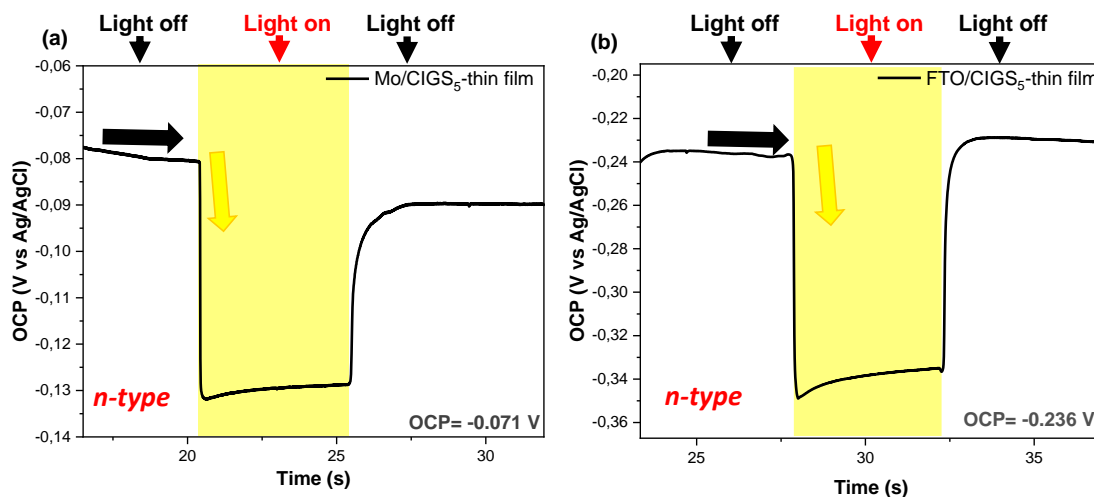


Figure 26: Chronopotentiometry curves under illumination (indicated by the yellow region) and under dark of thin films: a) SLG/Mo/CIGS₅. b) SLG/FTO/CIGS₅.

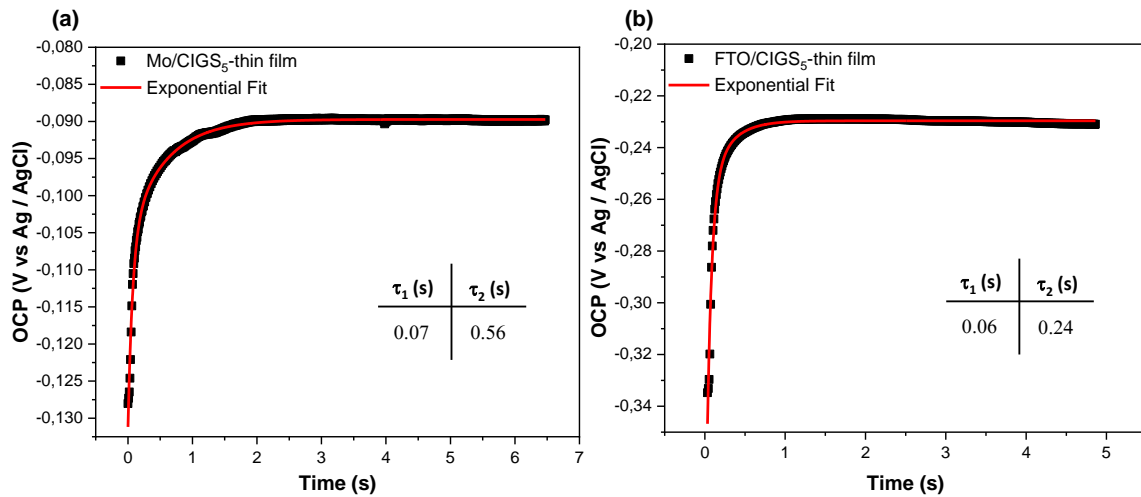


Figure 27: Open circuit curves under dark fitted using the exponentials in order to determine the charge carrier lifetime for of thin films: a) SLG/Mo/CIGS₅. b) SLG/FTO/CIGS₅.

The chopped-light IV (current potential) curve of the thin films are given in the Figure 28. Interestingly, it shows both types of semiconductors. An n-type pattern demonstrated with an increase of oxidation current and then switched to p-type nature with the increase of the reduction current at $E_i = -0.01$ V and $E_i = -0.2$ V for SLG/Mo/CIGS₅ and SLG/FTO/CIGS₅ respectively. Yet, the n-type pattern is more favoured for both samples as the oxidation photocurrent detected is much more important than the reduction photocurrent.

This unusual behaviour was not observed in the case of CIGS₅ powder (that was recognized an n-type semiconductor according to the IV measurement); this can be due several reasons:

- The CIGS₅ thin film composition detected by STEM-EDX ($\text{Cu}_{0.63}\text{Ga}_{1.26}\text{In}_{1.9}\text{S}_5$) was found close to the CIGS₅ powder ($\text{Cu}_{0.65}\text{In}_{1.75}\text{Ga}_{1.4}\text{S}_5$); however, it is not exactly similar. The mixed occupancy of tetrahedral sites by the elements Cu, In and Ga allows the chemical composition tuning, which can influence the semiconductor type.
- The risk of intergrowths on the composition can occur, and trace of the other lamellar compounds could be distinguished, considering the Van der Waals gap between the blocks, which might affects the diffusion according the axis c.

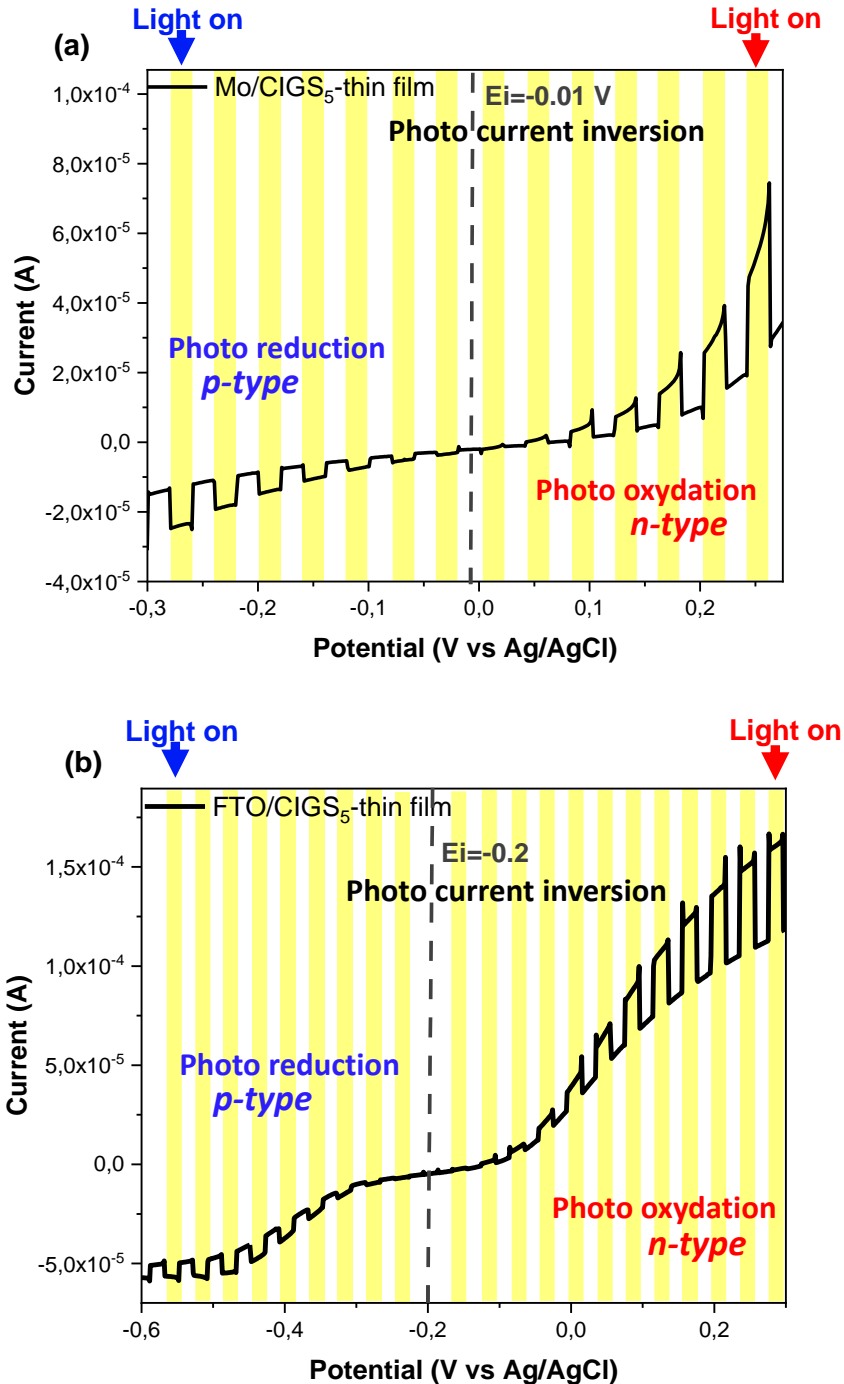


Figure 28: Current-potential curve measured under chopped simulated sunlight with the yellow part corresponds to the illumination time for CIGS₅ thin films: a) SLG/Mo/CIGS₅. b) SLG/FTO/CIGS₅.

In the next section of the chapter, we will explore the performances of the solar cell devices based on CIGS₅ absorber. For this purpose, two architectures were evaluated: the classical CIGS architecture in order to compare with CIGS chalcopyrite performances and the second one is an n-i-p architecture considering our absorbers as intrinsic material.

3.4. Device assemblies

3.4.1. Classical CIGS architecture

The first proposed architecture is the common classical CIGS assembly described previously (Figure 5), and it was conducted to compare with the well-studied CIGS chalcopyrite.

For the tests, the co-evaporated thin films were completed by the deposition of the buffer layer, window layer and finally the metallic grids. As shown in the Figure 29, several devices with different back contacts (either Mo, FTO or ITO) and different buffer layers (CdS or ZnOS) were examined.

Different growth techniques used to prepare the final device are those mentioned previously. The back contacts used in this PhD are either Mo deposited on SLG using DC sputtering, or the commercial FTO and ITO substrates. The absorber is then co-evaporated as explained above. This deposition is followed by a buffer layer of either CdS or Zn(O,S) deposited by a chemical bath in an open reactor under standard conditions.^{15,54} Finally the double layer ZnO:i/ZnO:Al are RF-sputtered before using the electron beam evaporator to deposit the grids. The final device samples are pictured on the Figure 30.

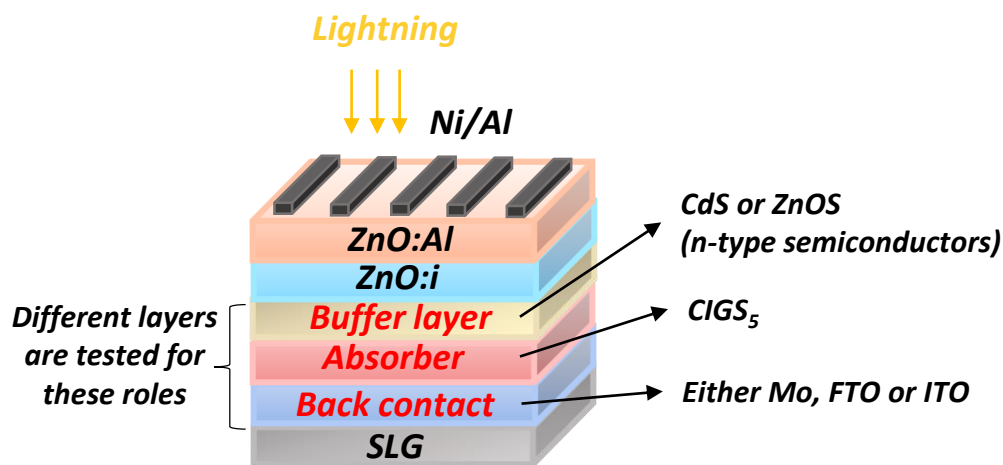


Figure 29: Schematic representation of the prepared device, with the different layers used.

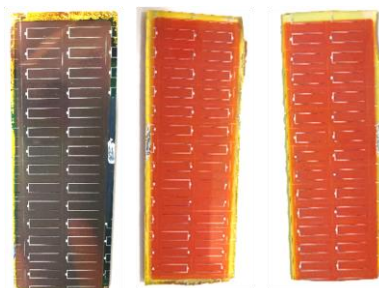


Figure 30: Picture of the final device samples on different substrates.

The JV curves in dark and under illumination (AM1.5G, 1000 W/m² at 25°C). of the different fabricated devices as well as their photovoltaic parameters and external quantum efficiency are presented on the Figures 31-32 and the Table 5.

Our first observation is that the JV curves difference under dark and simulated sunlight prove that the CIGS₅ lamellar compound present a photovoltaic effect with the maximum conversion efficiency obtained corresponds to the device with Mo as a back contact and Zn(O,S) as a buffer layer instead of CdS (Figure 31 and Table 5). However, the obtained photovoltaic parameters are still very low similarly to EQE. The shape of the EQE curve reveals several serious losses within the fabricated cell, that are related either to the absorption limitations in the buffer layer and the window layer carriers recombination or to the losses caused by the carriers recombination at the interfaces (Figure 32a). In addition, band gap energy of the material was also determined by the EQE² as a function of energy (Figure 32b).

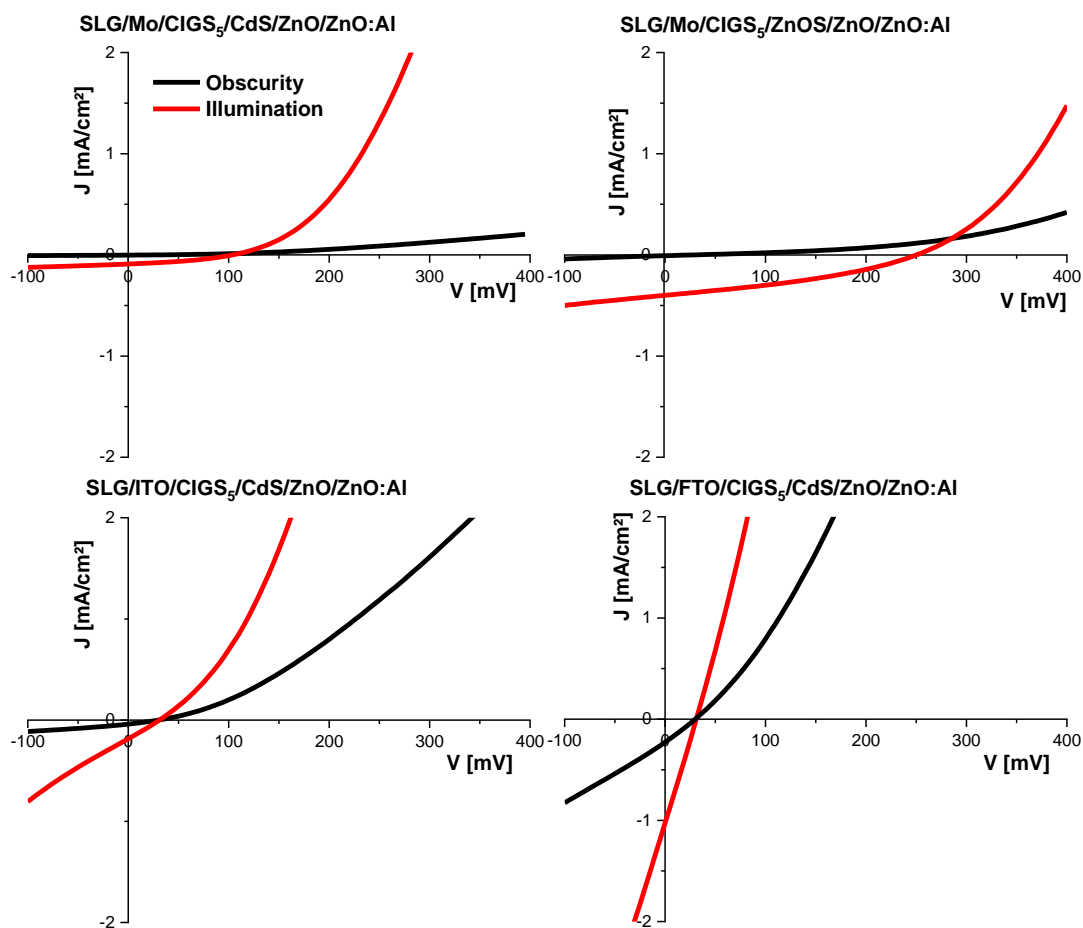


Figure 31: current voltage (JV) curves measured in dark and under illumination of the solar cells prepared from the different investigated films

Table 5: The obtained photovoltaics parameters of the solar cells investigated.

Device	V_{oc} [mV]	J_{sc} [mA/cm ²]	FF [%]	η [%]
SLG/Mo/CIGS ₅ /ZnOS/ZnO/ZnO:Al	250	0.4	36.1	0.04
SLG/Mo/CIGS ₅ /CdS/ZnO/ZnO:Al	104	0.1	36.7	0.003
SLG/FTO/CIGS ₅ /CdS/ZnO/ZnO:Al	31	1.0	25.5	0.008
SLG/ITO/CIGS ₅ /CdS/ZnO/ZnO:Al	31	0.2	26.4	0.001

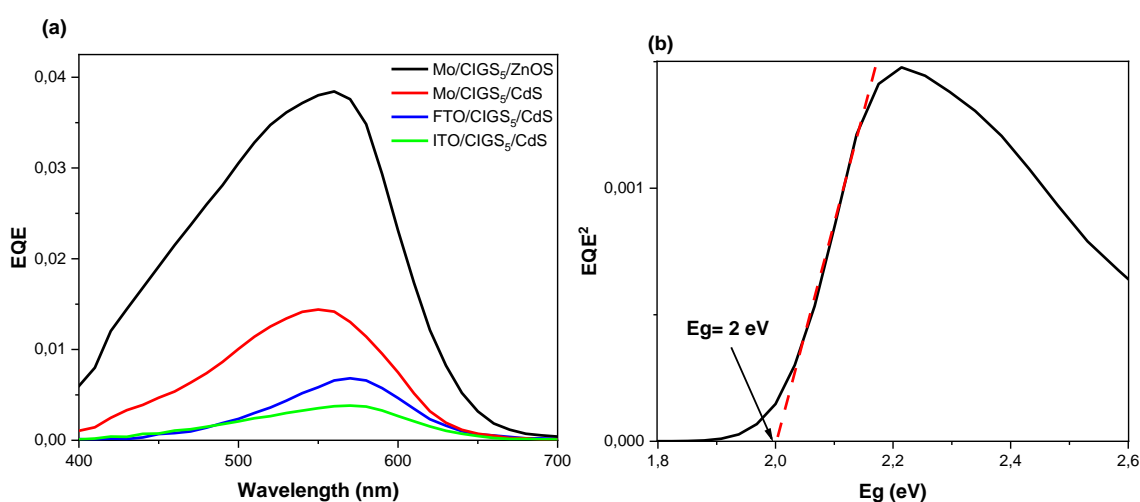


Figure 32: (a) External quantum efficiency (EQE) curves of the prepared devices. (b) Band gap determination from external quantum efficiency (EQE) curve of the CIGS₅ absorber.

The limitations might be explained due to several reasons:

1- The bands alignments:

As presented in Figure 33, the energy diagrams obtained for CIGS₅ absorbers are not well positioned relative to the buffer layers CdS and ZnOS,^{55,56} unlike the CIGS chalcopyrite. Therefore, the potential of charge carriers at the interface is very limited, resulting a very low V_{oc} , as demonstrated by current voltage curves.

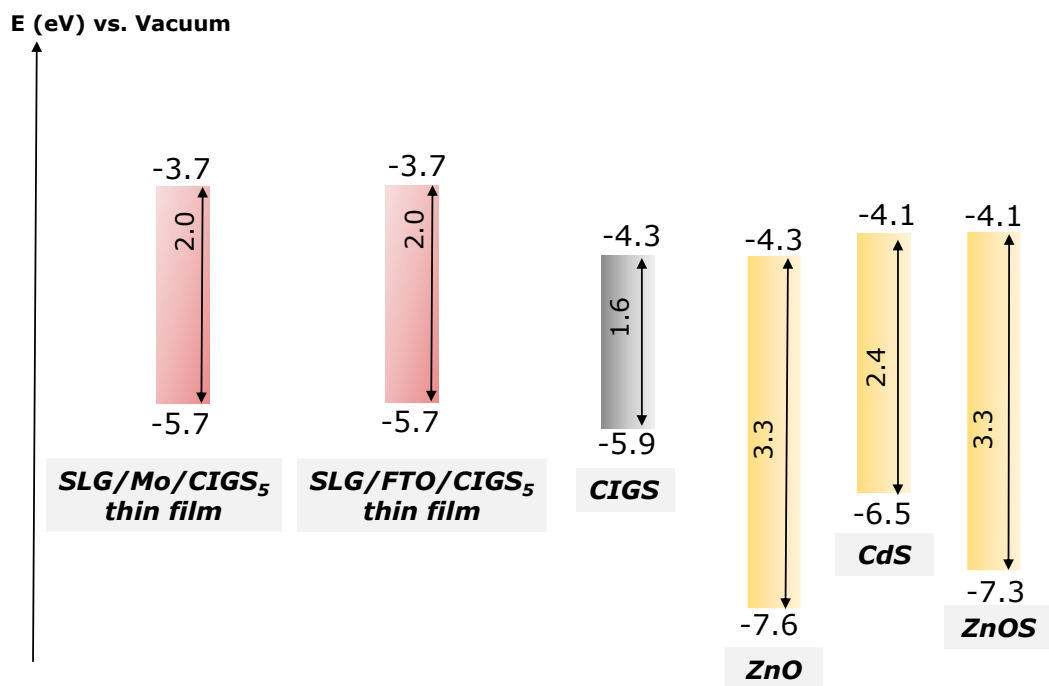


Figure 33: Schematic energy diagrams of CIGS₅ thin films and CIGS compound compared to those of main buffer layers used in CIGS-based solar cells.

2- The type of the buffer layer:

Both buffer layers chosen in the classical architecture are n-type semiconductors in order to create a p-n junction with the CIGS absorber that is well known as a p-type semiconductor; this is not the case with the lamellar compounds that show an n-type semiconductor. Instead of fabricating a p-n junction, in fact it was an n-n junction, since CIGS₅ presents mostly the n-type semiconductor. This might cause a non-efficient electron-hole pairs separation.

3- The morphology:

SEM images of the absorbers are illustrated in Figure 34. It shows the cross sections of the deposited thin films on different substrates: glass, Mo-covered SLG and FTO-covered SLG. Looking at the grains in the images of the thin films, as a first observation the microstructure of the grains is different from a sample to another. In the case of the SLG substrate, the layers are deposited on different orientations unlike for the film deposited on Mo, it is clear that the majority of the layers are oriented vertically. However, the cross sections of the film deposited on the FTO/SLG show a dense packed morphology. This might be due to the lamellas that are misaligned. From the morphology obtained of the thin films, we can conclude that the orientation of the layers needs to be controlled to better optimize the solar cell.

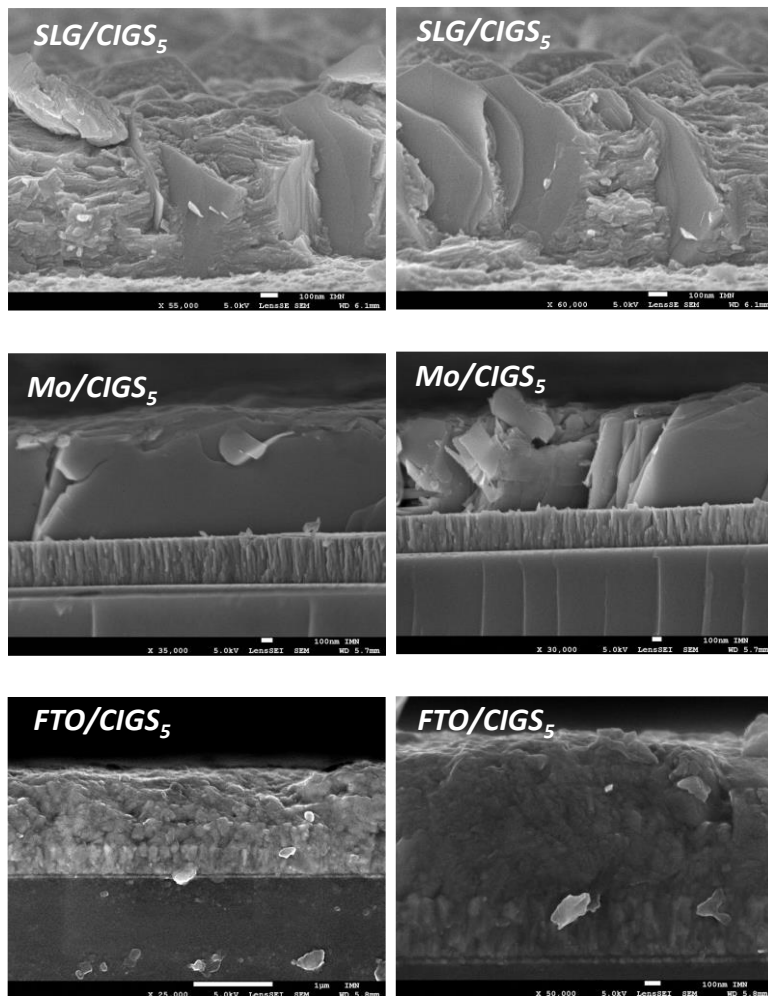


Figure 34: SEM images of cross sections for investigated $CIGS_5$ thin films with different substrates.

4- $CIGS_5$ lamellar compound defects:

As explained previously, $CIGS_n$ lamellar compounds structure contain different defects, mixed occupancies and vacancies in the tetrahedral sites. Clearly confirmed from the photoluminescence analyses (Figure 20). The amount of defects in the $CIGS_5$ lamellar thin film is much more than for the CIGS chalcopyrite. This increases carrier recombination and lowers their mobility, which affects the cell efficiency.

These first attempts show that there is still a serious need to optimize the interfaces.

As a next step, two cell architectures will be tested:

- The first one is a total different architecture. Taking into account the IV photoelectrochemical measurements of $CIGS_5$ thin film presented previously in Figure 28 that proved the ambipolarity behaviour of this compound. Following this path, the n-i-p architecture will be tested considering $CIGS_5$ absorber as an intrinsic compound.

- The second one is keeping the classical architecture while using a p-type buffer layer in order to make a p-n junction, since CIGS₅ displays in majority the n nature.

3.4.2. n-i-p architecture

For n-i-p architecture, 2,21,7,71-tetrakis-(N,N-di-4-methoxyphenylamino)-9,91-spirobifluorene (Spiro-OMeTAD) was chosen to be used as the n-type semiconductor. Generally, it is an organic molecule (Figure 35) well used and explored in the perovskite solar cells providing high performances.^{57,58} In this architecture, the layer of the perovskite is covered by the spiro-OMeTAD that acts as the holes transporter layer. However, pristine spiro-OMeTAD present a limited hole mobility and a low conductivity resulting low photovoltaic efficiencies.⁵⁹ Therefore, dopants and additives are required to solve this issue and improve the device performance. Commonly, the most widely used p-type dopants are lithium bis(trifluoromethane) sulfonamide (Li-TFSI), 4-tert-butylpyridine (TBP).⁵⁸

Li-TFSI helps on achieving high hole mobility through the hole transporting material, in detail, adding this mixture into a thin film will affects the position of the Fermi level that shifts towards the valence band.^{60,61} Whereas TBP improves the conductivity and the morphology by allowing structural rearranging of the spiro-OMeTAD molecules from an amorphous structure to a better crystallized one during the oxidation process in the hole-transporting layer.⁶²

Tris(2-(1H-pyrazol-1-yl)-4-tert-butylpyridine)-cobalt(III)tris(bis(trifluoromethylsulfonyl)imide) (Co(III) complex) is another effective dopant that shown promising results for adjusting the spiro-OMeTAD conductivity and change its charge-transport properties in solar cells.⁶³

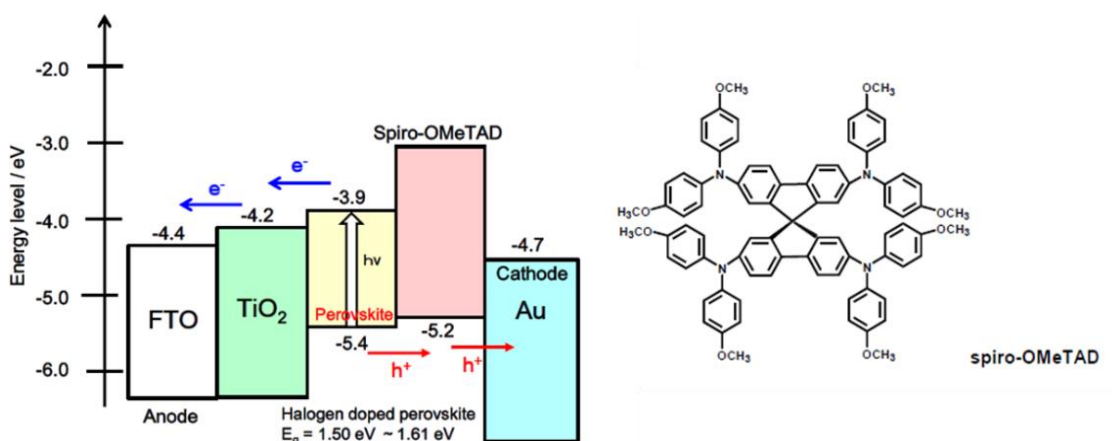


Figure 35: Energy diagrams of perovskite solar cell with crystal structure of spiro-OMeTAD. Figure from Suzuki et al.⁵⁷

The objective then, is to replace the perovskite layer in this architecture by CIGS_5 as shown in the Figure 36. For these tests, the co-evaporated CIGS_5 thin films on FTO and ITO coated glass substrates are completed by a layer of spiro-OMeTAD by spin coating, which is finalized by sputtered gold through a mask using physical vapour deposition PVD. Figure 37 presents the energy diagrams of the layers mechanism in the n-i-p architecture.

The spiro-OMeTAD solution (70 mM dissolved in chlorobenzene) was spin coated at 4000 rpm for 20s. This solution was doped with Li-TFSI, TBP and the Co(III) complex (FK209) with a molar ratio of 0.5, 3.3 and 0.03 respectively. This deposition was made by Amelle Rebai at IPVF laboratory.

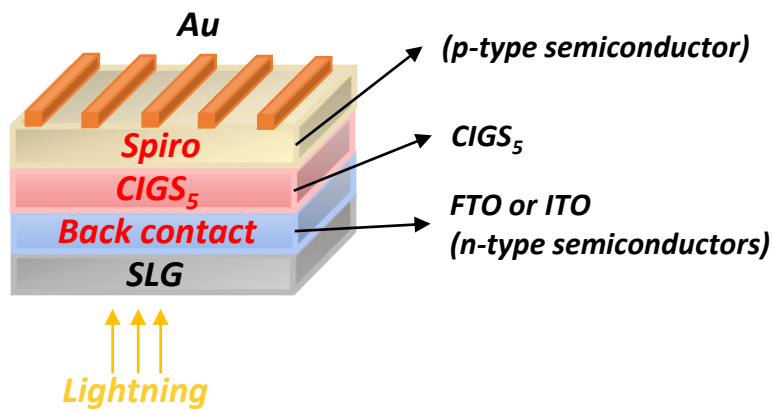


Figure 36: Schematic representation of the n-i-p prepared device, with the different layers used.

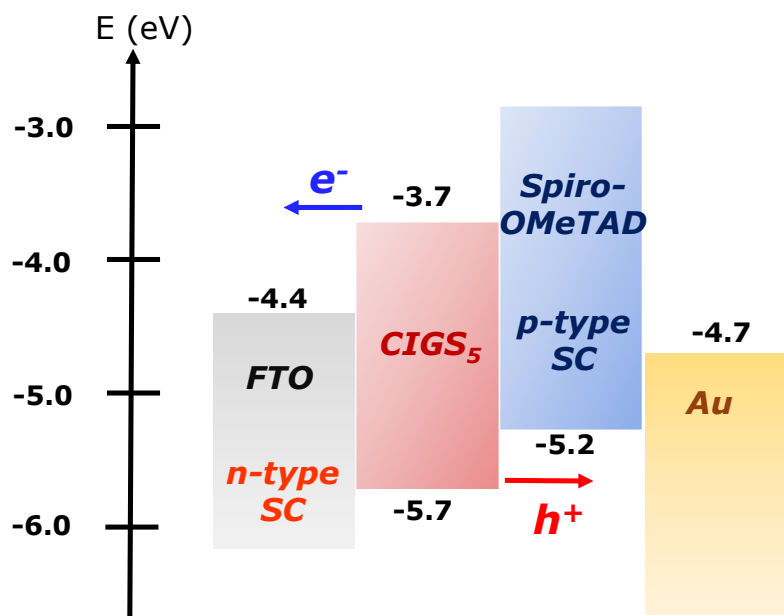


Figure 37: Energy diagrams of the prepared n-i-p architecture device at no contact.

However, according to the IV results obtained in the Figure 38 and the corresponding IV parameters in Table 6, the photovoltaics parameters of n-i-p architecture remains similar to the one of the classical ones. This confirms that the mechanism of transporting and transferring both holes and electrons did not take place, which could be due to the defects contribution, corroborating that CIGS₅ thin film is not adapted for PV.

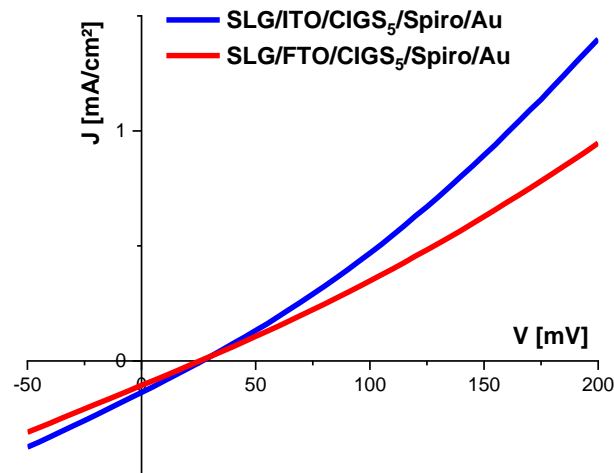


Figure 38: current voltage (JV) curves measured under illumination of the SLG/ITO/CIGS₅/Spiro-OMeTAD/Au and SLG/FTO/CIGS₅/Spiro-OMeTAD/Au.

Table 6: The obtained photovoltaics parameters of the solar cells investigated.

Device	V_{oc} [mV]	J_{sc} [mA/cm ²]	FF [%]	η [%]
SLG/FTO/CIGS ₅ /Spiro-OMeTAD/Au	26	0.17	25	0.002
SLG/ITO/CIGS ₅ /Spiro-OMeTAD/Au	27	0.17	25	0.001

Additionally, another assembly was fabricated, maintaining the classic architecture. However, this time we tested a p-type buffer layer instead of the usual n-type, by replacing the buffer layers used previously (CdS and ZnOS) by spiro-OMeTAD, as shown in Figure 39.

Figure 40 and Table 7 present the JV curves measured under illumination alongside the obtained photovoltaic parameters of the two fabricated devices with different back contact (SLG/Mo/CIGS₅/Spiro-OMeTAD/ZnO/ZnO:Al and SLG/ITO/CIGS₅/Spiro-OMeTAD/ZnO/ZnO:Al). The device with Mo as the back contact showed a higher V_{oc} than the ITO, however the photovoltaic parameters are still very low and comparable to those obtained previously (conventional and n-i-p architectures). This confirms once again that CIGS₅ thin film is not adapted for PV applications.

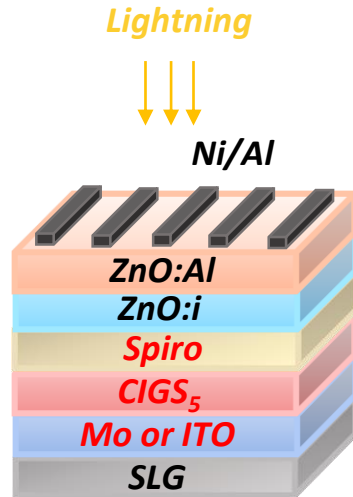


Figure 39: Schematic representation of the assembly prepared using spiro-OMeTAD as a buffer layer, with the different layers used.

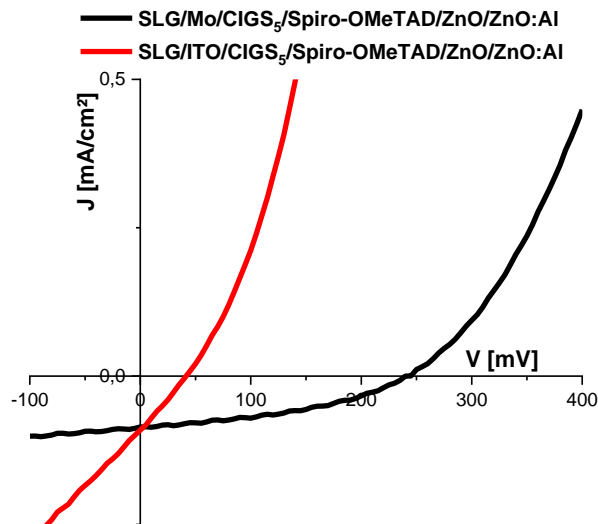


Figure 40: current voltage (JV) curves measured under illumination of the SLG/Mo/CIGS5/Spiro-OMeTAD/ZnO/ZnO:Al and SLG/ITO/CIGS5/Spiro-OMeTAD/ZnO/ZnO:Al.

Table 7: The obtained photovoltaics parameters of the solar cells investigated.

Device	V_{oc} [mV]	J_{sc} [mA/cm ²]	FF [%]	η [%]
SLG/Mo/CIGS ₅ /Spiro-OMeTAD/ZnO/ZnO:Al	241	0.09	41	0.008
SLG/ITO/CIGS ₅ /Spiro-OMeTAD/ZnO/ZnO:Al	41	0.09	26	0.001

4. Conclusions

One of the objectives of the thesis is to develop CIGS_n thin films. Thus, thin films of CIGS_5 and CIGS_6 on different substrates were synthesized using co-evaporation process. The study was based essentially on CIGS_5 thin film, since it was the only lamellar compound successfully obtained as a monophasic thin film.

Moreover, an investigation was performed using electrochemical measurements. As a result, optoelectronic properties and energy diagram with the different energy levels were determined. The established energy diagram of the CIGS_5 thin film is close to the one obtained with the reference high temperature powder, with similar Fermi level position, also confirmed from the KPFM analyses. Finally, two different solar cells configurations are tested, attaining very low efficiencies.

The intrinsic properties of the CIGS_n thin films demonstrated that they are not adapted to photovoltaic application. This is due to their high resistivity and the complex structure of the lamellar compounds that is full of detrimental defects. In addition, when comparing the properties of the CIGS_5 lamellar thin film with the requirements needed for an efficient CIGS cell, reported in section 2.2, several shortcomings become apparent. Although CIGS_5 thin film exhibits a high absorption and a suitable band gap, it does not meet all the other important requirements. Specifically, the carriers density of the absorber is extremely low, the absorber is not a p-type semiconductor and its band gap presented a direct transition with an elevated density of intrinsic defects.

During this PhD, the orientation of the deposited layers was not controlled. Therefore, to optimize the solar cell, we need to look for a substrate with lattice parameters close to CIGS_n lamellar compounds in order to provide a better controlled growth of the absorber and improve its microstructure, resulting in better charge carriers transport and increasing cells V_{oc} .

In addition, the quality of the dispositive could be improved by changing the buffer layer with a suitable one that allows a better conduction and valance bands alignment at the interface, resulting better photovoltaic parameters.

Appendix chapter 3

X-ray diffraction

The thin films XRD (X-ray diffraction) measurements were performed using a Bruker D8 diffractometer in a Bragg-Brentano θ - 2θ configuration. To perform a test on thin films, a slide of the layer will be cut, in order to fit on the sample holder and then will be stick to it with a modelling clay to have a flat surface.

Thin films might have a preferential orientation due to the substrate used; this is why another method was used in order to avoid this issue. In this case, the powder scratched from the thin film was analysed by INEL diffractometer with a Debye Scherrer geometry equipped with a 120° curve-Position Sensitive Detector, using a capillary of a diameter of 0.1 mm or 0.2 mm. This capillary will carry our sample that will be in a rotation during the measurements.

Powder X-ray diffraction patterns were also recorded on a XtaLAB Synergy-S Rigaku equipped with a Hypix 6000 hybrid photon detector and a micro source tube with Mo anode ($\lambda=0.707 \text{ \AA}$) to improve the signal to noise ratio. The samples are also prepared in capillary form. Finally, the patterns are presented and compared in dhkl, due to the different wavelengths of the X-ray sources of the different diffractometers used during this PhD.

Scanning transmission electron microscopy

Using Scanning transmission electron microscopy (STEM) technique, we can detect the chemical composition of compounds at the nanometric scale and also investigate its homogeneity using the energy dispersive X-ray spectroscopy (EDX) equipped on STEM. Furthermore, we can also check the stacking layers of our compounds by HAADF High Angle annular dark field imaging.

In a transmission electron microscope (TEM), a beam of electrons, produced by an electron gun and then accelerated by a potential difference (100-300kV), is directed at a very thin sample using magnetic lenses called condensers (see Figure 41a). The parallel electron beam, illuminating the entire area to observe, then passes through the sample, modifying it according to its crystalline structure and chemical composition. A first enlarged image of the sample (image mode), and the corresponding electron diffraction pattern (diffraction mode), are formed by the objective lens. The chosen operating mode (image or diffraction) is determined by the current of the intermediate lenses.

The other lenses of the microscope are used to progressively enlarge the image or diffraction pattern formed by the objective. To observe a sub-nanometer detail in the image formed, a magnification of the order of a million is required. Since the image is formed by lenses (indirect image), its resolution is strongly limited by optical aberrations.

The STEM variant (Figure 41b) used in this work focuses the beam on a very small area, of which the size will determine the image resolution. The electron probe is then systematically deviated over the entire area to be observed. As it passes through the sample, some electrons are deflected. These electrons are detected by sensors and used to construct direct images with atomic resolution. The basic configuration consists of an annular detector that captures electrons that have undergone elastic shocks, and a central detector that collects those that have lost energy.

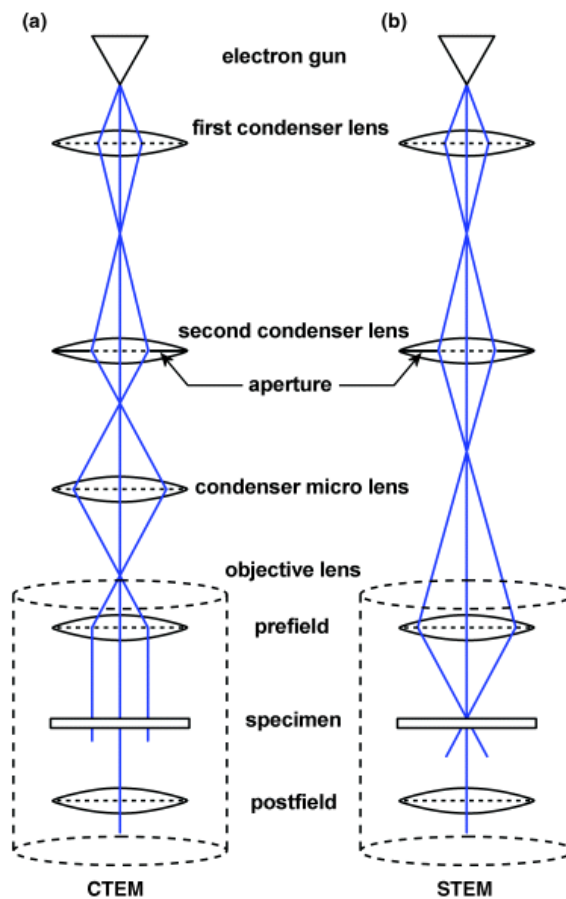


Figure 41: Simplified schematic of principle of (a) TEM and (b) the scanning mode STEM.⁶⁴

The annular detector can be extended to collect electrons deviated at very high angles by atomic nuclei (Rutherford scattering). The contrast of the image obtained depends on the atomic number (Z) of the scattering atoms. This wide-angle mode, known as HAADF (high angle annular dark field) or "Z-contrast", can therefore be used to directly visualize atomic columns (Figure 42).

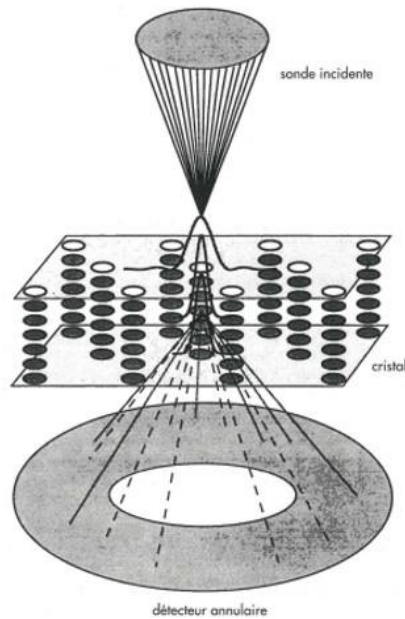


Figure 42: Principle of HAADF contrast formation.⁶⁵

On the other hand, as in a TEM, the incident beam ionizes the atoms, which emit X-rays on de-excitation; the X-rays emitted will have a different wavelength for each atom. We can therefore get a precise idea of the chemical composition of the sample by using an energy analyser to sort X-ray photons according to their energy (EDX spectroscopy). Detectors are incorporated into the microscope column around the sample.

One of the advantages of STEM is that we can easily select a small area (a few angstroms) for chemical analysis. We can therefore map the chemical composition of the sample. Chemical mapping images (chemical imaging) are constructed by selecting only the X-ray photons corresponding to the chemical element we wish to analyse.

Our experiments were carried out using a Themis-Z scanning transmission electron microscope (S/TEM) (Thermo Fisher Scientific) in TEM and STEM mode, with the following experimental conditions: at 300 kV accelerating voltage, 21 mrad convergence angle and 63-200 mrad collection angles. The powder scratched from the thin films was crushed in ethanol, and then deposited on a carbon sheet with holes that is placed on a copper grid for the tests. We use Velox software to analyse the HAADF images and the EDX analyses results (mapping and zone EDX spectra). Figure 43 presents a screenshot of the corresponding main window of the software.

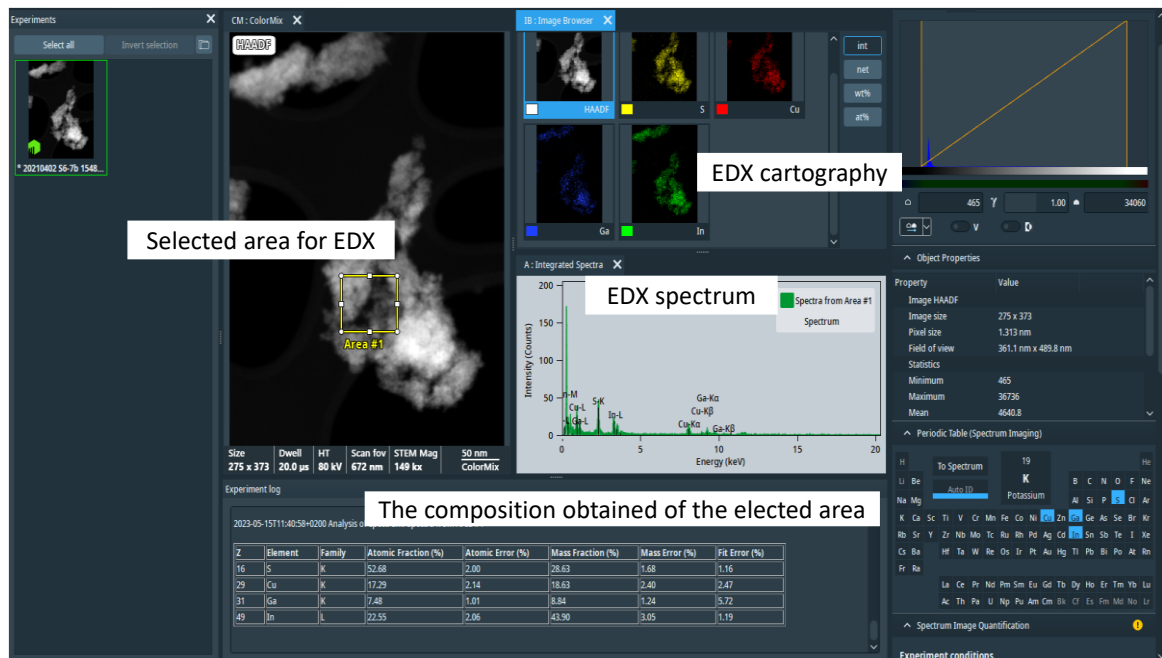


Figure 43: Main window of the Velox software used to analyse HAADF images and EDX analysis results.

Raman spectroscopy

Raman vibrational spectroscopy measurements have been carried out with a Renishaw InVia spectrometer combined with a microscope in a backward scattering geometry using an excitation wavelength of 514 nm (green line) of an argon ion laser at room temperature. The spectra were collected between 20 and 1400 cm^{-1} wavenumber range under the conditions: an objective of x50, a laser power about 5%, with 12-scan accumulation and an exposure time of 10s. The spectra of the thin films and the powders were characterized at the same conditions in order to compare between them.

Glow discharge optical emission spectrometry GDOES

As a complement measurement of the compositional techniques performed. Glow discharge optical emission spectrometry GDOES technique allow us to analyse the elementary profile of thin films on both surface and through its depth revealing the different compositions along the layers. A measurement that occurs under argon under low pressure. When a discharge is created between the anode and the sample (which acts in this test as a cathode) a plasma will be generated. Then atoms will be removed from the surface of the thin film and then projected into the plasma, in where they get activated. Once they return to their stable state, they emit a radiation that is analysed by a detector.

Reflectance diffuse

To calculate the optical gap of the thin film, UV-visible-NIR spectroscopy was used in two different configurations: Transmittance and reflection modes, in the spectral range between 500 and 1200 nm. The tests were carried out on the sample CIGS₅ deposited on glass for its transparency in the visible range.

Using the collected data of the reflection and transmittance spectra, the absorption coefficient can be approximated using the following equation (3)⁶⁶⁻⁶⁸

$$\alpha = \frac{1}{d} \times \ln \left(\frac{(1 - R)^2}{T} \right) \quad (3)$$

where R is the reflection, T is the transmittance and d is the thickness of the thin film.

The absorption coefficient can be determined also by the Fresnel method,⁴⁹ which involves writing R and T already obtained as Fresnel coefficients. First, a fitting algorithm is required in order to reduce the Root Mean Square (RMS) error between the experimental and the computed data. The fitted data depend on the complex refractive indices N of both the thin film and the substrate (N=n+ik with n refractive index and k the extinction coefficient) and their thicknesses at each applied λ wavelength, with subtracting the SLG substrate input from the equation.⁴⁹

The absorption coefficient could be calculated following the corresponding formula (4)

$$\alpha = 4\pi k/\lambda \quad (4)$$

According the Tauc^{50,51} plot method we can determine the optical gap (E_g) of the thin film semiconductor materials, which is related to the absorption coefficient as shown in the equation (5)

$$(\alpha h\nu)^n = A(h\nu - E_g) \quad (5)$$

where h is the Planck constant, ν is the incident photon frequency, A is a constant that depends on the mobility probability in the material and the exponent n is a value that depends on the nature of the band gap; for direct allowed transition semiconductors n=2 while for indirect allowed transition semiconductors it equals to n=1/2.

Finally, we can estimate the optical gap value from the extrapolation of the linear part of the plotted $(\alpha h\nu)^n$ versus (h ν) photon energy curve at $(\alpha h\nu)^n = 0$.

Kelvin probe force microscopy

Kelvin probe force microscopy (KPFM), a derived technique from Atomic force microscopy AFM, was used. It is a method to characterize the electronic properties of the metal and the semiconductors materials and exactly the work function.

The work function for a metal is the minimal energy that is supplied to an electron located at the Fermi level, in order to pull it out from the metal surface and bring it to the vacuum level (the vacuum level is the energy of an electron at rest outside the solid).⁶⁹

As shown in Figure 44, we can also define the work function for a semiconductor as the difference between the vacuum level (E_{vac}) and the Fermi energy (E_F) (equation 6). But, with defining another parameter χ the electron affinity that presents the energy provided to an electron from the minimum conduction band to be removed from the semiconductor.^{69,70}

$$\Phi_{semiconductor} = E_{vac} - E_F \quad (6)$$

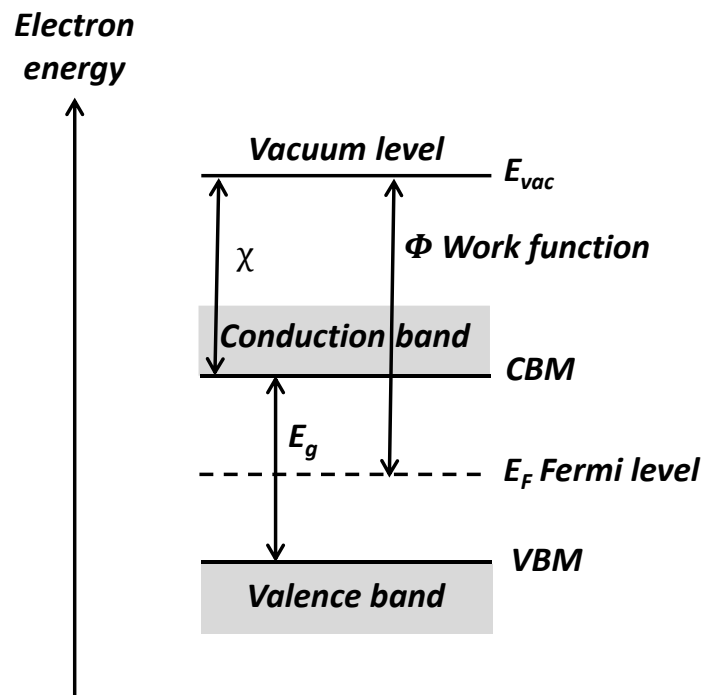


Figure 44: Schematic representation of the energy diagram of a semiconductor.

KPFM provide the potential difference between the probe tip and the sample surface known by CPD (contact potential difference). The tip and the sample are two conductors of different nature not in contact and characterized by two different work functions Φ_t and Φ_s respectively.

When the tip is brought into contact with the surface, a charge balance is created and an alignment of the Fermi levels will take place, then the contact potential between the two materials will manifest as an electrostatic force following the equation (7)

$$V_{CPD} = \frac{\Phi_t - \Phi_s}{|e|} \quad (7)$$

with e is the elementary charge = 1.602×10^{-19} C.

After measuring the VCPD from KPFM and according to the equation 8, it is possible to calculate the work function if the tip's work function value is defined.

$$\Phi_s = \Phi_t - eV_{CPD} \quad (8)$$

Using a reference sample with a well-known work function, we can determine the work function of the tip. In this work, HOPG (Highly Oriented Pyrolytic Graphite) ($\Phi_{HOPG} = 4.6$ eV) was used for calibration. In this case, Φ_t is given as (equation 9):

$$\Phi_t = \Phi_{HOPG} + eV_{CPD(HOPG)} \quad (9)$$

Finally, the work function of our sample will be calculated as followed (equation 10):

$$\Phi_s = \Phi_{HOPG} + eV_{CPD(HOPG)} - eV_{CPD(s)} \quad (10)$$

Device characterization

Current-voltage JV

To characterize the operation of the prepared CIGS₅ devices and determine their photovoltaic conversion efficiency, current-voltage JV measurements were carried in the standard conditions: a sunlight simulator (1000 W/m² light power under AM1.5G spectrum) at 25°C.

Figure 45 shows an example of the JV curve of a CIGS thin-film cell. The main photovoltaic parameters deduced from this technique are:

- V_{oc} : the open circuit voltage is the highest voltage that the solar cell is capable of producing and it happens at current equal to zero.
- J_{sc} : the short circuit current is the current flows through the cell when there is no voltage crossing the cell.
- FF %: the fill factor is the ratio of the maximum power to the power obtained by J_{oc} and V_{sc} , and is given by (equation 11):

$$FF = \frac{V_{max} \cdot J_{max}}{V_{oc} \cdot J_{sc}} = \frac{P_{max}}{V_{oc} \cdot J_{sc}} \quad (11)$$

- η : the conversion efficiency which is defined as the incident power light transformed to electricity following (equation 12):

$$\eta = \frac{P_{delivered}}{P_{incident}} = \frac{P_{max}}{P_{incident}} = \frac{FF \cdot V_{oc} \cdot J_{sc}}{P_{incident}} \quad (12)$$

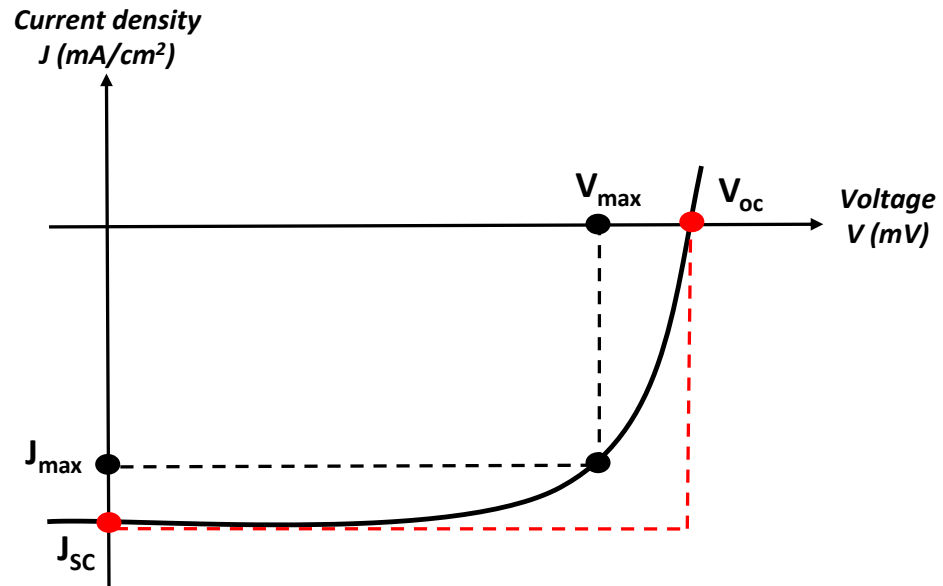


Figure 45: Characteristic JV (current density versus voltage) curve of a solar cell under illumination.

External quantum efficiency

Besides, external quantum efficiency EQE is a measurement that complete the IV characterizations of a photovoltaic device. It measures the ratio between the collected electrons by the solar cell external circuit and the incident photons flow as a function of wavelength (equation 13).

$$EQE = \frac{\text{number of the collected electrons}}{\text{number of the incident photons}} \quad (13)$$

EQE analysis allows us to determine the capacity of carrier generation of the solar cell and the different limitations and losses in the current as presented in the Figure 46.

Beyond the value of the absorber's gap, the quantum efficiency is zero because the photons are no longer absorbed by the cell. Therefore, it is possible to determine the electronic gap of the absorber from EQE results and exactly by linear extrapolation at low energy of the curve EQE^2 as a function of energy.

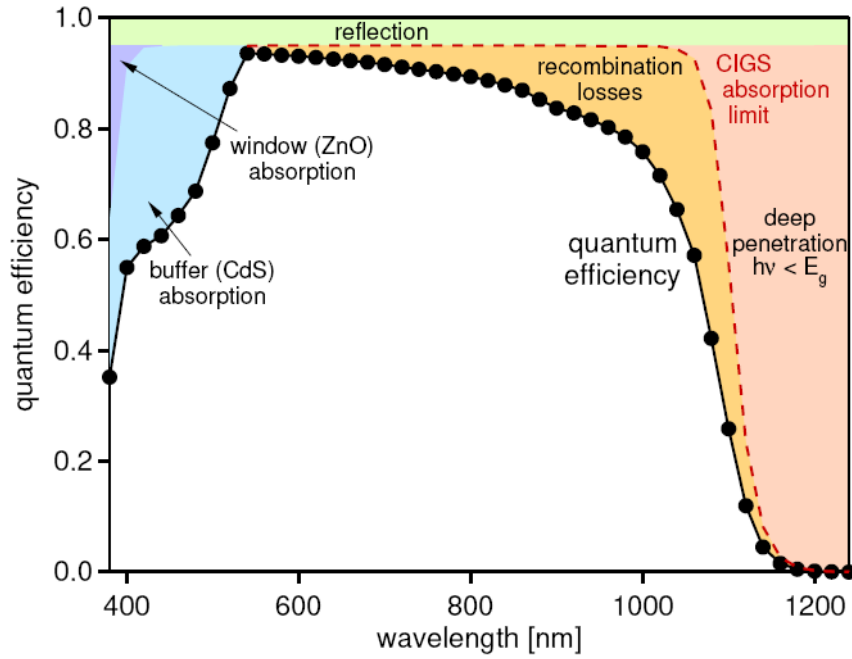


Figure 46: Quantum efficiency (EQE) spectrum of CIGS solar cell with the characteristics of different layers.⁷¹

Imagery

The morphology of the thin films deposited on different substrates were observed using a scanning electron microscope SEM (JEOL 7600F) through cross sections of the samples. To perform the tests, we cut a section of the layer on a small size adjusted to the metal pad, then will be glued by silver lacquer on the pad and finally carbonized before the analysis.

References

- (1) Marques Lameirinhas, R. A.; Torres, J. P. N.; de Melo Cunha, J. P. A Photovoltaic Technology Review: History, Fundamentals and Applications. *Energies* **2022**, *15* (5), 1823. <https://doi.org/10.3390/en15051823>.
- (2) Green, M. A. Photovoltaic Principles. *Phys. E Low-Dimens. Syst. Nanostructures* **2002**, *14* (1), 11–17. [https://doi.org/10.1016/S1386-9477\(02\)00354-5](https://doi.org/10.1016/S1386-9477(02)00354-5).
- (3) Goetzberger, A.; Luther, J.; Willeke, G. Solar Cells: Past, Present, Future. *Sol. Energy Mater. Sol. Cells* **2002**, *74* (1), 1–11. [https://doi.org/10.1016/S0927-0248\(02\)00042-9](https://doi.org/10.1016/S0927-0248(02)00042-9).
- (4) Green, M. A. Silicon Photovoltaic Modules: A Brief History of the First 50 Years. *Prog. Photovolt. Res. Appl.* **2005**, *13* (5), 447–455. <https://doi.org/10.1002/pip.612>.
- (5) *Reference Air Mass 1.5 Spectra*. <https://www.nrel.gov/grid/solar-resource/spectra-am1.5.html> (accessed 2023-04-05).
- (6) Shockley, W.; Queisser, H. J. Detailed Balance Limit of Efficiency of P-n Junction Solar Cells. *J. Appl. Phys.* **2004**, *32* (3), 510–519. <https://doi.org/10.1063/1.1736034>.
- (7) Thomere, A. Absorbeurs Chalcogénures à Grand Gap $\sim 1,7$ EV Pour La Réalisation de Cellules Solaires En Couches Minces. These de doctorat, Nantes, 2020. <https://www.theses.fr/2020NANT4001> (accessed 2023-06-07).
- (8) Rivalland, A. Elaboration et Caractérisation de Cellules Solaires Photovoltaïques Tandem CuGaSe₂ / Silicium Cristallin : Vers Une Approche Monolithique à Deux Terminaux. These de doctorat, Nantes, 2020. <https://theses.fr/2020NANT4065> (accessed 2023-06-28).
- (9) Sinha, S.; Nandi, D. K.; Pawar, P. S.; Kim, S.-H.; Heo, J. A Review on Atomic Layer Deposited Buffer Layers for Cu(In,Ga)Se₂ (CIGS) Thin Film Solar Cells: Past, Present, and Future. *Sol. Energy* **2020**, *209*, 515–537. <https://doi.org/10.1016/j.solener.2020.09.022>.
- (10) *Best Research-Cell Efficiency Chart*. <https://www.nrel.gov/pv/cell-efficiency.html> (accessed 2023-01-27).
- (11) Ramanujam, J.; Singh, U. P. Copper Indium Gallium Selenide Based Solar Cells – a Review. *Energy Environ. Sci.* **2017**, *10* (6), 1306–1319. <https://doi.org/10.1039/C7EE00826K>.
- (12) Nakamura, M.; Yamaguchi, K.; Kimoto, Y.; Yasaki, Y.; Kato, T.; Sugimoto, H. Cd-Free Cu(In,Ga)(Se,S)₂ Thin-Film Solar Cell With Record Efficiency of 23.35%. *IEEE J. Photovolt.* **2019**, *9* (6), 1863–1867. <https://doi.org/10.1109/JPHOTOV.2019.2937218>.
- (13) Jackson, P.; Wuerz, R.; Hariskos, D.; Lotter, E.; Witte, W.; Powalla, M. Effects of Heavy Alkali Elements in Cu(In,Ga)Se₂ Solar Cells with Efficiencies up to 22.6%. *Phys. Status Solidi RRL – Rapid Res. Lett.* **2016**, *10* (8), 583–586. <https://doi.org/10.1002/pssr.201600199>.
- (14) Hiroi, H.; Iwata, Y.; Adachi, S.; Sugimoto, H.; Yamada, A. New World-Record Efficiency for Pure-Sulfide Cu(In,Ga)S₂ Thin-Film Solar Cell With Cd-Free Buffer Layer via KCN-Free Process. *IEEE J. Photovolt.* **2016**, *6* (3), 760–763. <https://doi.org/10.1109/JPHOTOV.2016.2537540>.
- (15) Barreau, N.; Bertin, E.; Crossay, A.; Durand, O.; Arzel, L.; Harel, S.; Lepetit, T.; Assmann, L.; Gautron, E.; Lincot, D. Investigation of Co-Evaporated Polycrystalline

- Cu(In,Ga)S₂ Thin Film Yielding 16.0 % Efficiency Solar Cell. *EPJ Photovolt.* **2022**, *13*, 17. <https://doi.org/10.1051/epjpv/2022014>.
- (16) Bär, M.; Bohne, W.; Röhrich, J.; Strub, E.; Lindner, S.; Lux-Steiner, M. C.; Fischer, Ch.-H.; Niesen, T. P.; Karg, F. Determination of the Band Gap Depth Profile of the Ternary Cu(In_{1-X}Ga_X)(S_{1-Y}Se_{1-Y})₂ Chalcopyrite from Its Composition Gradient. *J. Appl. Phys.* **2004**, *96* (7), 3857–3860. <https://doi.org/10.1063/1.1786340>.
- (17) Shukla, S.; Sood, M.; Adeleye, D.; Peedle, S.; Kusch, G.; Dahliah, D.; Melchiorre, M.; Rignanese, G.-M.; Hautier, G.; Oliver, R.; Siebentritt, S. Over 15% Efficient Wide-Band-Gap Cu(In,Ga)S₂ Solar Cell: Suppressing Bulk and Interface Recombination through Composition Engineering. *Joule* **2021**, *5* (7), 1816–1831. <https://doi.org/10.1016/j.joule.2021.05.004>.
- (18) Balestrieri, M.; Achard, V.; Hildebrandt, T.; Lombez, L.; Jubault, M.; Posada, J.; Lincot, D.; Donsanti, F. Structural Characterization of Coevaporated Cu(In,Ga)Se₂ Absorbers Deposited at Low Temperature. *J. Alloys Compd.* **2019**, *794*, 654–661. <https://doi.org/10.1016/j.jallcom.2019.04.135>.
- (19) Kessler, F.; Rudmann, D. Technological Aspects of Flexible CIGS Solar Cells and Modules. *Sol. Energy* **2004**, *77* (6), 685–695. <https://doi.org/10.1016/j.solener.2004.04.010>.
- (20) Kaigawa, R.; Wada, T.; Bakehe, S.; Klenk, R. Three-Stage Evaporation of Cu(In,Ga)S₂ Solar Cell Absorber Films without KCN Treatment and Na Control. *Thin Solid Films* **2006**, *511–512*, 430–433. <https://doi.org/10.1016/j.tsf.2005.11.073>.
- (21) *Effects of Sodium on Polycrystalline Cu(In,Ga)Se₂ and Its Solar Cell Performance - Kronik - 1998 - Advanced Materials - Wiley Online Library.* <https://onlinelibrary.wiley.com/doi/abs/10.1002/%28SICI%291521-4095%28199801%2910%3A1%3C31%3A%3AAID-ADMA31%3E3.0.CO%3B2-3> (accessed 2023-02-06).
- (22) Theelen, M.; Tomassini, M.; Barreau, N.; Steijvers, H.; Branca, A.; Harel, S.; Vroon, Z.; Zeman, M. The Impact of Selenisation on Damp Heat Degradation of the CIGS Back Contact Molybdenum. In *2012 IEEE 38th Photovoltaic Specialists Conference (PVSC) PART 2*; 2012; pp 1–6. <https://doi.org/10.1109/PVSC-Vol2.2012.6656703>.
- (23) Hadouda, H.; Pouzet, J.; Bernede, J. C.; Barreau, A. MoS₂ Thin Film Synthesis by Soft Sulfurization of a Molybdenum Layer. *Mater. Chem. Phys.* **1995**, *42* (4), 291–297. [https://doi.org/10.1016/0254-0584\(96\)80017-4](https://doi.org/10.1016/0254-0584(96)80017-4).
- (24) Assmann, L.; Bernède, J. C.; Drici, A.; Amory, C.; Halgand, E.; Morsli, M. Study of the Mo Thin Films and Mo/CIGS Interface Properties. *Appl. Surf. Sci.* **2005**, *246* (1), 159–166. <https://doi.org/10.1016/j.apsusc.2004.11.020>.
- (25) Jackson, P.; Hariskos, D.; Lotter, E.; Paetel, S.; Wuerz, R.; Menner, R.; Wischmann, W.; Powalla, M. New World Record Efficiency for Cu(In,Ga)Se₂ Thin-Film Solar Cells beyond 20%. *Prog. Photovolt. Res. Appl.* **2011**, *19* (7), 894–897. <https://doi.org/10.1002/pip.1078>.
- (26) Lincot, D.; Guillemoles, J. F.; Taunier, S.; Guimard, D.; Sicx-Kurdi, J.; Chaumont, A.; Roussel, O.; Ramdani, O.; Hubert, C.; Fauvarque, J. P.; Bodereau, N.; Parissi, L.; Panheleux, P.; Fanouillere, P.; Naghavi, N.; Grand, P. P.; Benfarah, M.; Mogensen, P.; Kerrec, O. Chalcopyrite Thin Film Solar Cells by Electrodeposition. *Sol. Energy* **2004**, *77* (6), 725–737. <https://doi.org/10.1016/j.solener.2004.05.024>.

- (27) Bhattacharya, R. N.; Hiltner, J. F.; Batchelor, W.; Contreras, M. A.; Noufi, R. N.; Sites, J. R. 15.4% $\text{CuIn}_{1-x}\text{Ga}_x\text{Se}_2$ -Based Photovoltaic Cells from Solution-Based Precursor Films. *Thin Solid Films* **2000**, 361–362, 396–399. [https://doi.org/10.1016/S0040-6090\(99\)00809-3](https://doi.org/10.1016/S0040-6090(99)00809-3).
- (28) Aksu, S.; Pinarbasi, M. Electrodeposition Methods and Chemistries for Deposition of CIGS Precursor Thin Films. In *2011 37th IEEE Photovoltaic Specialists Conference*; 2011; pp 000310–000314. <https://doi.org/10.1109/PVSC.2011.6185907>.
- (29) Arnou, P.; Cooper, C. S.; Malkov, A. V.; Bowers, J. W.; Walls, J. M. Solution-Processed $\text{CuIn}(\text{S},\text{Se})_2$ Absorber Layers for Application in Thin Film Solar Cells. *Thin Solid Films* **2015**, 582, 31–34. <https://doi.org/10.1016/j.tsf.2014.10.080>.
- (30) Liu, Y.; Kong, D.; Li, J.; Zhao, C.; Chen, C.; Brugger, J. Preparation of $\text{Cu}(\text{In},\text{Ga})\text{Se}_2$ Thin Film by Solvothermal and Spin-Coating Process. *Energy Procedia* **2012**, 16, 217–222. <https://doi.org/10.1016/j.egypro.2012.01.036>.
- (31) Park, S. J.; Cho, J. W.; Lee, J. K.; Shin, K.; Kim, J.-H.; Min, B. K. Solution Processed High Band-Gap CuInGaS_2 Thin Film for Solar Cell Applications. *Prog. Photovolt. Res. Appl.* **2014**, 22 (1), 122–128. <https://doi.org/10.1002/pip.2354>.
- (32) Lee, D.; Yong, K. Non-Vacuum Deposition of CIGS Absorber Films for Low-Cost Thin Film Solar Cells. *Korean J. Chem. Eng.* **2013**, 30 (7), 1347–1358. <https://doi.org/10.1007/s11814-013-0101-0>.
- (33) Todorov, T. K.; Gunawan, O.; Gokmen, T.; Mitzi, D. B. Solution-Processed $\text{Cu}(\text{In},\text{Ga})(\text{S},\text{Se})_2$ Absorber Yielding a 15.2% Efficient Solar Cell. *Prog. Photovolt. Res. Appl.* **2013**, 21 (1), 82–87. <https://doi.org/10.1002/pip.1253>.
- (34) Noufi, R.; Gabor, A. M.; Tuttle, J. R.; Tennant, A. L.; Contreras, M. A.; Albin, D. S.; Carapella, J. J. Method of Fabricating High-Efficiency $\text{Cu}(\text{In},\text{Ga})(\text{SeS})_2$ Thin Films for Solar Cells. US5441897A, August 15, 1995. <https://patents.google.com/patent/US5441897A/en> (accessed 2023-02-14).
- (35) Gloeckler, M.; Sites, J. R. Efficiency Limitations for Wide-Band-Gap Chalcopyrite Solar Cells. *Thin Solid Films* **2005**, 480–481, 241–245. <https://doi.org/10.1016/j.tsf.2004.11.018>.
- (36) Merdes, S.; Sáez-Araoz, R.; Ennaoui, A.; Klaer, J.; Lux-Steiner, M. Ch.; Klenk, R. Recombination Mechanisms in Highly Efficient Thin Film $\text{Zn}(\text{S},\text{O})/\text{Cu}(\text{In},\text{Ga})\text{S}_2$ Based Solar Cells. *Appl. Phys. Lett.* **2009**, 95 (21), 213502. <https://doi.org/10.1063/1.3266829>.
- (37) Ennaoui, A.; Bär, M.; Klaer, J.; Kropp, T.; Sáez-Araoz, R.; Lux-Steiner, M. Ch. Highly-Efficient Cd-Free CuInS_2 Thin-Film Solar Cells and Mini-Modules with $\text{Zn}(\text{S},\text{O})$ Buffer Layers Prepared by an Alternative Chemical Bath Process. *Prog. Photovolt. Res. Appl.* **2006**, 14 (6), 499–511. <https://doi.org/10.1002/pip.682>.
- (38) Persson, C.; Platzer-Björkman, C.; Malmström, J.; Törndahl, T.; Edoff, M. Strong Valence-Band Offset Bowing of $\text{ZnO}_{1-x}\text{S}_x$ Enhances p-Type Nitrogen Doping of ZnO -like Alloys. *Phys. Rev. Lett.* **2006**, 97 (14), 146403. <https://doi.org/10.1103/PhysRevLett.97.146403>.
- (39) Kodigala, S. R. Chapter 8 - $\text{Cu}(\text{In}_{1-x}\text{Ga}_x)\text{Se}_2$ and $\text{CuIn}(\text{Se}_{1-x}\text{S}_x)_2$ Thin Film Solar Cells. In *Thin Films and Nanostructures*; Kodigala, S. R., Ed.; $\text{Cu}(\text{InGa})\text{Se}_2$ Based Thin Film Solar Cells; Academic Press, 2010; Vol. 35, pp 505–679. <https://doi.org/10.1016/B978-0-12-373697-0.00008-0>.

- (40) Toward a 25%-efficient polycrystalline thin-film tandem solar cell: practical issues. <https://ieeexplore.ieee.org/document/1305207/?arnumber=1305207> (accessed 2023-02-10).
- (41) Nishiwaki, S.; Siebentritt, S.; Walk, P.; Ch. Lux-Steiner, M. A Stacked Chalcopyrite Thin-Film Tandem Solar Cell with 1.2 V Open-Circuit Voltage. *Prog. Photovolt. Res. Appl.* **2003**, *11* (4), 243–248. <https://doi.org/10.1002/pip.486>.
- (42) Nakada, T.; Hirabayashi, Y.; Tokado, T.; Ohmori, D.; Mise, T. Novel Device Structure for Cu(In,Ga)Se₂ Thin Film Solar Cells Using Transparent Conducting Oxide Back and Front Contacts. *Sol. Energy* **2004**, *77* (6), 739–747. <https://doi.org/10.1016/j.solener.2004.08.010>.
- (43) Mazzer, M.; Rampino, S.; Spaggiari, G.; Annoni, F.; Bersani, D.; Bissoli, F.; Bronzoni, M.; Calicchio, M.; Gombia, E.; Kingma, A.; Pattini, F.; Gilioli, E. Bifacial CIGS Solar Cells Grown by Low Temperature Pulsed Electron Deposition. *Sol. Energy Mater. Sol. Cells* **2017**, *166*, 247–253. <https://doi.org/10.1016/j.solmat.2016.10.048>.
- (44) Hamada, N.; Nishimura, T.; Chantana, J.; Kawano, Y.; Masuda, T.; Minemoto, T. Fabrication of Flexible and Bifacial Cu(In,Ga)Se₂ Solar Cell with Superstrate-Type Structure Using a Lift-off Process. *Sol. Energy* **2020**, *199*, 819–825. <https://doi.org/10.1016/j.solener.2020.02.084>.
- (45) Heinemann, M. D.; Efimova, V.; Klenk, R.; Hoepfner, B.; Wollgarten, M.; Unold, T.; Schock, H.-W.; Kaufmann, C. A. Cu(In,Ga)Se₂ Superstrate Solar Cells: Prospects and Limitations. *Prog. Photovolt. Res. Appl.* **2015**, *23* (10), 1228–1237. <https://doi.org/10.1002/pip.2536>.
- (46) Caldes, M. T.; Guillot-Deudon, C.; Thomere, A.; Penicaud, M.; Gautron, E.; Boullay, P.; Bujoli-Doeuff, M.; Barreau, N.; Jobic, S.; Lafond, A. Layered Quaternary Compounds in the Cu₂S–In₂S₃–Ga₂S₃ System. *Inorg. Chem.* **2020**, *59* (7), 4546–4553. <https://doi.org/10.1021/acs.inorgchem.9b03686>.
- (47) Shukla, S.; Adeleye, D.; Sood, M.; Ehre, F.; Lomuscio, A.; Weiss, T. P.; Siopa, D.; Melchiorre, M.; Siebentritt, S. Carrier Recombination Mechanism and Photovoltage Deficit in 1.7-EV Band Gap near-Stoichiometric Cu(In,Ga)S₂. *Phys. Rev. Mater.* **2021**, *5* (5), 055403. <https://doi.org/10.1103/PhysRevMaterials.5.055403>.
- (48) Álvarez-García, J.; Marcos-Ruzafa, J.; Pérez-Rodríguez, A.; Romano-Rodríguez, A.; Morante, J. R.; Scheer, R. MicroRaman Scattering from Polycrystalline CuInS₂ Films: Structural Analysis. *Thin Solid Films* **2000**, *361–362*, 208–212. [https://doi.org/10.1016/S0040-6090\(99\)00847-0](https://doi.org/10.1016/S0040-6090(99)00847-0).
- (49) Vargas, W. E.; Azoifeifa, D. E.; Clark, N. Retrieved Optical Properties of Thin Films on Absorbing Substrates from Transmittance Measurements by Application of a Spectral Projected Gradient Method. *Thin Solid Films* **2003**, *425* (1), 1–8. [https://doi.org/10.1016/S0040-6090\(02\)01117-3](https://doi.org/10.1016/S0040-6090(02)01117-3).
- (50) Tauc, J.; Grigorovici, R.; Vancu, A. Optical Properties and Electronic Structure of Amorphous Germanium. *Phys. Status Solidi B* **1966**, *15* (2), 627–637. <https://doi.org/10.1002/pssb.19660150224>.
- (51) Viezbicke, B. D.; Patel, S.; Davis, B. E.; Birnie III, D. P. Evaluation of the Tauc Method for Optical Absorption Edge Determination: ZnO Thin Films as a Model System. *Phys. Status Solidi B* **2015**, *252* (8), 1700–1710. <https://doi.org/10.1002/pssb.201552007>.

- (52) Urbach, F. The Long-Wavelength Edge of Photographic Sensitivity and of the Electronic Absorption of Solids. *Phys. Rev.* **1953**, *92* (5), 1324–1324. <https://doi.org/10.1103/PhysRev.92.1324>.
- (53) Caselli, V. M.; Wei, Z.; Ackermans, M. M.; Hutter, E. M.; Ehrler, B.; Savenije, T. J. Charge Carrier Dynamics upon Sub-Bandgap Excitation in Methylammonium Lead Iodide Thin Films: Effects of Urbach Tail, Deep Defects, and Two-Photon Absorption. *ACS Energy Lett.* **2020**, *5* (12), 3821–3827. <https://doi.org/10.1021/acsenerylett.0c02067>.
- (54) Buffière, M.; Harel, S.; Arzel, L.; Deudon, C.; Barreau, N.; Kessler, J. Fast Chemical Bath Deposition of Zn(O,S) Buffer Layers for Cu(In,Ga)Se₂ Solar Cells. *Thin Solid Films* **2011**, *519* (21), 7575–7578. <https://doi.org/10.1016/j.tsf.2011.01.104>.
- (55) Kaur, K.; Kumar, N.; Kumar, M. Strategic Review of Interface Carrier Recombination in Earth Abundant Cu–Zn–Sn–S–Se Solar Cells: Current Challenges and Future Prospects. *J. Mater. Chem. A* **2017**, *5* (7), 3069–3090. <https://doi.org/10.1039/C6TA10543B>.
- (56) Haque, F.; Daeneke, T.; Kalantar-zadeh, K.; Ou, J. Z. Two-Dimensional Transition Metal Oxide and Chalcogenide-Based Photocatalysts. *Nano-Micro Lett.* **2017**, *10* (2), 23. <https://doi.org/10.1007/s40820-017-0176-y>.
- (57) Suzuki, A.; Okada, H.; Oku, T. Fabrication and Characterization of CH₃NH₃PbI_{3-x-y}Br_xCl_y Perovskite Solar Cells. *Energies* **2016**, *9* (5), 376. <https://doi.org/10.3390/en9050376>.
- (58) Hawash, Z.; Ono, L. K.; Qi, Y. Recent Advances in Spiro-MeOTAD Hole Transport Material and Its Applications in Organic–Inorganic Halide Perovskite Solar Cells. *Adv. Mater. Interfaces* **2018**, *5* (1), 1700623. <https://doi.org/10.1002/admi.201700623>.
- (59) Tan, B.; Raga, S. R.; Chesman, A. S. R.; Furer, S. O.; Zheng, F.; McMeekin, D. P.; Jiang, L.; Mao, W.; Lin, X.; Wen, X.; Lu, J.; Cheng, Y.-B.; Bach, U. LiTFSI-Free Spiro-OMeTAD-Based Perovskite Solar Cells with Power Conversion Efficiencies Exceeding 19%. *Adv. Energy Mater.* **2019**, *9* (32), 1901519. <https://doi.org/10.1002/aenm.201901519>.
- (60) Schölin, R.; Karlsson, M. H.; Eriksson, S. K.; Siegbahn, H.; Johansson, E. M. J.; Rensmo, H. Energy Level Shifts in Spiro-OMeTAD Molecular Thin Films When Adding Li-TFSI. *J. Phys. Chem. C* **2012**, *116* (50), 26300–26305. <https://doi.org/10.1021/jp306433g>.
- (61) Hawash, Z.; Ono, L. K.; Raga, S. R.; Lee, M. V.; Qi, Y. Air-Exposure Induced Dopant Redistribution and Energy Level Shifts in Spin-Coated Spiro-MeOTAD Films. *Chem. Mater.* **2015**, *27* (2), 562–569. <https://doi.org/10.1021/cm504022q>.
- (62) Lamberti, F.; Gatti, T.; Cescon, E.; Sorrentino, R.; Rizzo, A.; Menna, E.; Meneghesso, G.; Meneghetti, M.; Petrozza, A.; Franco, L. Evidence of Spiro-OMeTAD De-Doping by Tert-Butylpyridine Additive in Hole-Transporting Layers for Perovskite Solar Cells. *Chem* **2019**, *5* (7), 1806–1817. <https://doi.org/10.1016/j.chempr.2019.04.003>.
- (63) Burschka, J.; Dualeh, A.; Kessler, F.; Baranoff, E.; Cevey-Ha, N.-L.; Yi, C.; Nazeeruddin, M. K.; Grätzel, M. Tris(2-(1H-Pyrazol-1-yl)Pyridine)Cobalt(III) as p-Type Dopant for Organic Semiconductors and Its Application in Highly Efficient Solid-State Dye-Sensitized Solar Cells. *J. Am. Chem. Soc.* **2011**, *133* (45), 18042–18045. <https://doi.org/10.1021/ja207367t>.

- (64) Advanced Characterization Techniques for Thin Film Solar Cells.
- (65) Hawkes, P. *ELECTRONS ET MICROSCOPES : Vers Les Nanosciences. Préface de Raimond Castaing*; Croisée des Sciences; Belin/CNRS Editions: Paris, 1995.
- (66) Zanatta, A. R. Revisiting the Optical Bandgap of Semiconductors and the Proposal of a Unified Methodology to Its Determination. *Sci. Rep.* **2019**, 9 (1), 11225. <https://doi.org/10.1038/s41598-019-47670-y>.
- (67) Khemiri, N.; Kanzari, M. Investigation on Dispersive Optical Constants and Electrical Properties of CuIn5S8 Thin Films. *Solid State Commun.* **2013**, 160, 32–36. <https://doi.org/10.1016/j.ssc.2013.02.016>.
- (68) Optical Properties of Silicon Nanocrystallites in Polycrystalline Silicon Films Prepared at Low Temperature by Plasma-Enhanced Chemical Vapor Deposition. *Thin Solid Films* **2001**, 382 (1–2), 47–55. [https://doi.org/10.1016/S0040-6090\(00\)01208-6](https://doi.org/10.1016/S0040-6090(00)01208-6).
- (69) Kahn, A. Fermi Level, Work Function and Vacuum Level. *Mater. Horiz.* **2016**, 3 (1), 7–10. <https://doi.org/10.1039/C5MH00160A>.
- (70) Shao, G. Work Function and Electron Affinity of Semiconductors: Doping Effect and Complication Due to Fermi Level Pinning. *ENERGY Environ. Mater.* **2021**, 4 (3), 273–276. <https://doi.org/10.1002/eem2.12218>.
- (71) enlijoseph. *Quantum Efficiency / Definition, Equation, Application, Calculating » We Enlighten Your Ideas!* <https://enltechnology.com/blog/qe/quantum-efficiency-01/> (accessed 2023-03-08).

Chapter 4: CIGS_n-type nanopowders for photocatalysis application

This chapter covers the elaboration of CIGS_n lamellar materials with the objective to examine their potentialities as visible light photocatalysts.

In a preliminary part, the concept of photocatalysis and some of its basic principles are developed. The main photocatalytic mechanisms of hydrogen production using water splitting and dehydrogenation of alcohols are then reported.

The second section provides a description of nanopowders preparation using microwave-assisted solvothermal synthesis and their characterization. We will be focused especially on the CIGS₆ lamellar compound, which exhibits an interesting ambipolar behaviour, alongside with CIGS chalcopyrite considered as a reference during this PhD project. Therefore, it reviews the different strategies introduced for CIGS₆ synthesis followed by the chemical, structural and optoelectronic characterisations.

Finally, photocatalytic experiments under visible illumination were performed on the prepared photocatalysts using different alcohols. The hydrogen production yields are presented, allowing a comparison with literature.

1. A look to photocatalysis

1.1. Photocatalysis

The “photocatalysis” term was introduced for the first time in 1964, by Doerffler and Hauffe who studied the oxidation of CO on ZnO.¹ It is a particular type of catalysis.

Basically speaking, catalysis is the process of reducing the activation energy of a reaction in order to accelerate its rate. This is achieved by using a catalyst, which is presented in a smaller amount than the reactants, because it is not consumed during the reaction and remains unchanged at the end of it.²

There are two main types of catalysis:

- Homogeneous catalysis: where the reactants and catalyst are in the same phase, usually liquid phase.

- Heterogeneous catalysis: where the reactants and the catalyst are in different phases, usually the catalyst is in a solid form while the reactants are in liquid or gas phase.

In heterogeneous catalysis, the chemical reaction will take place on the surface of the catalyst, in order to initiate the reaction; it requires the reactants to be adsorbed onto the surface of the catalyst. Depending on the strength of the interactions between the reactants and the catalyst, this can be either physisorption or chemisorption.

Therefore, heterogeneous photocatalysis is a type of catalysis that uses light as an energy source to activate reactions, rather than heat.^{3,4} As shown in Figure 1, heterogeneous photocatalysis is based on endergonic reactions⁵, storing solar energy in chemical energy to produce solar fuels (the quantity stored is ΔG in Figure 2), while exergonic reactions is releasing the chemical energy in order to power a system.⁶

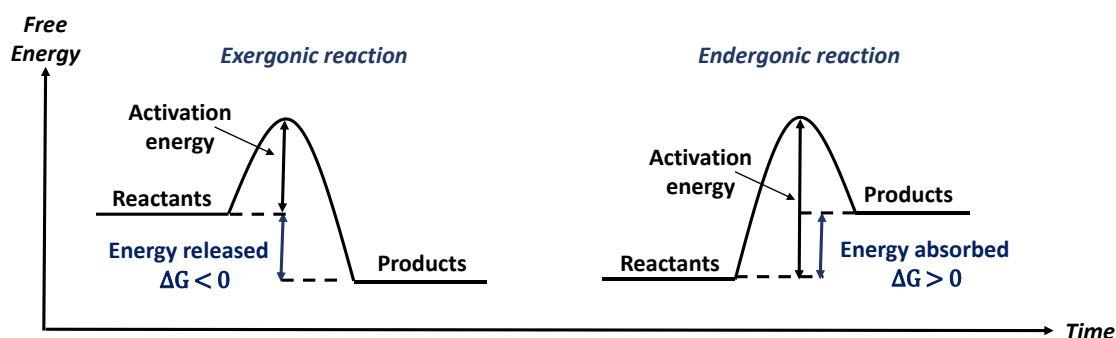
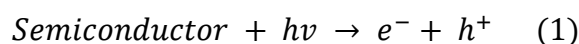


Figure 1: Energetic diagrams of exergonic and endergonic reactions. Endergonic reaction presents the involved reaction on the photocatalysis applications.

1.2. Heterogeneous photocatalysis principle

A schematic representation of the fundamental principle of heterogeneous photocatalysis⁷⁻¹² is presented in the Figure 2. The photocatalytic material is a semiconductor generally in a solid phase that is dispersed in a reagent liquid, forming a colloidal suspension. The heterogeneous photocatalysis mechanism is based on the semiconductor absorption of photons with an energy equal or higher than the value of its optical gap ($h\nu \geq E_g$) following the equation (1),



This will promote the movement of an electron from the valence band to the conduction band, creating a hole in the valence band, and thus generating electron hole pairs (Figure 2).

The photogenerated electrons (e^- , presented on reduction site) and holes (h^+ , presented on oxidation site) will migrate to the surface of the photocatalyst involving oxidation

reaction on the valence band and reduction reaction on the conduction band. Otherwise, if no driving force separate the electron-hole pair, for instance the absence of chemical reaction, a recombination phenomenon occurs (Figure 2).

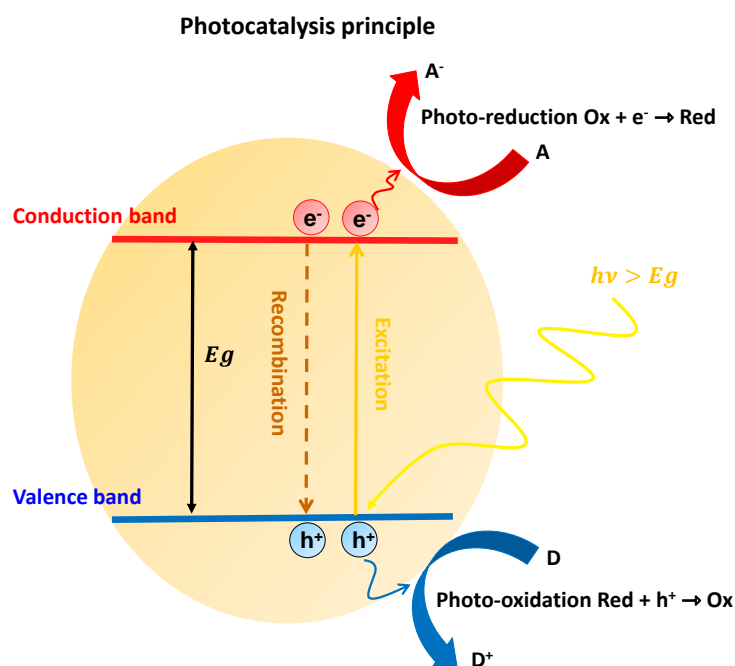


Figure 2: Schematic illustration of the basic mechanism of heterogeneous photocatalysis process.

Moreover, the photocatalysts materials can be divided to 2 categories¹³: single materials (either an n-type or p-type semiconductor) and heterojunctions materials by combining two different semiconductors with unequal band structure.

The heterojunction photocatalysts can be classified based on their energy band alignments (type I, type II, and type III),¹⁴ as shown in Figure 3.

Usually, heterojunctions exhibit better performance compared to single material photocatalysts, because carrier separation is improved and recombination losses-reduced. However, it is difficult to achieve efficient charge separation and strong redox capability simultaneously. To maximize redox potential of the heterojunctions, an electron transfer mechanism in Z-scheme have been proposed. In this kind of heterojunction, the transfer of electrons from the conduction band (CB) of one semiconductor to the valence band (VB) of the other one, through an electron mediator, ensures a larger difference between oxidation and reduction energy levels (Figure 3).

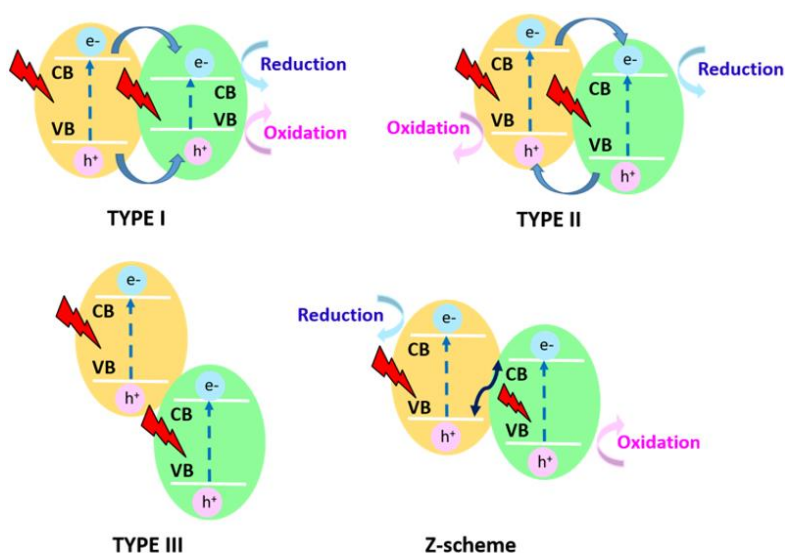


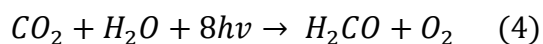
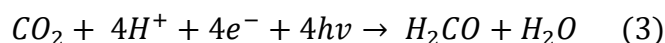
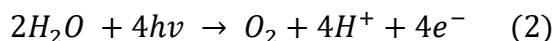
Figure 3: Schematic illustration of the different heterojunction photocatalysts classified based on their energy band alignments (type I, type II, and type III).

There are different types of (photo)catalysis reactions: as selective mild oxidation reactions, total oxidation reactions in presence of water (humid air or aqueous phase), CO₂ reduction and photocatalytic reactions involving hydrogen (water splitting and hydrogen evolution from alcohols).^{15–17}

1.3. Photocatalytic hydrogen production

1.3.1. Water splitting - artificial photosynthesis

Photosynthesis is a natural process that transforms carbon dioxide and water to oxygen and carbohydrates using solar light, which takes place in the chloroplasts of plant cells following the two half reactions (equations 2, 3), which are combined to make a full photosynthesis reaction (equation 4).^{18,19}



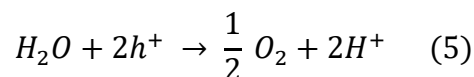
This process is crucial for both the creation of oxygen and the global carbon cycle.

On the other side, artificial photosynthesis is a man-made procedure that aims to imitate the natural process of photosynthesis in a controlled laboratory environment. It includes directing the chemical reactions necessary for photosynthesis, generally in a photoelectrochemical cell or a photoreactor, using light-absorbing substances and catalysts for water splitting or CO₂ reduction.^{20,21}

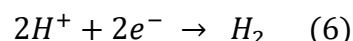
Water splitting in photocatalysis is a simple clean application that involves water decomposition into hydrogen and oxygen molecules using light activation.^{17,21–23} As shown in Figure 4.

The mechanism of water splitting follows two half-reactions:

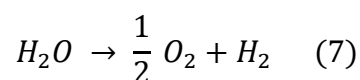
Water oxidation by photogenerated holes (equation 5)



And proton reduction by photogenerated electrons (equation 6)



obtaining the combined followed equation 7. Water splitting is an endothermic reaction that requires a chemical energy $\Delta G = 237 \text{ kJ/mol}$.²²



In order to induce these reactions, the first requirement is that the photocatalyst used should present a conduction band with an electrochemical potential more negative than the redox couple H^+/H_2 (0 V) to reduce hydrogen and have a valence band with an electrochemical potential higher than that of the redox couple O_2/H_2O (1.23 V) to oxidize water (Figure 4).^{17,22,24}

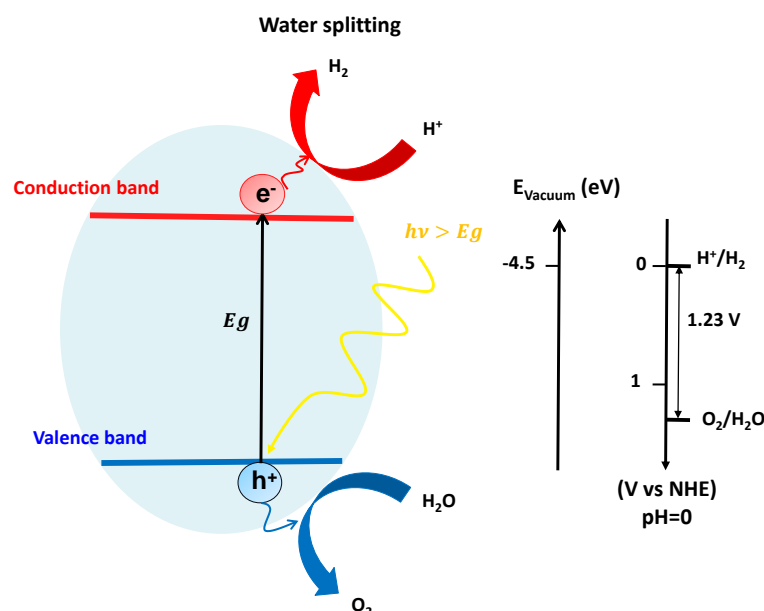


Figure 4: Schematic representation of the overall water splitting, showing the band edge positions of redox potentials of water splitting.

1.3.2. Photocatalytic H₂ production from alcohols

Water splitting remains a limited reaction in the case of numerous photocatalysts, as long as one of the involved half reactions does not fit well.^{25,26} To overcome this limitation, photocatalytic H₂ production from alcohols-water mixture is another approach considered for hydrogen evolution.^{6,26-30} It consists of several steps allowing the hydrogen extraction from the water molecule and leading to the formation of CO₂ and H₂.

Generally, the added alcohol to the photocatalysed reaction is named a sacrificial reagent.^{22,31} Depending on the sacrificial reagents used, we can perform either the hydrogen evolution reaction (HER) or oxygen evolution reaction (OER), implementing respectively sacrificial electron donors (SED) or sacrificial electron acceptors (SEA).^{29,38}

As presented in the Figure 5, in the first case (HER) the photogenerated holes will irreversibly oxidize the SED in place of water, restricting the O₂ formation and thus enhancing H₂ production, while in the second case (OER) the photogenerated electrons will be consumed by the SEA, limiting the H₂ evolution and thereby increasing the O₂ production.

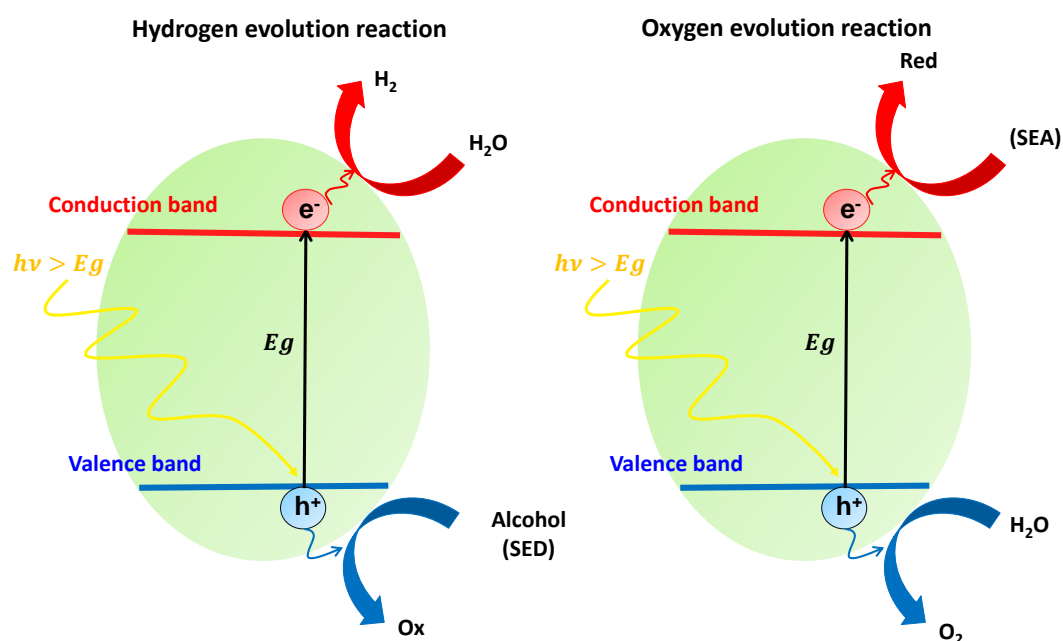


Figure 5: Schematic representation of the principle of hydrogen and oxygen production reactions using an alcohol as sacrificial reagent.

1.4. Photocatalytic materials

1.4.1. Requirements of an efficient photocatalyst

The photocatalytic activity will occur, if the chosen photocatalyst meets the following properties:

- A semiconductor behaviour with a suitable band gap, for a good light absorption in order to generate electron-hole pairs.
- Appropriate conduction and valence bands potentials for the targeted reactions.
- Ability to separate the photogenerated carriers (i.e long carriers lifetime).
- Good molecules adsorption on the surface of the semiconductor, therefore it is necessary to have a large number of active sites on the surface and a large specific surface (m^2/g).
- Good stability in the aqueous solution.

Currently, titanium dioxide TiO_2 is the most widely used among the different photocatalysts for green hydrogen production.^{32,33} As illustrated in Figure 6 b, TiO_2 band positions are well placed compared to the redox potentials required to split water. However, TiO_2 large band gap (3.0 - 3.2 eV) allows the absorption of only a small part of the solar spectrum (the ultraviolet region).³⁴ As a result, the solar to hydrogen conversion efficiency is quite low. Until today, the majority of the used photocatalysts can perform water dissociation only under the UV light irradiation, which covers only 4% of the solar energy. For this reason, it is important to develop photocatalyst candidates that are able to operate under visible light, which concerns 47% of the solar energy (Figure 6 a).³⁵

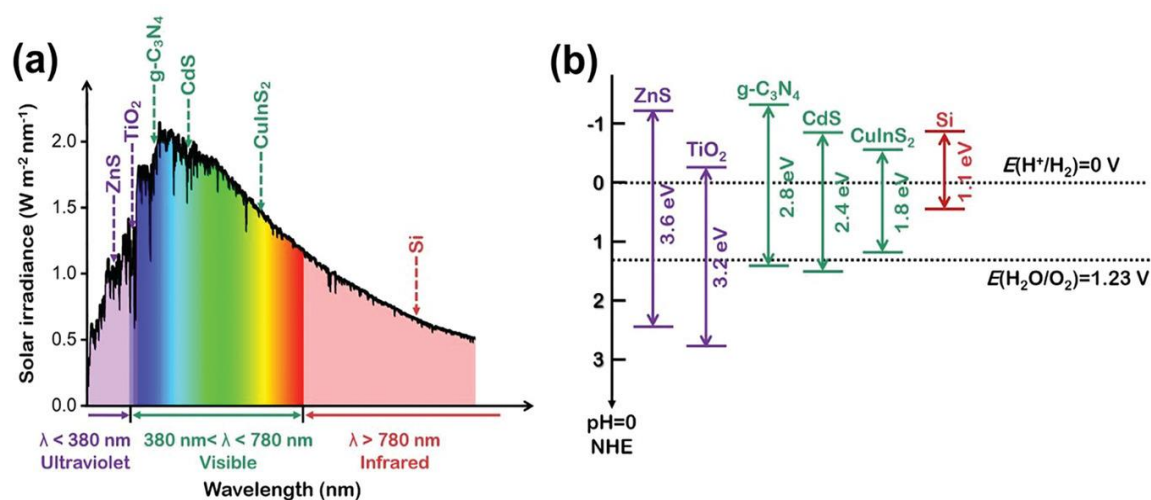


Figure 6: a) The solar spectrum, showing the energy content of UV, visible light and IR parts of the sunlight. b) Band edge positions of some semiconductors photocatalysts concerning H_2 and O_2 evolution. Figure from Zhang et al.³⁴

1.4.2. Chalcogenides

Following this path, metal chalcogenides stand out as attractive photocatalysts candidates compared to metal oxides for visible light photocatalysis.³⁶ Typically, chalcogenides have the advantage of displaying an optical gap lower than 3 eV, since the S2p orbital are less negative than O2p.³⁷ Consequently, they show a greater response on the solar spectrum and they also present a low effective mass of carriers, which promotes their separation and migration.

Among them, two-dimensional (2D) metal chalcogenides show complementary advantages.³⁸ Therefore, their larger surface area provide abundant active sites adsorption of the reactants, for redox reactions and for desorption of the products. Moreover, the 2D character decreases the diffusion length of charge carriers leading to photocatalytic reaction kinetics improvement. Finally, the bandgap energies and band positions of 2D materials are commonly strongly dependent on their thickness, which can be used to adjust their redox properties.

Recently, two layered sulphides $ZnIn_2S_4$ (ZIS₄)^{39–43} and $Zn_3In_2S_6$ (ZIS₆)^{26,29,44} (see Figure 7), have received a huge interest from the scientific community, as emerging visible-light photocatalysts for hydrogen evolution and CO₂ reduction. As shown in Figure 7, these materials present a 2D structure with a Van der Waals gap separating structural blocks, with zinc atoms in tetrahedral sulphur environments and indium atoms in both, tetrahedral and octahedral ones. In addition, no intrinsic vacancies are described.

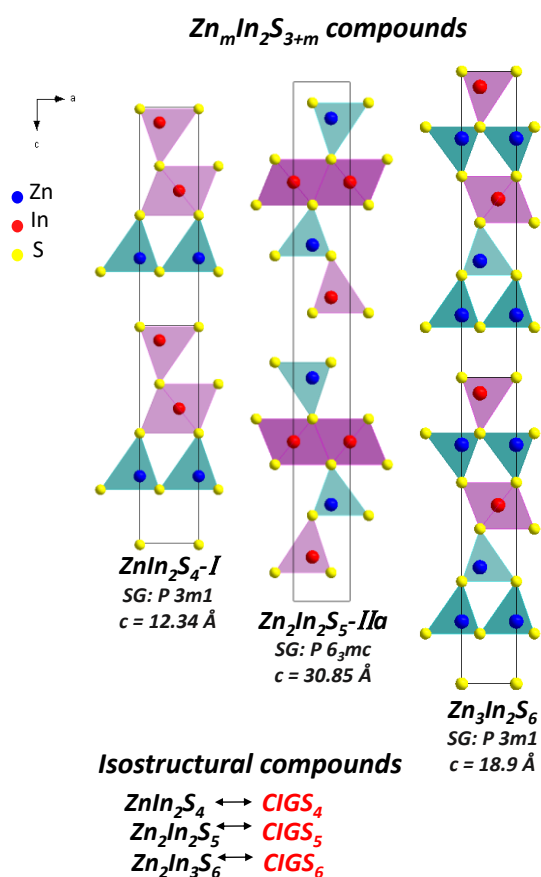


Figure 7: Structures of $Zn_mIn_2S_{3+m}$ compounds ($m = 1, 2$ and 3) isostructural of $CIGS_n$ compounds.

However, even though these compounds present smaller band gap (2.4 eV for ZIS₄ and 2.8 eV for ZIS₆) than TiO₂ (3.2 eV), it remains wide enough to limit the use of solar light efficiently. Moreover, a fast carrier recombination significantly limits their hydrogen generation efficiency.

To tackle these shortcomings, several methods are introduced to optimize the photocatalytic efficiency such as adding a co-catalyst and establishing heterojunctions. One of the most promising co-catalysts for 2D heterojunctions is MoS₂, in contrast to single ZIS_n photocatalysts, MoS₂/ZnIn₂S₄⁴⁵ and MoS₂/Zn₃In₂S₆⁴⁶ heterojunctions provide higher hydrogen generation efficiency for water splitting (i.e. almost 16 times higher).

On the other hand, defect engineering (vacancy, doping) is also considered as improving efficiency approach. In addition, ZIS_n are easily exfoliated as they exhibit a Van der Waals gap. Thus, a thickness tuning approach coupled with vacancy engineering, has been also achieved to optimize their photocatalytic activity. It allowed to prepare ultrathin 2D catalyst (e.g. one-unit-cell ZnIn₂S₄ thick) with an electronic-structure tailored, boosting solar-driven CO₂ reduction and hydrogen production up to ten times higher than that of bulk material.⁴⁷

1.4.3. CIGS_n lamellar compounds as potential visible light photocatalysts

CIGS_n compounds can be suggested as potential visible light photocatalysts looking to their optical gap (1.7 eV - 1.9 eV), as well as to the fact that they are isostructural to the ZIS_n compounds⁴⁸ (see Figure 7).

Nevertheless, CIGS_n lamellar compounds expose additional benefits in comparison with ZIS_n as:

- Bigger absorption range: CIGS_n exhibit lower band gap (1.7 eV - 1.9 eV) than ZIS_n (2.2 eV – 2.8 eV).
- Mixed occupancy on the tetrahedral sites Td (In, Ga and Cu) of the CIGS_n materials structures: which enables chemical composition to be adjusted in order to increase the spectral response and improve light absorption.
- The presence of intrinsic cationic vacancies on the Td sites of the CIGS_n materials structures: multiple research investigations highlight the advantageous positive effects of defects (such as cationic vacancies) on photocatalysis, allowing an efficient separation of the photogenerated electron-hole pairs, facilitating their participation in the associated relevant redox reactions and preventing the carrier recombination.⁴⁹
- The ambipolar behaviour of CIGS_n: unlike ZIS_n that are conventional unipolar materials, CIGS_n compounds could present an ambipolar behaviour (p-type/n-type). Since ambipolar materials are not constrained by the mobility of minority charge carriers, we anticipate that more effective simultaneous oxidative and reductive processes could be obtained.

In this regard, the rest of the chapter intends to study CIGS_n lamellar compounds as visible light photocatalysts for the production of H₂, focusing first on CIGS₆ given its ambipolar behaviour.

2. Elaboration of CIGS_n-type photocatalysts

2.1. Synthesis and characterization of CIGS₆ and CIGS photocatalysts

We focus on preparing CIGS₆ and CIGS chalcopyrite (CuIn_{0.7}Ga_{0.3}S₂) photocatalysts in order to compare their photocatalytic activities towards HER. To employ these compounds as photocatalysts, the microstructure of the samples must be optimized moving towards nanometric powders with higher specific surface, in order to increase molecules adsorption and light absorption capacities. Moreover, nanoparticles are interesting for photocatalysts because the photogenerated charge carriers have to travel a smaller distance to reach the surface reaction than in the case of microparticles, which reduces the probability of recombination.

During my thesis, all the nanopowders were prepared using microwave-assisted solvothermal synthesis (MW-ST). The synthesis were carried out at IMN with the help of Dr H el ene BRAULT.

2.1.1. Microwave assisted solvothermal synthesis

Before describing the followed protocol to synthesize nanopowder photocatalysts, some notions of MW-ST synthesis are given.

Microwaves are electromagnetic waves that have a wavelength between 1 mm and 1 m and a frequency between 0.3 and 300 GHz. The frequency of microwave synthesis equipment as well as commercial domestic microwave ovens is 2.45 GHz.⁵⁰ The fundamental principle of microwave chemistry is based on the ability of the solvent to absorb microwave irradiations energy and restore it as heat. This is the thermal dielectric effect that is based on two main heating mechanisms: the dipolar polarization and ionic conduction.^{50,51} To simplify, electrical energy is transformed into kinetic energy, which is then converted directly into thermal energy. Microwave energies are too low to break a bond, and hence microwaves are unable to directly cause chemical reactions. In contrast, they have a unique thermal effect that can be beneficial for synthesis.

The molecules of the solvent used are assimilated to dipoles and the efficiency of a solvent to absorb microwaves is impacted by its dielectric properties. Under the effect of an oscillating electric field, the molecules rotate to align themselves, causing friction and generating heat. Ions also oscillate with the electric field, creating collisions between charged particles and surrounding atoms or molecules, resulting in the generation of thermal energy.^{50,51} In our work, we used ethylene glycol (EG) whose energy dissipation factor is equal to 1.350.

When compared to conventional heating techniques, the microwave radiation's interaction with polar molecules and conducting ions produces fast volumetric heating and resulting a shorter reaction time and faster reaction rate.⁵²⁻⁵⁴

Traditionally, heat transfer in organic synthesis occurs via convection from the heat source to the flask surface, and subsequently the surface heats the flask content. As a result, there are two steps of heat transfer, which lengthens the process and increases energy losses. In microwave synthesis, microwaves pass through the glassware and interact directly with the molecules. Due to this direct heating effect, which begins from the core of the solution, there is little heat loss and heating is significantly faster (Figure 8).

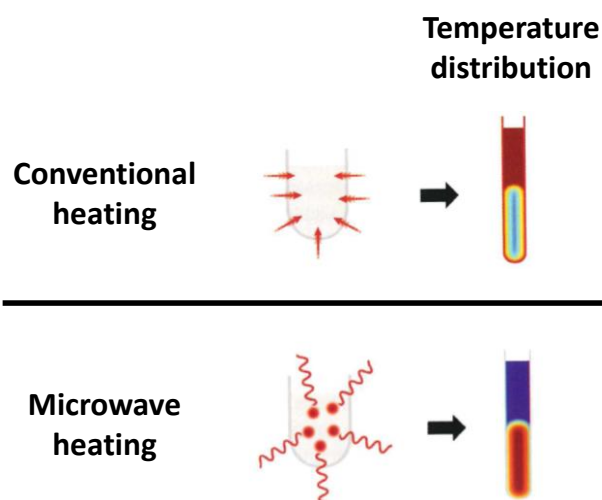


Figure 8: Temperature distribution by heating mode.

The microwaved-assisted reactions have the advantage to reduce the reaction time, rise rapidly temperature leading to obtain extremely small particles. A second strength of this technique over conventional solvothermal method is the ability to obtain single-phase nanopowders with higher yields, due to the possibility of superheating the solvents in a shorter time. Otherwise, the strict control of nanoparticles synthesis conditions is an important step, due to the strong correlation existing between their nanostructure and their optoelectronic properties. Microwave ovens allow accurate control of synthesis conditions by tuning precisely experimental parameters (e.g. power, time reaction, pressure). Thus, it is possible to adapt morphology and nanoparticles size from the classical solvothermal syntheses.

Table 1: Comparison of solvothermal synthesis methods.

Parameters	Microwave-assisted	Classical solvothermal ⁵⁵
Temperature	170 °C	180°C
Time	15 min	12 h
Precursors price	Low	High
Security	Perfectly secured	Possible incident

The objective of using MW-ST synthesis is to prepare CIGS_n nanomaterials with high specific area with an energy efficient, faster and low-cost method (Table 1). We drew

inspiration from the synthesis protocol described in the literature for CuInS_2 ⁵⁵⁵⁶. It is made up of three major steps as shown below in Figure 9.

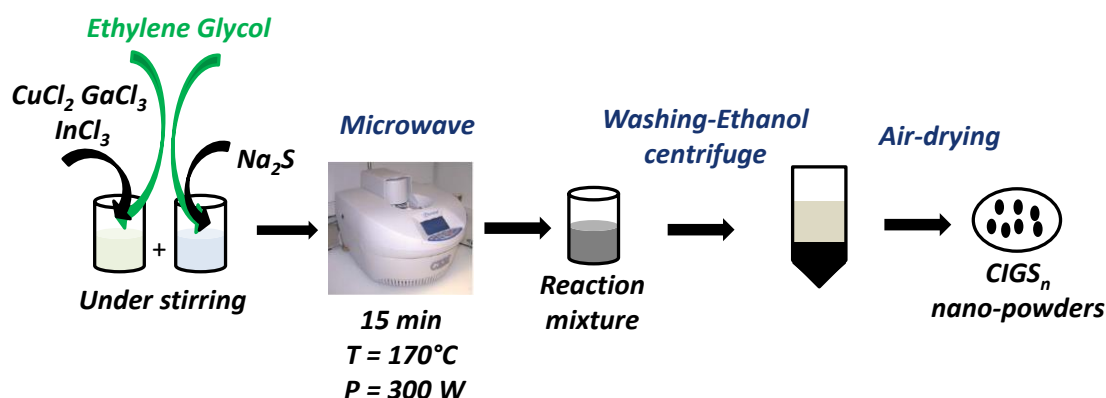


Figure 9: Synthesis protocol followed to prepare the CIGS_n nanopowders using microwave-assisted solvothermal synthesis.

In a glove box the sulphide of di-sodium and the chlorides of copper, indium and gallium (Na_2S , CuCl_2 , GaCl_3 and InCl_2) precursors are weighed in stoichiometric proportions or with an excess of 30% of Ga and 50% of S. They are then dissolved separately by stirring in 2.5 mL of ethylene glycol. Subsequently, in order to optimize and facilitate the weighing step, stock solutions were prepared, corresponding to the stoichiometry of the chemical elements in the composition of studied compounds. Each compound's stock solution was made separately and for each synthesis, 2.5 mL of each solution is used to create a 10 mL solution, starting by the homogenisation of all the cations before gradually adding the sulphur. Then, the mixed solution is irradiated using microwave for 15 min at 170°C , with an initial power of 300 W and in a reactor of 35 mL. The microwave is linked to a software that allows to launch the heating protocol and follow the parameters in real time while the reaction. Finally, the obtained sample will be washed and separated from the ethylene glycol using ethanol in a centrifuge, during 10 min at 7500 rpm for three times and finally air-dried in a crystalliser.

Table 2 compares the high-temperature synthesis used in this PhD thesis with the microwave-assisted solvothermal synthesis, demonstrating that the latter is more advantageous as it requires much less time and heat.

Table 2: Comparison of solid-state reaction synthesis and microwave-assisted solvothermal synthesis conditions used in this PhD.

Parameters	Microwave-assisted	High temperature
Temperature	170°C	800°C
Time	15 min	48 h

2.1.2. Synthesis and characterisation of chalcopyrite $\text{CuIn}_{0.7}\text{Ga}_{0.3}\text{S}_2$ (CIGS)

As mentioned before, the chalcopyrite $\text{CuIn}_{0.7}\text{Ga}_{0.3}\text{S}_2$ (noted CIGS-MW) was prepared by MW-ST synthesis, by modifying the CuInS_2 protocol in order to introduce gallium. The syntheses carried out and the different experimental parameters considered are summarised in the Table 3 below. Only the samples shown in table have been characterised, as other samples prepared have equivalent protocols.

Table 3: Summary table of $\text{CuIn}_{0.7}\text{Ga}_{0.3}\text{S}_2$ syntheses chosen for characterisation.

Chalcopyrite	Precursor		Excess 30% Ga	Volume (mL)		Pre-stirring 30'	Temperature (°C)		Synthesis time	
	Glove box	Stock solution		20	10		170	200	15'	1 h
CIGS-MW-1		X		X			X		X	
CIGS-MW-2	X			X			X			X
CIGS-MW-3		X	X		X	X	X		X	
CIGS-MW-4		X	X		X	X		X	X	

The CIGS-MW-1 sample was synthesised at 170°C for 15', without excess of any precursor and using stock solutions. This protocol minimised sources of error and optimised glove box working time. Before carrying out structural studies, a chemical analysis by STEM-EDX mapping was performed (see Figure 10).

The table inserted in Figure 10 compares atomic ratios of experimental average composition of nanograins, with theoretical ones of the targeted composition $\text{CuIn}_{0.7}\text{Ga}_{0.3}\text{S}_2$. Unfortunately, the expected amount of Ga is not reached. In addition, the chemical contrast observed in EDX maps is not homogeneous, revealing the coexistence of different compositions.

In view of these results, several hypotheses can be considered: i) the reaction is not complete and ii) gallium stock solution degraded over time. In order to check these two hypotheses, CIGS-MW-2 sample was therefore synthesised with a longer reaction time (1 h) using glove box precursors, to avoid any possible instability of the stock solutions over time.

EDX mapping of the CIGS-MW-2 sample (Figure 11) still shows an inhomogeneous chemical composition of the agglomerates and a notable gallium deficit (see table in Figure 11). We can therefore conclude that increasing the synthesis time is not relevant. However, the addition of an excess of gallium during synthesis is certainly necessary.

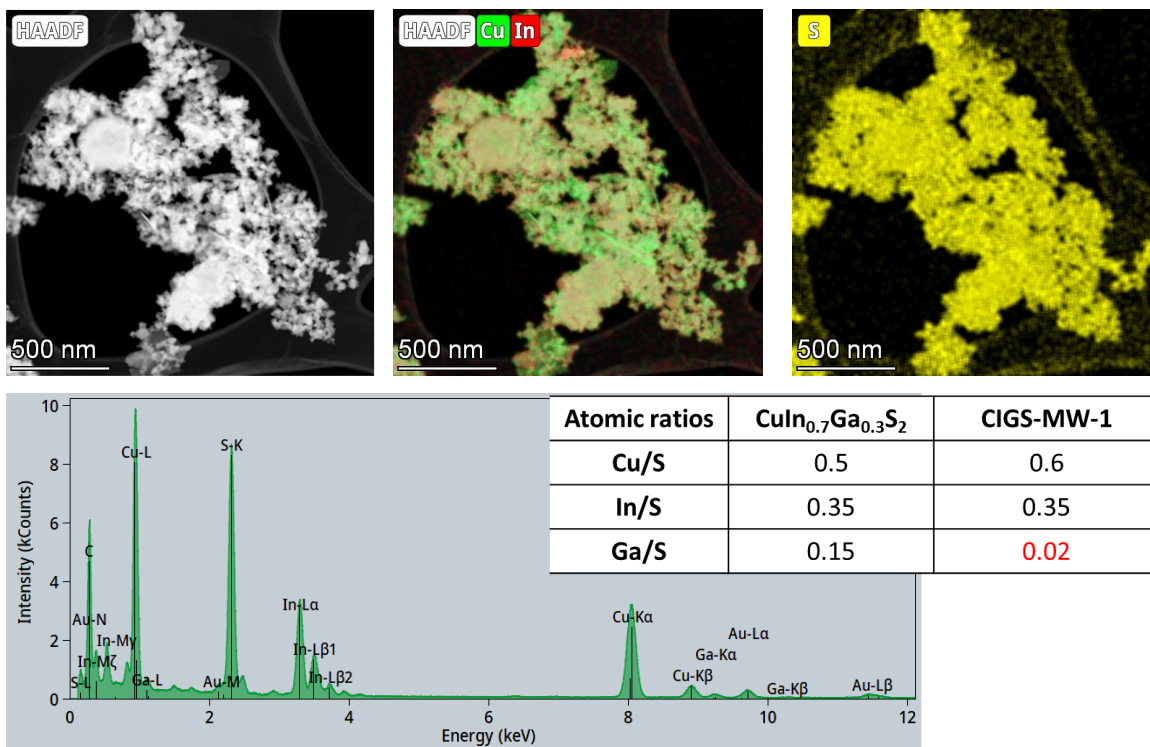


Figure 10: HAADF image and EDX mapping of CIGS-MW-1 nanograins revealing an inhomogeneous sample. The inserted table compares atomic ratios of experimental average composition of the nanograins agglomerates, with theoretical ones of the chalcopyrite $\text{CuIn}_{0.7}\text{Ga}_{0.3}\text{S}_2$. A significant gallium deficit is highlighted.

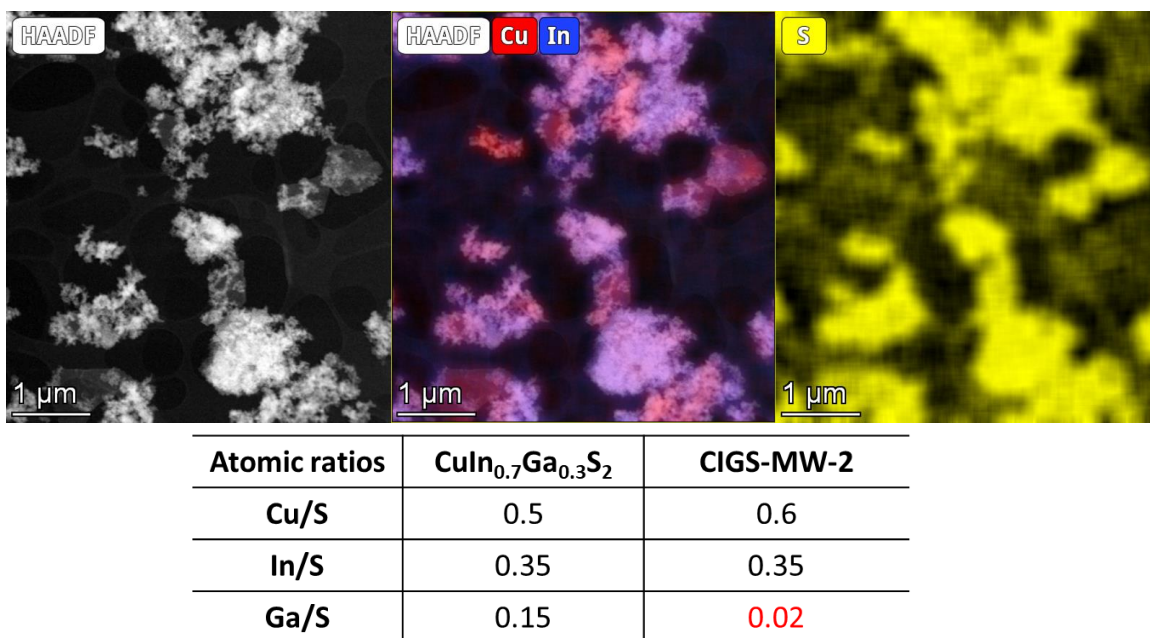


Figure 11: EDX mapping of sample CIGS-MW-2 showing an inhomogeneous chemical composition of the nanograins agglomerates. A significant gallium deficit compared to the target composition $\text{CuIn}_{0.7}\text{Ga}_{0.3}\text{S}_2$ is noted (see inserted table).

Consequently, CIGS-MW-3 and CIGS-MW-4 compounds were synthesised with an excess of 30% gallium using stock solutions. The synthesis volume was reduced to 10 mL (i.e. 2.5 mL of each basic stock solutions), in order to facilitate temperature and precursors homogenisation in the reactor. For CIGS-MW-4, the temperature reaction was also increased up to 200°C.

The CIGS-MW samples synthesised with a gallium excess are homogeneous in composition. Although EDX analyses still show a deficit of Ga, the composition of nanocrystals is compatible with a chalcopyrite-type structure, slightly richer in indium and less rich in gallium than targeted composition (see table in Figure 12). The electron diffraction pattern shown in Figure 12 confirms that agglomerates are made up of nanocrystals, 20-30 nm sized approximately according to TEM image.

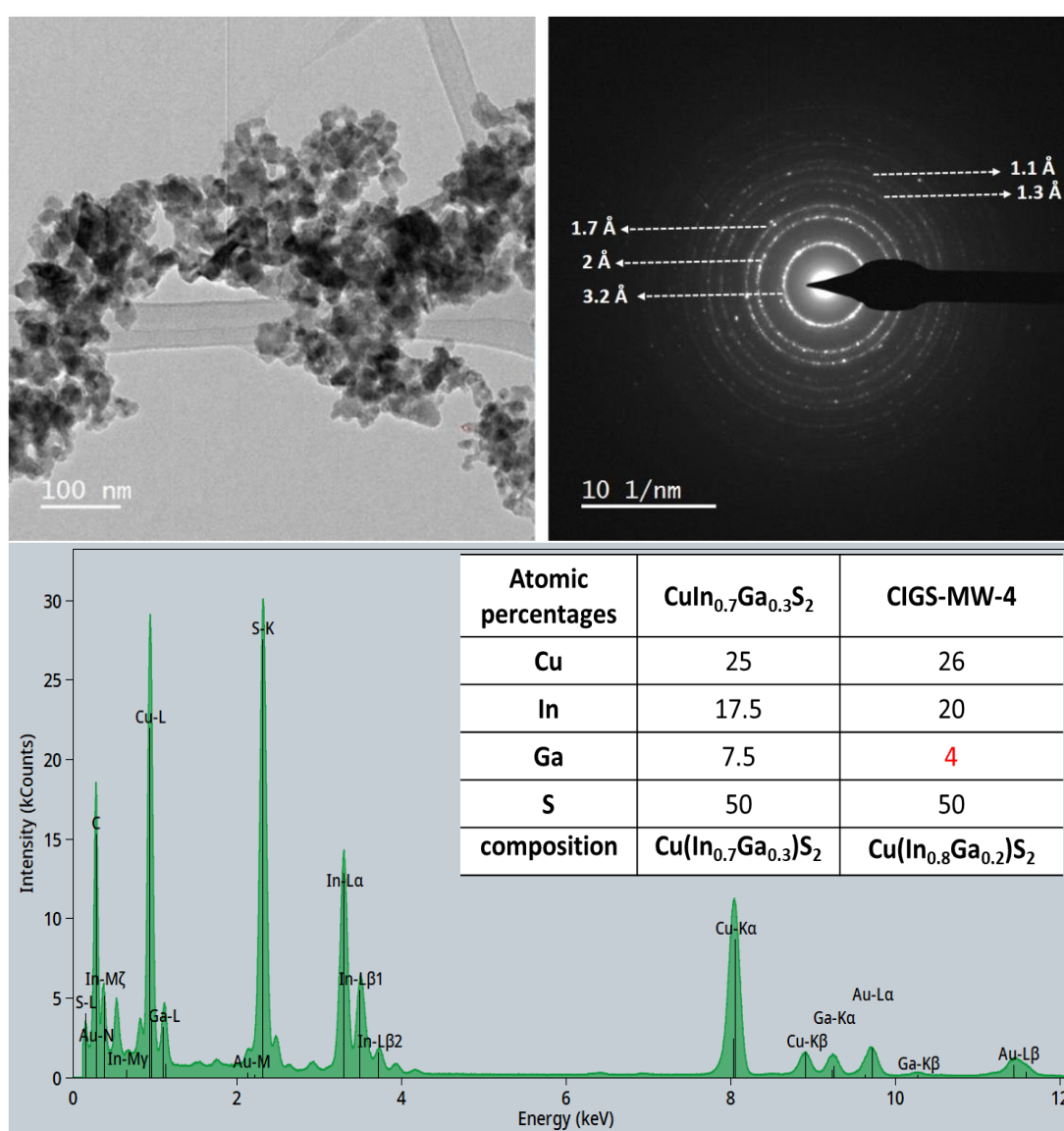


Figure 12: EDX spectrum of CIGS-MW-4 and TEM image showing agglomerates of nanocrystals. The inserted table presents CIGS-MW-4 atomic percentages obtained from EDX compared to theoretical ones.

As shown in Figure 13, X-ray diffraction patterns of CIGS-MW-3 and CIGS-MW-4 are identical. As expected for nanocrystals, reflections are significantly wide. Even though, the X-ray profile overlap quite well with that of CIGS prepared at high temperature (CIGS-HT), used as a reference in this work. In addition, the interplanar distances measured in the ED pattern shown in Figure 20, correspond well to a chalcopyrite-type structure. We can therefore expect that CIGS-MW compounds exhibit a chalcopyrite-type structure.

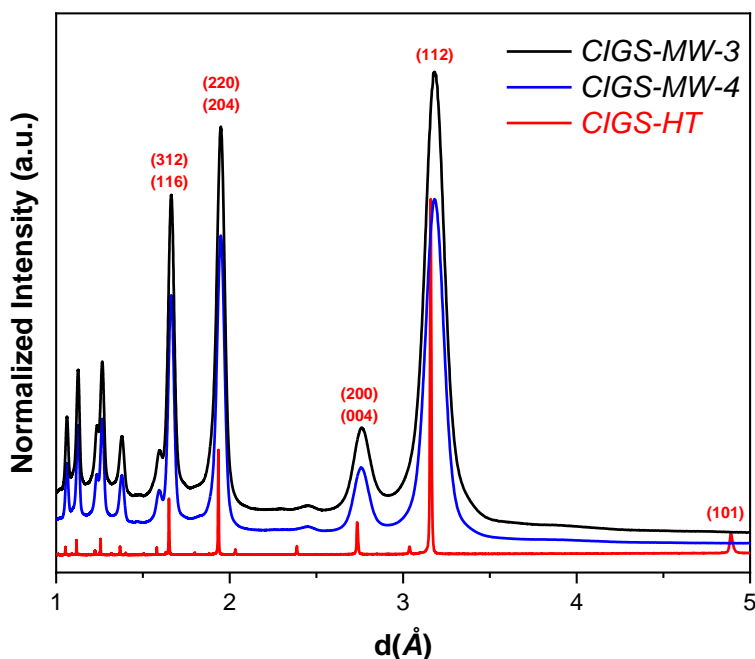


Figure 13: X-ray diffraction patterns of CIGS-MW-3 and CIGS-MW-4 compounds compared to that of CIGS-HT.

Raman spectroscopy in fingerprint mode, allowed us to confirm a chalcopyrite structural type. Figure 14 compares Raman spectra of CIGS-MW-3 and CIGS-MW-4 measured at 514 nm to that of the reference CIGS-HT. The characteristic peak at 294 cm^{-1} which is the vibrational signature of the chalcopyrite-type structure⁵⁷, is clearly observed in both compounds prepared.

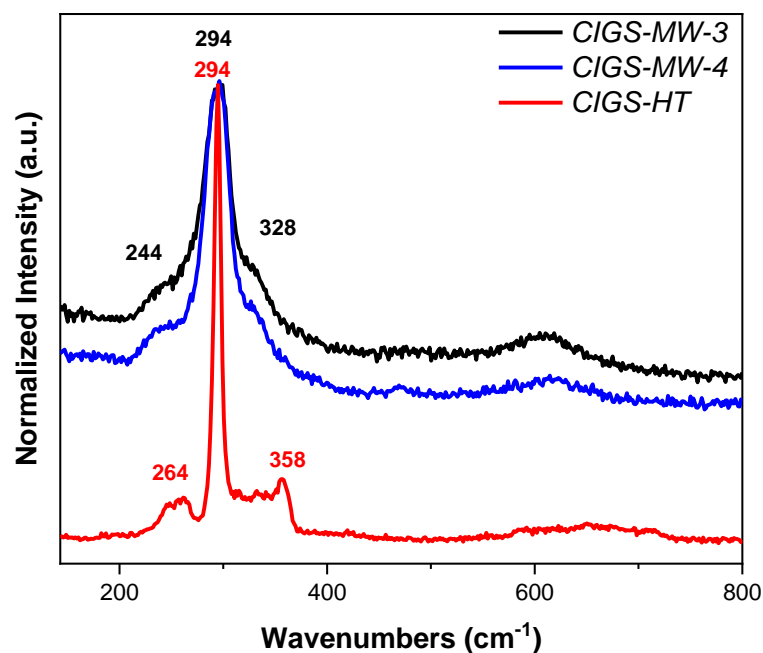


Figure 14: Raman spectra measured at 514 nm of CIGS-MW-3 and CIGS-MW-4 compounds compared to that of CIGS-HT.

As shown in Figure 15, the optical gap values of CIGS-MW-3 and CIGS-MW-4 measured by diffuse reflectance (close to 1.5 eV), are close to that of CIGS-HT (1.6 eV) but slightly lower, as expected for a chalcopyrite richer in indium.⁵⁸

These results validates the Ga-excess protocol presented here, to prepare a quaternary chalcopyrite $\text{Cu}(\text{In,Ga})\text{S}_2$ by microwave-assisted solvothermal synthesis. As two compounds are identical, the lowest reaction temperature will be retained (i.e. 170°C).

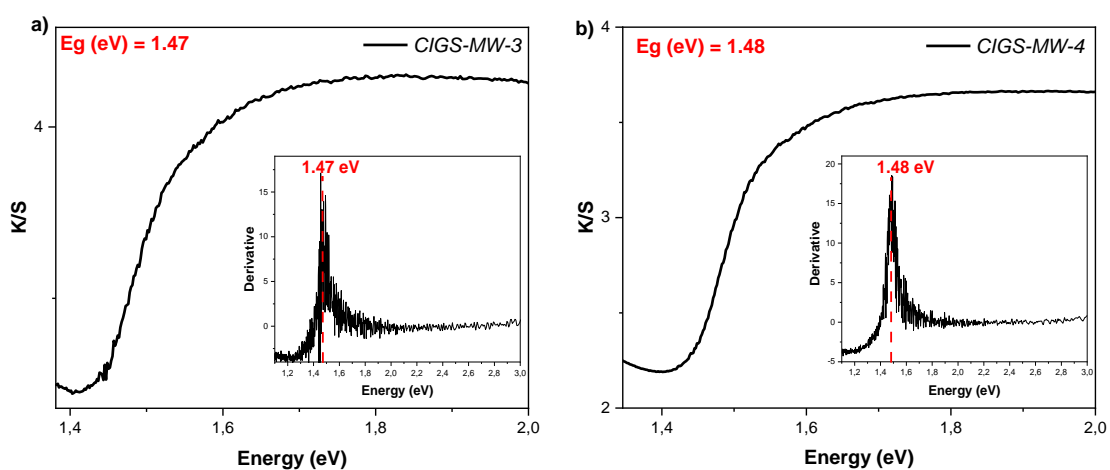


Figure 15: Kubelka-Munk transformed reflectance spectra of a) CIGS-MW-3 and b) CIGS-MW-4 compounds.

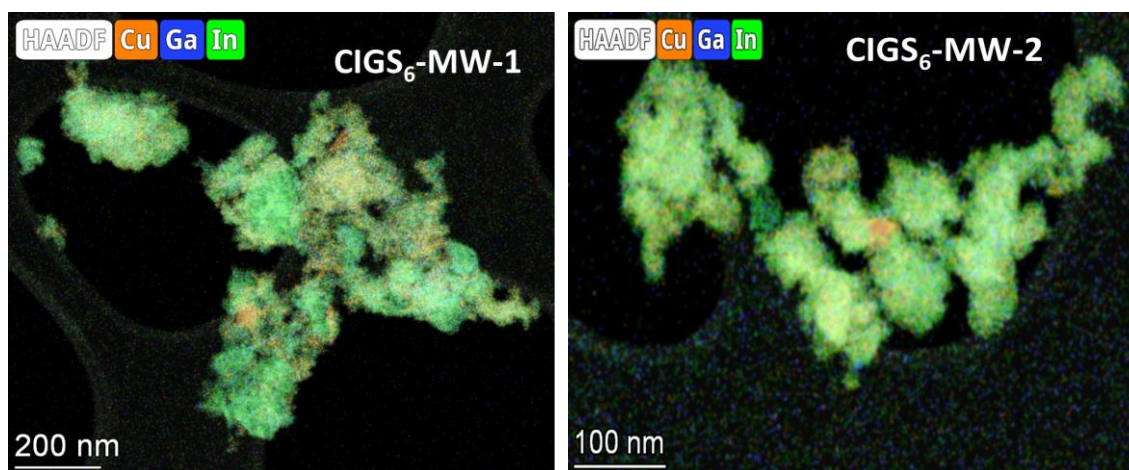
2.1.3. Synthesis and characterisation of $\text{Cu}_{1.44}\text{In}_{2.77}\text{Ga}_{0.76}\text{S}_6$ (CIGS₆)

Different protocols were tried to obtain CIGS₆ nanopowders (noted CIGS₆-MW). The Table 4 summarises the synthesis conditions for each sample. As in the case of CIGS-MW, although various synthesis were produced for each of the protocols investigated, only those presented in the table were fully characterised and could therefore be presented in this report.

Table 4: Summary table of CIGS₆-MW syntheses selected for characterisation.

CIGS ₆	Precursor		Excess		Volume (mL)		Temperature (°C)				Synthesis time		
	Glove box	Stock solution	30% Ga	50% S	10	20	100	160	170	190	15'	30'	1h
CIGS ₆ -MW-1	X					X			X		X		
CIGS ₆ -MW-2		X				X				X	X		
CIGS ₆ -MW-3	X				X				X			X	
CIGS ₆ -MW-4		X	X	X	X				X		X		
CIGS ₆ -MW-5		X	X	X	X				X			X	

The CIGS₆-MW-1 sample was synthesised according to the initial protocol: 170°C for 15' in 20 mL without any excess gallium. EDX mapping (Figure 16) shows that the chemical composition of the agglomerates of nanograins is not homogeneous. The average composition of the sample is close to the target one for copper and indium, but a gallium deficit was once again detected (see table in Figure 16). In view of these results, we decided to study the influence of several parameters: synthesis temperature, reaction time and reaction volume.



Atomic ratio	$\text{Cu}_{1.44}\text{In}_{2.77}\text{Ga}_{0.76}\text{S}_6$	CIGS ₆ -MW-1	CIGS ₆ -MW-2
Cu/S	0.24	0.2	0.2
In/S	0.46	0.4	0.3
Ga/S	0.13	0.07	0.06

Figure 16: EDX mapping of CIGS₆-MW-1 and CIGS₆-MW-2 samples, showing an inhomogeneous chemical composition of the nanograins agglomerates. A significant gallium deficit compared to the target composition $\text{Cu}_{1.44}\text{In}_{2.77}\text{Ga}_{0.76}\text{S}_6$ is detected (see inserted table).

In the case of the CIGS₆-MW-2 sample, we therefore increased the reaction temperature to 190°C while keeping same reaction time and volume. Although the EDX mapping (see Figure 16) shows a sample with a slightly more homogeneous average composition, the gallium deficit is still present.

As temperature had no influence on gallium deficit, we then explored the influence of reaction time and solution volume. To do this, we carried out a synthesis (CIGS₆-MW-3) keeping the reaction temperature at 170°C, while increasing the reaction time (30') and decreasing the synthesis volume (10 mL). EDX mapping (Figure 17) shows a homogeneous grain composition in very good agreement with the target composition $\text{Cu}_{1.44}\text{In}_{2.77}\text{Ga}_{0.76}\text{S}_6$ (see table in Figure 17).

However, the value of the optical gap is 1.3 eV (see Figure 17), which is low for a lamellar compound (i.e. 1.9 - 1.6 eV) but close to that of the chalcopyrite CuInS_2 .⁵⁸ In fact, the composition of the lamellar phase CIGS₆ ($\text{Cu}_{1.44}\text{In}_{2.77}\text{Ga}_{0.76}\text{S}_6$) can also be formulated as a copper-poor chalcopyrite CuInS_2 -type with a partial substitution of copper and indium by gallium and charge balance ensured by vacancies: $(\text{Cu}_{0.48}\text{Ga}_{0.17}\square_{0.35})(\text{In}_{0.92}\text{Ga}_{0.08})\text{S}_2$.

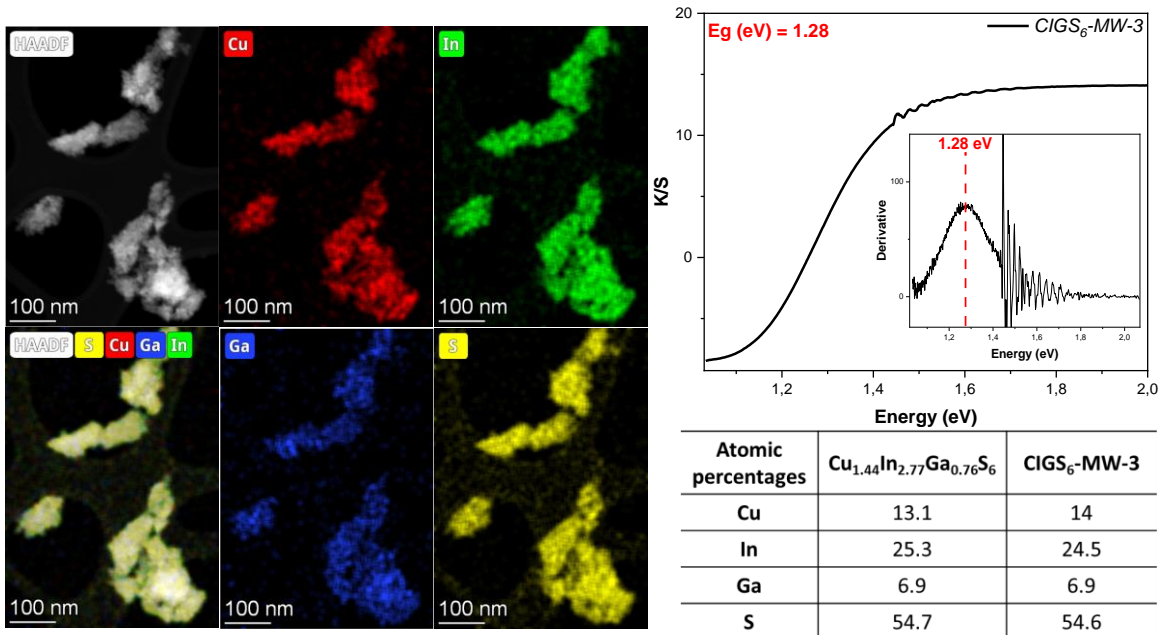


Figure 17: EDX mapping of sample $\text{CIGS}_6\text{-MW-3}$, showing a homogeneous composition of the nanograins agglomerates close to the target composition $\text{Cu}_{1.44}\text{In}_{2.77}\text{Ga}_{0.76}\text{S}_6$ (see inserted table). In the top right, Kubelka-Munk transformed reflectance spectra of $\text{CIGS}_6\text{-MW-3}$ compound.

Raman spectroscopy results do suggest the existence of a lamellar-chalcopyrite mixture (CIGS_6 - CIGS). Indeed, as shown in Figure 18, the $\text{CIGS}_6\text{-MW-3}$ spectrum could be explained by overlapping the spectra of the two references synthesised at high temperature (CIGS-HT and $\text{CIGS}_6\text{-HT}$).

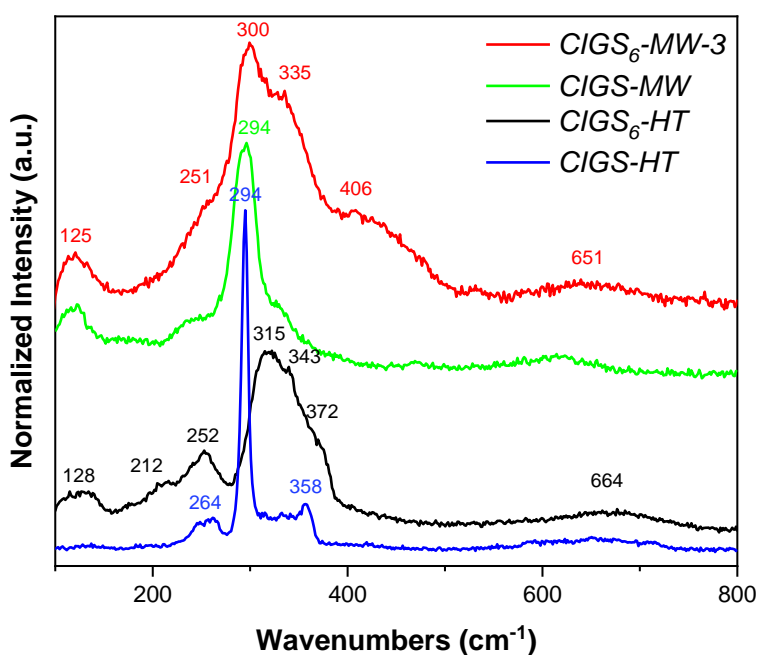


Figure 18: Raman spectra measured at 514 nm of $\text{CIGS}_6\text{-MW-3}$ compared to those of CIGS-MW , $\text{CIGS}_6\text{-HT}$ and CIGS-HT .

In order to favour the formation of the lamellar CIGS_6 phase, which has a much lower Cu/S ratio than chalcopyrite (e.g. 0.24 vs 0.5), we decided to work with an excess of 50% at. of sulphur, for the rest of our investigation. Besides, to promote the reaction of the precursor of gallium, an excess of 30%at. of gallium was also introduced.

Thus, two samples with different reaction times, $\text{CIGS}_6\text{-MW-4}$ (15') and $\text{CIGS}_6\text{-MW-5}$ (30') were prepared. We wanted to know if excess precursors would allow us to obtain nanograins with a homogeneous chemical composition, without having to increase reaction time. In addition, as smaller reaction volumes lead to homogeneous compounds, a volume of 10 mL was selected. As shown in Figure 19, the XRD patterns of both compounds overlap quite well, indicating that the phases involved are the same.

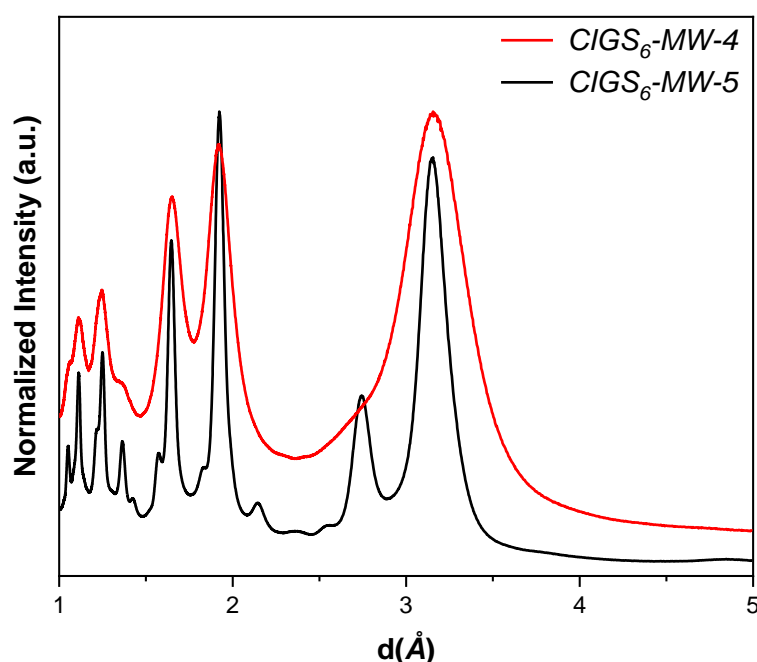


Figure 19: X-ray diffraction patterns of $\text{CIGS}_6\text{-MW-4}$ (15') and $\text{CIGS}_6\text{-MW-5}$ (30').

However, in the case of $\text{CIGS}_6\text{-MW-4}$ (15') X-ray diffraction peak width is significantly greater, probably due to a smaller crystallite size. Indeed, a TEM image of a nanoparticles agglomerate is presented in Figure 20, showing crystallised domains of nanometric size that could explain reflections broadening. As photocatalysis requires the largest possible specific surface area, we chose $\text{CIGS}_6\text{-MW-4}$ for photocatalytic tests. Thus, the reaction time was set to 15 minutes for further microwave experiments.

The EDX mapping of $\text{CIGS}_6\text{-MW-4}$ reveals a chemical composition homogeneous (see Figure 20), in good agreement with the expected one. This time, the optical gap measured is very close to that of the compound prepared at high temperature $\text{CIGS}_6\text{-HT}$ (1.6 eV).

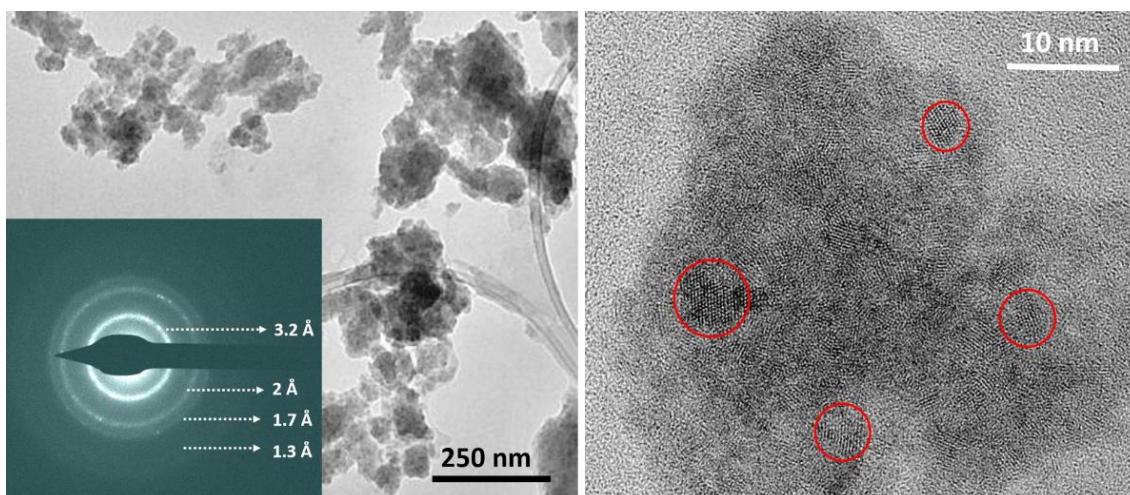


Figure 19: TEM images of CIGS₆-MW-4 (15') showing agglomerates of nanocrystals. In the bottom left, electronic diffraction pattern of the compound CIGS₆-MW-4.

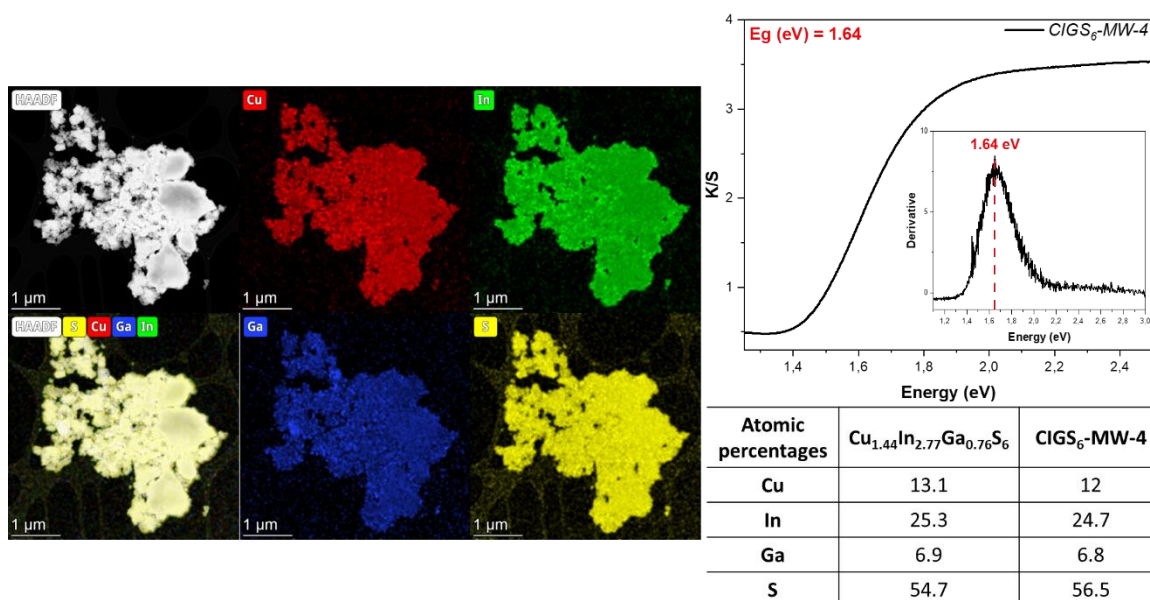


Figure 20: EDX mapping of CIGS₆-MW-4 sample, showing a homogeneous composition of the nanograins agglomerates close to the target composition Cu_{1.44}In_{2.77}Ga_{0.76}S₆ (see inserted table). In the top right, Kubelka-Munk transformed reflectance spectra of CIGS₆-MW-4 compound.

Indeed, the XRD pattern of CIGS₆-MW-4 (see Figure 21) fits quite well with that of the high temperature reference (CIGS₆-HT). However, given peak widths, it is still difficult to rule out the presence of a chalcopyrite as impurity, because their most intense reflections overlap with the main ones of the CIGS₆ phase. The electron diffraction pattern shown in Figure 19 does not make the difference either. Unfortunately, Raman spectroscopy could not rule out the presence of a chalcopyrite phase.

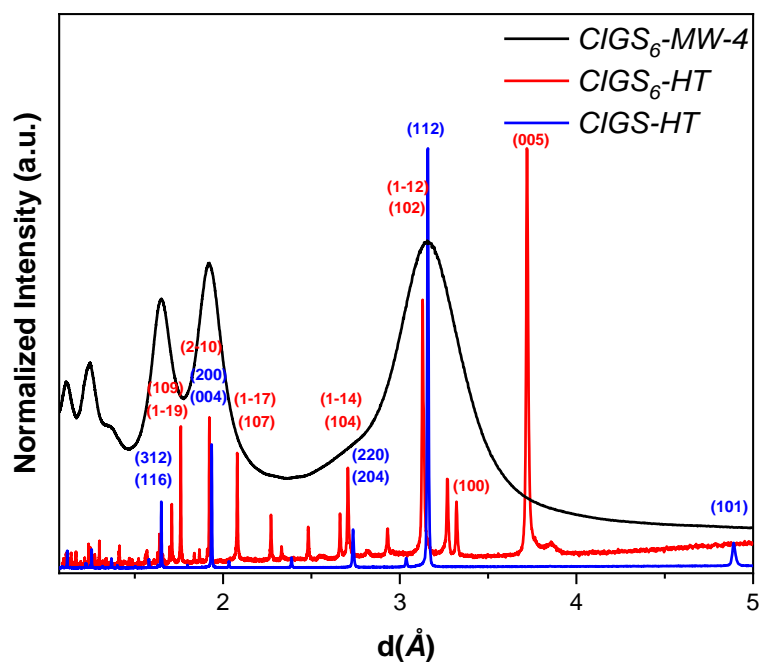


Figure 21: X-ray diffraction patterns of CIGS₆-MW-4 compared to the high temperature standards (CIGS₆ and CIGS chalcopyrite).

In Figure 22, the Raman spectrum of the sample CIGS₆-MW-4 is compared to those of the compounds CIGS₆-HT and CIGS-HT. Again, the overall shape of the spectrum could be explained by overlapping spectra of two high temperatures references.

Considering this uncertainty, we have attempted to develop strategies for obtaining single-phase nanopowders with a CIGS₆-type structure.

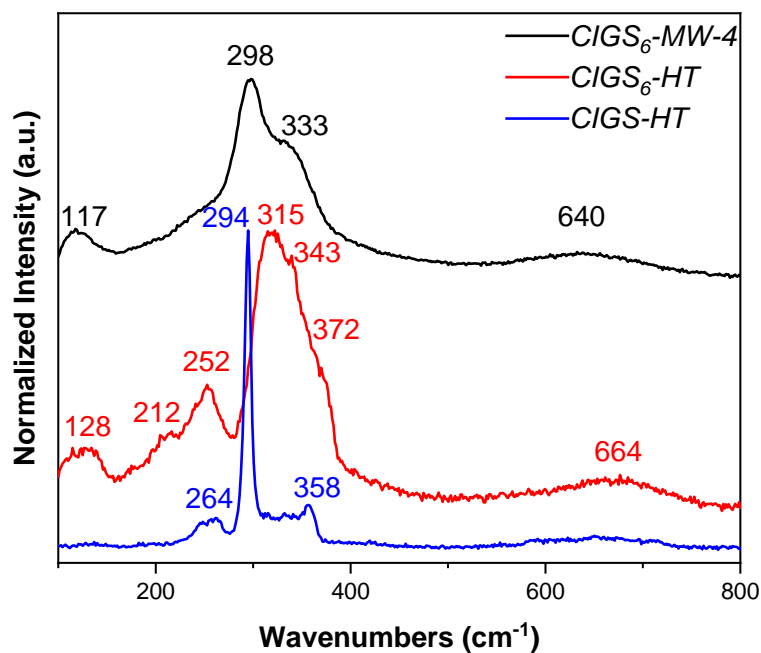


Figure 22: Raman spectra measured at 514 nm of CIGS₆-MW-4 compared to the CIGS and CIGS₆ high temperature powders.

2.2. $\text{Zn}_3\text{In}_2\text{S}_6$ and GaInS_3 approach

In an attempt to prepare nanopowders with a CIGS_6 -type structure without CIGS as impurity, a cationic substitution strategy was implemented. We chose to carry out cationic substitution in two compounds isostructural of CIGS_6 : $\text{Zn}_3\text{In}_2\text{S}_6$ and GaInS_3 . In fact, although these materials have different polymorphs, none exhibits a chalcopyrite-type structure.

- From $\text{Zn}_3\text{In}_2\text{S}_6$ (ZIS): zinc was partially substituted by copper and gallium according to the formula: $\text{Zn}_{3-x}(\text{Ga}_{0.5}\text{Cu}_{0.5})_x\text{In}_2\text{S}_6$ (ZIS-x). As zinc is bivalent, gallium trivalent and copper monovalent, a zinc atom can be replaced by one copper atom and one gallium atom.
- From GaInS_3 : the second strategy consists in gradually substituting gallium by copper in GaInS_3 (GIS) in order to obtain a quaternary compound, according to the formula: $\text{Cu}_3\text{Ga}_{1-x}\text{InS}_3$ (GIS-x). Indeed, GIS presents many polymorphs, some of which have CIGS_n -type structures (Figure 23). Due to the trivalent nature of gallium and the monovalent nature of copper, three copper atoms must replace a gallium atom, in order to maintain the charge neutrality of the compounds.

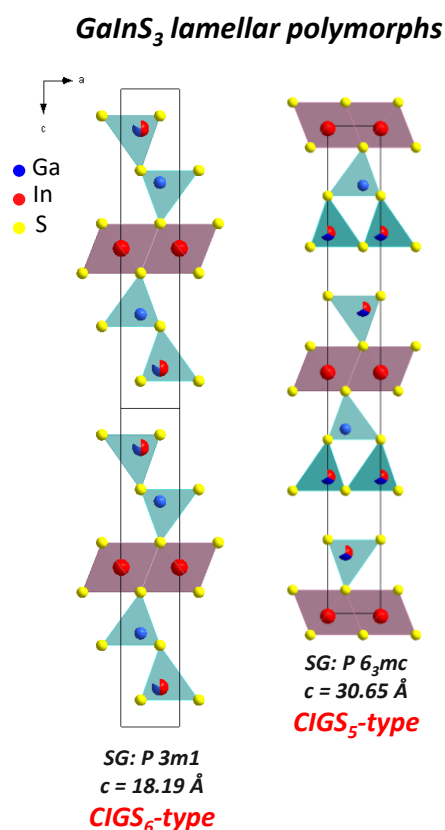


Figure 23: Lamellar polytypes of GaInS_3 : CIGS_6 -type and CIGS_5 -type.

2.2.1. Synthesis and characterization of $Zn_{3-x}(Ga_{0.5}Cu_{0.5})_xIn_2S_6$ series

The synthesis of $Zn_{3-x}(Ga_{0.5}Cu_{0.5})_xIn_2S_6$ (ZIS-x) were performed with a volume of 12.5 mL (5 times 2.5 mL of the stock solution of each compound) within 15 min at 170°C without excess. Three samples were prepared in this thesis: $x=0, 0.3$ and 0.6 (see Table 5).

Table 5: Nomenclature of prepared compounds.

$Zn_{3-x}(Ga_{0.5}Cu_{0.5})_xIn_2S_6$		
Sample code	x	Composition
ZIS	0	$Zn_3In_2S_6$
ZIS-0.3	0.3	$Zn_{2.7}Ga_{0.15}Cu_{0.15}In_2S_6$
ZIS-0.6	0.6	$Zn_{2.4}Ga_{0.3}Cu_{0.3}In_2S_6$

Using this synthesis method, the copper-free ZIS compound could not be obtained as a single-phase product, even when using an excess of precursors. However, ZIS-0.3 and ZIS-0.6 were able to be synthesised from stoichiometric ratios. EDX analysis were undertaken on ZIS-0.3 and ZIS-0.6 compounds. As shown in Table 6, experimental averaged compositions are similar to the targeted ones.

Table 6: Summary table of targeted and experimental compositions measured by EDX of the ZIS compounds family.

Element	Atomic % ZIS-0.3		Atomic % ZIS-0.6	
	Theoretical	Experimental	Theoretical	Experimental
Zn	24.5	24.0	21.8	20.9
In	18.1	17.6	18.1	18.3
Cu	1.4	2.0	2.7	3.8
Ga	1.4	1.7	2.7	2.5
S	54.5	54.6	54.5	54.6

However, EDX maps for ZIS-06 nanopowders (see Figure 24) show an inhomogeneous distribution of gallium, copper and zinc. Moreover, the atomic fraction profile indicates a correlation between these elements (e.g. zinc content decreases as gallium content increases). This chemical inhomogeneity could explain the extended transitions (i.e. over several eV) observed in the reflectance spectra of ZIS-0.3 and ZIS-0.6 compounds (see Figure 25).

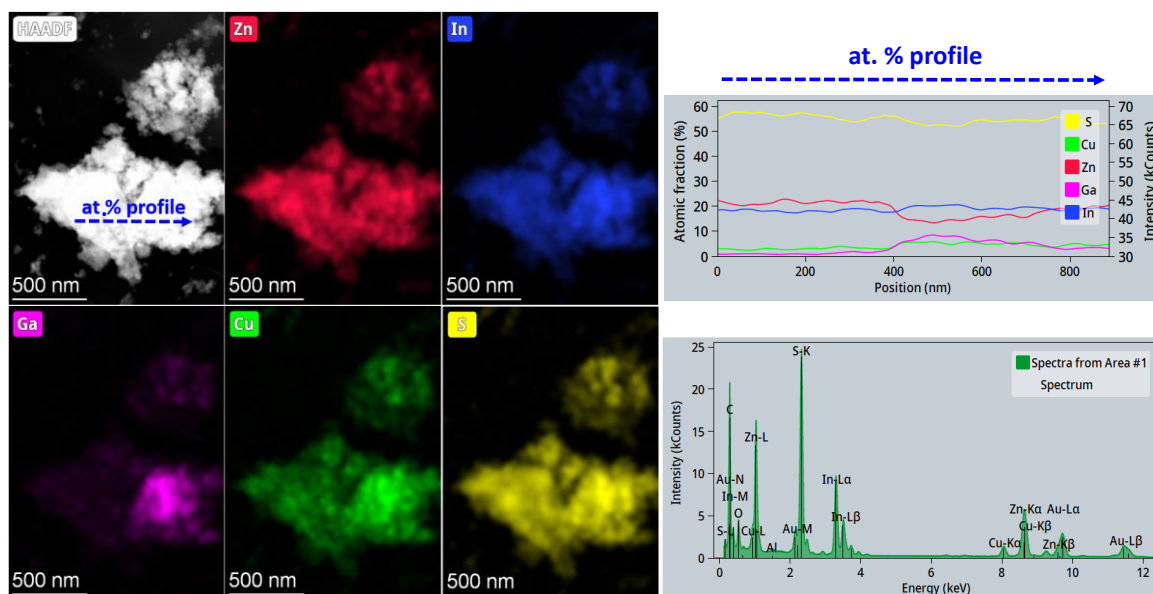


Figure 24: EDX mapping and atomic fraction profile of ZIS-0.6, showing the inhomogeneity of the sample. In the bottom right, the EDX spectrum of ZIS-0.6 compound.

The substitution of zinc by copper and gallium leads to an optical gap decreasing. Thus, although the gap value of the ZIS-0.3 compound (2.7 eV) is similar to that of $\text{Zn}_3\text{In}_2\text{S}_6$ (2.8 eV), that of ZIS-0.6 is significantly lower (2 eV).

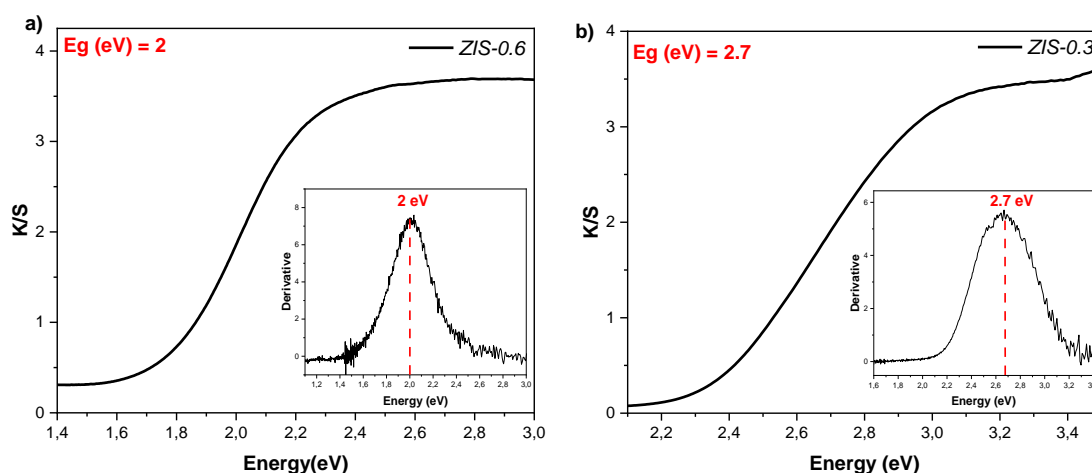


Figure 25: Kubelka-Munk transformed reflectance spectra of the a) ZIS-0.6 and b) ZIS-0.3 samples.

As shown in Figure 26, XRD patterns of ZIS-0.3 and ZIS-0.6 overlap perfectly, indicating a similar $\text{Zn}_3\text{In}_2\text{S}_6$ type structure. However, taking into account the reflections broadening observed in X-ray patterns, Raman spectroscopy was carried out to confirm structural conclusions.

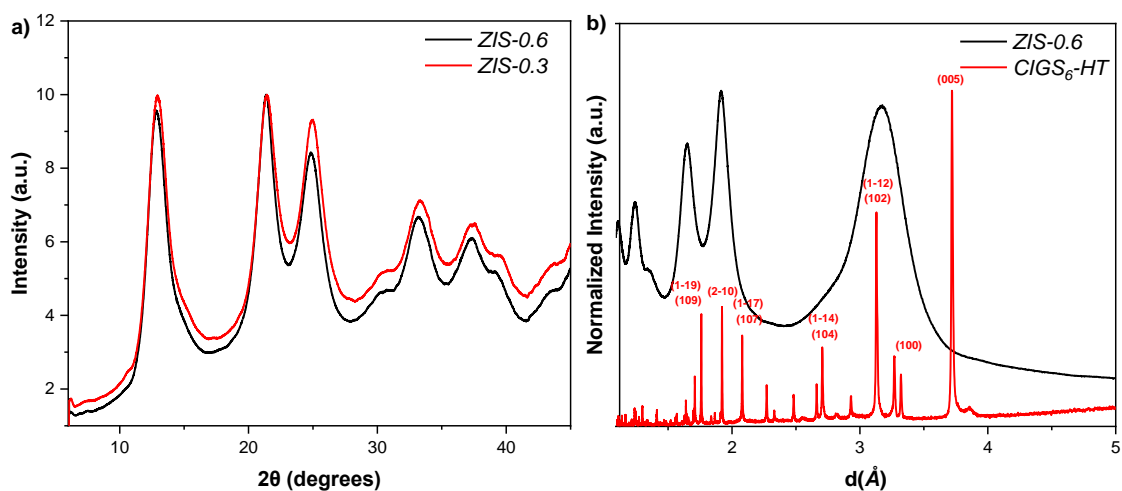


Figure 26: X-ray patterns of a) the prepared ZIS samples and b) the ZIS-0.6 sample compared to CIGS₆-HT.

In Figure 27 a, the spectra of the ZIS-0.3 and ZIS-0.6 samples overlap, indicating that the nature of the phases involved is the same. Moreover, the Raman spectra obtained are comparable to that of Zn₃In₂S₆ Raman in the literature^{59,60} (see Figure 27 b). According to the literature, the two main bands observed in Figure 27a are associated with vibration modes characteristic of the layer stacking observed in ZIS_n compounds. The first band around 244 cm⁻¹ is attributed to the vibration of sulphur atoms in the Van der Waals gap (A_{1g} mode), while the second band at 344 cm⁻¹ is attributed to the octahedral vibrational mode of In₂S₃ (E_g mode).^{59,60} Therefore, Raman spectroscopy confirms that ZIS-0.3 and ZIS-0.6 compounds exhibit a Zn₃In₂S₆-type structure.

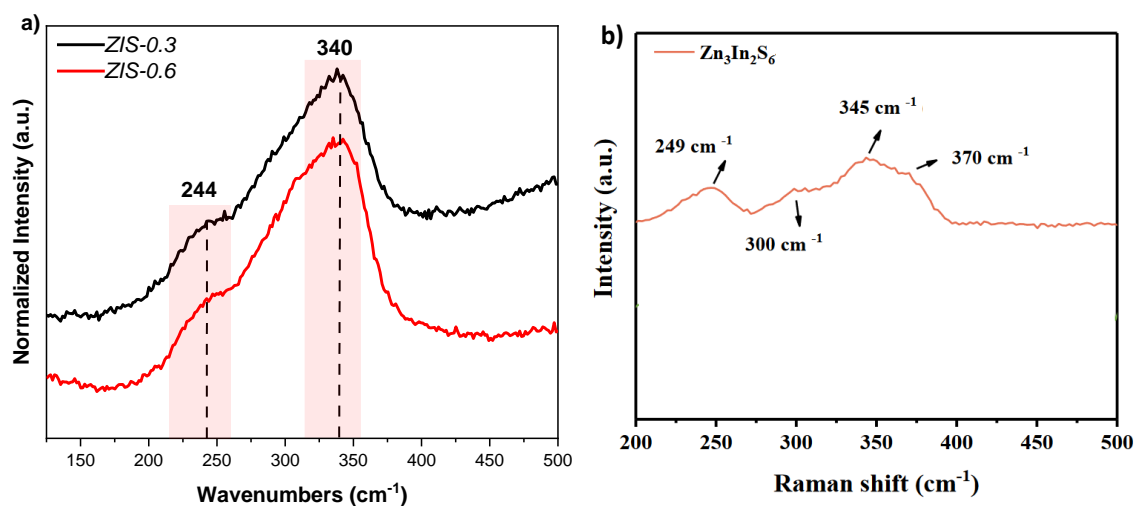


Figure 27: a) Raman spectra at 514 nm of ZIS-0.3 and ZIS-0.6 samples. b) Raman spectra of Zn₃In₂S₆. Figure modified from the reference Luo et al.⁶⁰

2.2.2. Synthesis and characterization of the $\text{Cu}_{3x}\text{Ga}_{1-x}\text{InS}_3$ compounds

The GaInS_3 compound displays lamellar polymorphs, as already mentioned. Following this strategy, we can approach the composition of CIGS_n by replacing the gallium gradually with copper to prepare a lamellar compound.

The procedure followed for the synthesis is the same: using a reaction volume of 10 mL for 15 min at 170 °C from mother solutions and without any precursors excess.

$\text{Cu}_{3x}\text{Ga}_{1-x}\text{InS}_3$ (GIS) samples were prepared for various x values. Regardless, only two samples will be provided in this thesis: a copper-poor compound GIS-0.1 and a copper-rich compound GIS-0.4 (Table 7).

Table 7: Sample codes of prepared compounds.

$\text{Cu}_{3x}\text{Ga}_{1-x}\text{InS}_3$		
Sample code	x	Composition
GIS-0.1	0.1	$\text{Cu}_{0.3}\text{Ga}_{0.9}\text{InS}_3$
GIS-0.4	0.4	$\text{Cu}_{1.2}\text{Ga}_{0.6}\text{InS}_3$

According to EDX analysis summarised in Table 8, the copper-rich sample GIS-0.4 reveals a chemical composition closer to that of chalcopyrite. This outcome was validated by XRD and Raman spectroscopy by comparing to the CIGS-HT reference data (Figures 28 and 29 a).

Table 8: Theoretical and experimental compositions measured by EDX spectroscopy.

Element	Atomic % GIS-0.1		Atomic % GIS-0.4		Atomic % CIGS
	Theoretical	Experimental	Theoretical	Experimental	
Cu	6.0	5.5	21.0	27.4	25.0
In	19.0	22.2	17.0	17.3	17.5
Ga	17.3	14.6	10.0	5.3	7.5
S	58.0	57.8	52.0	50.0	50.0

Indeed, both XRD patterns superimpose and the main vibrational band of the Raman spectra of GIS-0.4 located at 294 cm^{-1} , is characteristic of a chalcopyrite-type structure. Besides, the Raman spectra is identical to that obtained for CIGS-MW (Figure 29 b).

Further, the optical gap was found to be 1.5 eV that is quite close to that of the chalcopyrite $\text{CuIn}_{0.7}\text{Ga}_{0.3}\text{S}_2$ prepared at high temperature (CIGS-HT) 1.6 eV, confirming once again the structural identification.

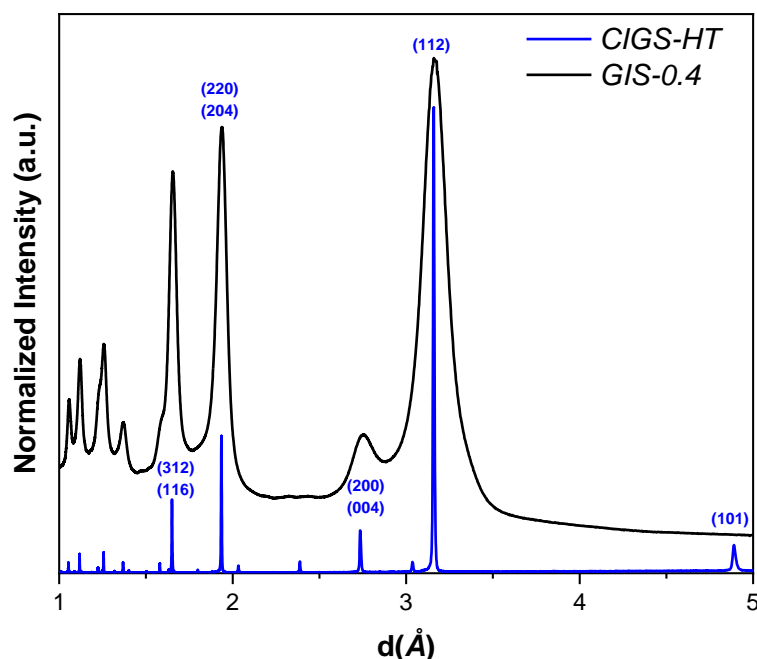


Figure 28: X-ray pattern of copper rich sample GIS-0.4 compared to that of CIGS chalcopyrite.

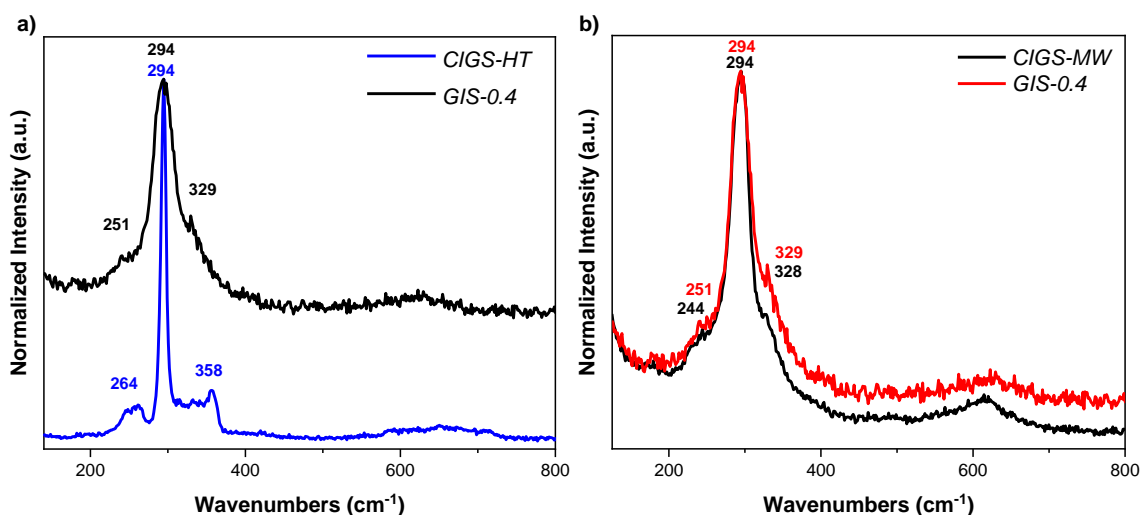


Figure 29: Raman spectra of GIS-0.4 copper rich sample compared to a) CIGS chalcopyrite high temperature reference and b) CIGS-MW chalcopyrite prepared by microwaves.

For GIS-0.1, EDX elemental mapping (Figure 30) shows a homogeneous chemical composition close to the target one. As mentioned above, GaInS_3 exhibits two lamellar polymorphs with CIGS_6 and CIGS_5 -type structures. Therefore, we have reformulated GIS-0.1 (Table 9) according to these two polytypes. The chemical compositions of corresponding reference compounds, prepared at high temperature, are also presented for comparison. Note that the composition of GIS-0.1 is closer to that of the reference CIGS_5 -HT than to that of the compound CIGS_6 -HT. We can therefore expect that GIS-0.1 will exhibit a CIGS_5 -type structure.

Table 9: Reformulated chemical compositions of GIS-0.1 based on GaInS_3 lamellar polymorphs of CIGS_6 and CIGS_5 type structures, compared to the reference compounds.

<i>GIS-0.1 as polytype CIGS_6-type</i>	<i>CIGS_6-HT</i>	<i>GIS-0.1 as polytype CIGS_5-type</i>	<i>CIGS_5-HT</i>
$\text{Cu}_{0.6}\text{Ga}_{1.8}\text{In}_2\text{S}_6$	$\text{Cu}_{1.44}\text{In}_{2.77}\text{Ga}_{0.76}\text{S}_6$	$\text{Cu}_{0.5}\text{Ga}_{1.5}\text{In}_{1.7}\text{S}_5$	$\text{Cu}_{0.65}\text{In}_{1.75}\text{Ga}_{1.4}\text{S}_5$

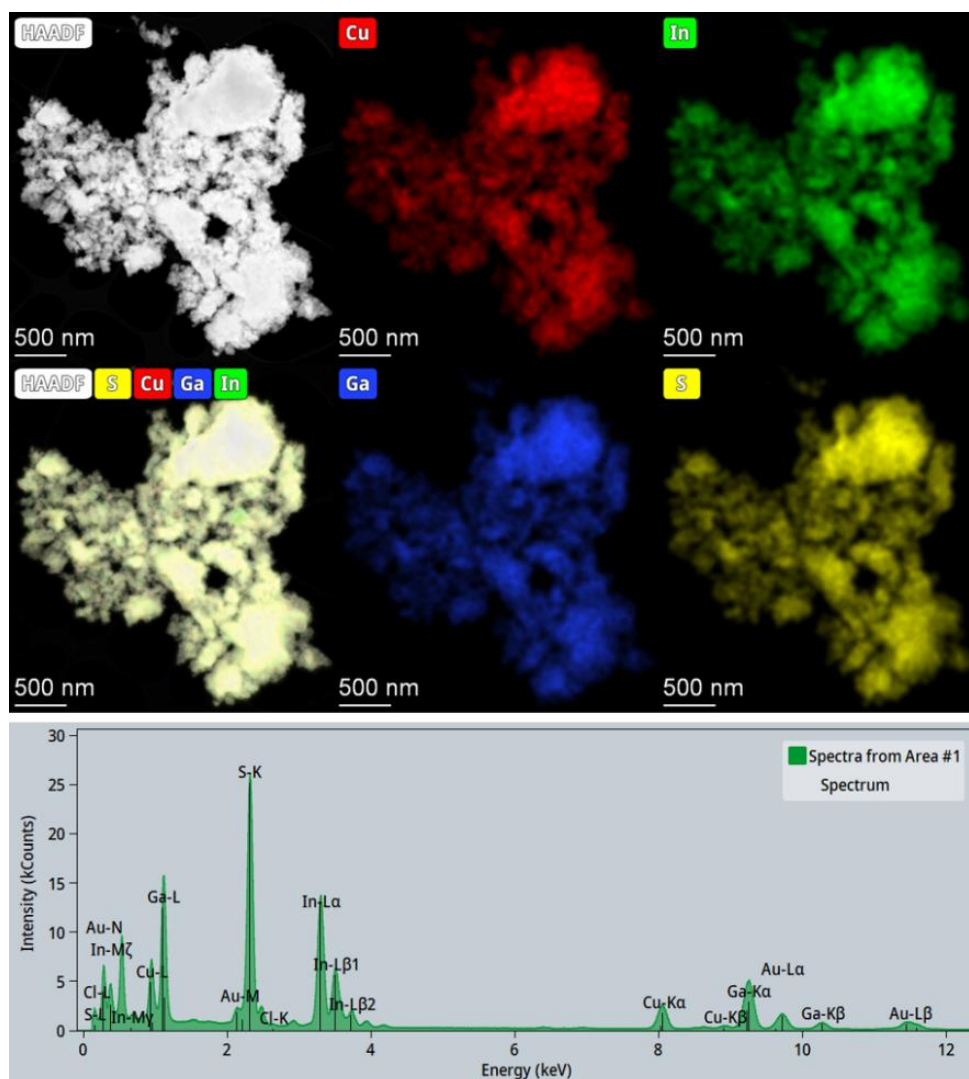


Figure 30: EDX mapping and EDX spectrum of GIS-0.1 copper poor compound.

X-ray diffraction does not allow us to differentiate between two polytypes, since both structures could explain the DRX pattern of compound GIS-0.1 (Figure 31). However, the difference could be done using Raman spectroscopy. As shown in Figure 32 a, it is possible to differentiate CIGS_n lamellar phases from chalcopyrite one, based on the vibrational modes connected to in-plane vibrations of S-atoms in the vdW gap (around 130 and 260 cm^{-1}) and those corresponding to In_2S_3 octahedral layers

(i.e. 340 - 390 cm^{-1}). These vibrational modes do not exist in the chalcopyrite structure, where all cations are tetrahedrally coordinated by sulphur atoms. Moreover, it seems also possible to differentiate between the two lamellar compounds, based on the position of their most intense vibration mode: 340 cm^{-1} for CIGS_5 and 315 cm^{-1} CIGS_6 .

As shown in Figure 32 b, the main mode in the Raman spectre of GIS-0.1 appears to 340 cm^{-1} , which confirms a CIGS_5 structural type. Indeed, the value of the optical gap 1.8 eV (Figure 33) and the colour of the powder (dark red) are quite close of those of CIGS_5 (1.9 eV).

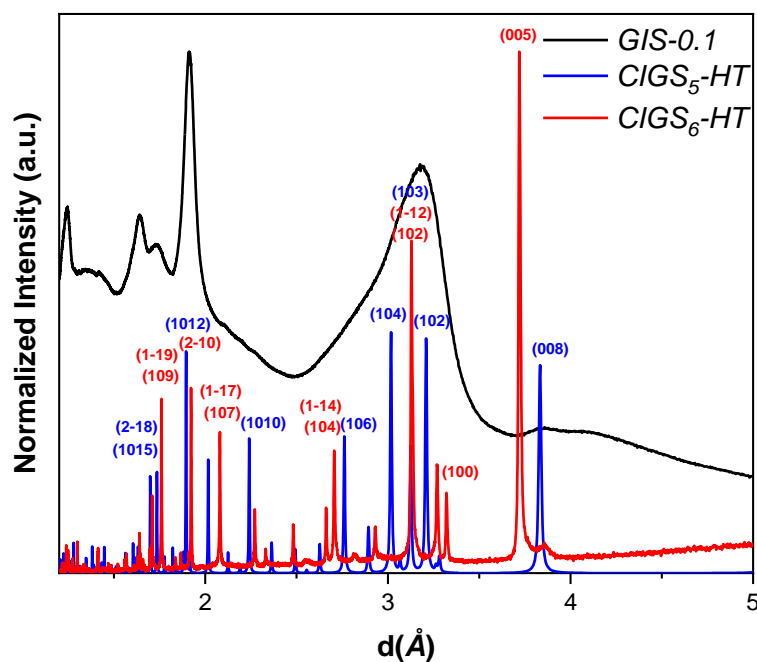


Figure 31: X-ray patterns of GIS-0.1 compared to CIGS_5 and CIGS_6 references.

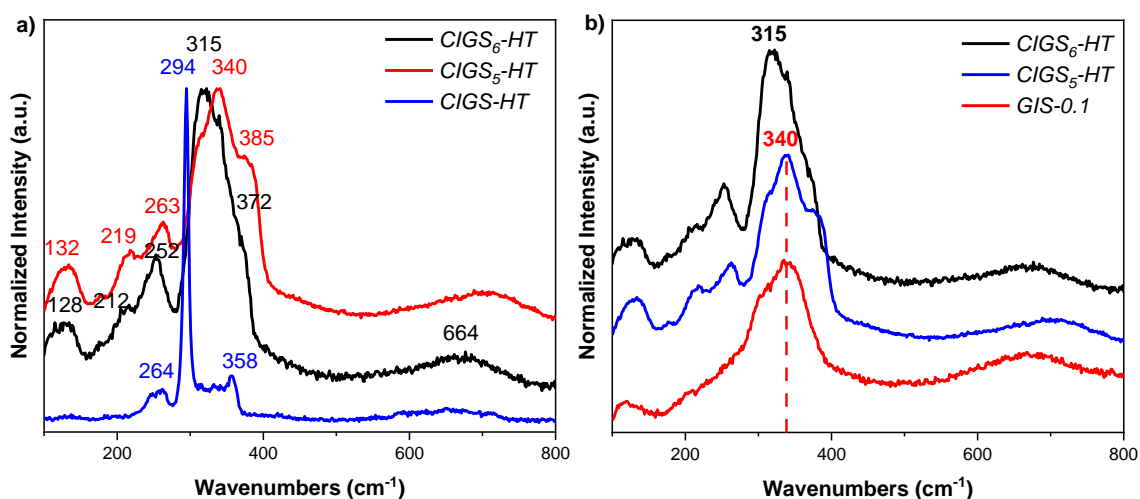


Figure 32: Raman spectra a) of reference compounds $\text{CIGS}_6\text{-HT}$, $\text{CIGS}_5\text{-HT}$ and $\text{CIGS}_6\text{-HT}$ and b) of GIS-0.1 compared to the CIGS_5 and CIGS_6 references.

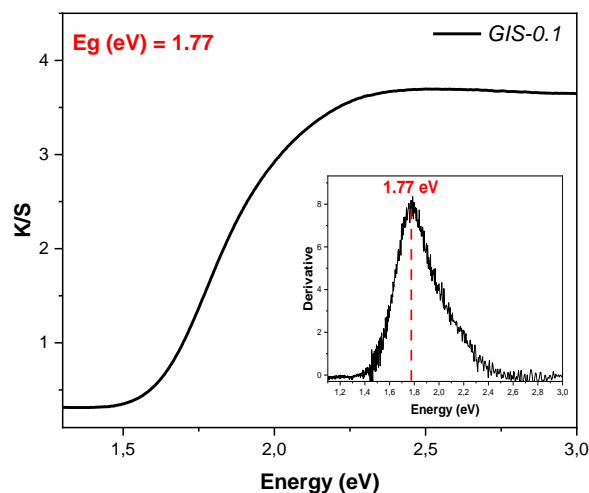


Figure 33: Kubelka-Munk transformed reflectance spectrum of GIS-0.1 copper poor sample.

2.3. Summary

Microwave-assisted solvothermal protocols were adapted from the reference CuInS_2 ,⁵⁶ then developed with gallium addition. Targeted nanopowders were successfully prepared. However, a systematic study is necessary to optimise the synthesis conditions for each compound.

Photocatalysts based on nanopowders of CIGS and CIGS_6 have been obtained. In addition, the two alternative strategies implemented to obtain CIGS_6 -type compounds without CIGS as impurity were effective. In fact, two additional photocatalysts were prepared: ZIS-0.6, derived from $\text{Zn}_3\text{In}_2\text{S}_6$, which has a CIGS_6 type structure, and GIS-0.1, derived from GaInS_3 , with a CIGS_5 type structure. Structural identification was essentially carried out by Raman spectroscopy.

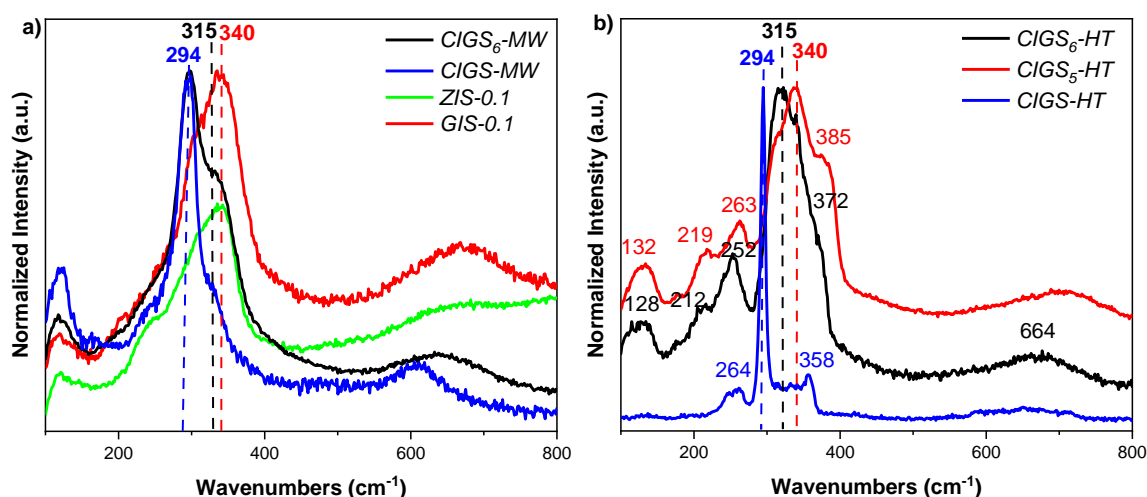


Figure 34: Raman spectra a) of CIGS and all the lamellar compounds prepared by microwave-assisted solvothermal synthesis and b) of reference compounds CIGS-HT, CIGS_5 -HT and CIGS_6 -HT.

Indeed, as shown in Figure 34, the vibrational modes connected to in-plane vibrations of S-atoms in vdW gap and to In_2S_3 octahedral layers make it easy to distinguish between CIGS_n compounds and chalcopyrite. In addition, the transition from one structural type to another in lamellar compounds (e.g. $\text{CIGS}_6 \rightarrow \text{CIGS}_5$) is accompanied by a shift in band positions, enabling them to be identified.

Beforehand, BET (Brunner-Emmett-Teller) measurement is used to characterise the microstructure and measure the specific surface of the samples (see Table 10). The specific surface of CIGS -MW was estimated at a value of about $60 \text{ m}^2/\text{g}$ that is 10 times greater than high temperature. Similarly, GIS-0.1 and ZIS-0.6 were provided with a high specific surface $90 \text{ m}^2/\text{g}$ and $60 \text{ m}^2/\text{g}$ respectively, while only $15 \text{ m}^2/\text{g}$ for CIGS_6 -MW.

Table 10 summarises some characteristics of these compounds, on which we will perform photocatalysis tests.

Table 10: Samples selected for photocatalytic tests.

Structure type	CIGS_n -type			CIGS chalcopyrite
	CIGS_6 -type		CIGS_5 -type	
Samples	CIGS_6 -MW	ZIS-0.6	GIS-0.1	CIGS -MW
Experimental composition	$\text{Cu}_{1.27}\text{In}_{2.62}\text{Ga}_{0.72}\text{S}_6$	$\text{Zn}_{2.3}\text{Ga}_{0.27}\text{Cu}_{0.41}\text{In}_{2.01}\text{S}_6$	$\text{Cu}_{0.47}\text{Ga}_{1.27}\text{In}_{1.92}\text{S}_5$	$\text{CuIn}_{0.8}\text{Ga}_{0.2}\text{S}_2$
Optical gap (eV)	1.64	2.0	1.77	1.48
BET (m^2/g)	15	60	90	60

As already mentioned in chapter 2, our materials cannot perform overall water splitting reaction, so we will study the hydrogen evolution reaction using sacrificial electron donors.

In the next part of the chapter, as for photocatalytic tests we will only be working with samples prepared by MW-ST synthesis, nomenclature will be simplified by removing "MW".

3. Photocatalytic hydrogen production

In this section, the photocatalytic tests of hydrogen production are presented. These measurements were performed at CEISAM laboratory with the help of Dr Fabrice ODOBEL and Dr Deborah ROMITO. As already mentioned in chapter 2, our materials cannot perform by themselves overall water splitting reaction, so we will study the hydrogen evolution reaction using sacrificial electron donors.

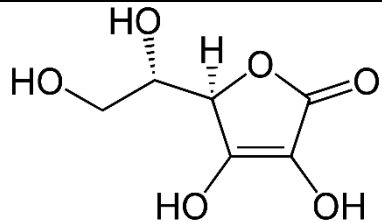
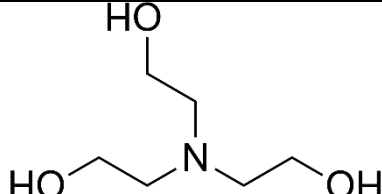
3.1. Sacrificial electron donor selected

Sacrificial electron donor (SED) are used to collect the unpaired holes from the photocatalysts. In this work, we used ascorbic acid (AA) and triethanolamine (TEOA) as hole scavengers (see Table 11 and Figure 36). They continue to be among the most used SEDs, although the selection of the suitable SED depends more on the systems employed. In practice, it is stated that SEDs perform best when the pH is near to their pKa.⁶¹

Generally, AA is known for its water solubility, and its potential to operate in neutral and acidic environment. Meanwhile, TEOA needs basic medium to work.^{31,62} The suggested SED should be consistent with reaction's kinetics enabling electron transfer to the photogenerated holes and capable of consuming these holes rapidly and thus preventing charge recombination that is harmful to proton reduction in the conduction band.⁶³

For this reason, as we do not know yet which environment (whether acidic or basic) our compounds can withstand, we investigated both mediums.

Table 11: Sacrificial electron donors used during this work.

Sacrificial reagent	Structure	pH	Redox potential E_{ox} (V vs.SCE)	Medium
Ascorbic acid (AA)		4	0.20 ⁶²	Aqueous
Triethanolamine (TEOA)		8	0.85 ⁶²	Aqueous

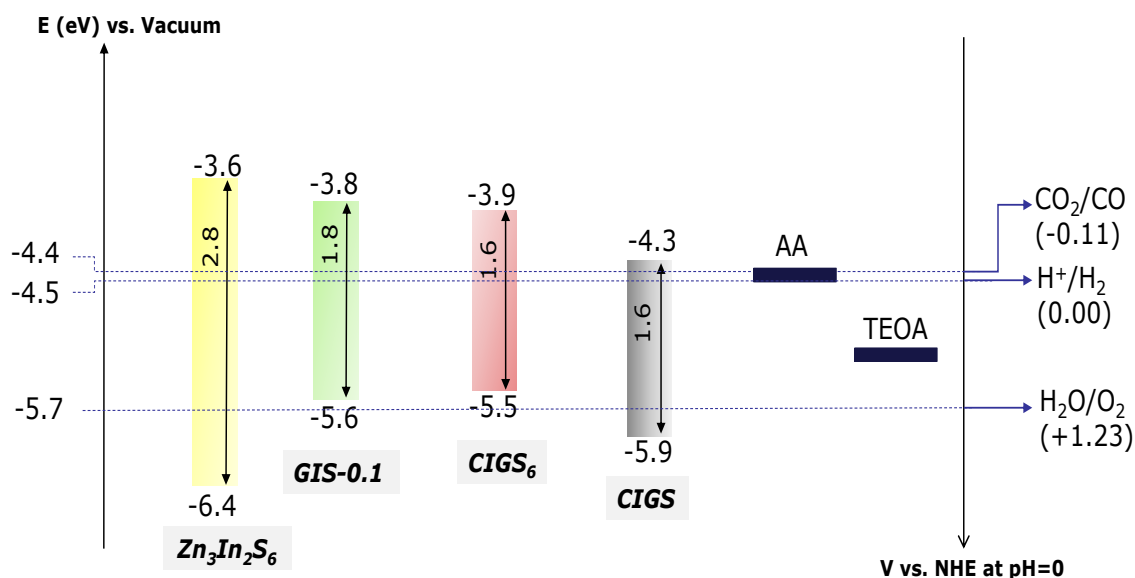


Figure 36: Energy diagram of the CIGS₆, GIS-0.1, CIGS (either measured or calculated, chapter 2) and Zn₃In₂S₆^{46,64} positioned to redox potential of the sacrificial electron donors used (AA and TEOA).

3.2. Photocatalytic Set-Up

Figure 37 presents a schematic illustration of the typical set-up used for the photocatalytic experiments. The hydrogen evolution was conducted in a closed reactor (a quartz round-bottom flask). 10 mg of the nanopowder is added under stirring into 5 ml of 0.1 M SED solution, containing either AA at pH=4 or TEOA pH=8. To reach the desired pH, the solutions are acidified by HCl or basified by NaOH before dispersing the photocatalyst. The reaction mixture is then evacuated by purging oxygen from it using nitrogen gas under sonification for 15-20 min prior to the reaction. A white lamp (AM1.5G, 400 ≤ λ ≤ 700 nm) was used as visible light source.

The quantity of the hydrogen generated (mainly expressed in mole per time unit) is measured periodically (every 1.5 hours), by collecting the obtained gas sampling using a gastight syringe, which is then analysed in the gas chromatography GC. The amount of H₂ is estimated according to the area of the H₂ peak using a calibration curve.

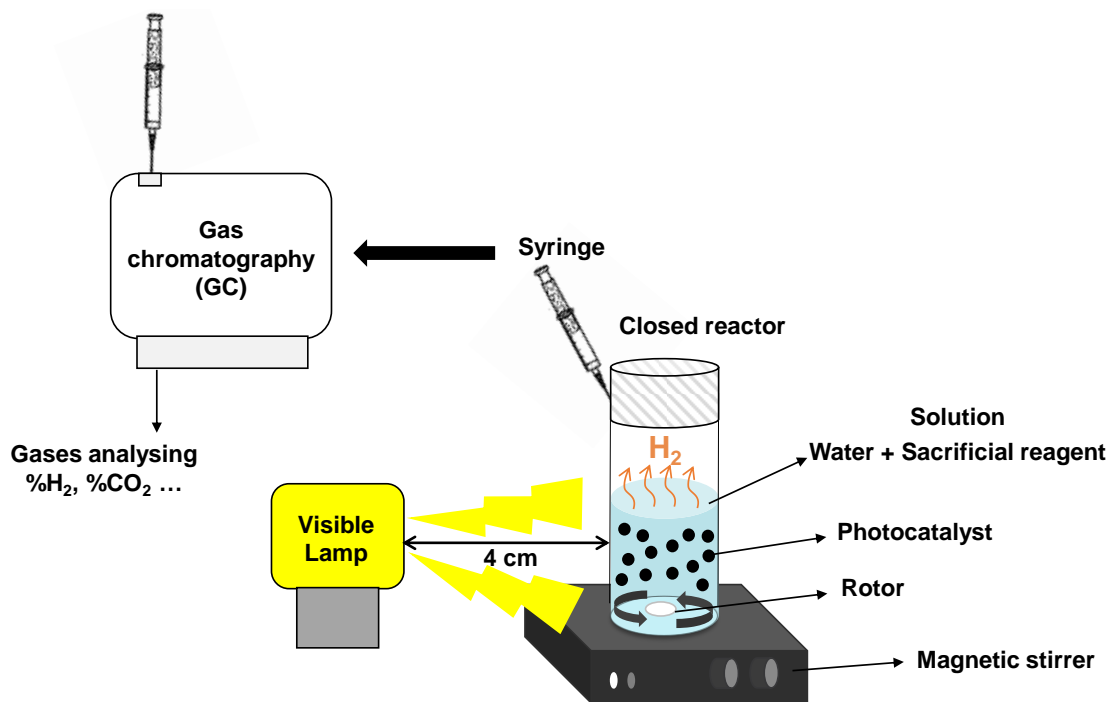


Figure 37: A schematic representation of the set-up used for photocatalytic hydrogen production.

3.3. Hydrogen production results

Table 12 summarises all the different experiments carried out for hydrogen production, which will be developed in this section. The tests were based on the experimental protocol above.

Table 12: Summary table of all the different experiments carried out for hydrogen production.

Samples	Sacrificial agent	Lamp	Co-catalyst	Hydrogen production
CIGS ₆	0.1M AA pH=4	White lamp	--	X
		UV lamp	Pt(cod)Cl ₂	X
	0.1M TEOA pH=8	White lamp	--	X
	0.6M i-PrOH (10 mg in 5 mL)	UV lamp	--	X
			--	X
CIGS ₆ + MPA + TMAH	0.1M AA pH=4	White lamp	50 nmol NiCl ₂	X
ZIS-0.6	0.1M AA pH=4	White lamp	--	√
	0.1M TEOA pH=8			√
ZIS-0.6 + MPA + TMAH	0.1M AA pH=4	White lamp	50 nmol NiCl ₂	√
CIGS	0.1M AA pH=4	White lamp	--	√
	0.1M TEOA pH=8			X
CIGS + MPA + TMAH	0.1M AA pH=4	White lamp	50 nmol NiCl ₂	√
GIS-0.1	0.1M AA pH=4	White lamp	--	√
	0.1M TEOA pH=8			X

3.3.1. Hydrogen evolution using acid ascorbic as sacrificial electron donor

In the first step, we examined for hydrogen evolution, the four prepared photocatalysts presented in Table 10 (i.e. CIGS₆, ZIS-0.6, GIS-0.1, CIGS), using acid ascorbic (pH=4) as hole scavenger. Figure 38, displays the amount of evolved hydrogen, as a function of time. Two lamellar compounds (ZIS-0.6 and GIS-0.1) along with the CIGS chalcopyrite demonstrated H₂ generation. Whereas, H₂ has unfortunately not been detected in the case of CIGS₆. This might be attributed to its low specific surface (15 m²/g), compared to (60 - 90 m²/g) the rest of the compounds.

From Figure 38, it is clear that ZIS-0.6 produces the highest H₂ amount compared to other materials. For all compounds, the production of H₂ is only measured after 1.5 hours. For lamellar compounds, it keeps strongly increasing within 24 hours, to reveal a maximum H₂ amount of 28.91 μmol and 11.91 μmol for ZIS-0.6 and GIS-0.1, respectively. Meanwhile, the CIGS chalcopyrite H₂ generation started 4 hours after the lamp irradiation and rapidly stabilises after 6 hours, exhibiting the lowest H₂ amount 3.6 μmol.

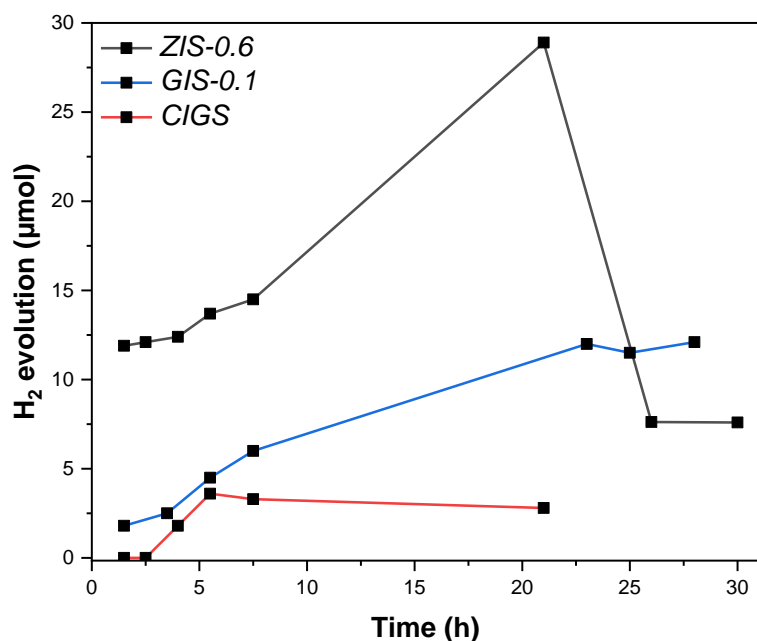


Figure 38: Photocatalytic H₂ evolution as a function of time of ZIS-0.6, GIS-0.1 and CIGS using acid ascorbic (pH=4) as sacrificial electron donor.

Nevertheless, the H₂ evolution rate of ZIS-0.6 decreases significantly after 20 hours of increased yield. This could be due to several factors. It is possible that the reactor had a leak, but this would not be the case as the other compounds did not behave as expected for a leak. Additionally, it is also possible that H₂ reacts with the sulphur in the compound, forming H₂S during the photocatalytic test. Moreover, various sulphide-based photocatalysts are affected by photocorrosion when exposed to prolonged light and reaction conditions, including ZIS compounds.^{65,66} The efficiency of hydrogen evolution can be compromised by photocorrosion, limiting the number of the available active sites.

Indeed, the photocorrosion of metal sulphide-based catalysts are triggered by photogenerated hole-induced oxidation instability.^{67,68} Under illumination, a photon is absorbed and an electron is excited from the valence to the conduction band creating a hole. For metal sulphides, the photogenerated electrons are easily transferred to the surface, whereas the transfer of the photogenerated holes is challenging.⁶⁷ Therefore, holes will accumulate and oxidize the surface of the catalyst. The surface sulphur ions of the photocatalyst will oxidize to sulphur in the absence of oxygen and to sulphate in the presence of oxygen.^{67,68} Among the time, the photocatalytic activity will therefore decrease.

In addition, the photocatalyst deactivation might also be due to the carrier recombination and the limited charges separation. In the case of ZIS photocatalysts, numerous attempts have been made to modify the compounds in order to limit the recombination processes of the photogenerated charge carriers such as controlling its morphology,^{69,70} elemental doping^{70,71} and heterojunction structures.⁴⁰

On the contrary to ZIS-0.6 and GIS-0.1, as shown in Figure 38, CIGS chalcopyrite takes around 4 hours to generate hydrogen. This slow H₂ ignition period could be due to the limited amount of active sites or the high recombination rates, limiting the available number of charge carriers for the reaction. Additionally, the redox potential of the sacrificial agent can also influence its effectiveness.

However, to confirm these assumptions, it would be necessary to explore and understand the mechanism behind the reaction kinetics.

3.3.2. Hydrogen evolution using acid ascorbic and a co-catalyst

Adding a co-catalyst to a photocatalytic reaction is an effective approach to enhance the performance by providing more active sites. In addition, they improve the carrier's movement and prevent their recombination.⁷² Platine and nickel are widely employed as co-catalysts.

The tests presented in this section were based on the experimental protocol described in the literature for CuGa₂In₃S₈.⁷³ The photocatalytic tests were thus carried out using Ni salt as a co-catalyst and AA (pH=4) as SED. Initially, a ligand exchange treatment with 3-mercaptopropionic acid (MPA) and tetramethylammonium hydroxide (TMAH) is performed according to a literature procedure.⁷³ 100 mg of the sample (ZIS-0.6, CIGS₆ or CIGS) was dispersed into a solution of 0.5 mL of MPA with 10 mL chloroform and 5 mL methanol where the pH was balanced to pH=11 with TMAH and stirred for 6 hours. The mixture is then filtered, washed using ethanol and finally dried under vacuum. Afterwards, 10 mg of the resulted compound was added to 3 mL of 0.1M AA and 2 mL of 50 nmol NiCl₂ and the co-catalyst photodeposition was successfully achieved for hydrogen production. The following steps remain similar to the earlier reactions. Unfortunately, in the time allocated to this thesis, we could not perform the same photocatalytic test on GIS-0.1.

Similarly to the previous experiment, H₂ was apparently not detected in the case of CIGS₆. The obtained results of CIGS and ZIS-0.6 are presented in Figure 39, compared to the ones without Ni²⁺. For both samples, the addition of Ni salt as co-catalyst brought no advantage in terms of stability.

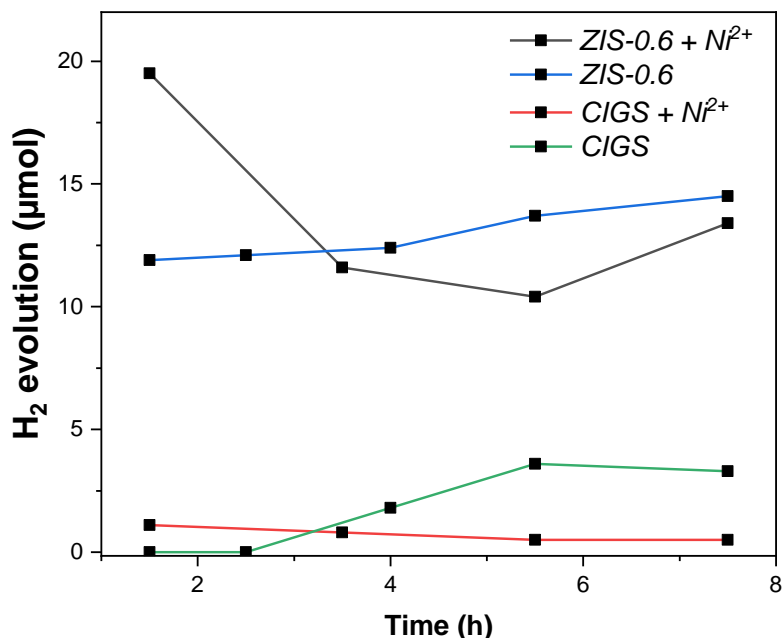


Figure 39: Photocatalytic H₂ evolution as a function of time of ZIS-0.6 and CIGS using acid ascorbic (pH=4) as sacrificial electron donor and NiCl₂ as co-catalyst.

In the case of CIGS, it is evident that higher H₂ amount is produced in shorter durations, we were able to measure 1 µmol of H₂ after only 1.5 hours while the untreated CIGS took 4 hours for H₂ evolution. Nevertheless, it is obvious that the presence of the Ni²⁺ is poisoning the experiment, since the H₂ generation is stopped after a short period. Therefore, this might be contributed to photocorrosion due to the formation of NiS during the experiment, which is detrimental. Otherwise, the catalyst could be also unstable in the presence of Ni²⁺ or the reaction conditions are not suitable for the co-catalyst, leading to a photocatalyst degradation and passivation.

For ZIS-0.6, a higher amount of H₂ is also produced over a short period before declining. The evolved H₂ after 1.5 hours increased up to 20 µmol in the presence of Ni salt, almost twice higher than the amount measured in 1.5 hours for the same blank sample (11 µmol). However, after a certain time, the amount of H₂ decreases and reaches a level close to that detected without Ni salt. This can be attributed to the passivation of the co-catalyst, since it can be observed that the catalyst does not suffer from producing H₂ over time, but instead continues the H₂ production in an equivalent quantity to that detected without Ni²⁺.

3.3.3. Hydrogen evolution using triethanolamine as sacrificial electron donor

A series of investigations was conducted using triethanolamine (pH=8) as sacrificial electron donor following previous protocol. The lamellar compounds (ZIS-0.6, GIS-0.1 and CIGS₆) alongside with CIGS were tested.

As shown in the Figure 40, only ZIS-0.6 was able to produce H₂ using TEOA as SED. After 1.5 hours, the compound starts to produce a very low quantity of H₂, and keeps increasing over 30 hours attaining a value of 4.5 μmol, four times lower than using AA as SED. Although the activity with TEOA is lower than that observed with AA, no drop is observed in basic medium. This may be linked to the fact that there is less photocorrosion in a basic environment. This stability is expected based on the literature, as ZIS compounds were reported compatible with TEOA for hydrogen production.⁷⁴

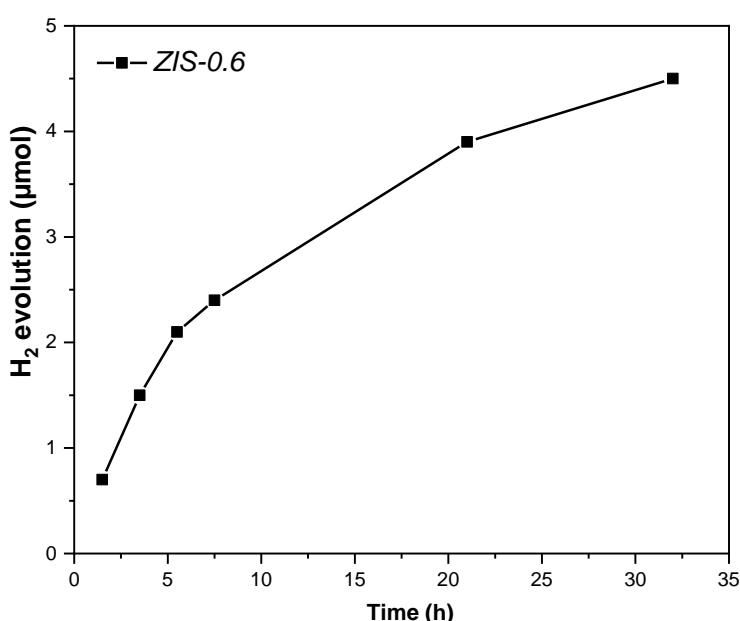


Figure 40: Photocatalytic H₂ evolution as a function of time of ZIS-0.6 using triethanolamine (pH=8) as sacrificial electron donor.

On the other hand, GIS-0.1, CIGS₆ and CIGS compounds did not produce hydrogen with TEOA as SED. In fact, there are no publications in the literature reporting the use of TEOA for quaternary Cu-In-Ga-S materials, for which AA⁷³ and Na₂SO₃/Na₂S⁷⁵ are commonly used as SEDs. Indeed, as shown in the Figure 36, the compound Zn₃In₂S₆ which has a chemical composition very similar to that of ZIS-0.6, exhibits a positioning of the VBM more negative with respect to the redox potential of TEOA than those of GIS-0.1, CIGS₆ and CIGS compounds.

Furthermore, by comparing ZIS-0.6 in AA acidic medium and TEOA basic medium, we observe that the amount of hydrogen produced with TEOA is lower than that obtained with AA. This fact could possibly be due to Cu and Ga doping, which induces a change in bands energy positioning in relation to TEOA.

4. Discussion

To conclude, nanopowders of CIGS and lamellar CIGS_n-type compounds were successfully synthesized by microwave-assisted solvothermal synthesis. Among these compounds, ZIS-0.6, GIS-0.1 and CIGS exhibit specific surfaces relatively high, allowing an efficient photocatalytic activity for hydrogen production. Contrarily, the low specific surface of CIGS₆ could explain the lack of photocatalytic activity.

In Table 13, we compare the hydrogen evolution rate of our compounds with those of materials studied in the literature, presenting either similar structures or similar compositions. In fact, this comparison is made in terms of photocatalytic activity performance criteria. Due to time constraints, the influence of the mass on the amount of H₂ produced was not studied. However, considering that we are working with 10 mg of photocatalyst and that usually the plateau is observed above 50 mg,^{76,77} it was reasonable to normalize our activity by the mass of photocatalyst for comparative purposes.

Table 13: A recap of H₂ evolution rates of the prepared compounds compared to the literature.

Material	Sacrificial agent	H₂ evolution rate ($\mu\text{mol}\cdot\text{h}^{-1}$)	H₂ evolution rate ($\mu\text{mol}\cdot\text{g}^{-1}\cdot\text{h}^{-1}$)
ZIS-0.6	AA	1.376	137.6
	TEOA	0.185	18.5
ZIS ₆	Formic acid	12.88 ⁴⁴ (0.1 g)	128.8
ZIS ₄	Na ₂ SO ₃ /Na ₂ S	-	265.9 ⁷⁸
Pt/ZIS ₄ (Solvothermal)	Na ₂ SO ₃ /Na ₂ S	-	136.5 ⁴⁰
Pt/ZIS ₄ (Microwave assisted hydrothermal)	Na ₂ SO ₃ /Na ₂ S	69.2 ⁴⁰ (0.1 g)	692
GIS-0.1	AA	0.521	52.1
CuGa ₂ In ₃ S ₈	Na ₂ SO ₃ /Na ₂ S	4 ⁷⁹ (0.1 g)	40
Ru/CuGa ₂ In ₃ S ₈	Na ₂ SO ₃ /Na ₂ S	338 ⁷⁹ (0.1 g)	3380
Ni ²⁺ /CuGa ₂ In ₃ S ₈	AA	25 ⁷³ (0.001 g)	-
CIGS	AA	0.143	14.3
Cu(In _{0.7} ,Ga _{0.3})S ₂	Na ₂ SO ₃ /Na ₂ S	-	750 ⁷⁵

According to chalcogenides photocatalysts literature, Na₂SO₃/Na₂S is much more widely used as SED. However, in this work, AA was first tested as SED alongside with TEOA, in order to compare photocatalysts activity under both acidic and basic conditions. Then, for

the addition of a co-catalyst, we have chosen to follow the same protocol used for the lamellar compound $\text{CuGa}_2\text{In}_3\text{S}_8$ ⁷³ in order to facilitate the comparison.

In view of our results, it is obvious that the lamellar compounds reported higher performances for hydrogen evolution in acidic conditions than CIGS chalcopyrite: 137.6, 52.1 and 14.3 $\mu\text{mol}\cdot\text{g}^{-1}\cdot\text{h}^{-1}$ for ZIS-0.6, GIS-0.1 and CIGS, respectively. However, this is not the case in the literature when $\text{Na}_2\text{SO}_3/\text{Na}_2\text{S}$ are used as SED.⁷⁵

ZIS-0.6 photocatalyst exhibits the higher performances and it was the only sample generating H_2 from both acidic and basic conditions. Significantly, it was found that the mean apparent H_2 yield measured (137 $\mu\text{mol}\cdot\text{g}^{-1}\cdot\text{h}^{-1}$) is comparable to that of pure ZnS (using formic acid as a SED)⁴⁴ and also of Pt/ZnS_4 (using $\text{Na}_2\text{SO}_3/\text{Na}_2\text{S}$ as a SED)⁴⁰ photocatalysts, but in the case of ZIS-0.6 the addition of a co-catalyst is not required (Table 13). In addition, we should note that the reaction medium plays a critical role in improving photocatalytic activity. According to literature, the ZnS_4 prepared by microwave-assisted hydrothermal synthesis³⁹, i.e. using water as a reaction medium, exhibits much higher performances than that of ZIS-0.6 compound prepared in ethylene glycol.

Besides, as presented in the Table 13, the H_2 generation rate of GIS-0.1 (52.1 $\mu\text{mol}\cdot\text{g}^{-1}\cdot\text{h}^{-1}$) is comparable to the one reported for $\text{CuGa}_2\text{In}_3\text{S}_8$ using $\text{Na}_2\text{SO}_3/\text{Na}_2\text{S}$ as a SED (40 $\mu\text{mol}\cdot\text{g}^{-1}\cdot\text{h}^{-1}$), which exhibits a chemical composition quite close to that of GIS-0.1 ($\text{Cu}_{0.74}\text{Ga}_2\text{In}_{3.1}\text{S}_8$). However, the protocol presented in this manuscript requires a significantly lower temperature and reaction time than those described in the literature for $\text{CuGa}_2\text{In}_3\text{S}_8$ ⁷⁹. Thus, GIS-0.1 was prepared by microwave-assisted solvothermal in only 15 min at 170 °C, compared to $\text{CuGa}_2\text{In}_3\text{S}_8$ nanoparticles that were prepared by a hot-injection method in 15 h reaching a temperature up to 270 °C.^{73,79}

In the literature, the addition of a co-catalyst (e.g. Ni salt or Ru) significantly improves yields, as shown in the Table 13. This was not the case in this work. In fact, when using Ni salt as co-catalyst a poisoning effect is noticed during the experiment.

Furthermore, a test with Pt as co-catalyst was also carried out. However, the attempt failed since we were unable to successfully photodeposit Pt on the test sample. The photodeposition approach requires having a photocatalyst already providing enough electrons or holes to, reduce or oxidize, respectively, the salt at the surface of the photocatalyst. This could be mainly due to the morphology of our nanopowders (section 2.2) that might not facilitate the grafting of the co-catalysts.

Finally, promising visible light photocatalysts have been provided, opening up to new perspectives such as testing CO_2 reduction and completing the hydrogen production studies using alternative sacrificial electron donors as $\text{Na}_2\text{SO}_3/\text{Na}_2\text{S}$. Suitable co-catalysts could be also successfully grafted/deposited onto the prepared samples, in order to

improve their efficiency without causing any destructive effects. To further explore, CIGS_n-type photocatalysts with high specific surface and various nanocrystal morphologies must be prepared.

References

- (1) Doerffler, W.; Hauffe, K. Heterogeneous Photocatalysis I. The Influence of Oxidizing and Reducing Gases on the Electrical Conductivity of Dark and Illuminated Zinc Oxide Surfaces. *J. Catal.* **1964**, *3* (2), 156–170. [https://doi.org/10.1016/0021-9517\(64\)90123-X](https://doi.org/10.1016/0021-9517(64)90123-X).
- (2) Zagorodni, A. A. Chapter 18 - Subjects That Do Not Fit in Other Chapters. In *Ion Exchange Materials*; Zagorodni, A. A., Ed.; Elsevier: Oxford, 2007; pp 377–395. <https://doi.org/10.1016/B978-008044552-6/50019-8>.
- (3) Kumari, P.; Lal, S.; Singhal, A. 22 - Advanced Applications of Green Materials in Catalysis Applications. In *Applications of Advanced Green Materials*; Ahmed, S., Ed.; Woodhead Publishing in Materials; Woodhead Publishing, 2021; pp 545–571. <https://doi.org/10.1016/B978-0-12-820484-9.00022-2>.
- (4) Pan, Z.-Z.; Li, Y.; Zhao, Y.; Zhang, C.; Chen, H. Bulk Phase Charge Transfer in Focus – And in Sequential along with Surface Steps. *Catal. Today* **2021**, *364*, 2–6. <https://doi.org/10.1016/j.cattod.2020.09.023>.
- (5) Wang, H.; Tian, Y.-M.; König, B. Energy- and Atom-Efficient Chemical Synthesis with Endergonic Photocatalysis. *Nat. Rev. Chem.* **2022**, *6* (10), 745–755. <https://doi.org/10.1038/s41570-022-00421-6>.
- (6) Maheu, C. Study of Titania Supported Transition Metal Sulfides for the Photocatalytic Production of Hydrogen. These de doctorat, Lyon, 2019. <https://www.theses.fr/2019LYSE1172> (accessed 2023-04-07).
- (7) Ibhaddon, A. O.; Fitzpatrick, P. Heterogeneous Photocatalysis: Recent Advances and Applications. *Catalysts* **2013**, *3* (1), 189–218. <https://doi.org/10.3390/catal3010189>.
- (8) Serpone, N.; Emeline, A. V. Semiconductor Photocatalysis — Past, Present, and Future Outlook. *J. Phys. Chem. Lett.* **2012**, *3* (5), 673–677. <https://doi.org/10.1021/jz300071j>.
- (9) Wen, J.; Xie, J.; Chen, X.; Li, X. A Review on G-C₃N₄-Based Photocatalysts. *Appl. Surf. Sci.* **2017**, *391*, 72–123. <https://doi.org/10.1016/j.apsusc.2016.07.030>.
- (10) Nunes, D.; Pimentel, A.; Branquinho, R.; Fortunato, E.; Martins, R. Metal Oxide-Based Photocatalytic Paper: A Green Alternative for Environmental Remediation. *Catalysts* **2021**, *11* (4), 504. <https://doi.org/10.3390/catal11040504>.
- (11) Zhang, Y.; Ram, M. K.; Stefanakos, E. K.; Goswami, D. Y. Synthesis, Characterization, and Applications of ZnO Nanowires. *J. Nanomater.* **2012**, *2012*, e624520. <https://doi.org/10.1155/2012/624520>.
- (12) Herrmann, J.-M. Bases de la photocatalyse hétérogène. *L'actualité Chim. - Juin-Juillet 2015 - N° 397-398*.
- (13) Djurišić, A. B.; He, Y.; Ng, A. M. C. Visible-Light Photocatalysts: Prospects and Challenges. *APL Mater.* **2020**, *8* (3), 030903. <https://doi.org/10.1063/1.5140497>.
- (14) Low, J.; Yu, J.; Jaroniec, M.; Wageh, S.; Al-Ghamdi, A. A. Heterojunction Photocatalysts. *Adv. Mater.* **2017**, *29* (20), 1601694. <https://doi.org/10.1002/adma.201601694>.
- (15) Herrmann, J.-M. Heterogeneous Photocatalysis: State of the Art and Present Applications In Honor of Pr. R.L. Burwell Jr. (1912–2003), Former Head of Ipatieff Laboratories, Northwestern University, Evanston (Ill). *Top. Catal.* **2005**, *34* (1–4), 49–65. <https://doi.org/10.1007/s11244-005-3788-2>.

- (16) Ulmer, U.; Dingle, T.; Duchesne, P. N.; Morris, R. H.; Tavasoli, A.; Wood, T.; Ozin, G. A. Fundamentals and Applications of Photocatalytic CO₂ Methanation. *Nat. Commun.* **2019**, *10* (1), 3169. <https://doi.org/10.1038/s41467-019-10996-2>.
- (17) Takata, T.; Domen, K. Development of Non-Oxide Semiconductors as Light Harvesting Materials in Photocatalytic and Photoelectrochemical Water Splitting. *Dalton Trans.* **2017**, *46* (32), 10529–10544. <https://doi.org/10.1039/C7DT00867H>.
- (18) Fukuzumi, S. Production of Liquid Solar Fuels and Their Use in Fuel Cells. *Joule* **2017**, *1* (4), 689–738. <https://doi.org/10.1016/j.joule.2017.07.007>.
- (19) Purchase, R.; Vriend, H.; Groot, H.; Harmsen, P.; Bos, H. *Artificial Photosynthesis for the Conversion of Sunlight to Fuel*; 2015.
- (20) Gust, D.; Moore, T. A.; Moore, A. L. *Solar Fuels via Artificial Photosynthesis*. ACS Publications. <https://doi.org/10.1021/ar900209b>.
- (21) Armaroli, N.; Balzani, V. Solar Electricity and Solar Fuels: Status and Perspectives in the Context of the Energy Transition. *Chem. – Eur. J.* **2016**, *22* (1), 32–57. <https://doi.org/10.1002/chem.201503580>.
- (22) Kudo, A.; Miseki, Y. Heterogeneous Photocatalyst Materials for Water Splitting. *Chem. Soc. Rev.* **2008**, *38* (1), 253–278. <https://doi.org/10.1039/B800489G>.
- (23) *Principe de la photocatalyse*. Techniques de l'Ingénieur. <https://www.techniques-ingenieur.fr/base-documentaire/procedes-chimie-bio-agro-th2/gestion-durable-des-dechets-et-des-polluants-42495210/la-photocatalyse-depollution-de-l-eau-ou-de-l-air-et-materiaux-autonettoyants-j1270/principe-de-la-photocatalyse-j1270niv10001.html> (accessed 2023-05-03).
- (24) Jing, D.; Guo, L.; Zhao, L.; Zhang, X.; Liu, H.; Li, M.; Shen, S.; Liu, G.; Hu, X.; Zhang, X.; Zhang, K.; Ma, L.; Guo, P. Efficient Solar Hydrogen Production by Photocatalytic Water Splitting: From Fundamental Study to Pilot Demonstration. *Int. J. Hydrog. Energy* **2010**, *35* (13), 7087–7097. <https://doi.org/10.1016/j.ijhydene.2010.01.030>.
- (25) Jiang, D.; Chen, X.; Zhang, Z.; Zhang, L.; Wang, Y.; Sun, Z.; Irfan, R. M.; Du, P. Highly Efficient Simultaneous Hydrogen Evolution and Benzaldehyde Production Using Cadmium Sulfide Nanorods Decorated with Small Cobalt Nanoparticles under Visible Light. *J. Catal.* **2018**, *357*, 147–153. <https://doi.org/10.1016/j.jcat.2017.10.019>.
- (26) Ye, X.; Chen, Y.; Wu, Y.; Zhang, X.; Wang, X.; Chen, S. Constructing a System for Effective Utilization of Photogenerated Electrons and Holes: Photocatalytic Selective Transformation of Aromatic Alcohols to Aromatic Aldehydes and Hydrogen Evolution over Zn₃In₂S₆ Photocatalysts. *Appl. Catal. B Environ.* **2019**, *242*, 302–311. <https://doi.org/10.1016/j.apcatb.2018.10.004>.
- (27) Rodriguez, J. Production d'hydrogène Par Photocatalyse et Conversion Electrochimique Dans Une Pile à Combustible.
- (28) Marchal, C. Synthèse et Réactivité de Nanocomposites Au / g-C₃N₄ / TiO₂ Pour La Production d'hydrogène Par Procédé Photocatalytique Sous Illumination Solaire et Visible. These de doctorat, Strasbourg, 2017. <https://www.theses.fr/2017STRAF011> (accessed 2023-05-03).
- (29) Zhang, J.; Meng, S.; Ye, X.; Ling, C.; Zhang, S.; Fu, X.; Chen, S. Synergistic Effect of Photocatalysis and Thermocatalysis for Selective Oxidation of Aromatic Alcohols to Aromatic Aldehydes Using Zn₃In₂S₆@ZnO Composite. *Appl. Catal. B Environ.* **2017**, *218*, 420–429. <https://doi.org/10.1016/j.apcatb.2017.06.078>.

- (30) Meng, S.; Ye, X.; Zhang, J.; Fu, X.; Chen, S. Effective Use of Photogenerated Electrons and Holes in a System: Photocatalytic Selective Oxidation of Aromatic Alcohols to Aldehydes and Hydrogen Production. *J. Catal.* **2018**, *367*, 159–170. <https://doi.org/10.1016/j.jcat.2018.09.003>.
- (31) Pellegrin, Y.; Odobel, F. Sacrificial Electron Donor Reagents for Solar Fuel Production. *Comptes Rendus Chim.* **2017**, *20* (3), 283–295. <https://doi.org/10.1016/j.crci.2015.11.026>.
- (32) Guo, Q.; Zhou, C.; Ma, Z.; Yang, X. Fundamentals of TiO₂ Photocatalysis: Concepts, Mechanisms, and Challenges. *Adv. Mater.* **2019**, *31* (50), 1901997. <https://doi.org/10.1002/adma.201901997>.
- (33) Schneider, J.; Matsuoka, M.; Takeuchi, M.; Zhang, J.; Horiuchi, Y.; Anpo, M.; Bahnemann, D. W. Understanding TiO₂ Photocatalysis: Mechanisms and Materials. *Chem. Rev.* **2014**, *114* (19), 9919–9986. <https://doi.org/10.1021/cr5001892>.
- (34) Zhang, L.; Zhang, J.; Yu, H.; Yu, J. Emerging S-Scheme Photocatalyst. *Adv. Mater.* **2022**, *34* (11), 2107668. <https://doi.org/10.1002/adma.202107668>.
- (35) Wang, Q.; Domen, K. Particulate Photocatalysts for Light-Driven Water Splitting: Mechanisms, Challenges, and Design Strategies. *Chem. Rev.* **2020**, *120* (2), 919–985. <https://doi.org/10.1021/acs.chemrev.9b00201>.
- (36) Chandrasekaran, S.; Yao, L.; Deng, L.; Bowen, C.; Zhang, Y.; Chen, S.; Lin, Z.; Peng, F.; Zhang, P. Recent Advances in Metal Sulfides: From Controlled Fabrication to Electrocatalytic, Photocatalytic and Photoelectrochemical Water Splitting and Beyond. *Chem. Soc. Rev.* **2019**, *48* (15), 4178–4280. <https://doi.org/10.1039/C8CS00664D>.
- (37) Sivula, K.; van de Krol, R. Semiconducting Materials for Photoelectrochemical Energy Conversion. *Nat. Rev. Mater.* **2016**, *1* (2), 1–16. <https://doi.org/10.1038/natrevmats.2015.10>.
- (38) Haque, F.; Daeneke, T.; Kalantar-zadeh, K.; Ou, J. Z. Two-Dimensional Transition Metal Oxide and Chalcogenide-Based Photocatalysts. *Nano-Micro Lett.* **2017**, *10* (2), 23. <https://doi.org/10.1007/s40820-017-0176-y>.
- (39) *Revisiting Polytypism in Hexagonal Ternary Sulfide ZnIn₂S₄ for Photocatalytic Hydrogen Production Within the Z-Scheme | Chemistry of Materials.* <https://pubs.acs.org/doi/10.1021/acs.chemmater.9b03539> (accessed 2023-04-07).
- (40) Janani, R.; Preethi V, R.; Singh, S.; Rani, A.; Chang, C.-T. Hierarchical Ternary Sulfides as Effective Photocatalyst for Hydrogen Generation Through Water Splitting: A Review on the Performance of ZnIn₂S₄. *Catalysts* **2021**, *11* (2), 277. <https://doi.org/10.3390/catal11020277>.
- (41) Shen, S.; Chen, J.; Wang, X.; Zhao, L.; Guo, L. Microwave-Assisted Hydrothermal Synthesis of Transition-Metal Doped ZnIn₂S₄ and Its Photocatalytic Activity for Hydrogen Evolution under Visible Light. *J. Power Sources* **2011**, *196* (23), 10112–10119. <https://doi.org/10.1016/j.jpowsour.2011.08.103>.
- (42) Fan, B.; Chen, Z.; Liu, Q.; Zhang, Z.; Fang, X. One-Pot Hydrothermal Synthesis of Ni-Doped ZnIn₂S₄ Nanostructured Film Photoelectrodes with Enhanced Photoelectrochemical Performance. *Appl. Surf. Sci.* **2016**, *370*, 252–259. <https://doi.org/10.1016/j.apsusc.2016.02.125>.
- (43) Li, Y.; Zhang, K.; Peng, S.; Lu, G.; Li, S. Photocatalytic Hydrogen Generation in the Presence of Ethanolamines over Pt/ZnIn₂S₄ under Visible Light Irradiation. *J. Mol.*

- Catal. Chem.* **2012**, 363–364, 354–361.
<https://doi.org/10.1016/j.molcata.2012.07.011>.
- (44) Duan, S.; Zhang, S.; Chang, S.; Meng, S.; Fan, Y.; Zheng, X.; Chen, S. Efficient Photocatalytic Hydrogen Production from Formic Acid on Inexpensive and Stable Phosphide/Zn₃In₂S₆ Composite Photocatalysts under Mild Conditions. *Int. J. Hydrog. Energy* **2019**, 44 (39), 21803–21820.
<https://doi.org/10.1016/j.ijhydene.2019.06.179>.
- (45) Li, W.; Lin, Z.; Yang, G. A 2D Self-Assembled MoS₂/ZnIn₂S₄ Heterostructure for Efficient Photocatalytic Hydrogen Evolution. *Nanoscale* **2017**, 9 (46), 18290–18298.
<https://doi.org/10.1039/C7NR06755K>.
- (46) Zhang, S.; Duan, S.; Chen, G.; Meng, S.; Zheng, X.; Fan, Y.; Fu, X.; Chen, S. MoS₂/Zn₃In₂S₆ Composite Photocatalysts for Enhancement of Visible Light-Driven Hydrogen Production from Formic Acid. *Chin. J. Catal.* **2021**, 42 (1), 193–204.
[https://doi.org/10.1016/S1872-2067\(20\)63584-7](https://doi.org/10.1016/S1872-2067(20)63584-7).
- (47) Jiao, X.; Chen, Z.; Li, X.; Sun, Y.; Gao, S.; Yan, W.; Wang, C.; Zhang, Q.; Lin, Y.; Luo, Y.; Xie, Y. Defect-Mediated Electron–Hole Separation in One-Unit-Cell ZnIn₂S₄ Layers for Boosted Solar-Driven CO₂ Reduction. *J. Am. Chem. Soc.* **2017**, 139 (22), 7586–7594. <https://doi.org/10.1021/jacs.7b02290>.
- (48) Haeuseler, H.; Srivastava, S. K. Phase Equilibria and Layered Phases in the Systems A₂X₃-M₂X₃-M'X (A = Ga, In; M = Trivalent Metal; M' = Divalent Metal; X = S, Se). *Z. Für Krist. - Cryst. Mater.* **2000**, 215 (4), 205–221.
<https://doi.org/10.1524/zkri.2000.215.4.205>.
- (49) Xiong, J.; Di, J.; Xia, J.; Zhu, W.; Li, H. Surface Defect Engineering in 2D Nanomaterials for Photocatalysis. *Adv. Funct. Mater.* **2018**, 28 (39), 1801983.
<https://doi.org/10.1002/adfm.201801983>.
- (50) Bilecka, I.; Niederberger, M. Microwave Chemistry for Inorganic Nanomaterials Synthesis. *Nanoscale* **2010**, 2 (8), 1358–1374.
<https://doi.org/10.1039/B9NR00377K>.
- (51) Polshettiwar, V.; Varma, R. S. Aqueous Microwave Chemistry: A Clean and Green Synthetic Tool for Rapid Drug Discovery. *Chem. Soc. Rev.* **2008**, 37 (8), 1546–1557.
<https://doi.org/10.1039/B716534J>.
- (52) Chumha, N.; Thongtem, T.; Thongtem, S.; Kittiwachana, S.; Kaowphong, S. Cyclic Microwave Radiation Synthesis, Photoconductivity, and Optical Properties of CuInS₂ Hollow Sub-Microspheres. *Appl. Surf. Sci.* **2018**, 447, 292–299.
<https://doi.org/10.1016/j.apsusc.2018.03.210>.
- (53) Mubiayi, K. P.; Guilhermitti Neto, D. M.; Morais, A.; Nogueira, H. P.; Santos, T. E. de A.; Mazon, T.; Moloto, N.; Moloto, M. J.; Freitas, J. N. Microwave Assisted Synthesis of CuInGaSe₂ Quantum Dots and Spray Deposition of Their Composites with Graphene Oxide Derivatives. *Mater. Chem. Phys.* **2020**, 242, 122449.
<https://doi.org/10.1016/j.matchemphys.2019.122449>.
- (54) Zhao, Y.; Hong, J.-M.; Zhu, J.-J. Microwave-Assisted Self-Assembled ZnS Nanoballs. *J. Cryst. Growth* **2004**, 270 (3), 438–445.
<https://doi.org/10.1016/j.jcrysgr.2004.06.036>.
- (55) Kremsner, D. J. M.; Stadler, D. A. A Chemist's Guide to Microwave Synthesis.
- (56) Chumha, N.; Pudkon, W.; Chachvalvutikul, A.; Luangwanta, T.; Randorn, C.; Inceesungvorn, B.; Ngamjarujana, A.; Kaowphong, S. Photocatalytic Activity of CuInS₂ Nanoparticles Synthesized via a Simple and Rapid Microwave Heating

- Process. Mater. Res. Express **2020**, 7 (1), 015074. <https://doi.org/10.1088/2053-1591/ab6885>.
- (57) Shukla, S.; Adeleye, D.; Sood, M.; Ehre, F.; Lomuscio, A.; Weiss, T. P.; Siopa, D.; Melchiorre, M.; Siebentritt, S. Carrier Recombination Mechanism and Photovoltage Deficit in 1.7-EV Band Gap near-Stoichiometric Cu(In,Ga) S_{2} . *Phys. Rev. Mater.* **2021**, 5 (5), 055403. <https://doi.org/10.1103/PhysRevMaterials.5.055403>.
- (58) Thomere, A. Absorbours Chalcogénures à Grand Gap $\sim 1,7$ EV Pour La Réalisation de Cellules Solaires En Couches Minces. These de doctorat, Nantes, 2020. <https://www.theses.fr/2020NANT4001> (accessed 2023-06-07).
- (59) Jing, L.; Xie, M.; Xu, Y.; Tong, C.; Zhao, H.; Zhong, N.; Li, H.; Gates, I. D.; Hu, J. Multifunctional 3D MoS_x/Zn₃In₂S₆ Nanoflower for Selective Photothermal-Catalytic Biomass Oxidative and Non-Selective Organic Pollutants Degradation. *Appl. Catal. B Environ.* **2022**, 318, 121814. <https://doi.org/10.1016/j.apcatb.2022.121814>.
- (60) Luo, J.; Wei, X.; Qiao, Y.; Wu, C.; Li, L.; Chen, L.; Shi, J. Photoredox-Promoted Co-Production of Dihydroisoquinoline and H₂O₂ over Defective Zn₃In₂S₆. *Adv. Mater.* **2023**, 35 (10), 2210110. <https://doi.org/10.1002/adma.202210110>.
- (61) Reynal, A.; Pastor, E.; A. Gross, M.; Selim, S.; Reisner, E.; R. Durrant, J. Unravelling the PH-Dependence of a Molecular Photocatalytic System for Hydrogen Production. *Chem. Sci.* **2015**, 6 (8), 4855–4859. <https://doi.org/10.1039/C5SC01349F>.
- (62) Baron, T. Conception et Synthèse de Colorants Sélectifs Du Proche Infrarouge Pour Des Applications En Cellules Solaires Hybrides Transparentes et Incolores Ainsi Que Pour La Production d'hydrogène. These de doctorat, Nantes, 2021. <https://www.theses.fr/2021NANT4069> (accessed 2023-05-12).
- (63) Pal, U.; Ghosh, S.; Chatterjee, D. Effect of Sacrificial Electron Donors on Hydrogen Generation over Visible Light-Irradiated Nonmetal-Doped TiO₂ Photocatalysts. *Transit. Met. Chem.* **2012**, 37 (1), 93–96. <https://doi.org/10.1007/s11243-011-9562-3>.
- (64) Xu, S.; Zhang, K.; Du, L.; Gong, D.; Lu, G.; Qiu, P. Zn₃In₂S₆/TiO₂ Nanocomposites for Highly Efficient Photocathodic Protection to Carbon Steel. *ACS Appl. Nano Mater.* **2022**, 5 (12), 18297–18306. <https://doi.org/10.1021/acsanm.2c04149>.
- (65) High-Performance ZnIn₂S₄/Ni(DmgH)₂ for Photocatalytic Hydrogen Evolution: Ion Exchange Construction, Photocorrosion Mitigation, and Efficiency Enhancement by Photochromic Effect. *J. Colloid Interface Sci.* **2023**, 642, 100–111. <https://doi.org/10.1016/j.jcis.2023.03.123>.
- (66) Li, C.; Che, H.; Yan, Y.; Liu, C.; Dong, H. Z-Scheme AgVO₃/ZnIn₂S₄ Photocatalysts: “One Stone and Two Birds” Strategy to Solve Photocorrosion and Improve the Photocatalytic Activity and Stability. *Chem. Eng. J.* **2020**, 398, 125523. <https://doi.org/10.1016/j.cej.2020.125523>.
- (67) Weng, B.; Qi, M.-Y.; Han, C.; Tang, Z.-R.; Xu, Y.-J. Photocorrosion Inhibition of Semiconductor-Based Photocatalysts: Basic Principle, Current Development, and Future Perspective. *ACS Catal.* **2019**, 9 (5), 4642–4687. <https://doi.org/10.1021/acscatal.9b00313>.
- (68) Chen, S.; Huang, D.; Xu, P.; Xue, W.; Lei, L.; Cheng, M.; Wang, R.; Liu, X.; Deng, R. Semiconductor-Based Photocatalysts for Photocatalytic and Photoelectrochemical

- Water Splitting: Will We Stop with Photocorrosion? *J. Mater. Chem. A* **2020**, *8* (5), 2286–2322. <https://doi.org/10.1039/C9TA12799B>.
- (69) Shi, L.; Yin, P.; Dai, Y. Synthesis and Photocatalytic Performance of ZnIn₂S₄ Nanotubes and Nanowires. *Langmuir* **2013**, *29* (41), 12818–12822. <https://doi.org/10.1021/la402473k>.
- (70) Zhang, G.; Chen, D.; Li, N.; Xu, Q.; Li, H.; He, J.; Lu, J. Preparation of ZnIn₂S₄ Nanosheet-Coated CdS Nanorod Heterostructures for Efficient Photocatalytic Reduction of Cr(VI). *Appl. Catal. B Environ.* **2018**, *232*, 164–174. <https://doi.org/10.1016/j.apcatb.2018.03.017>.
- (71) Tateishi, I.; Furukawa, M.; Katsumata, H.; Kaneco, S. Improvement of Photocatalytic H₂-Generation under Visible Light Irradiation by Controlling the Band Gap of ZnIn₂S₄ with Cu and In. *Catalysts* **2019**, *9* (8), 681. <https://doi.org/10.3390/catal9080681>.
- (72) Xiao, N.; Li, S.; Li, X.; Ge, L.; Gao, Y.; Li, N. The Roles and Mechanism of Cocatalysts in Photocatalytic Water Splitting to Produce Hydrogen. *Chin. J. Catal.* **2020**, *41* (4), 642–671. [https://doi.org/10.1016/S1872-2067\(19\)63469-8](https://doi.org/10.1016/S1872-2067(19)63469-8).
- (73) Kandiel, T. A.; Hutton, G. A. M.; Reisner, E. Visible Light Driven Hydrogen Evolution with a Noble Metal Free CuGa₂In₃S₈ Nanoparticle System in Water. *Catal. Sci. Technol.* **2016**, *6* (17), 6536–6541. <https://doi.org/10.1039/C6CY01103A>.
- (74) Peng, S.; Dan, M.; Guo, F.; Wang, H.; Li, Y. Template Synthesis of ZnIn₂S₄ for Enhanced Photocatalytic H₂ Evolution Using Triethanolamine as Electron Donor. *Colloids Surf. Physicochem. Eng. Asp.* **2016**, *504*, 18–25. <https://doi.org/10.1016/j.colsurfa.2016.05.055>.
- (75) Yu, X.; An, X.; Shavel, A.; Ibáñez, M.; Cabot, A. The Effect of the Ga Content on the Photocatalytic Hydrogen Evolution of CuIn_{1-x}Ga_xS₂ Nanocrystals. *J. Mater. Chem. A* **2014**, *2* (31), 12317–12322. <https://doi.org/10.1039/C4TA01315H>.
- (76) Maheu, C.; Puzenat, E.; Afanasiev, P.; Cardenas, L.; Geantet, C. Photocatalytic Production of H₂ Is a Multi-Criteria Optimization Problem: Case Study of RuS₂/TiO₂. *Catal. Today* **2021**, *377*, 166–175. <https://doi.org/10.1016/j.cattod.2020.07.041>.
- (77) Qureshi, M.; Takanabe, K. Insights on Measuring and Reporting Heterogeneous Photocatalysis: Efficiency Definitions and Setup Examples. *Chem. Mater.* **2017**, *29* (1), 158–167. <https://doi.org/10.1021/acs.chemmater.6b02907>.
- (78) Guan, Z.; Xu, Z.; Li, Q.; Wang, P.; Li, G.; Yang, J. AgIn₅S₈ Nanoparticles Anchored on 2D Layered ZnIn₂S₄ to Form 0D/2D Heterojunction for Enhanced Visible-Light Photocatalytic Hydrogen Evolution. *Appl. Catal. B Environ.* **2018**, *227*, 512–518. <https://doi.org/10.1016/j.apcatb.2018.01.068>.
- (79) Kandiel, T. A.; Anjum, D. H.; Takanabe, K. Nano-Sized Quaternary CuGa₂In₃S₈ as an Efficient Photocatalyst for Solar Hydrogen Production. *ChemSusChem* **2014**, *7* (11), 3112–3121. <https://doi.org/10.1002/cssc.201402525>.

General conclusion

The aim of this thesis was to explore the potential of *layered CIGS_n compounds* for photovoltaics and solar driven photocatalytic hydrogen production. We wished to obtain a *rapid overview of potentialities of these materials*, in order to focus our future research in the most promising area. Today, we believe that priority should be given to in-depth studies in the field of photocatalysis.

As mentioned before, several layered compounds with *four different structure types* were previously described by our group in the Cu₂S–In₂S₃–Ga₂S₃ system: Cu_{0.32}In_{1.74}Ga_{0.84}S₄ (*CIGS₄*), Cu_{0.65}In_{1.75}Ga_{1.4}S₅ (*CIGS₅*), Cu_{1.44}In_{2.77}Ga_{0.76}S₆ (*CIGS₆*), and Cu_{1.1}In_{2.49}Ga_{1.8}S₇ (*CIGS₇*).

We thought that these materials could potentially be interesting for photo-induced applications for two main reasons. First, CIGS_n compounds exhibit an *optical gap (1.7 - 1.9 eV) comparable to that of the chalcopyrite Cu(In_{0.7}Ga_{0.3})S₂* (1.6 eV), studied as absorber in tandem solar cells but also as photocatalyst for hydrogen evolution reaction (HER). Second, they are *isostructural of ZIS_n compounds* (i.e. ZnIn₂S₄ and Zn₃In₂S₆), extensively investigated as visible-photocatalysts for HER. In addition, the existence of native cationic vacancies and mixed-cationic occupancy in CIGS_n compounds, could be considered as an advantage over ZIS_n compounds, where such defects must be introduced by defect engineering.

To achieve our objective, the *optoelectronic properties of CIGS_n compounds* have been first studied and their *energy diagrams* were determined. This enabled to place these materials in relation to the specifications required for photovoltaic or photocatalysis, and to compare them to well-reported chalcopyrite Cu(In_{0.7}Ga_{0.3})S₂ (CIGS). This comparative study allowed us to select the materials to be favored for exploring applications.

Therefore, our work involved the preparation of *CIGS_n materials in different forms*: bulk samples for optoelectronic measurements, thin films for photovoltaic tests and nanopowders for photocatalytic tests.

The (photo)electrochemical study concludes that *CIGS₄ and CIGS₅ are n-type semiconductors*, unlike the chalcopyrite CIGS for which a p-type behaviour has been determined. *CIGS₆ shows a different behaviour*, generally highlighted in ambipolar materials, where the current is not clearly dominated by one type of charge carrier. Indeed, it exhibits an *ambipolar character* with a slight predominance of electron transport. The *Fermi levels of all lamellar CIGS_n compounds are similar (-4.5 eV)* and higher

in energy than that of the chalcopyrite CIGS (-5.1 eV). This is consistent with a higher electron density in lamellar phases that corroborates the n-type behaviour. In addition, the charge carriers density of *CIGS_n compounds* ($10^{14} - 10^{17} \text{ cm}^{-3}$) is significantly lower than that of CIGS (10^{20} cm^{-3}), which is consistent with their *higher resistivity*.

Photoluminescence measurements suggest *much more in-gap defect states in the lamellar compounds*. Indeed, defect-related emission band is broader and much more intense for CIGS_n compounds than for CIGS. This fact could be directly correlated to the complex crystal structure of CIGS_n compounds. Indeed, these materials exhibit intrinsic cationic vacancies and mixed occupancy on tetrahedral sites, leading to the formation of several intrinsic defects (e.g. V_{Cu}' , Cu_{Ga}'' or $\text{In}_{\text{Cu}}^{\circ\circ}$). These defects can notably affect the carriers recombination process. In fact, regarding the OCP decays observed during chronopotentiometry measurements, the lifetime associated to recombination process is calculated to be quite different from that of chalcopyrite CIGS.

The energy diagrams of the CIGS_n lamellar compounds besides the CIGS chalcopyrite have been established. The Table below is a summary of the results obtained for each of the compounds under investigation.

Table 1: Summary of the results obtained for the CIGS_n and CIGS compounds.

Sample	E _g (eV)	VBM/E _f	E _f (eV)	CBM (eV)	VBM (eV)	Carriers density N(cm ⁻³)	Conductivity (Ω ⁻¹ .cm ⁻¹)	Photoluminescence	Redox potentials (V vs NHE, eV vs Vac)
<i>CIGS₄</i> (n-type)	1.8	1.1	-4.5	-3.8	-5.6	$N_D \sim 10^{15}$	High resistivity	-	CO₂/CO (-0.11 V) (-4.4 eV) H⁺/H₂ (0.00 V) (-4.5 eV) H₂O/O₂ (+1.23 V) (-4.5 eV)
<i>CIGS₅</i> (n-type)	1.9	1.0	-4.4	-3.5	-5.4	$N_D \sim 10^{17}$		Wide intense main band (1.5 eV) red-shifted emission band	
<i>CIGS₆</i> <i>ambipolar</i> (n/p)	1.6	1.1	-4.4	-3.9	-5.5	$N_D \sim 10^{14}$ $N_A \sim 10^{12}$		Wide intense main band (1.4 eV) red-shifted emission band	
<i>CIGS</i> (p-type)	1.6	0.8	-5.1	-4.3	-5.9	$N_A \sim 10^{20}$		Narrow main band (1.7 eV) band to band emission	

The large number of in-gap defects of the CIGS_n compounds together with their low carriers density and high resistivity, can suggest that these compounds would not be suitable for photovoltaic applications. In fact, *all solar cell devices based on CIGS₅ absorber tested* in this work achieved *very low efficiencies*. The *CIGS₅ compound was preferred as absorber*, because the elaboration of single-phase thin films by co-evaporation process is quite simple. Conversely, in the case of CIGS₆ thin films, CuIn₅S₈ was identified as impurity. Given time constraints and the fact that CIGS₄ exhibits the lower carrier density and many polytypes, we did not attempt to prepare thin films.

CIGS₅ thin films exhibit an *ambipolar character* with a strong predominance of electron transport. In addition, their charge carriers density is extremely low (10^{11} cm^{-3}). Therefore, two cell designs have been evaluated: *conventional CIGS-based architecture and n-i-p architecture considering* CIGS₅ as intrinsic material. Different back contacts were used: Mo, FTO and ITO. For classical architecture, *either n-type (CdS and ZnOS) and p-type (spiro-OMeTAD) buffer layers were tested*. Unfortunately, all these tests were unsuccessful in terms of yield.

However, what was a disadvantage for photovoltaics could be an advantage for photocatalysis. Indeed, the *beneficial role of defects* on photocatalysis is widely discussed in the literature. Defects can serve as active site becoming thus directly involved in the catalytic reaction. Secondly, they can tune the electronic structure and improve light absorption by red shifting the absorption region. Finally, defects can serve to effectively separate photogenerated electron–hole pairs, facilitating their involvement in their corresponding redox reactions. For all these reasons, we expected that the existence of native cationic vacancies and mixed-cationic occupancy in CIGS_n compounds, could be considered an advantage over the chalcopyrite CIGS and even ZIS_n compounds. In addition, the ambipolar behaviour evidenced in CIGS_n compounds could enhance the efficiency of simultaneous oxidative and reductive reactions. For this reason, *the initial screening of photocatalytic properties of CIGS_n* materials for hydrogen evolution, it was mainly focused on the compound CIGS₆.

In fact, the energy band position of CIGS₆ (i.e. VBM and CBM) with respect to the water-splitting redox potentials shows that water reduction can be performed but not oxidation. However, using an alcohol as a sacrificial agent, CIGS₆ can presumably be used for hydrogen evolution reaction (HER).

Consequently, *photocatalysts based on nanopowders of CIGS and CIGS₆* were synthesised by microwave-assisted solvothermal synthesis. However, the single-phase nature of CIGS₆ nanopowders could not be clearly determined. Two strategies were implemented to obtain CIGS₆ type nanopowders without CIGS as an impurity. Therefore, cationic substitutions were performed in two isostructural compounds of CIGS₆ ($\text{Zn}_3\text{In}_2\text{S}_6$ and GaInS_3). In this way, *two additional photocatalysts* were prepared: *ZIS-0.6, derived from $\text{Zn}_3\text{In}_2\text{S}_6$* , which has a CIGS₆ type structure, and *GIS-0.1, derived from GaInS_3* , with a CIGS₅ type structure.

The photocatalytic experiments were based on the experimental protocol described in the literature for $\text{CuGa}_2\text{In}_3\text{S}_8$, which presumably exhibits a CIGS₅-type structure. The acid ascorbic (AA) was used as sacrificial electron donor (SED) alongside with triethanolamine (TEOA), in order to investigate photocatalysts activity under both acidic and basic conditions.

In view of our results and as expected based on the singularities of CIGS_n compounds described above, lamellar compounds showed higher performances than chalcopyrite CIGS for hydrogen evolution using AA as SED: 137.6, 52.1 and 14.3 $\mu\text{mol}\cdot\text{g}^{-1}\cdot\text{h}^{-1}$ for ZIS-0.6, GIS-0.1 and CIGS, respectively. However, no hydrogen production was detected for CIGS_6 , probably due to its low specific surface area. Moreover, the H_2 evolution rates of ZIS-0.6, GIS-0.1 photocatalysts are comparable to those reported in literature for related compounds $\text{Zn}_3\text{In}_2\text{S}_6$ (128.8 $\mu\text{mol}\cdot\text{g}^{-1}\cdot\text{h}^{-1}$) and $\text{CuGa}_2\text{In}_3\text{S}_8$ (40 $\mu\text{mol}\cdot\text{g}^{-1}\cdot\text{h}^{-1}$). The photocatalytic activity of these compounds is significantly enhanced by the use of co-catalysts. In our case, the addition of co-catalysts was not effective. It should be noted that comparing experimental yields with those in the bibliography is always a tricky matter, as the experimental conditions must be comparable in order to draw relevant conclusions.

The *main perspective* of this work is in the field of photocatalysis. Although the investigation of the photocatalytic properties of CIGS_n was initiated during the last year of this PhD, it proved to be the most promising application for these materials. The first task will be to optimise the protocol to prepare *single-phase CIGS_6 nanopowders*, with high specific surface area and optimized nanocrystals morphologies. Then, *nanopowders of compounds CIGS_4 , CIGS_5 and CIGS_7* will be also prepared. A second challenge will be to evolve our synthesis protocol towards more sustainable and scalable conditions. In the future, we would like to avoid the use of the glove box in using hydrated precursors and other solvents as water or/and ethanol.

To improve the photocatalytic activity of CIGS_n compounds, an approach based on tailoring their electronic structure by *tuning the catalyst thickness* can be used. In fact, these materials are Van der Waals layered sulphides and their structural slabs can probably be exfoliated by ultrasonication. A second solution would be to use *heterojunction photocatalysts*. In this thesis, CIGS_n compounds have been studied as single material photocatalysts, whereas their use in heterojunctions could improve their performance. In fact, heterojunctions generally show better performance compared to single material photocatalysts, as carrier separation is improved and recombination losses are reduced. In the literature, MoS_2 - ZnIn_2S_4 and MoS_2 - $\text{Zn}_3\text{In}_2\text{S}_6$ heterojunctions have been explored for water splitting and resulted in much higher hydrogen production efficiencies than single ZIS_n photocatalysts (i.e. almost 16 times higher). Therefore, as a next perspective, it would also be interesting to explore MoS_2 - CIGS_n heterojunctions.

The photocatalytic properties of CIGS_n need to be more deeply characterised. More fundamentally, the photocatalytic HER will be deeply characterized by employing SED adapted for chalcogenide photocatalysts as S^{2-} , SO_3^{2-} and $\text{S}_2\text{O}_6^{2-}$. Besides the photonic yield η and H_2 production rate r_{H_2} as function of photocatalyst mass and light intensity, the high-resolution action spectra ($\eta=f(\lambda)$) and the apparent energy activation of

photocatalytic reaction must be determined, in order to elucidate kinetics mechanisms involved in HER. Of course, photocatalytic reduction of CO₂ could be also considered later.

Concerning photovoltaics, CIGS₅ thin films demonstrated that they are not adapted to photovoltaic application probably due to their high electrical resistivity. However, CIGS_n are lamellar compounds that can exhibit large anisotropy in physical properties. In this PhD, the crystal orientation of the sheets with respect to the plane of the substrate was not controlled during co-evaporation process. If electrical conductivity is favoured within the layers of the (M_(Td))_{n-2}In_(Oh)S_n blocs, a textured depot would improve cell performances.

Finally, an *in-depth crystal chemistry study* to determine chemical composition ranges compatible with each CIGS_n structure-type identified (i.e. CIGS₄, CIGS₅, CIGS₆ and CIGS₇) will be carried out. In addition, the existence of these lamellar compounds in the Cu₂Se-In₂Se-Ga₂Se₃ system or in the mixed sulphide-selenide one is currently under investigation.

Titre : Exploration des potentialités des phases lamellaires CIGS_n pour des applications photoinduites

Mots clés : CIGS_n, lamellaire, électrochimie, photovoltaïque, photocatalyse, ambipolaire.

Résumé : De nouvelles phases lamellaires nommées CIGS_n, ont été identifiées dans le système Cu₂S-In₂S₃-Ga₂S₃. Ces composés présentent un caractère 2D marqué avec un gap de van der Waals (~ 3 Å). Leur gap optique (1,7 - 1,9 eV) est comparable à celui de la chalcopyrite Cu(In_{0.7}Ga_{0.3})S₂, étudiée comme absorbeur dans des cellules solaires tandem. D'autre part, les phases CIGS_n sont isostructurales des composés ZnIn₂S₄ et Zn₃In₂S₆, utilisés comme photocatalyseurs pour la production d'hydrogène dans le domaine visible. L'objectif de cette thèse est d'explorer le potentiel des composés CIGS_n pour des applications photovoltaïques et photocatalytiques, en comparaison avec la chalcopyrite Cu(In_{0.7}Ga_{0.3})S₂. Pour ce faire, les diagrammes d'énergie de ces composés ont été établis en combinant des mesures (photo)électrochimiques avec la spectroscopie

de photoélectrons X et la réflectance diffuse. Les bandes de conduction et de valence des composés CIGS_n, se positionnent de manière intéressante par rapport aux potentiels redox impliqués dans certaines réactions photocatalytiques. D'autre part, quelques-uns de ces composés présentent un comportement électrique ambipolaire (type p/n), ce qui les rend prometteurs. Des nanopoudres de CIGS_n ont été synthétisées par voie solvothermale assistée par micro-ondes, afin d'optimiser la microstructure et d'évaluer leur activité photocatalytique pour la production de l'hydrogène en présence d'alcools. Parallèlement, des couches minces de ces matériaux ont été préparées par co-évaporation afin de fabriquer et caractériser des cellules photovoltaïques avec différentes architectures.

Title : Exploring potentialities of CIGS_n lamellar phases for photoinduced applications

Keywords : CIGS_n, lamellar, electrochemistry, photovoltaics, photocatalysis, ambipolar.

Abstract : New lamellar phases, named CIGS_n, have been identified in the Cu₂S-In₂S₃-Ga₂S₃ system. These compounds exhibit a marked 2D character with a van der Waals gap (~ 3 Å). Their optical gap (1.7 - 1.9 eV) is comparable to that of the chalcopyrite Cu(In_{0.7}Ga_{0.3})S₂, studied as an absorber in tandem solar cells. The CIGS_n phases are isostructural of the compounds ZnIn₂S₄ and Zn₃In₂S₆, used as photocatalysts for hydrogen production under visible light. The aim of this thesis is to explore the potential of CIGS_n compounds for photovoltaic and photocatalytic applications, in comparison with the chalcopyrite Cu(In_{0.7}Ga_{0.3})S₂. To do this, their energy diagrams were established by combining (photo)electrochemical measurements with X-ray

photoelectron spectroscopy and diffuse reflectance. The conduction and valence bands of CIGS_n compounds are interestingly positioned in relation to the redox potentials involved in certain photocatalytic reactions. In addition, some of these compounds exhibit ambipolar electrical behaviour (p/n type), which makes them promising. CIGS_n nanopowders were synthesised using a microwave-assisted solvothermal process, to optimise their microstructure and to evaluate their photocatalytic activity for the evolution of hydrogen in the presence of alcohols. In parallel, thin films of these materials were prepared by co-evaporation in order to fabricate and characterise photovoltaic cells with different architectures.